

# **Development of a Scalable Reactor for Bioelectromethanogenesis and other Bioelectrochemical Applications**

zur Erlangung des akademischen Grades einer  
DOKTORIN DER INGENIEURWISSENSCHAFTEN

von der KIT-Fakultät für Chemieingenieurwesen und Verfahrenstechnik des  
Karlsruher Instituts für Technologie (KIT)  
genehmigte

DISSERTATION

von

Franziska Enzmann

---

Tag der mündlichen Prüfung: 17.12.2019

Erstgutachter/-in: Prof. Dr. Christoph Syldatk

Zweitgutachter/-in: Prof. Dr. Clemens Posten



## Acknowledgements

This doctoral thesis was developed between 2016 and 2019 at the DECHEMA Research Institute as part of the project MIKE, funded by the Bundesministerium für Bildung und Forschung (BMBF).

The work was supervised by Prof. Dr. Christoph Syldatk (Karlsruher Institute of Technology) and Dr. Dirk Holtmann (DECHEMA Research Institute). I wish to thank both of them for their constructive support over the course of the project.

Important support was also rendered by Dr. Florian Mayer and all members of the industrial biotechnology research group, including Denise Gronemeier and Marco Genuardi, who prepared their Bachelor thesis based on the project. Cora Kroner and Dr. Markus Stöckl helped a lot with electrochemical issues and Dr. Julia Patzsch with the physisorptions measurements. Andreas Butterhof organized the pipe for the pilot plant reactor. I wish to thank all of them for their collaboration. Special thanks to the DECHEMA workshop team, especially Henry Kopietz, Yvonne Hohmann and Jano Bender, for the construction of the reactors.

Thanks to the Studienstiftung des Deutschen Volkes, especially Prof. Reinhard Fischer and the Karlsruher house of young scientists (KYHS) for their support during my complete studies and especially during this project.

Thanks to my family, especially my partner Jochen, for the continuous support.

## Publications and Presentations

### Original Research Papers

F. Enzmann, F. Mayer, M. Stöckl, K.-M. Mangold, R. Hommel, D. Holtmann, „Transferring bioelectrochemical processes from H-cells to a scalable bubble column reactor,” *Chemical Engineering Science*, vol. 193, pp. 133-143, 2019.

T. Krieg, F. Enzmann, D. Sell, J. Schrader, D. Holtmann, “Simulation of the current generation of a microbial fuel cell in a laboratory wastewater treatment plant,” *Appl. Energy*, vol. 195, pp. 942–949, Jun. 2017.

Mayer, F., Enzmann, F., Lopez, A.M., Holtmann, D., “Performance of different methanogenic species for the microbial electrosynthesis of methane from carbon dioxide,” *Bioresour. Technol.* 121706, 2019.

F. Enzmann, F. Mayer, D. Holtmann, „Process parameters influence the extracellular electron transfer mechanism in bioelectromethanogenesis,” *Int. J. Hydrogen Energy*, accepted for publication 4.07.2019.

### Review Articles and Book Chapters

F. Enzmann, M. Stöckl, A.-P. Zeng, D. Holtmann, “Same but different - Scale-Up and numbering up in electrobiotechnology and photobiotechnology,” *Eng. Life Sci.*, Nov. 2018.

T. Krieg, J. Madjarov, L. F. M. Rosa, F. Enzmann, F. Harnisch, D. Holtmann, K. Rabaey, „Reactors for Microbial Electrobiotechnology,” In *Advances in biochemical engineering/biotechnology* (pp. 127–141), 2018.

F. Enzmann, F. Mayer, M. Rother, D. Holtmann, “Methanogens: biochemical background and biotechnological applications,” *AMB Express*, vol. 8, no. 1, p. 1, 2018.

### Further Publications

F. Mayer, F. Enzmann, A. M. Lopez, and D. Holtmann, “Die mikrobielle Elektrosynthese von Methan,” *BIOspektrum*, vol. 23, no. 4, pp. 471–473, 2017.

### Poster Presentations

F. Mayer, F. Enzmann, A. Martinez-Lopez, D. Holtmann: **Methanogens for Microbial Electrosynthesis**; Himmelfahrtstagung 2017 - Models for Developing and Optimizing Biotech Production, Neu-Ulm, 22.-24.5.2017

F. Enzmann, F. Mayer, D. Holtmann: **Reactor design for bioelectromethanogenesis**; Ismet 6, Lissabon, 3.-6.10.2017

F. Enzmann, D. Holtmann: **The BIG challenge - Using Similarity Theory for the Scale Up of BES**; 4<sup>th</sup> EU-ISMET , Newcastle upon Tyne, 12.-14.9.2018

F. Enzmann, F. Mayer, D. Holtmann: **Transferring bioelectrochemical processes from H-cell to scalable reactor concepts – Bioelectrochemical bubble column**; Himmelfahrtstagung 2018 - Heterogeneities - A key for understanding and upscaling of bioprocesses in up- and downstream, Magdeburg, 7.-9.5.2018

### Conference Talks

F. Enzmann: **Scalable reactors for the bioelectrochemical conversion of CO<sub>2</sub> to CH<sub>4</sub>**; Nachwuchsforscherkongress „24 Stunden für Ressourceneffizienz“ 2018, Pforzheim, 27./28.2.2018

F. Enzmann: **We do it our way – Influences on the mechanism of electron uptake in methanogens**; 4<sup>th</sup> EU-ISMET , Newcastle upon Tyne, 12.-14.9.2018

F. Enzmann: **Scale Up of Bioelectrochemical reactors**; Himmelfahrtstagung 2019: Intensification and digitalisation for integral bioprocessing, Hamburg, 25.5-28.5.2019

## Abstract

An upcoming technology in the field of biological research is bioelectrochemistry, which combines electrical energy and biological processes. The proof of concept for several bioelectrochemical processes was shown in lab-scale applications, and a variety of different bioelectrochemical systems were constructed. Since no common characterization strategies were applied to these reactors and no consensual performance parameters were used to show the results of the processes, comparisons are difficult. This was identified as a major drawback on the way to an industrial application of bioelectrochemistry, since rational optimizations are hardly possible. Only few processes were transferred to bigger scales so far, and long term operations under industrial conditions are rare.

The objective of this doctoral thesis was the design, characterization and Scale-Up of a bioelectrochemical system. The main application for this reactor was bioelectromethanogenesis, which was supposed to be continuously optimized during the project. In this technique, anaerobic methanogens are fed with electrons supplied by a cathode and CO<sub>2</sub>, and convert these substrates to methane. Since fossil fuels are about to be depleted during the next decades, methane could be a substitute fuel, base chemical or substrate for further biological conversions.

A bioelectrochemical system with a bubble column working chamber was designed. The working volume of the device was one liter, with a surrounding counter chamber of 10 liters. The working electrode was placed in the center of the reactor, while the counter electrode was wrapped around the working chamber. The reactor was abiotically characterized using various methods, such as cyclic voltammetry, chronoamperometry and  $k_{L,a}$  measurements to allow comparability to other set-ups. It could be shown by calculation of the Wagner number, that the electrical field within the system was evenly distributed and by calculation of the Reynolds, Bond and Weber number that a laminar, homogeneous, bubbly flow established itself in the working chamber.

By continuous gassing with oxygen-free in-gas streams, it was possible to host anaerobic methanogenic archaea, to provide them with gaseous CO<sub>2</sub> contained in the in-gas and electrons from the working electrode as substrates and to produce methane. A pure culture of *Methanococcus maripaludis* was used as biocatalyst to allow comparison to published research data.

The first setup already showed a methane production of 0.23 mmol\*d<sup>-1</sup>, which equaled a specific methane production rate of 33.8 mmol\*d<sup>-1</sup>\*m<sup>2</sup> at a Coulombic efficiency of 51.0 %. This was higher than reported for bioelectromethanogenesis with *M. maripaludis* before. The space-time-yield was comparable to commonly used H-cell reactors tested for comparison, which contain a working volume of 100 ml. The process of bioelectromethanogenesis was further optimized, leading to a 9.8 fold increase in methane production rate to 2.3 mmol\*d<sup>-1</sup> at a Coulombic efficiency of 56.4 %. The specific methane production rate in this case was 81.4 mmol\*d<sup>-1</sup>\*m<sup>2</sup>, which was also comparable to data shown for bioelectromethanogenesis with mixed cultures, which do usually result in higher production

rates. The results obtained with the bubble column reactor were also comparable to those obtained in a bioelectrochemical stirred tank reactor with similar operating conditions and better than in H-cells under similar conditions, including same electrode material, membrane material and working potential.

The most efficient step of optimization was the shift of the applied working potential from -0.9 V vs. Ag/AgCl to -1.1 V vs. Ag/AgCl, which caused a 143.2 % higher total methane production rate, followed by the quadrupling of the electrode surface area, leading to a 139.6 % improvement of the total methane production rate, although the specific methane production rate based on the geometrical surface area declined. The change of the electrode type caused a 54.3 % improvement. The change of the CO<sub>2</sub> content in the in-gas from 20 % to 100 % was increasing the total methane production rate by 83.9 %. The increase of the gassing rate from 30 ml\*min<sup>-1</sup> to 90 ml\*min<sup>-1</sup> improved the total methane production rate by 35.8 %. Taking the various influences of the different optimizations into account, it seems likely that the electron availability is the main limitation of the process, followed by the CO<sub>2</sub> availability.

No significant improvement of the process was observed when adding 3-(N-morpholino)-propanesulfonic acid buffer to the medium, when increasing the anode area or when changing the initial optical density of the microorganisms. The biological aspect of the system is therefore not limiting the process. Also the change of the membrane type from proton exchange to cation exchange membrane did not lead to a significant increase of the methane production rate. The fact that the main limitation was the electron supply was further confirmed by applying a high current of -100 mA to the system, instead of an applied working potential, which could increase the methane production rate to 5.7 mmol\*d<sup>-1</sup> at a similar Coulombic efficiency, showing that the biocatalyst still converted the same percentage of electrons supplied to methane and was therefore not limiting. The high current led also to a more negative potential at the working electrode, so that all in all the abiotic hydrogen production was more efficient than the biocatalyzed methane production.

The energy efficiency of the process was extremely low (0.002 %) when taking the heating of the system into account. Assuming that waste energy can be used for heating, the energy efficiency amounted to 17.7 % under optimized conditions. In terms of industrial use, it could be demonstrated that the process recovered quickly after system failures, e.g. a power gap or a breakdown of the gassing. In contrast, bioelectromethanogenesis did not fully recover after a breakdown of the temperature control or sudden changes of the in-gas composition.

The developed concept was transferred into pilot-scale by a rational Scale-Up based on Similarity Theory, which was not shown before for bioelectrochemical systems. The pilot scale reactor had a working volume of 50 liters and a counter volume of 150 liters. The total methane production rate added up to 11.7 mmol\*d<sup>-1</sup>, which was the highest reported for pure culture bioelectromethanogenesis

so far. In contrast, the specific methane production rate was low,  $10.2 \text{ mmol}\cdot\text{d}^{-1}\cdot\text{m}^2$  only, although the energy efficiency increased to 27.0 % and the Coulombic efficiency reached 113.6 %, which could not conclusively be explained. Apart from Scale-Up, also different Numbering-Up strategies were used to enlarge the working volume. It was demonstrated that by operating three reactors as reactor cascade, the specific methane production rate increased from  $60.4 \text{ mmol}\cdot\text{d}^{-1}\cdot\text{m}^2$  to  $178.5 \text{ mmol}\cdot\text{d}^{-1}\cdot\text{m}^2$ . An additional electrical connection could not further improve the performance of bioelectromethanogenesis significantly.

The developed bioelectrochemical bubble column reactor was also tested as microbial fuel cell, to show the transferability of the reactor to other processes. These experiments revealed that the reactor was capable of producing  $627 \text{ mA}\cdot\text{m}^2$  current at a Coulombic efficiency of 23.1 %. This was comparable to the results obtained in a bioelectrochemical stirred tank reactor.

This work introduces a new, scalable and flexible reactor design to the field of bioelectrochemistry. Due to its flexibility this reactor could be used for various bioelectrochemical processes, process optimization and offers comparability to existing systems. It can therefore serve as a starting point for the development of industrially relevant research and encourage the transfer of bioelectrochemistry from lab-scale to industrial application.

## Zusammenfassung

Als relativ junges Forschungsfeld der Biotechnologie erlaubt es die Bioelektrotechnologie, elektrische Energie und biologische Katalyse zu koppeln. Verschiedene Studien konnten bereits mehrere mögliche Anwendungen demonstrieren, wobei die dazu konstruierten bioelektrochemischen Systeme sich noch auf den Labormaßstab beschränkten. Diese Systeme wurden nur in seltenen Fällen einheitlich charakterisiert und eine universelle Angabe der Leistungsparameter konnte sich noch nicht durchsetzen, was dazu führt dass derzeit Vergleiche der unterschiedlichen Reaktoren und Prozesse nur schwer möglich sind. Dieser Umstand ist ein generelles Hindernis auf dem Weg zur industriellen Anwendung der Bioelektrotechnologie, da durch die fehlende Vergleichbarkeit auch eine rationale Optimierung erschwert wird. Nur wenige Prozesse wurden bisher in größere Maßstäbe übertragen und unter industrienahen Bedingungen über längere Zeit hinweg betrieben.

Ziel dieser Doktorarbeit ist die Konzipierung, Charakterisierung und Maßstabsübertragung eines bioelektrochemischen Systems. Die hauptsächliche Anwendung des Reaktors soll die Bioelektromethanogenese sein. Dieser Prozess soll während der Arbeit optimiert werden. Anaerobe Mikroorganismen wandeln dabei Elektronen von einer Kathode und  $\text{CO}_2$  zu Methan um. Methan könnte einen Ersatz für Erdöl darstellen, da es sowohl als Brennstoff, zur chemischen Synthese wie auch in biologischen Prozessen als Ausgangsstoff eingesetzt werden kann.

Es wurde ein bioelektrochemisches System konstruiert, dessen Arbeitskammer als Blasensäule gestaltet ist. Das Arbeitsvolumen in dieser Kammer betrug einen Liter, während die Gegenkammer, die die Arbeitskammer umgab, zehn Liter fasste. Die Arbeitselektrode wurde in der Mitte der Arbeitskammer platziert, die Gegenelektrode um die Arbeitskammer gewickelt. Der Reaktor wurde durch verschiedene Methoden abiotisch charakterisiert. Diese umfassten unter anderem Cyclovoltammetrie, Chronoamperometrie und  $k_L a$ -Messung, wodurch es ermöglicht werden sollte, verschiedene Reaktortypen miteinander zu vergleichen. Die Berechnung der Wagnerzahl konnte beispielsweise zeigen, dass das elektrische Feld im Reaktor gleichmäßig verteilt war, während die resultierenden Reynolds-, Bond- und Weberzahlen belegten, dass sich in der Arbeitskammer eine laminare, homogene Blasenströmung entwickelte.

Anaerobe Methanogene wurden in der Arbeitskammer mit  $\text{CO}_2$  aus dem sauerstofffreien Eingangsgasstrom und Elektronen von der Arbeitselektrode versorgt, um Methan produzieren zu können. *Methanococcus maripaludis* wurde als Reinkultur verwendet, da dieser Organismus bereits in der Literatur als elektroaktiv beschrieben wurde und somit Vergleichsdaten vorlagen.

In den ersten Versuchen konnte bereits eine absolute Methanproduktionsrate von  $0,23 \text{ mmol} \cdot \text{d}^{-1}$  erzielt werden, was einer spezifischen Methanproduktionsrate von  $33,8 \text{ mmol} \cdot \text{d}^{-1} \cdot \text{m}^2$  entsprach. Dabei wurde eine Coulombeffizienz von 51,0 % erreicht. Die gemessene Produktionsrate lag damit höher als bislang für Bioelektromethanogenese mit *M. mariplauds* beschrieben. Die Raum-Zeit-

Ausbeute im neu entwickelten Reaktor war vergleichbar mit der, die in den üblicherweise im Labor genutzten H-Zellen ermittelt wurde.

Die Bioelektromethanogenese wurde im Anschluss weiter optimiert, was eine Verbesserung der absoluten Methanproduktionsrate um den Faktor 9,8 auf  $2,3 \text{ mmol}\cdot\text{d}^{-1}$  (spezifische Methanproduktionsrate:  $81,4 \text{ mmol}\cdot\text{d}^{-1}\cdot\text{m}^{-2}$ ) einbrachte. Die Coulombeffizienz lag dabei bei 56,4 %. Die erzielte spezifische Methanproduktion lag damit im Bereich von beschriebenen Produktionsraten, die mit Mischkulturen erreicht wurden, welche üblicherweise höhere Ausbeuten erlauben. Die Ergebnisse aus der bioelektrochemischen Blasensäule sind vergleichbar mit Ergebnissen, die in einem bioelektrochemischen Rührkesselreaktor erzielt wurden und höher als in einer H-Zelle unter vergleichbaren Bedingungen (Elektroden- und Membranmaterial, Arbeitspotential, Eingangsgaszusammensetzung).

Die höchste Verbesserung von 143,2 % konnte erreicht werden, indem das Arbeitspotential von -0,9 V vs. Ag/AgCl auf -1,1 V vs. Ag/AgCl herabgesetzt wurde. Ebenfalls sehr effektiv war die Vervierfachung der Elektrodenfläche mit einer um bis zu 139,6 % Steigerung der absoluten Methanproduktionsrate, obwohl die spezifische Methanproduktionsrate durch die Vergrößerung der Elektrodenfläche sank. Auch durch die Veränderung des Arbeitselektrodenmaterials konnte die absolute Methanproduktionsrate um 54,3 % erhöht werden. Bezüglich der Begasung steigerte die Veränderung der Eingangsgaszusammensetzung von 20 %  $\text{CO}_2$  zu 100 % die Methanproduktionsrate um 83,9 %, gefolgt von einer 35,8 %igen Verbesserung durch die Erhöhung des Eingangsgasstroms von  $30 \text{ ml}\cdot\text{min}^{-1}$  auf  $90 \text{ ml}\cdot\text{min}^{-1}$ . Diese Ergebnisse lassen folgern, dass die Elektronenverfügbarkeit die größte Limitierung der Bioelektromethanogene darstellt, gefolgt von den  $\text{CO}_2$  Verfügbarkeit.

Keine signifikante Steigerung der Methanproduktion konnte hingegen bei der Zugabe von 3-(N-morpholino)-Propansulfonsäure Puffer zum Medium beobachtet werden. Auch die Vergrößerung der Anode oder die Veränderung der anfänglichen optischen Dichte im Reaktor konnte die Produktion nicht erhöhen. Das lässt darauf schließen, dass der Biokatalysator den Prozess nicht limitiert. Auch die Verwendung einer Kationenaustauschmembran anstelle einer Protonenaustauschmembran verbesserte die Methanproduktion nicht signifikant. Durch einen weiteren Test konnte bestätigt werden, dass die Elektronenverfügbarkeit tatsächlich die größte Limitierung des Prozesses darstelle: Durch Anlegen eines Stroms von -100 mA statt eines Arbeitspotentials konnte die absolute Methanproduktionsrate bei gleichbleibender Coulombeffizienz auf  $5,7 \text{ mmol}\cdot\text{d}^{-1}$  gesteigert werden. Dies zeigt, dass die Mikroorganismen auch den zusätzlichen Strom genauso effizient zu Methan umsetzen können, also der Strom die Limitierung darstellt. Der hohe angelegte Strom führte allerdings auch zu einem negativeren Arbeitspotential an der Arbeitselektrode, dass die abiotische Wasserstoffentstehung energieeffizienter erlaubt als die biokatalysierte Methanerzeugung.

Die Energieeffizienz des Prozesses war sehr niedrig (0,002 %), wenn die Heizleistung in die Energieberechnung mit einbezogen wurde. Falls Abwärme aus anderen Prozessen in einem integrierten Wärmekonzept genutzt werden könnte, würde die Energieeffizienz ohne Heizleistung nach der Optimierung 17,7 % betragen.

Bezüglich der industriellen Anwendbarkeit des Prozesses ließ sich zeigen, dass die Bioelektromethanogenese sich nach Störfällen schnell wieder stabilisiert, beispielsweise nach Strom- oder Begasungsausfällen. Im Gegensatz dazu wurden nach plötzlichen Schwankungen in der Gaszusammensetzung oder Temperaturschwankungen nicht die gleichen Methanproduktionsraten erzielt wie vor der Störung.

Das entwickelte Reaktorkonzept wurde über eine rationale, auf der Ähnlichkeitstheorie beruhende Maßstabsübertragung in den Pilotmaßstab übertragen. Die Pilotanlage fasste ein Arbeitsvolumen von 50 Liter und in der Gegenkammer 150 Liter. Die absolute Methanproduktionsrate betrug  $11,7 \text{ mmol} \cdot \text{d}^{-1}$  und erzielte somit die höchste bis dahin beschriebene Produktion. Allerdings lag die spezifische Methanproduktionsrate bezogen auf die geometrische Oberfläche der Arbeitselektrode nur bei  $10,2 \text{ mmol} \cdot \text{d}^{-1} \cdot \text{m}^{-2}$ , obwohl die Energieeffizienz ohne Einberechnung der Heizleistung auf 27,0 % gesteigert werden konnte. Die Coulombeffizienz lag dabei bei 113,6 %, wobei dieser hohe Wert nicht abschließend erklärt werden konnte. Außerdem wurden verschiedene "Numbering-Up" Ansätze verfolgt, um das Arbeitsvolumen und damit die Methanproduktion zu steigern. Es konnte gezeigt werden, dass eine kaskadenartige Führung des Gasstromes durch drei Reaktoren die spezifische Methanproduktionsrate von  $60,4 \text{ mmol} \cdot \text{d}^{-1} \cdot \text{m}^{-2}$  auf  $178,5 \text{ mmol} \cdot \text{d}^{-1} \cdot \text{m}^{-2}$  steigerte. Eine zusätzliche elektrische Verbindung der drei Reaktoren konnte dieses Ergebnis nicht signifikant verbessern.

Die bioelektrochemische Blasensäule wurde auch als mikrobielle Brennstoffzelle genutzt um die universelle Einsetzbarkeit des Reaktors zu demonstrieren. Die Versuche erzielten eine Stromproduktion von  $627 \text{ mA} \cdot \text{m}^{-2}$  bei einer Coulombeffizienz von 23,1 %. Die Ergebnisse waren vergleichbar mit Daten aus dem bioelektrochemischen Rührkesselreaktor.

Diese Dissertation stellt einen neuen, flexiblen und skalierbaren bioelektrochemischen Reaktortyp vor. Dieser kann für unterschiedliche bioelektrochemische Prozesse genutzt werden und ist geeignet, um darin Prozessoptimierungen durchzuführen. Vergleiche zu anderen Reaktortypen sind möglich. Das System kann daher als Ausgangspunkt für die Entwicklung industrierelevanter Prozesse dienen und könnte damit den Übergang der Bioelektrotechnologie aus dem Labor hin zu industriellen Anwendungen beschleunigen.

## Table of Contents

Acknowledgements .....	I
Publications and Presentations .....	II
Abstract .....	IV
Zusammenfassung .....	VII
Table of Contents .....	X
1 Introduction and Motivation .....	1
2 Scientific Background .....	3
2.1 Bioelectrochemistry .....	3
2.1.1 Microbial Fuel Cell .....	4
2.1.2 Bioelectromethanogenesis .....	6
2.2 Reactor Design .....	13
2.2.1 Microbial Electrosynthesis and Bioelectromethanogenesis Reactors .....	13
2.2.2 Reactor Characterization and Evaluation .....	16
2.2.3 Similarity Theory as Tool for Reactor Scale-Up .....	20
2.2.4 Electrode Materials .....	20
2.2.5 Membrane Materials .....	23
3 Tasks and Objectives .....	24
4 Results and Discussion .....	25
4.1 Development of a Bioelectrochemical Reactor .....	25
4.2 Abiotic Reactor Characterization .....	28
4.2.1 Electrochemical Characterization .....	28
4.2.2 Physical Characterization .....	37
4.3 Development and Optimization of the Bioelectromethanogenic Process .....	42
4.3.1 <i>Methanococcus maripaludis</i> as Electroactive Methanogen .....	42
4.3.2 Potential Optimization .....	46
4.3.3 Electrode Optimization .....	47
4.3.4 Membrane Optimization .....	55
4.3.5 Optimization of Mixing and Gassing .....	58

---

4.3.6	System Stability.....	65
4.3.7	Comparison to Other Reactors and Long Term Operation .....	73
4.3.8	Numbering-Up .....	77
4.3.9	Characterization and Operation of the Pilot Scale Reactor.....	80
4.3.10	Comparison to Literature Data.....	86
4.4	Microbial Fuel Cell .....	89
5	Conclusion and Outlook.....	92
6	Materials and Methods.....	95
6.1	Chemicals and Gases.....	95
6.2	Lab-Scale Reactors.....	95
6.2.1	Main Process Equipment.....	95
6.2.2	H-Cell.....	97
6.2.3	Bubble Column Reactor .....	98
6.2.4	Modified Stirred Tank Reactor.....	101
6.3	Reactor Characterization .....	102
6.3.1	Electrochemical Characterization.....	102
6.3.2	Physical Characterization .....	106
6.4	Electrode Materials .....	112
6.5	Membranes.....	116
6.6	Bioelectromethanogenesis .....	117
6.6.1	<i>Methanococcus maripaludis</i> .....	117
6.6.2	Process Development and Optimization in Lab-Scale .....	118
6.6.3	Numbering-Up of the Process .....	124
6.6.4	Scale-Up of the Process.....	126
6.6.5	Design and Operation of the Pilot Plant.....	128
6.7	Microbial Fuel Cell .....	132
	Symbols.....	134
	Abbreviations .....	136
	References.....	137
	List of Figures .....	146

---

List of Tables ..... 148

Appendix ..... 149

## 1 Introduction and Motivation

Some microorganisms are capable of exchanging electrons with solid inorganic materials. This phenomenon can be found naturally in various environments, where microorganisms exchange electrons with minerals, especially if no gaseous or organic electron donors or acceptors are available (Koch and Harnisch, 2016a, 2016b). Using this ability for technological applications combining an electrode for the exchange of electrons and “electroactive” microorganisms led to the research field of electrobiotechnology. During the last two decades, the electrobiotechnology received lots of interest, and various bioelectrochemical systems (BES) were developed. For this purpose, electrodes are introduced into a bioreactor containing electroactive microorganisms, which interact with the electrode surface (Schröder et al., 2015). If the electroactive microorganisms take up electrons from an electrode to produce a chemical compound, the system is referred to as microbial electrosynthesis cell (MES). An example for such an MES process is the production of methane out of CO<sub>2</sub>. Methane could be a suitable replacement for fossil oil, which is about to be depleted during the next decades (Olah, 2005; Strong et al., 2015). Methane can meet the requirements of an oil replacement in areas of application, which are the storage and transport of energy, e.g. via tanks and pipelines, the energy release during combustion in engines and power plants, and the use as a base chemical for chemical industry and also as substrate for biological processes (Olah, 2005; Strong et al., 2015). Methane could act as energy storage if produced by using electricity from decentralized and fluctuating renewable energy sources, like windcraft and photovoltaic (Bassani et al., 2015). It is an advantage that the methane grid in many countries is already well developed and methane-based power plants are widely spread. Methane can be used as fuel for cars and other vehicles, too, and is easier to store than hydrogen (Andriani et al., 2014). Several chemical syntheses work with methane as an educt, such as the production of methanol, formaldehyde, hydrogen, hydrocarbons, aromates and Syngas (Lunsford, 2000). From these substances, other syntheses can be carried out (Olah, 2005). Theoretically, these routes could replace the steam cracking route for the production of light olefins, although the energy demand is currently still too high (Ren et al., 2008). Additionally, methanotrophic bacteria can use methane as carbon source. Several applications are currently investigated, like production of polymers, lipids and enzymes (Strong et al., 2015).

Limited amounts of fossil methane can be found as natural gas. Apart from that, it can also be produced chemically via the Sabatier process (Brooks et al., 2007). Another way for methane production is the biological digestion of organic matter, such as energy crops, organic wastes or manure. The product of this biological digestion is biogas, a mixture mainly consisting of methane and carbon dioxide (Andriani et al., 2014). In Germany, more than 9000 biogas plants produce as much as 29.41 TWh energy in methane per year (Fachverband Biogas e.V., n.d.).

Another promising method for methane production is the conversion of CO<sub>2</sub> to methane using hydrogenotrophic methanogens. These are capable of producing methane solely out of CO<sub>2</sub> and hydrogen (Bassani et al., 2015). H<sub>2</sub> is usually produced by water electrolysis, a process in which electricity is used to split water and generate oxygen and hydrogen. An upcoming idea is to combine this electrochemical process with the biological methanogenesis to form an integrated bioelectromethanogenic process to avoid production, storage and transportation of explosive hydrogen (Xu et al., 2014). CO<sub>2</sub> is used as the carbon source in this process. The electricity for bioelectromethanogenesis could be gained from excess currents of renewable energy production. This would be interesting in terms of storage of electrical energy, but due to fluctuations it could be necessary to bridge power gaps (Bassani et al., 2015).

Currently, several research groups are investigating bioelectromethanogenesis (Geppert et al., 2016). It has been shown that the electrode material, the methanogenic strain or consortium and also the anodic reaction can affect the process of bioelectromethanogenesis, but up to now, no complete optimization of one of these parts was carried out. Under discussion are also the quantification of the overall energy efficiency and the biological mechanism. Another critical aspect is the design of a suitable reactor. Comparable studies of this topic are rare, and scalability is not given for most systems. The actual potential of the process is therefore not yet known (Blasco-Gómez et al., 2017; Geppert et al., 2016). Bioelectrochemistry in combination with methane production could be a feasible and environmentally friendly technology for the storage of electrical energy, while at the same time reducing CO<sub>2</sub> emissions of other processes like biogas purification. This thesis examines the optimization and Scale-Up of reactors for bioelectromethanogenesis to create an interesting process for industrial purposes.

## 2 Scientific Background

### 2.1 Bioelectrochemistry

Three main types of bioelectrochemical systems are currently discussed in research, which are the microbial fuel cell (MFC), the microbial electrolysis cell (MEC) and the microbial electrosynthesis cell (MES) (Figure 1) (Patil et al., 2015; Schröder et al., 2015; Sharma et al., 2014).

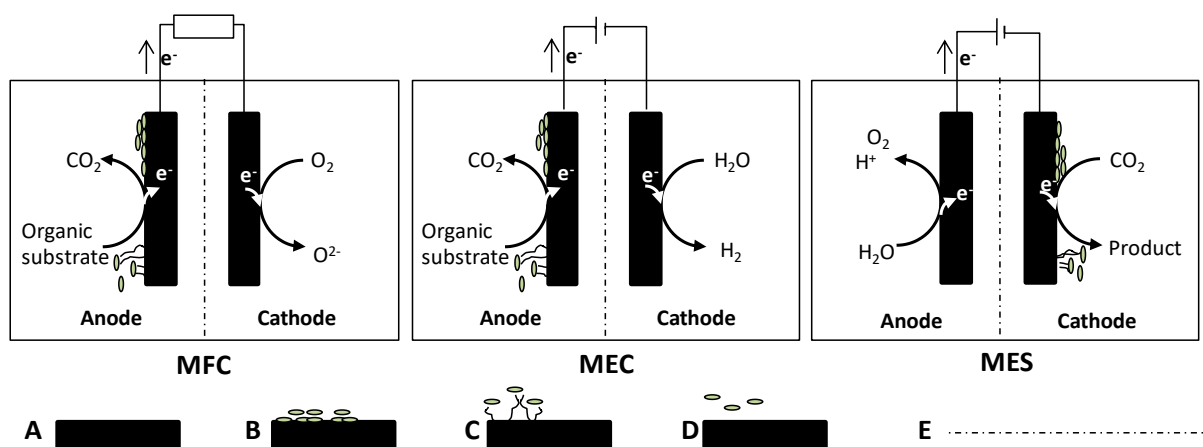


**Figure 1: Different bioelectrochemical applications**

Schematic overview of different electrochemical systems; MFC: microbial fuel cell, microorganisms are located at the anode; MEC: microbial electrolysis cell, microorganisms are located at the anode; MES: microbial electrosynthesis cell, microorganisms are located at the cathode; A) Electrode material; B) Electrode material with attached electroactive biofilm; C) Electrode with electroactive microorganisms attached via conductive filaments; D) Electrode with planctonic microorganisms; E) Ion exchange membrane.

In an MFC, microorganisms degrade organic substrates and transfer the released electrons in an anodic process to an electrode, producing an electrical current. This application can for example be integrated into waste water treatment. The MFC technology has already been studied intensively, and several Scale-Up tests have been carried out (Cheng and Logan, 2011; Logan, 2010a; Logan et al., 2006). A combination of the MFC technology with a cathodic process leads to an MEC, where an additional potential is applied to allow hydrogen or electrochemical methane production at the cathode. In contrast, MES are used for the production of more complex products, such as fuels, terpenes or alcohols (Cheng et al., 2009; Krieg et al., 2018b; Vassilev et al., 2018). There, the microorganisms take up electrons from the cathode to produce valuable products from electrical current and low molecular substrates (Bajracharya et al., 2017). The anodic process is often not of interest. Most of these cathodic processes are still restricted to lab-scale.

### 2.1.1 Microbial Fuel Cell

The best studied form of bioelectrochemical systems is the microbial fuel cell. In contrast to microbial synthesis cells, this system produces current out of chemical compounds via electroactive bacteria (Logan et al., 2006). These bacteria degrade organic matter and transfer the released electrons to an anode instead of using a chemical electron acceptor like oxygen (Logan et al., 2006). MFCs can be operated with an applied voltage to allow an easy electron transfer to the anode (Ye et al., 2017) or using an additional resistance between anode and cathode to gain usable voltages (Du et al., 2007). The MFC technology is especially interesting in the field of waste water treatment. Large amounts of organic matter could be used to produce electricity, which could then be transferred to energy intense operations of the sewage water plant (Sonawane et al., 2017).

Several studies and reviews have focused on microbial fuel cells so far. Most of them considered mixed cultures (e.g. out of sewage water plants) for current generation, but there have also been investigations using pure cultures (Kumar et al., 2018). The current production in mixed culture MFCs was usually higher than in pure culture MFCs (Sydow et al., 2014). For pure culture MFCs, mainly *Geobacter* and *Shewanella* species were used, two very well studied model organisms for electroactivity (Kumar et al., 2018). *Shewanella oneidensis* MR-1 is a fully sequenced bacterium, which shows manganese and iron reducing activity in its natural environment. It turned out that surplus electrons from its metabolism can also be transferred to electrodes instead of manganese reduction (Bretschger et al., 2007). In MFCs, *S. oneidensis* is often used, converting lactate to acetate, releasing four electrons per lactate molecule to the electrode (Equation1) (Lanthier et al., 2008).



In MFCs with *Shewanella oneidensis* strain MR-1, current densities produced in different systems were reported as summarized in Table 1.

Table 1: Current generation in MFCs inoculated with *S. oneidensis* MR-1

Current density [mA*m <sup>-2</sup> ]	Anode material	MFC System	Resistance/potential	Reference
137.5	Carbon felt	two-chamber	10 Ω	(Bretschger et al., 2007)
49	Graphite Stick	two-chamber	560 Ω	(Lanthier et al., 2008)
260	Carbon fiber brush	two chamber	1000 Ω	(Watson and Logan, 2010)
750	Carbon fiber brush	cube, single chamber	1000 Ω	(Watson and Logan, 2010)
1950	Carbon fiber brush	bottle, single chamber	1000 Ω	(Watson and Logan, 2010)
700	Graphite felt	single chamber	100 Ω	(Newton et al., 2009)
250	Glassy carbon	single chamber	0.24 v vs. SHE <sup>1)</sup>	(Ye et al., 2017)

<sup>1)</sup> SHE: Standard hydrogen electrode

The process of electricity generation does take place at the anode side of the MFC. At the cathode, oxygen reduction is often the counter reaction (Janicek et al., 2014). Therefore, gas diffusion cathodes can be used, which are directly exposed to the surrounding air (Shehab et al., 2013).

Different reactor types were tested for MFCs so far, including two chamber systems as well as single chamber systems (Du et al., 2007). Apart from the reactor type, also different electrode materials (Sonawane et al., 2017) and membranes (Kim et al., 2007) were examined in MFCs. There is not one optimal electrode material, but it turned out that three dimensional electrodes are advantageous (Sonawane et al., 2017). The effect of membrane type is only significant, if the electrode spacing is low; then, anion exchange membranes (AEMs) performed best (Kim et al., 2007). First Scale-Up experiments have been reported for MFC working with mixed cultures and wastewater (reviewed by (Janicek et al., 2014; Logan, 2010a)). Several systems in larger scale are cylindrical systems; the cathode usually surrounds the anode (or vice versa), separated by a membrane or isolator (Janicek et al., 2014). Other studies suggest a flat plate design for larger scale systems (Janicek et al., 2014). The conclusion that can be drawn from those experiments is that the performance is still too low for technical application (Janicek et al., 2014). The focus of MFC research lies currently on the reactor design and scalability (Kumar et al., 2018), the electrode optimization (Hindatu et al., 2017; Sonawane et al., 2017), and meanwhile also on the mathematical modelling and simulation (Krieg et al., 2017).

### 2.1.2 Bioelectromethanogenesis

Bioelectromethanogenesis via electron uptake from an electrode by electroactive methanogens was described by Cheng (Cheng et al., 2009) and was recently reviewed (Blasco-Gómez et al., 2017; Geppert et al., 2016). Bioelectromethanogenesis can be seen as a microbial electrosynthesis process, since an organic product is desired (Schröder et al., 2015). Although the biological mechanisms of electron transfer are not yet understood in detail, it is proposed that the methanogens can either take up electrons directly from the cathode surface to form methane, or hydrogen is produced at the cathode and methanogens take up the hydrogen to form methane indirectly. The following section will give an overview over electroactive methanogens.

#### 2.1.2.1 Electroactive Methanogens

Methanogens belong to the biological kingdom of archaea, a very diverse group of microorganisms. The common properties of all methanogens are the ability to produce methane and the obligate anaerobic growth, even though they might use different substrates, are different in shape, have different optimum growth conditions and various habitats (Garcia et al., 2000; Liu and Whitman, 2008). Methanogens are currently subdivided into 7 orders, which are *Methanobacteriales*, *Methanococcales*, *Methanomicrobiales*, *Methanosarcinales*, *Methanopyrales*, *Methanocellales* and *Methanomassiliicoccales* (Lang et al., 2015; Liu and Whitman, 2008), but new orders are under discussion after DNA-analysis (Alpana et al., 2017). Each of these orders is again subdivided into several families, except the order of *Methanopyrales*, which includes only one species (Garcia et al., 2000; Liu and Whitman, 2008).

Three main pathways of methane formation are known in methanogens. These are the hydrogenotrophic, the methylotrophic and the acetoclastic route, which differ in the substrate converted into methane; several methanogenic strains can use more than one of these paths (Liu and Whitman, 2008). The most common hydrogenotrophic path allows the conversion of H<sub>2</sub> and CO<sub>2</sub> or formate to methane. Methylotrophic methanogens, in general belonging to the group of *Methanosarcinales*, use methanol or methylated amines and sulfides as substrates. Acetoclastic methanogens (*Methanosarcinales* and *Methanosaeta*) convert acetate to methane (see also Figure 2) (Garcia et al., 2000; Liu and Whitman, 2008). In terms of bioelectromethanogenesis, the hydrogenotrophic metabolism is considered as the most important (Blasco-Gómez et al., 2017).

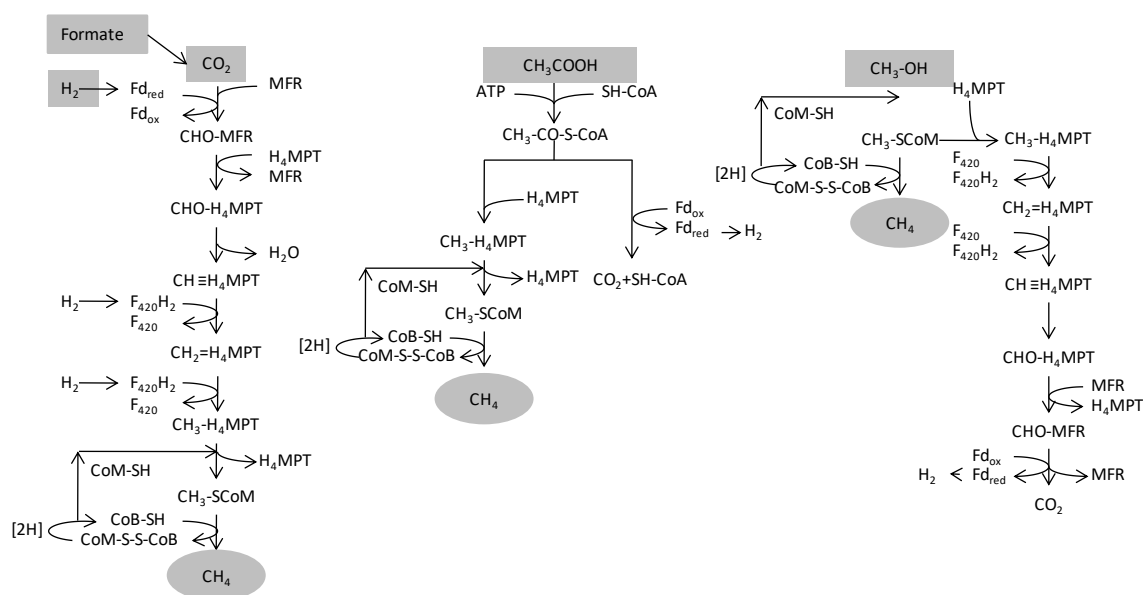


**Figure 2: Methanogenesis pathways**

Left: hydrogenotrophic methanogenesis from  $\text{CO}_2$  and/or formate and hydrogen to methane; middle: acetoclastic methanogenesis from acetate to methane; right: methylotrophic methanogenesis from methanol to methane, other methylated compounds could also be consumed.

In bioelectromethanogenesis, surface proteins and proteins released to the culture medium are likely to be relevant in terms of electron uptake (Deutzmann et al., 2015). The conversion of  $\text{CO}_2$  to methane within bioelectromethanogenesis takes place at the cathode. The complete mechanism of the electron uptake is not yet known in detail, but three means of electron transfer are suggested (Geppert et al., 2016). Firstly, the electrons at the cathode are transferred to protons, which were produced at the anode before, and form hydrogen. The methanogens could then produce methane out of hydrogen and  $\text{CO}_2$ . This would be referred to as an indirect electron transfer (IET) (Villano et al., 2010). Hydrogenases are crucial molecules for methanogenic metabolism, since they activate hydrogen for further usage within the cells (Thauer et al., 2010). These proteins would be involved in the indirect bioelectromethanogenesis by taking up hydrogen, but some hydrogenases can also convert  $\text{H}^+$  to  $\text{H}_2$  (Vignais and Billoud, 2007). This would lead to a bio-catalyzed hydrogen formation as a first step before indirect bioelectromethanogenesis.

But it was also proven that electron uptake without hydrogenases can be possible (Lohner et al., 2014). The methanogens could accept the electrons directly from the cathode surface and produce methane using electrons, protons and  $\text{CO}_2$ . This direct electron transfer (DET) could happen via surface proteins (e.g. cytochromes) or conductive filaments (Cheng et al., 2009). A property of the order of *Methanosarcina*, for example, is the presence of cytochromes, together with methanophenazine, on the cell surface (Garcia et al., 2000). This leads to differences in the energy metabolism of the organisms, compared to methanogens without cytochromes, and, in general, leads to a wider range of convertible substrates and higher methane yields (Thauer et al., 2008). It is highly possible that cytochromes play a major role in direct electron uptake from an electrode (Sydow et al., 2014). Since not all

methanogens which are considered electroactive by direct electron transfer do contain cytochromes, other means of DET must be involved. As an example, hydrogenases, which are present on the surface of all wild type methanogenic strains, are considered to be important for the direct electron uptake, too (Deutzmann et al., 2015). In a microbial consortium, it is also possible that other microorganisms than methanogens accept the electrons directly or indirectly from the cathode and perform a direct interspecies electron transfer (DIET) to the methanogens. It has been reported that this syntrophic transfer can happen very specifically between two species. Methanogens known to perform this type of electroactivity are for example *Methanosaeta harudinacea* and *Methanosarcina barkeri* (Deutzmann and Spormann, 2017; Gorby et al., 2006; Rotaru et al., 2014a, 2014b).

The electrons could also be transferred to the methanogens via mediator molecules (e.g. riboflavins or methanophenazine, added or secreted), which accept the electrons at the cathode surface and shuttle it to the microorganisms. The methanogens would then take up protons, electrons and  $\text{CO}_2$  to create methane. This version is called mediated electron transfer (MET) (Choi and Sang, 2016). The following scheme gives an overview of ways of methanogenic electron uptake at the cathode (Figure 3).

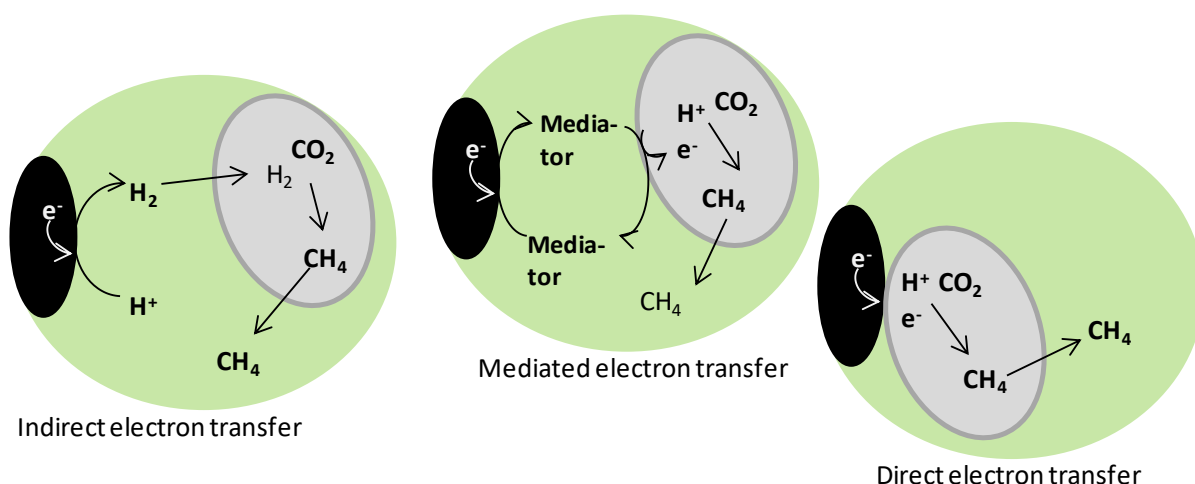


**Figure 3: Possible means of electron uptake in bioelectromethanogenesis**

Indirect electron transfer: hydrogen is produced electrochemically and consumed by the methanogens to convert  $\text{CO}_2$  to methane; mediated electron transfer: electrons from the electrode are shuttled to the methanogens by electroactive mediator molecules and used to convert protons and  $\text{CO}_2$  to methane; direct electron transfer: methanogens directly interact with the electrode surface to take up electrons and use them to produce methane from protons and  $\text{CO}_2$ .

Although it is not yet known, which methanogens are electroactive at all, not to mention which electron uptake mechanisms they perform in detail, it is supposed that all means of electron uptake contribute to the overall process, especially in mixed cultures (Zhen et al., 2015). Since the electron uptake is a surface dependent mechanism in any case, the design of a bioelectrochemical reactor and the integration of a suitable electrode are crucial for the efficiency of the process.

Most investigations on bioelectromethanogenesis used mixed methanogenic cultures, e.g. from biogas plants, wastewater treatment plants or even microbial fuel cells. Thinking of technical applications with possible environmental fluctuations, mixed cultures might be more stress resistant than pure cultures (Babanova et al., 2017). For basic research, it is hard to identify electroactive methanogenic strains out of electroactive consortia. Analysis of the consortium may identify enriched methanogenic strains, which are therefore likely to be electroactive. This is further confirmed, if electroactivity starts after long lag-phases during the start-up of a system with mixed cultures, in which the electroactive organisms are enriched (Pozo et al., 2015). Examples of methanogens which are dominant in electroactive consortia are given in Table 2. In various other publications, the dominant methanogenic strain was not identified (Jiang et al., 2013; Kuramochi et al., 2013; Schlager et al., 2017).

Only very few studies were carried out with pure cultures, proving the examined methanogens electroactive. Three certainly electroactive methanogens are *Methanothermobacter thermoautotrophicus* (Hara et al., 2013), *Methanococcus maripaludis* (Lohner et al., 2014) and a *Methanobacterium* like strain IM1 (Beese-Vasbender et al., 2015).

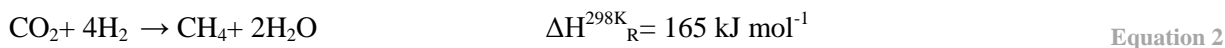
Only a minority of the known methanogenic strains was tested for electroactivity yet. Unfortunately, no specific marker for electroactivity was found, so that further electroactive microorganisms have to be revealed by bioelectrochemical experiments (Koch and Harnisch, 2016a). It is possible that in further investigations even more electroactive methanogens, also under more extreme conditions, will be detected.

Table 2: Enriched methanogens in electroactive microbial consortia (Jabłoński et al., 2015)

Strain and order	Substrate	Temperature	Reference
<i>Methanobacterium palustre</i> , <i>Methanobacteriales</i>	H <sub>2</sub> /CO <sub>2</sub> , formate, 2-propanol	mesophilic	(Batlle-Vilanova et al., 2015; Cheng et al., 2009; Jiang et al., 2014),
<i>Methanobacterium formicicum</i> , <i>Methanobacteriales</i>	H <sub>2</sub> /CO <sub>2</sub> , formate, 2-propanol, isobutanol	mesophilic	(Sasaki et al., 2013a)
<i>Methanobrevibacter arboriphilus</i> , <i>Methanobacteriales</i>	H <sub>2</sub> /CO <sub>2</sub>	mesophilic	(Jiang et al., 2014)
<i>Methanothermobacter</i> <i>thermautotrophicus</i> , <i>Methanobacteriales</i>	H <sub>2</sub> /CO <sub>2</sub>	thermophilic	(Fu et al., 2015; Sasaki et al., 2013a),
<i>Methanococcus aeolicus</i> , <i>Methanococcales</i>	H <sub>2</sub> /CO <sub>2</sub>	mesophilic	(Fu et al., 2015)
<i>Methanococcus maripaludis</i> , <i>Methanococcales</i>	H <sub>2</sub> /CO <sub>2</sub>	thermophilic	(Deutzmann and Spormann, 2017)
<i>Methanocorpusculum parvum</i> , <i>Methanomicrobiales</i>	H <sub>2</sub> /CO <sub>2</sub> , formate, 2-propanol	mesophilic	(Jiang et al., 2014)
<i>Methanocorpusculum bavaricum</i> , <i>Methanomicrobiales</i>	H <sub>2</sub> /CO <sub>2</sub> , formate, 2-propanol, butanol	mesophilic	(Kobayashi et al., 2013)
<i>Methanoculleus thermophiles</i> , <i>Methanomicrobiales</i>	H <sub>2</sub> /CO <sub>2</sub> , formate	thermophilic	(Sasaki et al., 2013a)
<i>Methanosarcina mazei</i> , <i>Methanosarcinales</i>	H <sub>2</sub> /CO <sub>2</sub> , methanol, acetate, methylated amines, butanol	mesophilic	(Fu et al., 2015)
<i>Methanosarcina thermophile</i> , <i>Methanosarcinales</i>	Acetate, methanol, methylated amines, butanol	thermophilic	(Sasaki et al., 2013a),
<i>Methanosaeta concilii</i> , <i>Methanosarcinales</i>	Acetate	mesophilic	(Xu et al., 2014)
<i>Methanobacterium petrolearium</i> , <i>Methanobacteriales</i>	H <sub>2</sub> /CO <sub>2</sub>	mesophilic	(Xu et al., 2014)
<i>Methanobacterium subterraneum</i> , <i>Methanobacteriales</i>	H <sub>2</sub> /CO <sub>2</sub> , formate	mesophilic	(Xu et al., 2014)

### 2.1.2.2 Comparison of Biomethanogenesis and Sabatier Reaction

In general, the conversion of CO<sub>2</sub> to fuels can be carried out biologically or electrochemically. The electrochemical route follows the Sabatier process, in which CO<sub>2</sub> and H<sub>2</sub> are converted to CH<sub>4</sub> and water vapor (given in Equation 2) (Brooks et al., 2007; Ghaib et al., 2016). CO can also act as a substrate (Bär et al., 2015).



Side reactions to alkanes or alkenes might occur, depending on the temperature and the catalyst (Ghaib et al., 2016). One of the major challenges in the Sabatier process is to find highly selective and affordable catalyst materials. These can for example be ruthenium (Brooks et al., 2007) or nickel (Bär et al., 2015), nickel catalysts can however lead to toxic side products (Ghaib et al., 2016). The process takes place at temperatures between 350 and 400 °C in fixed bed reactors, higher temperatures can be used in fluidized bed processes (Ghaib et al., 2016). The pressure can be set between 10 and 30 bar in fixed bed reactors, up to 60 bar are needed in fluidized beds (Bär et al., 2015; Ghaib et al., 2016). The total amount of electrical energy needed for a cubic meter of methane (16 bar) does not exceed 0.4 kWh with an overall energy efficiency of up to 82 % (Bär et al., 2015). To compare, the same amount of methane would contain 17.68 kWh of energy (calculated with the lower heating value (Martín et al., 2015)). Although the energy required is lower than in current biological processes, disadvantages are, as mentioned, the possibility of side products, the use of expensive and eventually toxic catalysts and the required purity of the educts; especially nickel based catalysts are sensitive against H<sub>2</sub>S and NH<sub>3</sub> (Bär et al., 2015). Advantageous are the high volumetric production rates leading to smaller reactors and the high energy efficiency especially when heat recovery strategies are applied (Bär et al., 2015).

The established biological methane production takes place within biogas plants. This process leads to a gas mixture mainly of methane and CO<sub>2</sub> due to the different reactions within an anaerobic digester (Weiland, 2010) (see also section 2.1.2.3). Therefore, biological methanation processes without the digestion of organic matter are currently designed, leading to a gas mixture containing up to 85 % of methane (Bär et al., 2015). Methanogens in external reactors are fed with CO<sub>2</sub> and electrochemically produced H<sub>2</sub>, the reaction itself is the same as for the Sabatier reaction (Equation 2) (Bär et al., 2015). Unfortunately, high methane concentrations in the product gas are only within reach when the volumetric production rate is low. The process can be operated at up to 65 °C at atmospheric pressure (Bär et al., 2015). This process is not in a commercial state yet, but first estimations showed that the amount of electric energy needed lies between 0.3 and 1.2 kWh\*m<sup>-3</sup> of methane (16 bar) with an overall energy efficiency of 58%. The lower energy efficiency resulted from the decreased heat recovery at the low temperature levels (Bär et al., 2015). Apart from the disadvantages of lower efficiency, lower production rates and lower product purity, the biological methanation does also have

advantages. These are the lower temperature and pressure ranges, the increased product specificity and the lower sensitivity against substrate stream impurities (Min et al., 2013).

Due to the high catalyst costs in electrochemical processes, the overall process costs of biological processes are only slightly higher than those of electrochemical processes, so biological methanation could turn out to be a reasonable alternative as soon as the process is implemented in larger scale (Bär et al., 2015). If so, fermentative processes can be more feasible than chemical processes, especially if impure substrate streams like biogas or waste gas streams shall be used (Min et al., 2013).

### 2.1.2.3 Sources of CO<sub>2</sub> for Bioelectromethanogenesis

CO<sub>2</sub> is often considered as a waste product in various processes. Sources for CO<sub>2</sub> are therefore exhaust gas streams from chemical production, fermentations and incinerations (Dürre and Eikmanns, 2015). CO<sub>2</sub> is also part of the surrounding air, but the concentration is usually not sufficient for economic processes (Geppert et al., 2016). The CO<sub>2</sub> used for bioelectromethanogenesis can also be gained from biogas, which was already suggested in literature (Xu et al., 2014). It was shown that it is possible to convert residual CO<sub>2</sub> out of biogas with methanogens by adding hydrogen, either in a second reactor (Luo et al., 2012) or integrated directly into the biogas plant (Luo and Angelidaki, 2012). Investigations were usually carried out with mixed cultures. The question remains, whether a pure methanogenic culture is inhibited by (toxic) components of the biogas. The upgrading of biogas in an external reactor using hydrogen was successfully brought to pilot-scale by the company Electrochaea (Butler and Lovley, 2016; Hafenbradl and Hein, 2015). The hydrogen used for this process has to be produced electrochemically via water electrolysis, which consumes a large amount of energy. Apart from that, the storage of H<sub>2</sub> is cost intensive (Butler and Lovley, 2016). To avoid external production of H<sub>2</sub>, a bioelectrochemical system can be used to intensify the process. The concept has already been proven (Xu et al., 2014), but as yet, a stable and scalable process has not been developed (Blasco-Gómez et al., 2017). Investigations showed that the electrodes can be inserted into the biogas plant directly to produce biogas with a higher methane content (Bo et al., 2014; Xu et al., 2014). This process was already scaled up for wastewater treatment by Cambrian Innovation; this company developed the so called EcoVolt reactor, a large-scale plant for wastewater treatment supported by bioelectrochemistry and leading to the production of clean water and biogas with high methane contents (Blasco-Gómez et al., 2017). Other investigations revealed that the step of bioelectromethanogenesis can be separated from the biogas production and be carried out in a second reactor (Batlle-Vilanova et al., 2016; Xu et al., 2014). Here, electrons from water splitting or organic matter degradation are transferred to the anode, while biogas or pure CO<sub>2</sub> is fed into the reactor as substrate for methanogens in a pure or mixed culture (Batlle-Vilanova et al., 2016; Dykstra and Pavlostathis, 2017; Geppert et al., 2016). Using water electrolysis as anodic process might be advantageous, since water is usually abundantly available and no toxic side products are formed (Butler and Lovley, 2016; Lovley and Nevin, 2013).

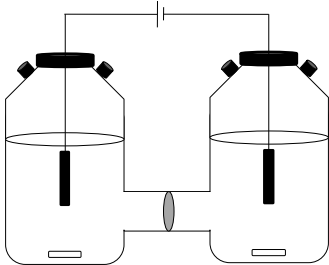
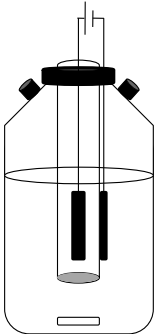
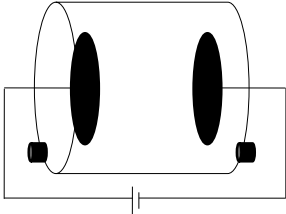
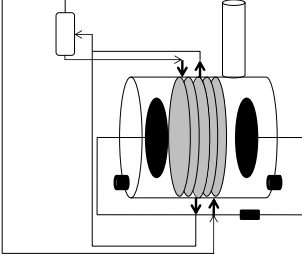
## 2.2 Reactor Design

Several reactor concepts for microbial electrosynthesis were developed, most of them for lab-scale applications. These designs are not necessarily scalable (Kadier et al., 2016; Krieg et al., 2014; Patil et al., 2015). This chapter will give an overview of the existing reactors used for MES in general and specially for bioelectromethanogenesis. The crucial characterization parameters for newly designed reactors are summarized as follows.

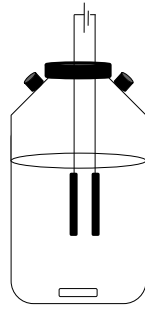
### 2.2.1 Microbial Electrosynthesis and Bioelectromethanogenesis Reactors

Two basic reactor concepts can be distinguished: separated two-chamber-systems and unseparated single-chamber-systems (Kadier et al., 2016). In two-chamber-systems, a cathode chamber and an anode chamber are separated by a semipermeable membrane. This membrane allows, depending on the membrane type, the flow of ions from one chamber to the other chamber to close the electric circuit, but hinders other, potentially reactive, medium components from diffusion between the chambers (Babanova et al., 2017). The advantages of two chamber systems, especially in bioelectromethanogenesis, are the avoidance of contact between anodically produced oxygen and oxygen sensitive methanogens at the cathode, the easy separation of the product stream from oxygen produced at the anode and the lower amount of culture medium needed since the anode chamber can be filled with water or buffer solutions (Babanova et al., 2017; Kadier et al., 2016). These advantages are also of high value in other MES approaches. Hence, higher product purities can be achieved. On the other hand, cathodically produced hydrogen or methane could diffuse through the membrane, resulting in product losses. Also, the membrane increases the electrical resistance of the cell, lowering the electrical current and the efficiency (Babanova et al., 2017). Single chamber systems avoid the additional resistance of the membrane. They were often used to produce methane, but in these cases, the anodic reaction was not water electrolysis, leading to the production of oxygen, but the digestion of organic matter using mixed microbial cultures (Cheng et al., 2009; Gajaraj et al., 2017; Sasaki et al., 2013b). Several types of reactors for bioelectromethanogenesis have been mentioned in literature. Apart from typical lab-scale reactors like H-cells and cube-reactors, which are used for most described MES processes, it was shown that commercial bioreactors can be modified to host electrodes, even though these have not yet been used for methane production (Hintermayer et al., 2016; Krieg et al., 2018a; Rosa et al., 2016). Table 3 shows several reactors used for electro-methanogenesis so far.

Table 3: Reactor types for methanogenic MES

Sketch	Advantages, Disadvantages	Reference
<p><b>H-Cell, two chambers</b></p> 	<ul style="list-style-type: none"> <li>+ widely spread</li> <li>+ suitable for screening</li> <li>+ various electrodes applicable</li> <li>- large electrode distance</li> <li>- Scale-Up not possible</li> <li>- limited variations in mixing and gassing</li> </ul>	<p>(Kadier et al., 2016; Sasaki et al., 2011; Schlager et al., 2017; Xu et al., 2014)</p>
<p><b>Concentric tubular reactor, two chambers</b></p> 	<ul style="list-style-type: none"> <li>+ easy to build</li> <li>+ variable membrane area</li> <li>+ small electrode distance</li> <li>+ better scalability than H-cell</li> <li>- limited electrode surface area</li> <li>- mixing hindered</li> <li>- complicated separation of anode and cathode off-gas</li> </ul>	<p>(Xu et al., 2014)</p>
<p><b>Cube type, single chamber</b></p> 	<ul style="list-style-type: none"> <li>+ Scale-Up possible to a certain point</li> <li>+ electrodes close together</li> <li>+ variable membrane area</li> <li>- may lead to dead zones in terms of mixing at the bottom or edges</li> <li>- toxic products from counter electrode (e.g. oxygen) inhibit biologic activity</li> </ul>	<p>(Cheng et al., 2009; Cusick et al., 2011; Rader and Logan, 2010)</p>
<p><b>Reverse electro-dialysis reactor, two chambers</b></p> 	<ul style="list-style-type: none"> <li>+ less additional voltage needed</li> <li>- additional energy for pumping</li> <li>- increased electrode distance</li> </ul>	<p>(Luo et al., 2014)</p>

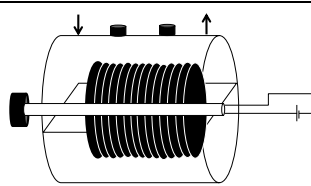
**Bottle type,  
single  
chamber**



- + very easy to create
- + small electrode distance
- + suitable for screening
- limited electrode geometries
- limited gassing and mixing
- not scalable
- toxic products from counter electrode (e.g. oxygen) inhibit biologic activity

(Guo et al., 2017)

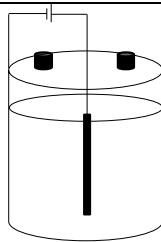
**Rotating  
disk  
reactor,  
single  
chamber**



- + methane produced in gas phase
- + high electrode surface
- complicated design
- toxic products from counter electrode (e.g. oxygen) inhibit biologic activity

(Cheng et al., 2011)

**Cylindrical  
reactor,  
single  
chamber**



- + symmetrical electrical field
- isolation to environment may be needed
- limited in electrode material (stainless steel)
- toxic products from counter electrode (e.g. oxygen) inhibit biologic activity

(Bo et al., 2014)

Most of the used reactors were not fully characterized and efficiencies were not reported. Because of that, comparisons and Scale-Up calculations are barely reliable (Patil et al., 2015). The next section will suggest parameters for the characterization of bioelectroreactors.

### 2.2.2 Reactor Characterization and Evaluation

New reactors have to be characterized to allow comparisons, Scale-Up calculations and economical evaluations. Several parameters are required for the characterization of a bioelectrochemical reactor and the bioelectrochemical process. Geometrical and physical properties of the reactor have to be described. This is especially important in terms of Scale-Up, since one method applied is the Similarity Theory, where geometrical ratios are taken into account (Durst, 2008; Takors, 2014). Table 4 gives examples of important geometrical and physical parameters characterizing the reactor and the process.

Table 4: Process characterization: Geometrical and physical parameters

	Parameters	Reference
<b>Reaction chamber</b>	Geometrical parameters of reactor: Height, diameter, volume Reaction volume: liquid level, liquid volume,	(Rossi, 2001)
<b>Gassing</b>	Available gaseous substrate: Headspace volume, gas stream, residence time, gas composition, superficial gas velocity, CO <sub>2</sub> transfer coefficient	(Patil et al., 2015; Rossi, 2001; Schmidt, 2005; Takors, 2014)
<b>Process parameters</b>	pH, temperature, pressure, total process time	(Patil et al., 2015; Williams, 2002)
<b>Mixing</b>	Stirrer diameter, stirrer tip velocity, mixing time	(Schmidt, 2005; Takors, 2014)
<b>Power input</b>	Power input by stirrer, gassing, heating...	(Takors, 2014)
<b>Dimensionless numbers</b>	Reynolds number, Newton number, Weber number, Bond number, aeration number	(Patil et al., 2015; Takors, 2014)

Secondly, the reactor needs to be characterized electrochemically. Basic electrochemical equations can be used to find the relationships between current generation, applied potential and internal resistance of the system, but a lot more electrochemical parameters influence the process. Important from an electro-technological point of view are the electrodes and their specific surface areas (Gil-Carrera et al., 2011) and the used membrane type (Zeppilli et al., 2016) (see also sections 2.2.3. and 2.2.4). Further important parameters are given in Table 5.

A careful reactor design can lower the internal resistance of the system, since high electric resistances lead to low efficiencies; one way could be a reduction of the electrode distance (Ki et al., 2016). The electrochemical characterization allows the comparison of bioelectrochemical systems not only with one another, but also with established electrochemical processes used for methane production. This

will be crucial for the decision to produce the industrial product either bioelectrochemical or electrochemical.

**Table 5: Process characterization: electrochemical parameters**

	<b>Parameters</b>	<b>Reference</b>
<b>Electrodes</b>	Area, specific area, current density, electrode distance, reference electrode	(Krieg et al., 2014; Patil et al., 2015; Ribot-Llobet et al., 2013; Sharma et al., 2014)
<b>Medium</b>	Conductivity, composition, possibility of side product formation (e.g. electrochemical formation of chlorine gas from chloride salts at the anode)	(Logan and Rabaey, 2012; Patil et al., 2015; Thrash and Coates, 2008)
<b>Reactor</b>	Ohmic resistance	(Ki et al., 2016)
<b>Membrane</b>	Type, area, proton transport number	(Babanova et al., 2017)
<b>Electron transfer</b>	Maximum current, potential, Electron uptake rate	(Patil et al., 2015)

Thirdly, the biological properties of the system have to be described. The microorganisms are the key element of the process; therefore optimal conditions need to be assured. Important biological parameters are summarized in Table 6.

**Table 6: Process characterization: biological parameters**

	<b>Parameters</b>	<b>Reference</b>
<b>Growth</b>	Start-up time, apparent growth rate, biofilm formation	(Patil et al., 2015)
<b>Substrate consumption</b>	Substrate threshold, CO <sub>2</sub> uptake rate, nutrient consumption	(Heijnen, 2002; Takors, 2014)
<b>Production</b>	CH <sub>4</sub> production rate	(Patil et al., 2015; Takors, 2014)

Finally, to compare the reactor systems, performance parameters need to be calculated (Patil et al., 2015). These can help to estimate the efficiency of the system concerning the energy needed and the substrate used. Examples are shown in Table 7. Since the process shall be used as an upgrading step, especially the purity of the product is important (Ditzig et al., 2007; Patil et al., 2015; Takors, 2014).

Table 7: Process characterization: Evaluation parameters

Production rate	$Y_P = \frac{w_{CH_4} * \left( \dot{V}_G * 86.4 \frac{m^3*s}{l*d} \right)}{24.05 \frac{l}{mol}}$	Equation 3
Specific production rate	$Y_{PEI} = \frac{Y_P}{A_{EI}}$	Equation 4
Space time yield	$Y_{ST} = \frac{Y_P}{V_R}$	Equation 5
Product purity of methane	$\gamma = w_{CH_4}$	Equation 6
Yield product/substrate	$Y_{PS} = \frac{w_{CH_4}}{w_{CO_2,ingas}}$	Equation 7
Coulomb efficiency (MES)	$\eta_{C,MES} = \frac{z * r_{e,m}}{r_{e,l}}$	Equation 8
Coulomb efficiency (MFC)	$\eta_{C,MFC} = \frac{r_{e,l}}{z * r_{e,m}}$	Equation 9
Total power input	$P_{In} = P_{EL} + P_G + P_S + P_{G,S} + P_H$	Equation 10
Total power output	$P_{Out} = \frac{Y_{CH_4} * 890.36 \frac{kJ}{mol} + Y_{H_2} * 285.82 \frac{kJ}{mol}}{86.4 \frac{kJ*s}{l*d}}$	Equation 11
Energy efficiency	$\eta_E = \frac{P_{Out}}{P_{In}} * 100\%$	Equation 12

The absolute production rate allows comparison of different process conditions within one reactor. For the calculation, a molar volume of  $24.05 \text{ l} \cdot \text{mol}^{-1}$  was calculated from ideal gas law, a conversion factor of  $86.4 \text{ m}^3 \cdot \text{s}^{-1} \cdot \text{d}^{-1}$  from  $\text{m}^3 \cdot \text{s}^{-1}$  to  $\text{l} \cdot \text{d}^{-1}$  was used. Based on that, the specific production rate was obtained per working electrode surface area. It allows comparison of different working electrodes. From the absolute production rate and the working volume, the space time yield can be used for the comparison of different reactors. The Coulombic efficiency of a bioelectrochemical system is defined as the ratio of the electron transfer rate to the desired product to the electron transfer rate from the electron source (Clauwaert et al., 2008). For microbial electrosynthesis, the electron source is electrical current and the product is a chemical compound, for microbial fuel cells, electrical current is the product while a chemical compound is the electron source. The number of mol electrons transferred from or to one mol of chemical compound ( $z$ ) has to be taken into account. The total power input is the sum of the power inputs caused by heating, gassing, stirring and potential application. For the calculation of the power output, the gross calorific values of the products methane ( $890,36 \text{ kJ} \cdot \text{mol}^{-1}$ ) and hydrogen ( $285,82 \text{ kJ} \cdot \text{mol}^{-1}$ ) are used (Leipertz, 2006).

Reactor performance could be described by mathematical modeling. A mathematical model can help to optimize the system and Scale-Up the reactor (Li and He, 2016). As yet, no complete model for all interactions in bioelectrochemical systems has been developed. Partial models are available for the ion transport (Dykstra et al., 2014) and current generation (Li and He, 2016), and well-known models for microbial growth, mass transport and biofilm formation are available (Rodriguez and Premier, 2010).

Scale-Up of microbial electrosynthesis systems was rarely accomplished by now. First attempts of Scale-Up to 1000 liter were shown for microbial electrolysis cells (Brown et al., 2014; Cusick et al., 2011; Escapa et al., 2015; Gil-Carrera et al., 2013; Heidrich et al., 2014). A first pilot-scale plant (1000 l) has been tested by Cusick (Cusick et al., 2011), which produced current, methane and hydrogen out of waste water. The Scale-Up was carried out considering mainly the electrode surface area in the used single chamber system, and the resulting current density was only 56.9 % of the current density obtained in the lab-scale tests. Also, the start-up phase was longer and the observed methane production could not be explained by the current alone but must also have resulted from the degradation of organic matter (Cusick et al., 2011). The approach to scale up by the electrode surface area was suggested before by Rader and Logan, who used multi-electrode systems (Rader and Logan, 2010). First Scale-Up studies for microbial fuel cells showed that too little is known about the process to develop a knowledge based Scale-Up method (Janicek et al., 2014; Logan, 2010a). Even in well-known fermentation processes, Scale-Up remains difficult (Schmidt, 2005). Several problems are related to the decreased mixing quality in larger reactors, such as insufficient substrate supply, stress and resulting metabolic shifts due to higher stirrer velocities and gas gradients within the medium (Schmidt, 2005). Since the biological answers to increased stress and inhomogeneous reaction zones are different in every process, a common Scale-Up approach seems to be impossible (Schmidt, 2005). A widely used method is using the Similarity Theory in combination with dimensional analysis, where dimensionless numbers are calculated out of combinations of physical process parameters (Durst, 2008). These dimensionless numbers are then, if possible, kept constant in the lab-scale and the scaled up design. Therefore, they give an indication of how to vary e.g. stirrer speed if varying stirrer diameter (Takors, 2014). Usually, in larger reactors the total power input per volume decreases compared to the lab-scale approach, while the superficial gas velocity increases (Rosellen and Gezork, 2017). Sometimes it is necessary to vary the geometric design of the reactor to avoid floating while maintaining the gas supply and a short mixing time (Rosellen and Gezork, 2017). For the Scale-Up of MES, new dimensionless numbers or specific variables need to be suggested to consider biological influences as well as electrochemical influences (Patil et al., 2015).

### 2.2.3 Similarity Theory as Tool for Reactor Scale-Up

Many studies suggested the Similarity Theory for Scale-Up in various fields of technology, e.g. granulation, fluid mechanics or electrode design (Durst, 2008; Nicolopoulou et al., 2013; Watano et al., 1996). The Similarity Theory is based on the idea that certain parameters need to be constant during the transfer of the technology from one system to another system, for example a different reactor type or a pilot plant (Durst, 2008; Günther, 1975). This is often combined with the calculation of characteristic ratios or dimensionless numbers which define mass transport, heat transport and other properties critical for the overall performance of a system (Durst, 2008). Exemplary, dimensionless numbers used are Reynolds number (flow processes) Peclet number (heat transfer) or Sherwood number (heat and mass transfer) (Durst, 2008). However, it was shown that for biological processes, the use of dimensionless numbers is not always successful. Therefore, often ratios of different parameters like the power input per volume or characteristic process values are kept constant for Scale-Up in bioengineering instead of the dimensionless numbers (Marques et al., 2010). The most common process characteristics used here are the  $k_L a$  value describing the gas transfer from gas phase to liquid phase, the volumetric power input, the mixing time and the impeller tip speed (reviewed in (Marques et al., 2010)). In many cases, it has to be decided which system properties are the most relevant to be kept constant during scale up, since usually not all characteristics or dimensionless numbers can be kept constant at the same time (Marques et al., 2010).

For the use of the Similarity Theory for the Scale-Up of bioelectrochemical systems, which was never described before, new ratios or dimensionless numbers have to be defined which are kept constant during scale up. The main challenge is the combination of a volume depending process (gas transfer) and a surface depending process (electron transfer).

### 2.2.4 Electrode Materials

Electrode material and geometry do affect the electrochemical properties as well as biological variables like cell attachment. It is crucial to know the dispersion of the cells within the reactor: planctonic cells, which interact with the electrodes by direct contact, need a highly accessible electrode surface. If the microbes grow as a biofilm on the cathode surface, a high specific electrode surface area and biocompatibility of the electrode is even more important than for planctonic cells (Rosa et al., 2016). Therefore, the electrode material is not only determining for the electrochemical properties of the system, but also for the biological performance; careful choice of electrode material is essential. Most investigations used carbon based electrode materials, although some publications demonstrated that metals, in particular copper, might be the better choice due to higher conductivity (Baudler et al., 2015). In contrast, some experiments showed that metal cathodes, e.g. stainless steel, corrode during a bioelectrochemical process. As anode, non-precious metals are often not suitable, since oxygen formation at the anode increases corrosion (Dykstra and Pavlostathis, 2017). Cathodes made of nickel decreased in performance over time (Selemba et al., 2009). Other publications used

graphite as carrier and coated it with metal webs or nano-particles (Siegert et al., 2014; Zhang et al., 2013). According to (Siegert et al., 2014), methane production worked best on graphite with platinum addition; plain graphite and carbon brush performed similar, while other metal powders even decreased performance, so the effect did not justify the additional costs. To increase biofilm formation, carbon fiber material (Sasaki et al., 2013a, 2013b) or graphite granulate (Villano et al., 2011) was added to support attached microbial growth. Since the electrode material turned out to be a major influence factor on MES, screening systems for electrode material have been developed (de Campos Rodrigues and Rosenbaum, 2014) and various publications compared electrode material performances.

Table 8: Cathode materials for MES

Cathode Material	Current density	Product and potential	Reference
Carbon cloth	-0.071 A*m <sup>-2</sup>	Acetate; Cathode potential -600 mV vs. Ag/AgCl	(Zhang et al., 2013)
Carbon cloth with chitosan	-0.475 A*m <sup>-2</sup>	Acetate; Cathode potential -600 mV vs. Ag/AgCl	(Zhang et al., 2013)
Carbon cloth with gold	-0.388 A*m <sup>-2</sup>	Acetate; Cathode potential -600 mV vs. Ag/AgCl	(Zhang et al., 2013)
Carbon cloth with nickel	-0.302 A*m <sup>-2</sup>	Acetate; Cathode potential -600 mV vs. Ag/AgCl	(Zhang et al., 2013)
Carbon cloth with palladium	-0.32 A*m <sup>-2</sup>	Acetate; Cathode potential -600 mV vs. Ag/AgCl	(Zhang et al., 2013)
Carbon nanotube (Nanoweb - Reticulated Vitreous Carbon (RVC))	37 A*m <sup>-2</sup> (proj. area); 2.91 A*m <sup>-2</sup> (total area)	Acetate; Cathode potential -850 mV vs. SHE; (-1050 vs. Ag/AgCl)	(Jourdin et al., 2014)
Graphite coated with nickel-nanowire	8.9 A*m <sup>-2</sup>	Acetate; Cathode potential -600 mV vs. Ag/AgCl	(Nie et al., 2013)
Nickel foam	2.4 A*m <sup>-2</sup>	Hydrogen; 900 mV applied voltage	(Ribot-Llobet et al., 2013)
Stainless steel mesh	8.08 A*m <sup>-2</sup>	Hydrogen; 900 mV applied voltage	(Zhang et al., 2010)
Stainless steel mesh coated with molybdenum disulfide	2.6 A*m <sup>-2</sup>	Hydrogen; 900 mV applied voltage	(Ribot-Llobet et al., 2013)
Stainless steel mesh coated with platinum	3.4 A*m <sup>-2</sup>	Hydrogen; 900 mV applied voltage	(Ribot-Llobet et al., 2013)
Stainless steel wool	1.7 A*m <sup>-2</sup>	Hydrogen; 900 mV applied voltage	(Ribot-Llobet et al., 2013)

From an economical point of view, many of the examined electrode materials are not viable for large-scale processes due to their high costs. This applies in particular for precious metals (Zhang et al., 2010), so this thesis will focus on carbon materials as low-cost alternatives. Table 8 shows examples for relatively cheap cathode materials with the measured current density, which were used in different MES processes. Experiments with different materials compared under the same conditions showed, that coating of carbon based materials enhances the current production (Zhang et al., 2013). Apart from that, it is hard to draw conclusions from Table 8, since the used microorganisms, the reactor type and the electrolyte vary between the studies. So this list may give examples, but cannot serve as a universal ranking of the materials. As an example, pretreatment of carbon electrodes with ammonia could increase the current production in microbial fuel cells (Cheng and Logan, 2007), whereas it had no positive effect in other studies (Zhang et al., 2013), so that it does not seem to be necessary in general.

The size and surface area of the cathode is vital to ensure sufficient electron supply. In general, bigger electrode surfaces lead to higher currents, therefore the current density is an important value to compare the processes (Patil et al., 2015). It is important to distinguish between the real surface area and the accessible surface area: small pores cannot be entered by the microorganisms and do therefore not efficiently transfer electrons, if direct contact between electrode and microorganisms is necessary (Zhang et al., 2010). It was investigated that not only the working electrode surface area, but also the counter electrode surface area influences the process (Gil-Carrera et al., 2011; Guo et al., 2017). It seems as if there is an optimum ratio of cathode to anode surface area, but it is not clear whether this effect resulted from an increased cathode size only. Further investigations would need to be carried out (Guo et al., 2017).

Apart from the electrode material itself, the addition of granulates like activated carbon granulate increases the efficiency of the MES. This might be due to the support of biofilm (Lee et al., 2016), the support of electron transfer between cells (Liu et al., 2012), or the reduction of the internal resistance of the reactor system (Wang et al., 2010).

### 2.2.5 Membrane Materials

Membranes with selective permeability are often used as separator between the two reaction chambers of a bioelectrochemical system. In bioelectromethanogenesis, protons from the anode chamber shall pass the membrane and enter the cathode chamber. The membrane should prevent the diffusion of oxygen from the anode to the cathode chamber and the diffusion of methane and hydrogen from the cathode to the anode chamber. The first would lead to toxic effects on the methanogens, the last to decreasing yields.

Most used membranes in bioelectrochemistry are proton exchange membranes (PEX). These are made of a fluor-carbon backbone with sulfate groups (Babanova et al., 2017). PEXs are often the first choice for microbial electrosynthesis since they are selectively permeable to protons and show a low Ohmic resistance (Babanova et al., 2017). Some disadvantages occur, which are high costs of up to 38 % of the whole system (Chae et al., 2008; Leong et al., 2013), a relatively high oxygen permeability (Chae et al., 2008; Kim et al., 2007), a high pH shift during the process (Babanova et al., 2017), the decreased proton transport at high cation concentrations since cations “block” the way for protons (Babanova et al., 2017; Chae et al., 2008; Harnisch et al., 2008) and the performance drops over time due to pH shift and decreasing proton transport (Babanova et al., 2017).

Alternatives to the proton exchange membrane are the cation exchange membrane (CEM) and the anion exchange membrane (AEM). In a direct comparison of PEX and AEM, the methane production in cells with PEX membrane was higher and the overall performance better than in cells with AEM (Zeppilli et al., 2016). It was assumed that  $\text{OH}^-$  passed the membrane from cathode to anode chamber when using AEM (Zeppilli et al., 2016). On the other hand, comparing AEM and CEM in a hydrogen producing system, the AEM showed a much lower internal resistance and therefore performed better (Sleutels et al., 2009). In a comparison of PEX and CEM, the PEX showed a better performance at first, but was less long term stable than the CEM and resulted in a larger pH shift (Babanova et al., 2017), so that CEM might be the better choice for continuous processes. It was also shown in MFCs that the membrane type contributes less to the overall internal resistance than e.g. the electrode distance, so that the reactor design itself might be more important than the membrane type for new developments (Kim et al., 2007). Some membranes can also be modified to decrease their Ohmic resistance (Yan et al., 2015). Depending on the membrane and the microbial community, biofouling may occur and decrease the performance of the process (Leong et al., 2013). It will therefore be necessary to try several membranes when developing a new BES.

Instead of a membrane, it would also be possible to use a salt bridge, for example based on a KCl solution (Beese-Vasbender et al., 2015). This approach is not used often in MES, maybe because of the more complex setup or higher internal resistances.

### 3 Tasks and Objectives

The main task of this doctoral thesis was to develop a reactor system which is capable of hosting methanogens for the bioelectrochemical conversion of  $\text{CO}_2$  to  $\text{CH}_4$ . Therefore, several steps had to be undertaken. First, a suitable bioelectrochemical reactor needed to be designed. Second, the process had to be optimized and different reactor concepts had to be compared. Third, the stability of the whole process according to gas composition, potential fluctuations and other environmental influences had to be investigated. Last but not least, the system had to be scaled up to pilot-scale (minimum 50 l, (Votruba and Sobotka, 1992)) and compared to Numbering-Up concepts.

The combination of electrochemistry and biotechnology leads to several challenges in terms of reactor design. The electrochemical reaction at the cathode surface is a two dimensional (i.e. surface limited) process, which has to be integrated in a three-dimensional reactor, characterized by a three-dimensional flow profile. This means, the substrate supply of the microorganisms combines a two dimensional process corresponding to the available electrons and a three dimensional process related to the C-source, which is regulated by the gas-to-liquid transfer of  $\text{CO}_2$ . Apart from that, the electrode chambers need to be separated to prevent the contact of anodically produced oxygen with the strictly anaerobe microorganisms. The arrangement of the two chambers needs to be horizontal, since the gas streams of anode chamber (oxygen) and cathode chamber (methane) must not mix. This arrangement will lead to a horizontal electrical field. In contrast, gas bubbles will move vertically, so that a  $\text{CO}_2$  gradient will also establish vertically. These facts, along with fluctuating power supply and changing in-gas mixtures have to be considered designing a reactor for bioelectromethanogenesis, which shall be used for further process development. It is crucial to optimize  $\text{CO}_2$  supply, electron supply and biocatalyst to gain a scalable process.

The objective of the thesis is to develop a scalable and efficient bioelectromethanogenesis reactor for methane production. The main questions to be answered are: What are the main limitations of the process? Can the corresponding parameters be optimized? Does the electrochemically assisted methane production work at pilot-scale? Can the developed process work long-term-stable and under instable conditions? These questions will be answered in this thesis.

To prove the reactor concept capable of hosting not only bioelectromethanogenesis but also other bioelectrochemical processes, a microbial fuel cell experiment will be carried out in the reactor. Furthermore, it will be compared to the commonly used H-cells and to a stirred tank reactor (STR) modified for bioelectrochemistry.

## 4 Results and Discussion

### 4.1 Development of a Bioelectrochemical Reactor

To turn bioelectromethanogenesis into an economically and ecologically feasible technology, the design of a scalable, efficient and variable reactor is essential. It might be advantageous to use one of the usual types of large-scale bioreactors, which are the stirred tank reactor, the bubble column reactor, the external loop reactor and the trickle-bed reactor (Williams, 2002). These reactors are well studied and verifiably suitable for large-scale fermentations. Changes in the known systems have to be made to integrate electrodes and to separate two electrode chambers for bioelectrochemical applications. The bubble column reactor, the stirred tank and the external loop reactor seem to be adaptable for a bioelectrochemical reaction. The trickle bed reactor could also be adapted to host BES-processes, if the trickle bed serves as electrode at the same time and the microorganisms are capable of growing in biofilms on the electrode surface.

It was already demonstrated that stirred tank bioreactors can be modified to host electrodes (Krieg et al., 2018a; Rosa et al., 2016). In this work, a bioelectrochemical bubble column reactor was designed which was not shown before.

The design was based on the following considerations: CO<sub>2</sub> as the main substrate in bioelectromethanogenesis is gaseous, requiring an efficient transfer of CO<sub>2</sub> from the gas phase to the liquid phase (Roy et al., 2016). A bubble column would be a suitable reactor for the optimization of gas transfer. To increase the transfer, the gassing rate or system pressure could be increased (Seifert et al., 2014). On the other hand, the gassing rate must not be too high, otherwise the reactor gets floated; the superficial gas velocity is too high to disperse the gas bubbles and large bubbles pass the reactor without sufficient gas transfer (Rosellen and Gezork, 2017). It was shown that a pressure increase improves the off-gas quality in bioelectromethanogenesis, whereas an increased gassing rate improves the total amount of methane produced (Seifert et al., 2014). The low solubility of methane in water ( $0.2121 \cdot 10^4 \text{ mol} \cdot \text{l}^{-1}$  at 35 °C and 1 bar (Wilhelm et al., 1977)) is advantageous, leading to product accumulation in the gas phase, whereas the solubility of CO<sub>2</sub> in water is higher ( $4.771 \cdot 10^4 \text{ mol} \cdot \text{l}^{-1}$  at 35 °C and bar, (Wilhelm et al., 1977)), allowing sufficient substrate supply (Xu et al., 2014). Since CO<sub>2</sub> and possibly H<sub>2</sub> act as substrates for the microorganisms, overpressure would increase the gas solubility of the substrates in the medium and the accessibility for the microorganisms (Seifert et al., 2014). It is not known so far whether biofilms are formed by the methanogens. Some methanogens have a very fragile cell wall (Stadtman and Barker, 1951). Therefore, high shear forces could negatively affect growth and product formation due to cell disruption. A stirred tank reactor could disturb the biofilm formation and the methanogenic performance by shear forces. A trickle bed reactor, which does in any case require biofilm growth, cannot be used if no biofilm is formed.

A working chamber which can be operated in bubble column mode and also with an external loop overcomes these issues.

Since bioelectromethanogenesis in this work shall not be coupled to the degradation of organic substances, a single-chamber-reactor is not suitable. Oxygen is likely to be produced at the anode and would inhibit the metabolism of strictly anaerobe methanogens at the cathode (Kiener and Leisinger, 1983). Because of that, single-chamber-reactors will not be discussed any further in this work. For the same reason, impermeability of the working chamber regarding gas entry from the surrounding environment is mandatory.

The important reaction of a bioelectrochemical process usually takes place in the working chamber, while the other chamber hosts a not necessarily defined counter reaction. Bioelectromethanogenesis and other MES for example take place in the cathode chamber of the system. So it is necessary to design a suitable, scalable working chamber, whereas the counter chamber can be designed as water basin. This basin could then act as heating jacket as well, or could be equipped with an outer heating jacket to avoid the interference of heaters or heating streams with the electrical field in the counter chamber. For a rational design it is important to consider the installation of gas and liquid inlets and outlets, mixing components and installations which could hinder or improve mixing, and cell retention in continuous processes. One point to mention is the importance of pH, which has to be in an optimum range for microbial growth; in separated electrochemical systems, a pH shift might occur since protons are released at the anode and consumed at the cathode (Ribot-Llobet et al., 2013). Therefore, it might be necessary to use buffered media for MES or pH control.

Taking all this into account, a bubble column working chamber with surrounding counter chamber was designed. The electrical connection between the chambers was ensured by four membrane windows included in the working chamber's outer wall. Medium ports allowed liquid exchange for continuous operation in terms of liquid medium or an external loop mode. To establish an evenly distributed electric field, the working electrode was placed in the center of the working chamber. Different types of electrode materials could be applied to allow process optimization. The exact measures of the resulting reactor are described in 6.2.3. The counter electrode was wrapped around the reactor to gain a large counter electrode surface area, as it was already suggested for MFCs since the counter electrode might limit the process at the working electrode (Rabaey et al., 2005; Scott et al., 2007).

During the experiments it turned out, that the reactor handling was practical, and as desired, it was possible to vary the working parameters in terms of working and counter electrode types and size, membrane area and membrane type. This was an advantage compared to the other tested reactors; especially the membrane area was not variable in H-cells or the adapted bioelectrochemical stirred tank reactor, since there is only one membrane window which had to be fully covered by the

membrane. In H-cells, it was at least possible to use different electrodes; in the stirred tank reactor a textile like electrode like carbon fabric or carbon laying had to be installed to fit into the electrode frame. The bubble column reactor was easier to clean than the other reactors due to the lower amount of movable parts and the cylindrical design. A disadvantage was the electrical connection between anode and potentiostat; the platinum wire contacting the anode was connected via a metal alligator clip; during the operation, the alligator clip strongly corroded when getting in touch with the buffer or the carbon fabric anode material, leading to increases in the terminal voltage and jumps in the current curves. Further sudden changes occurred when exchanging corroded clips against new ones. Another issue was the evaporation of buffer in the counter chamber, which led to an increasing terminal voltage since the overall reactor resistance increased when less counter electrode material was submerged. Sudden jumps in the terminal voltage occurred when the counter chamber was refilled. For future designs, these remarks should be taken into account and solved by application of a liquid level sensor with automated refilling and improved connection to the potentiostat. For comparison of the developed reactor to existing bioelectrochemical systems, the bubble column reactor, an existing stirred tank reactor and the existing H-cell were characterized prior to the bioelectrochemical experiments.

## 4.2 Abiotic Reactor Characterization

### 4.2.1 Electrochemical Characterization

An abiotic electrochemical characterization of the bubble column reactors was conducted as described in section 6.3.1. Prior to the biotic experiments, abiotic chronoamperometric experiments at -900 mV vs. Ag/AgCl were carried out in the bubble column reactor. These experiments revealed that with all different electrodes, a stable current adjusts after a polarization phase which was dependent on the electrode (Figure 4). When testing various electric connections of the anode and cathode, it turned out that the cathode can be electrically contacted via a titanium wire in all tested reactors, but the anode had to be connected using platinum, since stainless steel and titanium wires corroded in the anolyte on the contact points to the carbon fabric electrode, causing an increase in the requisite terminal voltage. Apart from that, the application of a working potential worked well for all tested reactors, resulting in a small, stable electrical current after the initial polarization time.

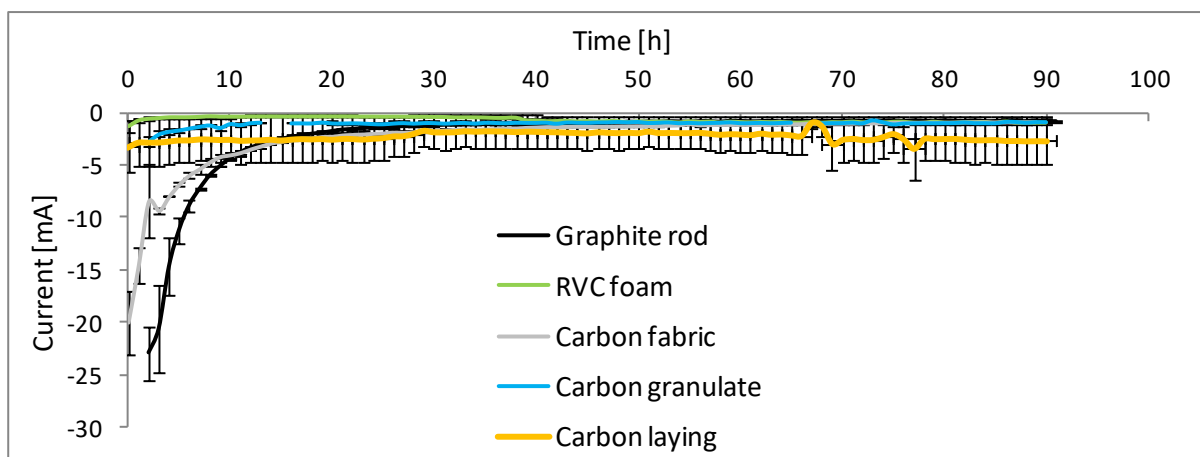


**Figure 4: Current time course in chronoamperometric, abiotic experiments with different electrodes**

Results show the absolute current measured for five different electrodes; based on the geometrical surface area the mean current densities were  $-131 \text{ mA}\cdot\text{m}^{-2}$  (graphite rod),  $-60 \text{ mA}\cdot\text{m}^{-2}$  (RVC foam),  $-287 \text{ mA}\cdot\text{m}^{-2}$  (carbon fabric),  $-4 \text{ mA}\cdot\text{m}^{-2}$  (carbon granulate) and  $-369 \text{ mA}\cdot\text{m}^{-2}$  (carbon laying).

The medium conductivity in the counter chamber did not change significantly throughout the chronoamperometric measurement and was between 13 and 15 mS in general, while the conductivity of the working medium decreased over 90 h by 9.2 mS on average, starting at around 40 mS. This trend was confirmed in all following experiments, abiotic as well as biotic ones. The decrease might result from the precipitation of salts at the cathode or at the membrane windows, which was observed in many experiments and seemed to be related to the magnitude of the electrical current. Ion chromatography revealed that the precipitations contain sodium, magnesium and carbonate.

As further described in 6.3.1, the system resistance of the reactors was tested by applying 5 mA to the system and measuring the potential between the working and the counter electrode. Figure 5 shows the calculated cell resistances for the different reactors.

The resistance for the H-cell was relatively high compared to that of the bubble column and the stirred tank reactor, probably caused by the smaller membrane area and diffusion limited zones in the bridge between the two chambers. In contrast, the bubble column reactor contained large membrane windows. The ion transport in the stirred tank reactor was improved by the stirrer power input, leading to the lowest resistance of the three systems compared.

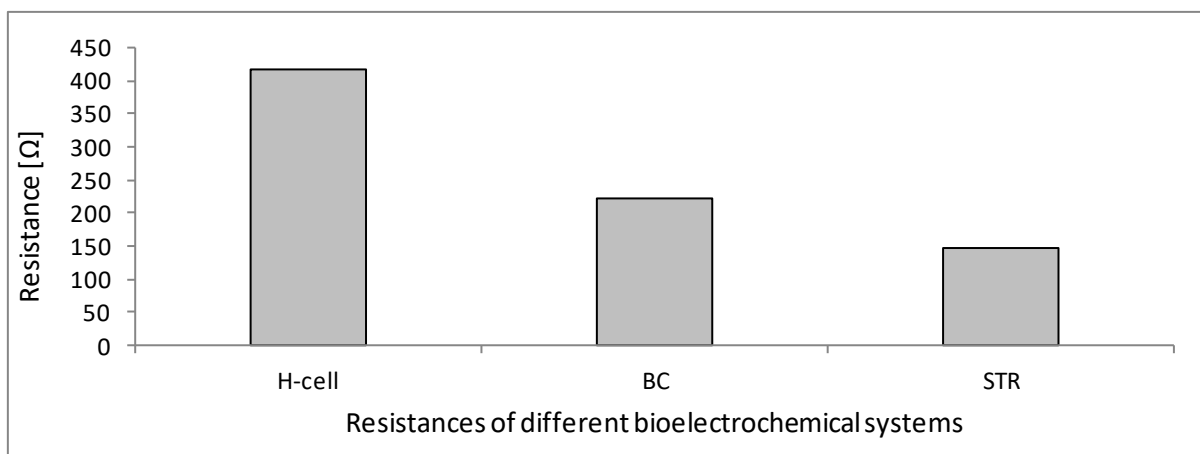


Figure 5: System resistances of three different systems

All systems equipped with carbon fabric as working and counter electrode; BC: bubble column reactor, STR: modified stirred tank reactor.

In the bubble column and the H-cell, the electrical resistances of the different system parts were tested using a graphite rod as working electrode and two reference electrodes to measure potential differences of various points in the systems at an applied current of 5 mA (Figure 6). It turned out that the largest resistances arose from the electrodes. In the H-cell, these electrode resistances were larger, maybe because the migration of charge carrying ions was limited by diffusion due to bad mixing conditions. In contrast, the membrane and the electrolyte showed much lower electrical resistances, again the resistances were higher in the H-cell because of the diffusion limited bridge, large electrode distance of 9 cm (instead of 6 cm in the bubble column reactor) and smaller membrane area.

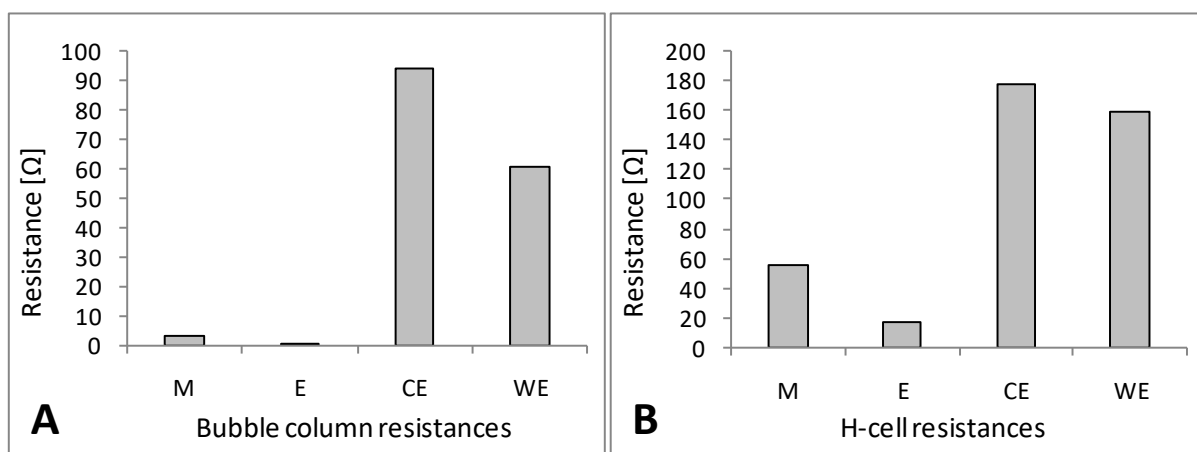


Figure 6: Resistances of the different system parts in bubble column reactor and H-cell

A) Resistances in bubble column reactor; B) Resistances in H-cell; (M: membrane resistance, E: electrolyte, CE: counter electrode, WE: working electrode).

The resistance of the working electrode within the system was different for different electrodes. Five different electrode materials were abiotically tested in the bubble column reactor. For these materials, several parameters were examined; the results are given in Table 9 below.

Table 9: Parameters of abiotically tested electrodes

	<b>Graphite rod</b>	<b>RVC foam,</b>	<b>Carbon fabric</b>	<b>Carbon granulate</b>	<b>Carbon laying</b>
Applied surface area [m <sup>2</sup> ]	935.8	7.9	3836.4	0.25	4.61
Applied outer surface [m <sup>2</sup> ]	0.0069	0.0124	0.0041	0.25	0.0057
Applied volume [m <sup>3</sup> ]	2.32*10 <sup>-5</sup>	4.00 *10 <sup>-5</sup>	8.3*10 <sup>-6</sup>	9.0*10 <sup>-6</sup>	1.38*10 <sup>-5</sup>
Applied weight [kg]	0.0371	0.0019	0.0023	0.15	0.0053
Specific electrical resistance [Ω*m]	0.00072	0.0184	0.016974	0.49	0.0024
Charge transfer resistance [Ω]	1.412	3076.92	258.82	25.00	26.92
Resistance in system [Ω]	61.7	143	118	70	184.8
Contact resistance [Ω]	0.7	5.9	109	n.a. <sup>1</sup>	4.4
Polarization time [h]	20	5	25	10	17
H <sub>2</sub> release at -0.9 V [μmol*h <sup>-1</sup> ]	1.05	1.86	0.00	4.25	1.03
Wagner number (Electrical field distribution at -0.9 V vs AgAgCl) [-]	2.5	2.1	0.5	119.6	3.3
Practicability <sup>2)</sup>	good	poor	Medium	poor	Medium
Surface alternation according to CV shift <sup>3)</sup>	yes	no	Yes	yes	Yes

<sup>1)</sup> n.a.: not applicable

<sup>2)</sup> practicability in terms of cleaning procedure; good practicability: easy to clean (e.g. by rinsing, storage in acid or grinding); medium practicability: mechanical cleaning not possible; poor practicability: mechanical cleaning not possible, chemical cleaning limited due to hydrophobic effects.

<sup>3)</sup> CV: cyclic voltammetry

Although the applied electrode volumes were similar, the applied surface areas calculated from the specific surface area differed significantly between the different materials. The glassy carbon granulate had the lowest surface area. Since the connection was done by a graphite rod, the surface taking part in the electrochemical reaction was probably the surface of the rod and not of the granulate. The applied surface areas of the carbon laying and the RVC foam were very low compared to graphite rod and carbon fabric at a similar volume, because the material densities and surface to volume ratio were low. Since the space in a bioreactor was limited, a low surface to volume ratio might become a limiting factor during process optimization, e.g. if the electrode surface shall be increased. The largest applied surface area was achieved with the carbon fabric material due to its high specific surface area. Because of its low density, the total applied electrode weight was less than 1/10 compared to the graphite rod at a three times higher total surface area, which might be a crucial parameter thinking about large-scale processes. However, it is not predictable whether all parts of the electrode surface participate in the desired reaction; it might be that pores are not accessible for the microorganisms, resulting in a lower active surface area. To achieve comparability in terms of process optimization, the geometrical surface area was used as base for calculations of specific ratios and current densities. For more mechanistic research, the total applied surface area would be the more important parameter.

The graphite rod showed the lowest specific resistance of  $0.7 \text{ m}\Omega \cdot \text{m}$ . The specific resistances of RVC foam, carbon laying and carbon fabric were comparable, but around 25 times higher than the resistance of the graphite rod. The highest specific resistance was obtained for the glassy carbon granulate bed. Similar specific resistances were reported in literature for carbon based electrode materials examined in microbial fuel cells (Fan et al., 2008).

Using the Nyquist plot obtained during a three-electrode electrochemical impedance spectroscopy measurement (example using carbon fabric electrode in the bubble column reactor see Figure 7), the charge transfer resistances of the different electrodes was estimated using the diameter of the resulting semi-circle (He and Mansfeld, 2009). The charge transfer resistance is a measure for the resistance during the formation of an electrical double layer on the electrode surface. The graphite rod showed the lowest charge transfer resistance, followed by the carbon granulate and the carbon laying. Interestingly, the charge transfer resistance of the carbon granulate bed is low compared to carbon fabric and RVC foam, which has the highest charge transfer resistance obtained from the impedance spectroscopy. The reason is most certainly that the charge transfer occurs mainly on the contacting graphite rod rather than on the glassy carbon beads. A very high charge transfer resistance was obtained for the RVC foam, which might also result from an insufficient electrical connection or the capture of gas bubbles in the foam.

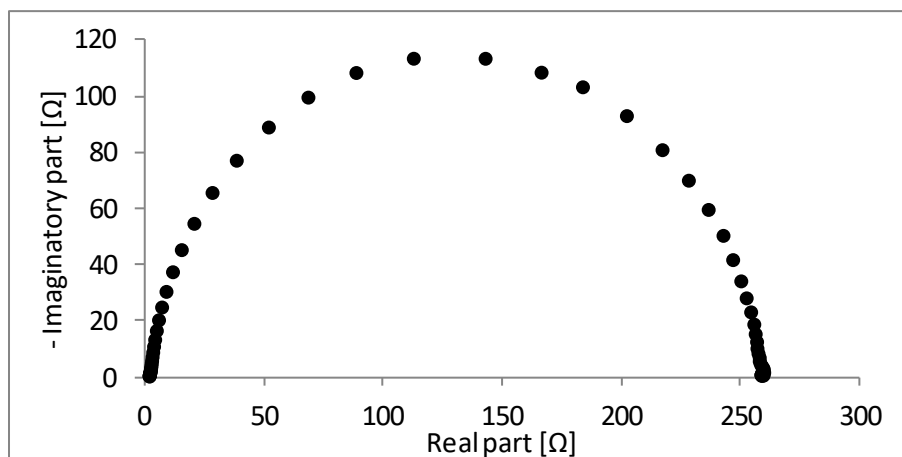


**Figure 7: Nyquist plot for carbon fabric electrode**

Nyquist plot obtained from electrochemical impedance spectroscopy; Imaginary part of the resistance plotted against real part of the resistance.

EIS could also be carried out with two electrodes only, but it would then not characterize the working electrode, but the system resistance (He and Mansfeld, 2009). Apart from the charge transfer resistance measured by impedance spectroscopy, the resistance of the electrode in the system measured by application of current and measurement of the resulting potential was investigated. The resulting values differed significantly from the charge transfer resistance, since the measuring mode is completely different. The electrode resistance measured at a constant current was more depending on the specific electrode resistance and the contact resistance than the formation of a double layer on the electrode. Graphite Rod and fixed bed of glassy carbon granulate led to similar resistances within the system, another hint that the electron transfer with the fixed bed electrode was mainly due to the contacting graphite rod. Surprisingly, the resistance of the carbon laying was rather high, although the contact resistance and the specific resistances were low. Possibly, the interaction between electrode surface and medium was low due to hydrophobicity.

The contact resistances between the electrode and the contacting titanium wire were measured. Titanium was used since it is relatively inert and non-corrosive (Logan, 2010b). The highest resistance was observed for the carbon fabric. It was not measured for the fixed bed, because due to the high specific resistance it was not possible to measure the additional (probably lower) contact resistance reliably. In literature, contact resistances below 1  $\Omega$  have been reported (Dewan et al., 2008). Only the graphite rod showed such a low contact resistance here, giving evidence that for all other electrodes the electrical connection should be improved by increasing the contact area between electrode material and titanium.

During abiotic chronoamperometric measurements at -900 mV, the polarization time of each electrode until the current stabilized was estimated. The longest polarization time occurred for carbon fabric, followed by the graphite rod. The RVC foam showed a very short polarization time of 5 hours, possibly due to the low specific area to polarize. The chronoamperometric experiments also showed

hydrogen formation in dependence of the electrode material. For all electrodes, the hydrogen production rates were low, and in case of the carbon fabric electrode, no hydrogen production occurred. Interestingly, the cyclic voltammogram of the carbon fabric electrode done prior to the chronoamperometric measurement revealed that hydrogen production should start at  $-0.85$  V vs. Ag/AgCl, indicated by a steep slope in the current curve. After the chronoamperometric measurement, this steep decrease did not occur anymore (Figure 8 C), leading to the conclusion that an alteration of the electrode surface during potential application hindered hydrogen evolution. In contrast, the CV of the RVC foam showed that a steep slope of the current curve already began at  $-0.9$  V vs. Ag/AgCl before and after the chronoamperometric experiment (Figure 8 D), suggesting that the electrode surface did not alter significantly during potential application. For graphite rod and carbon granulate, the shape of the CV did not allow conclusions about the hydrogen production potential, the CV occurred more like a resistor measurement, indicating that capacitive currents of the system overlaid oxidation and reduction peaks in the CV. For the carbon laying, the hydrogen evolution potential began around  $-0.9$  V vs. Ag/AgCl after the chronoamperometric measurement, but not prior to it (Figure 8 E), so that surface alteration during potential application in this case might be beneficial for the hydrogen production and later the methane production. Evaluating the cyclic voltammograms, a difference between pre-chronoamperometric and post-chronoamperometric was observed for all electrodes except the RVC foam (Figure 8). This led to the conclusion that a surface reaction took place at the electrodes. The CV of the carbon granulate bed looked similar to that of the graphite rod contacting it, another hint that the carbon granulate did not contribute much to the electrochemical behavior of the systems (Figure 8 D).

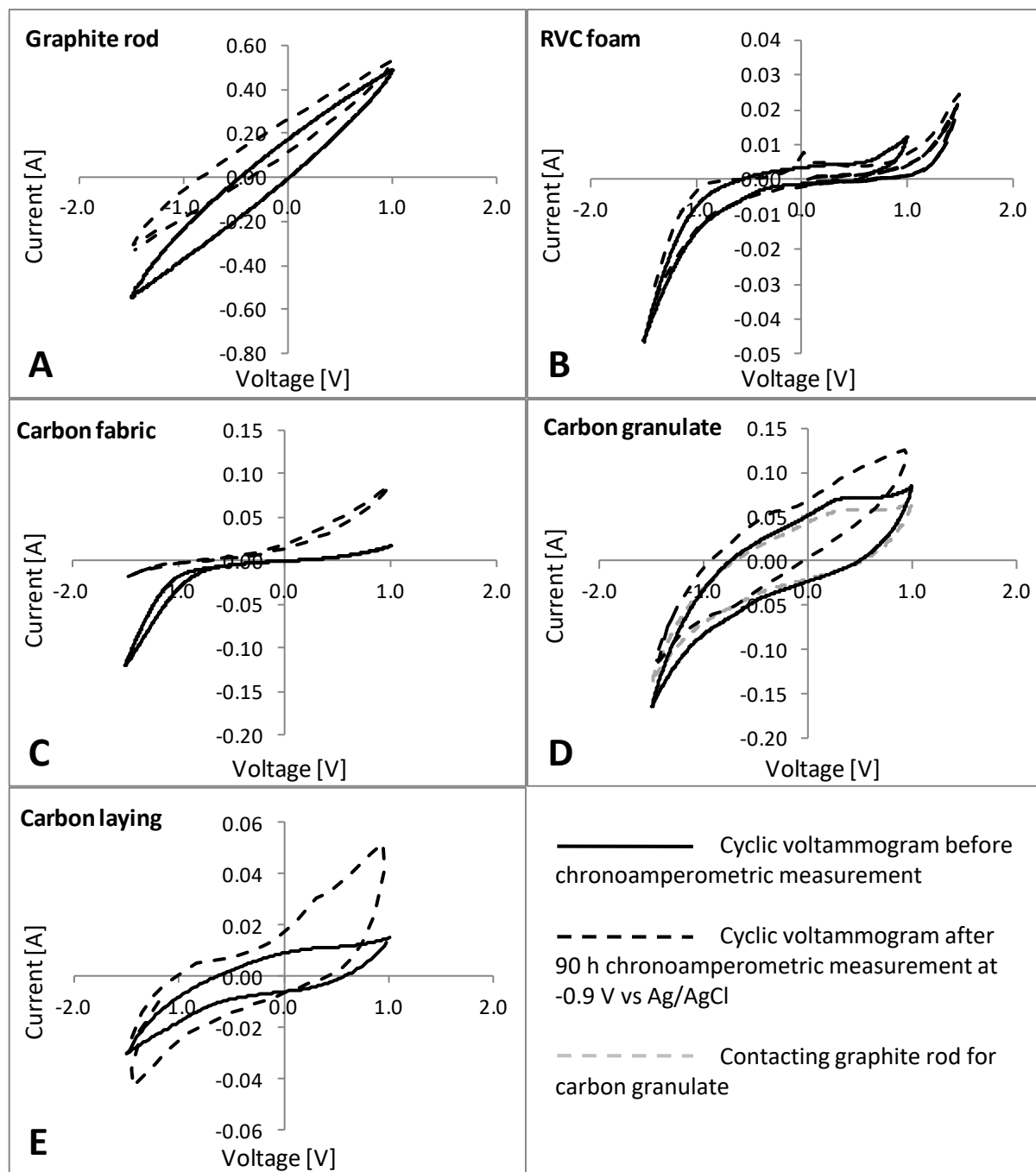


**Figure 8: Cyclic voltammograms of different electrodes**

Voltammograms done before and after chronoamperometric measurement for each electrode; A) Graphite rod electrode; B) RVC foam electrode; C) Carbon fabric electrode; D) Carbon granulate electrode; E) Carbon laying electrode; black solid lines: cyclic voltammogram before chronoamperometric measurement; black dashed line: cyclic voltammogram after chronoamperometric measurement; grey dashed line in D: cyclic voltammogram of graphite rod contacting the carbon granulate

From the voltammograms, Tafel plots were created to calculate the Wagner number (see example in section 6.3.1, Figure 47). The Wagner number is a measure for the distribution of the electrical field. Wagner numbers higher than 1 indicate an even field distribution; four electrodes showed Wagner numbers higher than two, accounting for a quite even field distribution. The highest Wagner number

was calculated for the fixed bed. A Wagner number below 1 was calculated for the carbon fabric, according to this value, the electrical field was not evenly distributed.

Apart from the calculation of the Wagner number, the electrical field distribution was tested by measurement of the potential difference between working electrode and a reference electrode placed at different spots within the reactor. The electrical field lines are rectangular to the equipotential lines which were obtained from these measurements (Figure 9). It has to be mentioned that the potential was depending on the immersion depth of the reference electrode used for the measurement, so it was made ascertained that the immersion depth was equal at all measuring spots. The immersion depth dependency might result from CO<sub>2</sub> and correspondingly pH gradients, influencing the medium conductivity.

The equipotential lines were relatively regularly shaped for all electrodes. The potential in the reactor filled with carbon granulate was constant at nearly all spots within the reactor, which confirmed the very high Wagner number calculated for this electrode. Although the Wagner number suggested an unevenly distributed electrical field for the carbon fabric electrode, the equipotential lines appeared relatively regular. For the RVC foam, the equipotential lines had a larger dent on the left side (Figure 9), suggesting that the electrical field is weaker on the left side than on the right side. This might result from a small difference in the submersion of the reference electrode, since the potential was different at various water levels.

From the electrochemical characterization it was concluded, that the graphite rod was the most suitable electrode for bioelectromethanogenesis, since it combined low resistances with a high specific surface area and an evenly distributed electrical field. The least suitable electrode material might be the carbon fabric electrode because of its high electrical resistance and low Wagner number, although the equipotential lines suggested a regular electrical field distribution. Although these indications allow first predictions of the electrode behavior in the biotic process, all five electrodes were tested biotically, since the results are not concrete enough to rule out the suitability of one electrode completely.

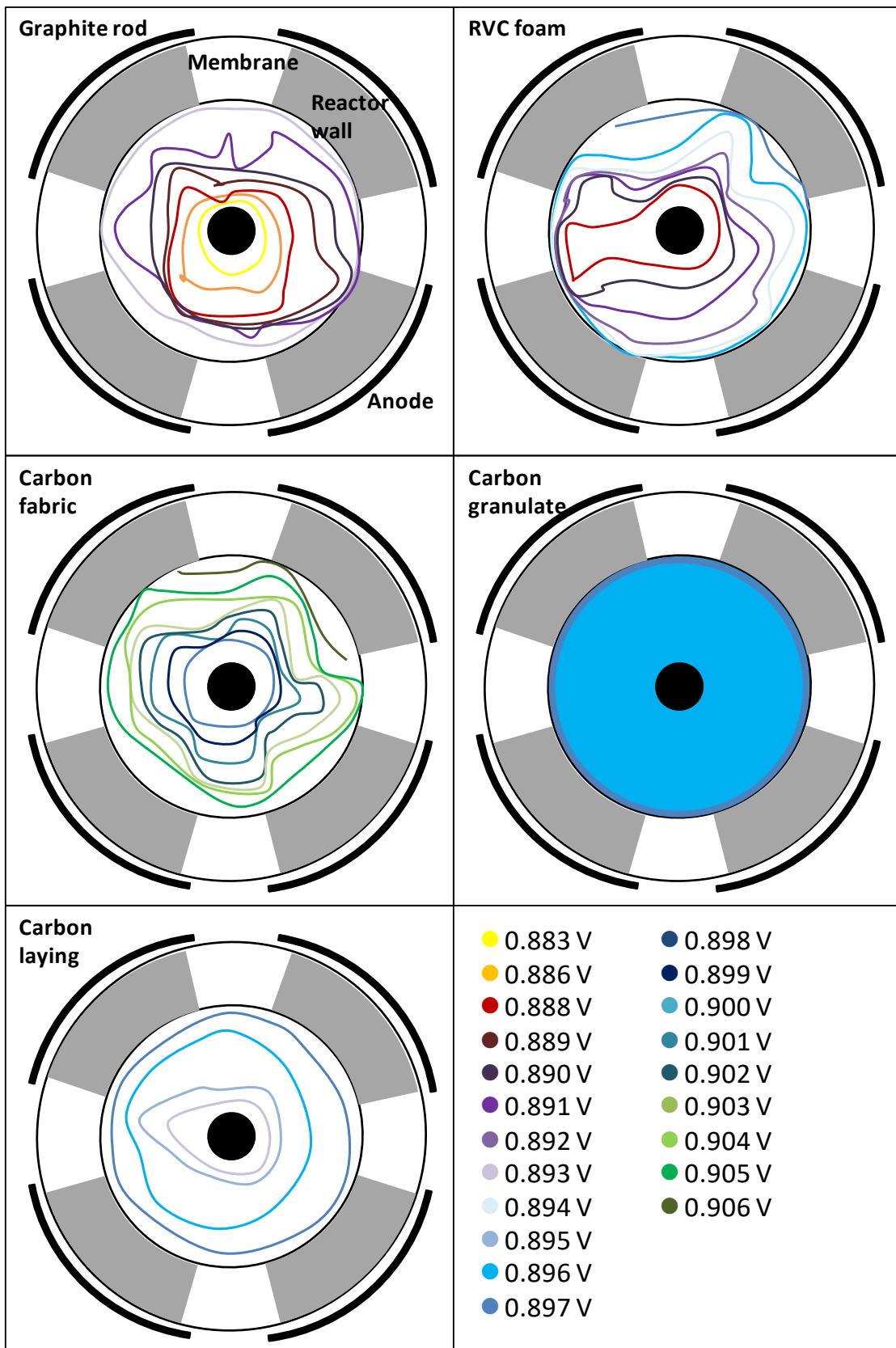


**Figure 9: Equipotential lines in bubble column reactor with different electrodes**

Equipotential lines (colored lines for different potentials) in reactors with five different working electrodes (central black dot in each figure). Potential always measured between working electrode and a reference electrode.

#### 4.2.2 Physical Characterization

The physical characterization of the system was done as described in section 6.3.2, also using results from the chronoamperometric measurements in the previous section (4.2.1).

The heating of the system using the heating jacket and the heating stick led to a stable temperature in the working and the counter chamber (Figure 10 A). When using an external loop for improved medium circulation, the temperature in the working chamber was on average 1.5 °C lower than the set temperature (Figure 10 B).

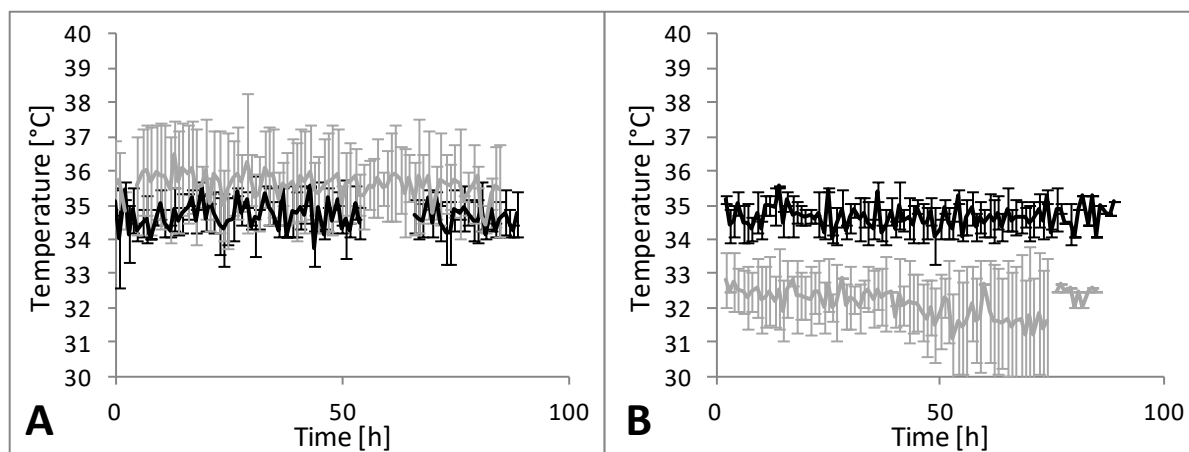


**Figure 10: Temperature in bubble column reactor**

A) Temperature time course in reactor without external loop, black: Temperature in anode chamber, grey: Temperature in cathode chamber; B) Temperature time course in reactor with external loop, black: Temperature in anode chamber, grey: Temperature in cathode chamber.

However, the calculation of the heat losses in the system reveal that a huge amount of energy is required to compensate for the heat losses through the boundaries of the system (Table 10). The heating energy was thus the highest energy demand of the system. This was not a specific problem of the bioelectrochemical reactor, but usually occurs in all lab-scale reactors, since the volume to surface ratio is unfavorable and the reactors often are not thermally isolated. The percentage of energy input by heating usually decreases with an increasing reactor size (Economy of Scales). To minimize the heat losses, an isolation of the heating jacket could be applied. For an industrial process, integrated heat management should be applied to use waste heat streams to maintain the reactor temperature. The gas stream through the bubble column reactor also contributed to the heat loss by heating of the gas within the reactor. The increasing temperature of the gas stream did not cause problems in the bubble column reactor, but in the stirred tank reactor: due to the small headspace height, the gas stream transported larger amounts of evaporated medium out of the stirred tank reactor. An exhaust gas cooler would be necessary to overcome this issue.

Table 10: Heat losses for the bubble column and the stirred tank reactor

System boundary	Heat loss
Bubble column wall (heating jacket and reactor upper part)	437.25 W + 8.05 W
Bubble column lid	541.5 W
Bubble column bottom	8.09 W
Bubble column gassing	0.0126 W (30 ml*min <sup>-1</sup> ) 0.0252 W (60 ml*min <sup>-1</sup> ) 0.0378 W (90 ml*min <sup>-1</sup> )
Bubble column water surface	5.457 W
Stirred tank wall	480.375 W
Stirred tank lid	1033.772 W
Stirred tank bottom	1033.772 W
Stirred tank gassing	0.0252 W (60 ml*min <sup>-1</sup> )

The pH of the working medium remained relatively stable during the chronoamperometric experiments, only slight decreases of the pH were measured in the counter chamber and slight increases in the working chamber. This was observed also for the biotic experiments.

In the bubble column reactor, it was not possible to apply an overpressure to the working chamber. The membrane cracked because of the pressure difference between working chamber and the counter chamber, since the counter chamber was open to the surrounding environment and could therefore not be pressurized. In H-cells and stirred tank reactor, pressure could be applied to both chambers, since both chambers can be operated as closed systems.

As desired, small bubbles through the PTFE sparger plate at the bottom of the bubble column reactor rose through the liquid. Table 11 gives an overview of the different gassing conditions in the three reactors. The bubble diameter was relatively large in the bubble column reactor. No trend for a correlation between bubble diameter and gassing rate could be detected. Using the second sparger plate with smaller perforations, the bubble diameter decreased to 0.0071 m on average. For the H-cell reactor, gassing was done by a cannula, leading to smaller bubbles with a higher ascend velocity due to the smaller size (Stoke's law). The gas bubbles in the stirred tank reactor were also smaller than in the bubble column reactor. The reason might be the different sparger and the distribution of bubbles caused by the stirrer. The vvm of the bubble column reactor and the stirred tank reactor was set to 0.03 as starting condition; in the bubble column, also higher gassing rates were tested. The vvm in the H-cell was higher, since the used rotameter did not allow reliable measurement of the volume flux below 5 ml\*min<sup>-1</sup> and the working volume is in both cases just 100 ml.

Table 11: Gassing parameters for different reactor systems

	Bubble column	Stirred tank	H-cell
Bubble diameter	0.0081 m (30 ml*min <sup>-1</sup> )	0.007 m	0.006 m
	0.0086 m (60 ml*min <sup>-1</sup> )		
	0.0075 m (90 ml*min <sup>-1</sup> )		
Bubble ascend velocity	0.244 m*s <sup>-1</sup> (30 ml*min <sup>-1</sup> )	0.24 m*s <sup>-1</sup>	0.735 m*s <sup>-1</sup>
	0.285 m*s <sup>-1</sup> (60 ml*min <sup>-1</sup> )		
	0.260 m*s <sup>-1</sup> (90 ml*min <sup>-1</sup> )		
vvm	0.03 l*min <sup>-1</sup> (30 ml*min <sup>-1</sup> )	0.03 l*min <sup>-1</sup>	0.05 l*min <sup>-1</sup>
	0.06 l*min <sup>-1</sup> (60 ml*min <sup>-1</sup> )		
	0.09 l*min <sup>-1</sup> (90 ml*min <sup>-1</sup> )		
Superficial gas velocity	8.8*10 <sup>-5</sup> m*s <sup>-1</sup> (30 ml*min <sup>-1</sup> )	9.7* 10 <sup>-5</sup> m*s <sup>-1</sup>	4.2*10 <sup>-5</sup> m*s <sup>-1</sup>
	1.8*10 <sup>-4</sup> m*s <sup>-1</sup> (60 ml*min <sup>-1</sup> )		
	2.6*10 <sup>-4</sup> m*s <sup>-1</sup> (90 ml*min <sup>-1</sup> )		
k <sub>L</sub> a	1.26 l*h <sup>-1</sup> (30 ml*min <sup>-1</sup> )	9.988 l*h <sup>-1</sup>	1.7 l*h <sup>-1</sup>
	2.232 l*h <sup>-1</sup> (60 ml*min <sup>-1</sup> )		
	3.852 l*h <sup>-1</sup> (90 ml*min <sup>-1</sup> )		
Hydraulic retention time	27.5 min (30 ml*min <sup>-1</sup> )	34.2 min	20.1 min
	13.8 min (30 ml*min <sup>-1</sup> )		
	9.3 min (90 ml*min <sup>-1</sup> )		
Gas hold up	0.0021 (30 ml*min <sup>-1</sup> )	0.027	0.0033
	0.0075 (60 ml*min <sup>-1</sup> )		
	0.0216 (90 ml*min <sup>-1</sup> )		
Power input gassing	0.00086 W (30 ml*min <sup>-1</sup> )	0.01007 W	4.15*10 <sup>-5</sup> W
	0.00172 W (60 ml*min <sup>-1</sup> )		
	0.00258 W (90 ml*min <sup>-1</sup> )		
Bond number	2.28 (30 ml*min <sup>-1</sup> )	1.70	1.17
	2.63 (60 ml*min <sup>-1</sup> )		
	1.95 (90 ml*min <sup>-1</sup> )		
Reynolds number	0.99 (30 ml*min <sup>-1</sup> )	0.94 (gassing) 4905.94 (stirring)	0.34
	2.12 (60 ml*min <sup>-1</sup> )		
	2.75 (90 ml*min <sup>-1</sup> )		
Weber number	3.42 (30 ml*min <sup>-1</sup> )	2.85	22.24
	5.01 (60 ml*min <sup>-1</sup> )		
	3.59 (90 ml*min <sup>-1</sup> )		

All superficial gas velocities were below  $0.05 \text{ m}\cdot\text{s}^{-1}$ , leading to the conclusion that the flow regime within the reactors was a homogeneous bubbly flow in all systems (Figure 50, section 6.3.2). The highest superficial gas velocity was calculated for the stirred tank reactor (excluding results obtained with increased vvm in the bubble column reactor). The hydraulic retention time calculated based on the superficial gas velocity and the liquid level was longest in the stirred tank reactor and the bubble column reactor, in the reactors with higher vvm's it was significantly shorter. The largest gas hold up was measured in the stirred tank reactor, since the bubbles did not only rise straight but also show a rotation move because of the stirring. In the bubble column, the gas hold up increased with increasing gas flux. In bioelectromethanogenesis, gaseous substrates and products appear; therefore, the gassing of the reactor is crucial for the process.

An important parameter for the gassing is the  $k_{L}a$  value, which allows comparison of the  $\text{CO}_2$  transfer from gas phase to liquid phase in different reactors. To be able to calculate the  $k_{L}a$ , it was necessary to measure the amount of  $\text{CO}_2$  dissolved in the medium. Dissolved  $\text{CO}_2$  probes based on the Severinghaus Principle (Severinghaus and Freeman Bradley, 1958) are available, but are sensitive against ammonium and acetate and can therefore not be used in the MES-medium (supplier information (PreSens Precision Sensing, Regensburg, Germany)). Pre-experiments using self-assembled  $\text{CO}_2$  probes based on the same principle using a standard pH probe and natural rubber membrane showed a strong drift of the sensor and were therefore not applicable. The used MES medium contained a carbonate buffer, therefore, the pH of the medium changes at different  $\text{CO}_2$  concentrations; the  $\text{CO}_2$  concentration was thus correlated to the medium pH for the calculation of the  $k_{L}a$  value.

Using the dynamic method, the stirred tank reactor showed the highest  $k_{L}a$  value because the gas transfer was increased by stirring. In the bubble column, the  $k_{L}a$  increased with increasing gas flux. Using an altered sparger plate with smaller perforations in the bubble column reactor improved the  $k_{L}a$  by 51 % to  $1.9 \text{ l}\cdot\text{h}^{-1}$  at a gas flux of  $30 \text{ ml}\cdot\text{min}^{-1}$ . The smaller bubbles caused by the decreased perforation diameter led to smaller bubbles with a higher gas-liquid interfacial area, resulting in a higher  $k_{L}a$  value. Comparable studies examining the methanation of  $\text{CO}_2$  showed  $k_{L}a$  ( $\text{CO}_2$ ) values between  $0.8$  and  $9.6 \text{ l}\cdot\text{h}^{-1}$  (Pauss et al., 1990), similar to the values measured in this work. Data for  $k_{L}a$  values obtained especially for BES were not reported so far. The introduction of an external loop with a circulation rate of  $47 \text{ ml}\cdot\text{min}^{-1}$  to the bubble column reactor did, in contrast to the alteration of the sparger plate, not alter the  $k_{L}a$  value.

The power input caused by gassing was calculated for bubble column reactor and H-cells using Equation 26. The power input calculated for the bubble column reactor was larger, based on the larger reaction volume and the high superficial gas velocity; it increased with increasing gas flux. For the stirred tank reactor, the power input by gassing had to be calculated using the power input for stirring. This was calculated assuming the Newton number as 5.1 according to the Newton-Reynolds diagram

(Figure 51) with the calculated stirrer Reynolds number (4906). At 100 rpm, the power input by stirring accounted for 4.87 mW, leading to the calculated power input by gassing shown in Table 11. Several other dimensionless numbers would allow the characterization of bioreactors and chemical reactors. There are for example numbers characterizing the mass transport and transport kinetics within the reactor, like the Schmidt number, the Sherwood number and the Damköhler number. In case of a bubble column reactor, the most important numbers refer to the gas transport, while the mass transport characterization is less effective for Scale-Up in a process with gaseous substrates. Therefore, only numbers characterizing gas transport and flow properties were calculated.

The calculated Bond numbers were higher than 1 in each of the reactors. The Weber numbers calculated were all higher than 2, showing that the gassing itself was not suppressed by the hydraulic pressure of the liquid medium. According to section 6.3.2 (Figure 50), this suggested an unstable gas bubble size. A significant size alteration could, however, not be observed by filming the rising gas bubbles and evaluating the bubble diameters at different height levels within the reactor. The Reynolds numbers calculated for the gassing in all reactors suggests a laminar flow regime. In the stirred tank reactor, the stirrer Reynolds number was significantly higher and predicted turbulent flow conditions within the reactor.

### 4.3 Development and Optimization of the Bioelectromethanogenic Process

If not stated otherwise, all following experiments are conducted in two independent biotic replicates with one abiotic control. The values given are the average over time of the mean values.

#### 4.3.1 *Methanococcus maripaludis* as Electroactive Methanogen

*Methanococcus maripaludis* was used as biocatalyst for bioelectromethanogenesis in an H-cell with an applied potential of -0.9 V vs. Ag/AgCl at the working electrode (see further operational conditions in section 6.6.1). This test confirmed the electroactivity of the methanogen, which was formerly reported in literature (Deutzmann et al., 2015; Lohner et al., 2014). A current consumption of  $-463.59 \pm 15.09 \text{ mA}\cdot\text{m}^{-2}$  was measured (current density of  $-175.65 \pm 11.32 \text{ mA}\cdot\text{m}^{-2}$  in the abiotic control under the same conditions) and a mean specific methane production rate of  $19.98 \pm 3.49 \text{ mmol}\cdot\text{d}^{-1}\cdot\text{m}^{-2}$  was reached; further results are shown in Table 12. As in other studies before, the amount of abiotically produced hydrogen in the control experiment ( $49.89 \pm 13.53 \text{ mmol}\cdot\text{d}^{-1}\cdot\text{m}^{-2}$  at a Coulombic efficiency of 39.59 %) could not explain the amount of methane found by indirect electron transfer via abiotically produced hydrogen (Siegert et al., 2014). 58.66 % of the methane obtained were produced via indirect electron transfer, the remaining 41.34 % were explainable via direct electron transfer, or mediated transfer via so far unknown mediators, possibly self-excreted, or by biotically produced hydrogen via hydrogenases present in the microorganisms (Deutzmann et al., 2015). The conversion rate of abiotically produced hydrogen was 94 %, suggesting that the microbial metabolism was as fast as the abiotical hydrogen production. Only  $3.0 \text{ mmol}\cdot\text{d}^{-1}\cdot\text{m}^{-2}$  hydrogen were released from the biotic experiment. The total energy efficiency could not be calculated, since the total energy loss through the incubator hood could not be determined; the energy efficiency excluding the heat loss was 22.24 %.

After *M. maripaludis* proved to be electroactive, a first test was carried out in the bubble column reactor with parameters given in section 6.6.2.1. As in the H-cell, a potential of -0.9 V vs. Ag/AgCl was applied to the working electrode. The results of this experiment are shown in Table 12.

Table 12: Results of the first bioelectromethanogenic tests at -0.9 V vs. Ag/AgCl

	$Y_P$ [mmol*d <sup>-1</sup> ]	$Y_{P,EI}$ [mmol* d <sup>-1</sup> *m <sup>-2</sup> ]	$Y_{ST}$ [mmol* d <sup>-1</sup> *l <sup>-1</sup> ]	$Y_{PS}$ [%]	$\gamma$ [%]	$\eta_{C,MES}$ [%]	$\eta_E$ [%]
<b>H-cell</b>	0.024 ± 0.004	19.98 ± 3.49	0.24 ± 0.04	0.039 ± 0.000	0.0079 ± 0.0014	47.27 ± 4.17	n.a.
<b>Bubble column</b>	0.23 ± 0.01	33.84 ± 1.65	0.23 ± 0.01	0.065 ± 0.00	0.0130 ± 0.0006	50.96 ± 9.64	$2.42 \cdot 10^{-4}$

To compare two reactors with different working volumes, the space-time yield  $Y_{ST}$  was used. In case of the bubble column reactor and the H-cell under the starting conditions, the space-time-yield was nearly the same, whereby the absolute methane production rate in the bubble column was nearly 10fold of that observed in the H-cell due to the larger working volume. It could thus be concluded that the bubble column reactor was suitable for the bioelectromethanogenesis process, the performance of the process was reproducible as indicated by the small deviations, and even more important, results obtained from H-cell screening experiments could be used to estimate the performance in a larger reactor. The Coulombic efficiency  $\eta_{C,MES}$  lies within the same range for biotic methane production, for the abiotic hydrogen production, the H-cell was more suitable. The Coulombic efficiency for abiotic hydrogen production was only 10.51 % in the bubble column reactor. In both systems, the use of a biocatalyst increased the efficiency of electron usage, confirming that the electroactive methanogens added value to the process. The yield per substrate based on  $CO_2$  usage was higher in the bubble column reactor, although still very low. This implied that the substrate availability was not yet the main limitation; otherwise the yield per substrate should be similar in both reactors. In the bubble column reactor, the hydrogen conversion rate (88.34 %) was slightly lower than in the H-cell, although the hydrogen production detected in the biotic experiments was also lower ( $0.78 \pm 0.64 \text{ mmol} \cdot \text{d}^{-1} \cdot \text{m}^{-2}$ ), at a lower abiotic specific hydrogen production ( $6.69 \text{ mmol} \cdot \text{d}^{-1} \cdot \text{m}^{-2}$ ). This also resulted in a higher percentage of direct electron transfer in the bubble column reactor, 95.63 % of the methane were produced via direct electron uptake. It seemed that in the bubble column reactor, the methanogens could more efficiently interact with the electrode, while the hydrogen production was less efficient. It might be that a higher hydrogen production would result in a higher methane production, thus providing a reason to optimize the applied potential. The specific yield  $Y_{P,EI}$  was higher in the bubble column reactor since the ratio between geometric electrode surface area and working volume was smaller. The product purity was very low in both systems, 0.0079 % in the H-cell and 0.013 % in the bubble column reactor. The energy efficiency in the bubble column was extremely low, showing that the process is not industrially applicable without optimization. The low energy efficiency was mainly due to the large amount of energy needed for heating. The total energy input to the bubble column was 933.17 W, mainly consisting of 926.35 W heating energy to compensate for the heat loss through the walls and at the water surface. 5.95 W additional heating energy needed to be supplied to compensate the heat loss caused by the gas stream, whereas only 0.00086 W power input resulted from the gassing power input and 0.009 W were direct electrical power at a current density of  $644.00 \pm 196.00 \text{ mA} \cdot \text{m}^{-2}$ . Excluding the energy for heating, the energy efficiency was 24.86 %, close to that observed in the H-cell. The overall energy efficiency could therefore be improved using an isolating jacket or using heat coupling when designing a reactor in a larger scale.

To optimize the process in terms of biology, the initial OD within the working chamber was doubled while maintaining all other conditions (according to section 6.6.2.5). As Figure 11 shows, this did not have any positive effect on the methane production; on the contrary, the absolute and specific methane

production rate as well as the space time yield nearly halved. Still, 91.50 % of the methane produced could be explained via direct electron transfer, whereby no hydrogen could be detected in the off-gas of the biotic experiment with higher initial OD, giving a 100 % conversion of the abiotic hydrogen. It has to be mentioned that the OD decreased to 0.11 on average if starting at OD 0.2, while the starting OD of 0.1 remained constant. This furnished evidence that the low amount of methanogens was not limiting the process. On the contrary, the methane production rate decreased, suggesting an inhibition of cells at higher ODs and a die off of the microorganisms. The Coulombic efficiency was not affected significantly, since the mean current density nearly halved when using the higher initial optical density. Due to the lower amount of methane, the product purity and yield per substrate also decreased. In contrast, the energy efficiency excluding heating increased at higher initial OD to 33.25 % because of the lower current density.

The test with an increased optical density was conducted again after several optimization steps which are shown in the following sections (4.3.2 to 4.3.5). The revised process conditions for the second OD optimization trial are shown in section 6.6.2.5. Again, the doubling of the initial OD did not result in a higher methane production rate (Figure 11) or an altered Coulombic efficiency, but a drop of absolute and specific methane production rate, product purity, space time yield and yield per substrate by 25 %. Again, the initial OD of 0.2 decreased to 0.16 on average. It seemed that the methanogens were still not limiting the process; as before the optimization, the methane production decreased and a die off of the methanogens occurred, although the die-off rate seemed to be lower. As under the conditions before optimization, the energy efficiency excluding heating increased with increasing OD from 21.73 % to 25.78 %, since the current density decreased from 2.5 A\*m<sup>2</sup> to 1.75 A\*m<sup>2</sup>. Including the heating energy, the energy efficiency was in both cases again extremely low, but higher with an initial OD of 0.1, since the large amount of heating energy outweighs the influence of the decreased current density.

The main limitation in this case might be the maintenance demand of the microorganisms on hydrogen, which was estimated to 0.69 mol\*d<sup>-1</sup> in the reactor (based on values in section 6.6.1). This was in no case compensated by the hydrogen produced abiotically in the bioelectrochemical system. Therefore, growth was not possible and the methanogens probably lacked energy for cell vitality. Since the doubled OD would consume even more hydrogen for maintenance, the viability probably decreased, resulting in a lower methane production rate.

To see if the starting OD of 0.1 was perhaps too high as well, the same conditions were used with half of the initial OD of 0.05, which led to a decrease in methane production and current consumption at a slightly decreased Coulombic efficiency. The conclusion was that the few microorganisms cannot get in touch with the electrode efficiently anymore for a direct electron transfer, since the contact rate is too low. The optical density should therefore not fall below 0.1.

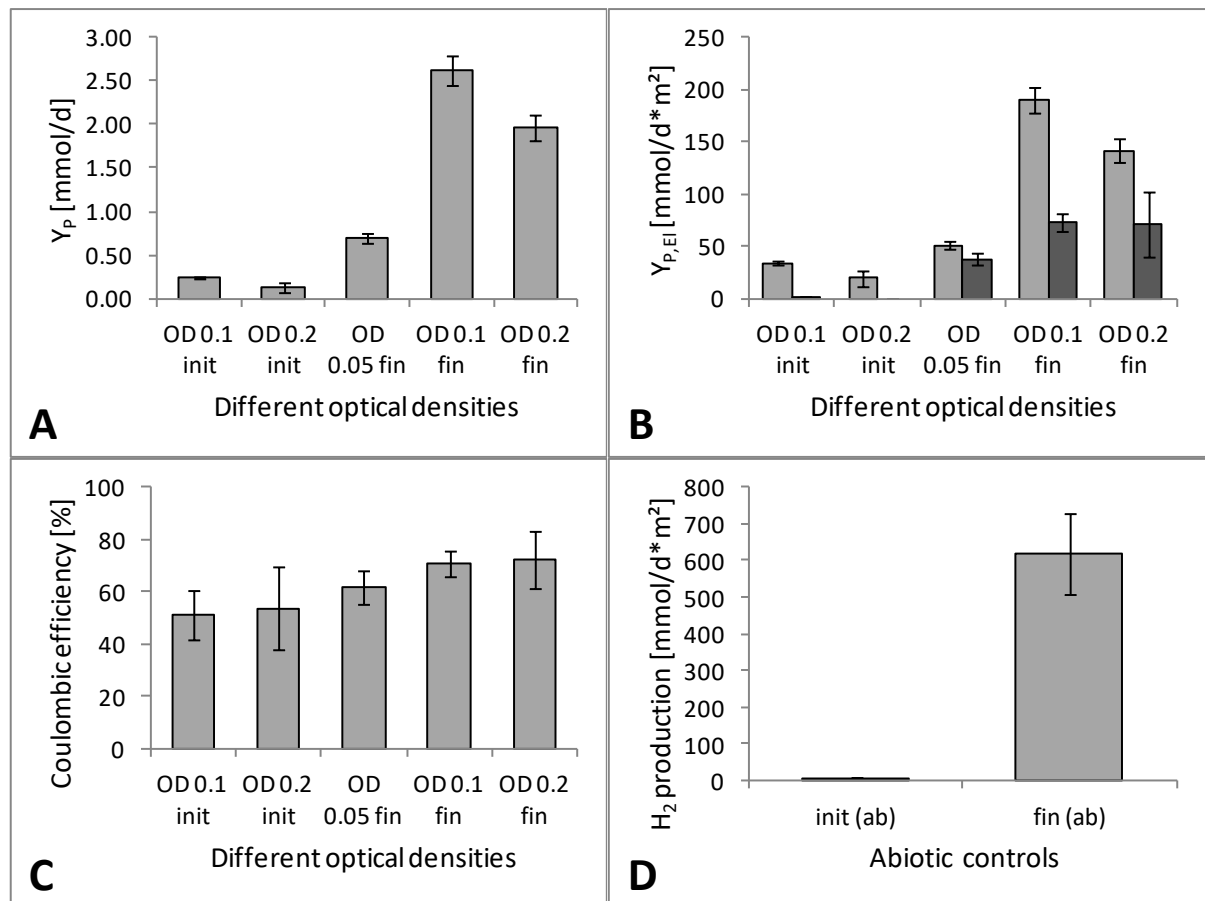


**Figure 11: Performance of bioelectromethanogenesis using different ODs**

A) Methane production rate using different ODs (init: initial (starting) conditions, fin: final (optimized) conditions) as described in section 6.6.2.5); B) Light grey: Specific methane production rate using different ODs; Dark grey: Specific biotic hydrogen production rate using different ODs; C) Coulombic efficiencies for biotic methane production using different ODs; D) Abiotic specific hydrogen production rate using initial (init) and optimized conditions (fin).

### 4.3.2 Potential Optimization

As shown in previous studies with *M. maripaludis*, the applied potential has an influence on the performance of the bioelectromethanogenesis process (Lohner et al., 2014). Here, three different working potentials were tested (see also section 6.6.2.2), resulting in different methane production rates as shown in Figure 12. As expected, the lowest potential of -1.1 V vs. Ag/AgCl led to the highest absolute methane production rate of  $0.57 \pm 0.7 \text{ mmol} \cdot \text{d}^{-1}$ , but resulted also in a shift to a more indirect electron transfer 41.96 % compared to 4.37 % at -0.9 V vs. Ag/AgCl. The abiotic hydrogen production increased significantly ( $144.05 \text{ mmol} \cdot \text{d}^{-1} \cdot \text{m}^2$ ) at the lower potential with a higher Coulombic efficiency for abiotic hydrogen evolution of 29.19 % (Figure 12), although this could not be predicted from the cyclic voltammograms (see 4.2.1). Apart from that, the Coulombic efficiency of methane production did not significantly change (Figure 12). The larger amount of abiotic hydrogen was still converted efficiently at a hydrogen conversion rate of 95.84 %, with  $5.99 \text{ mmol} \cdot \text{d}^{-1} \cdot \text{m}^2$  residual hydrogen in the biotic runs. The decreased working potential of -1.1 V vs. Ag/AgCl mainly improved the indirect electron transfer, but not the direct electron transfer; the absolute and specific methane production rate as well as the space time yield, the product purity and the yield per substrate increased by a factor of 2.4 when decreasing the potential from -0.9 V to -1.1 V vs. Ag/AgCl, but the amount of methane explainable by direct electron transfer was only affected by a factor of 1.4, the amount of methane via indirect electron transfer, in contrast, increased by a factor of 23.4. Since the overall Coulombic efficiency did not change, it was concluded that direct electron transfer is not more efficient than indirect electron transfer. In terms of energy efficiency, using -1.1 V led to a decrease in efficiency from 24.86 % to 19.78 % excluding the energy used for heating, since the electrical energy input increased because of increasing magnitude of terminal voltage (-2.7 V instead of -2.0 V) and increasing current density ( $1.58 \text{ A} \cdot \text{m}^2$  instead of  $0.64 \text{ A} \cdot \text{m}^2$ ). Including the heating energy, the efficiency increased from 0.00024 % to 0.00060 % because of the outweighing amount of heating energy. However, the energy efficiency for abiotic hydrogen production in the abiotic control was 38.87 %, at a working potential of -1.1 V excluding heating energy, indicating that under the used conditions the biocatalysis did not add value in terms of energy conversion, although the Coulombic efficiency was higher when applying the electroactive microorganisms. The reason was mainly the decreased electrical power input in an abiotic experiment due to lower current density and lower magnitude of terminal voltage.

At a higher potential of -0.7 V vs. Ag/AgCl, no methane formation could be detected. As Lohner et al. reported, the methane production decreased by two-thirds by shifting from -0.7 V vs. SHE (-0.9 V vs. Ag/AgCl) to -0.6 V vs. SHE (-0.8 V vs. Ag/AgCl), so it might be that the even higher potential of -0.7 V vs. Ag/AgCl does either not lead to a methane production or, more likely, the amount of methane is not detectable via gas chromatography. There was also no significant hydrogen production in an abiotic test at -0.7 V vs. Ag/AgCl.

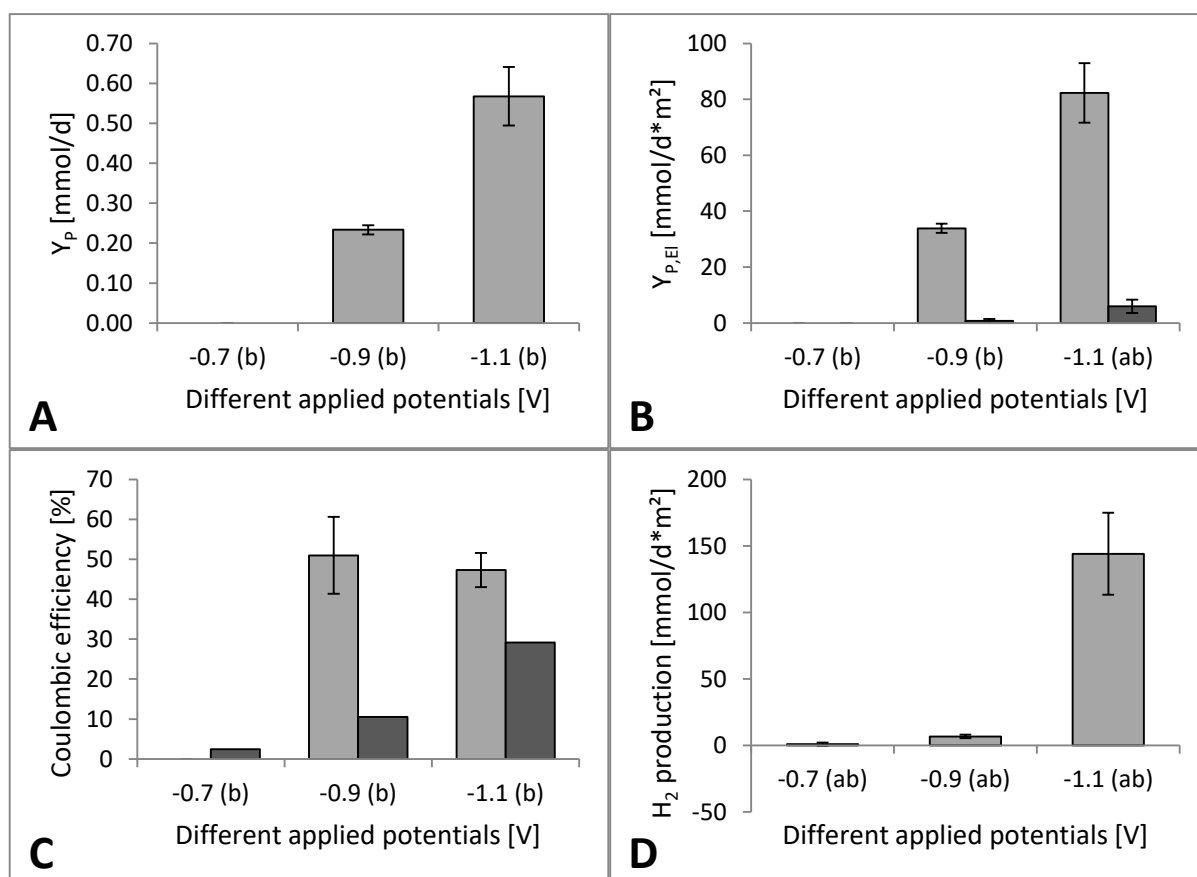


**Figure 12: Results of the potential optimization in the bubble column reactor**

A) Methane production rate using different potentials; B) Light grey: Specific methane production rate using different potentials; Dark grey: Specific biotic hydrogen production rate using different potentials; C) Light grey: Coulombic efficiencies to methane using different potentials; Dark grey: Coulombic efficiency to hydrogen under same conditions in abiotic experiment; D) Abiotic specific hydrogen production rate using different potentials.

The process conditions for the following optimization steps will be adjusted to -1.1 V vs. Ag/AgCl to lower the limitations caused by the potential. Certainly, using lower potentials might again increase the methane production, but as mentioned this would negate the benefits of the bioelectromethanogenesis since the potential would then be low enough to produce hydrogen directly in sufficient amounts for further processing. The benefit of bioelectrochemistry, namely using small potentials to save energy costs, would vanish.

#### 4.3.3 Electrode Optimization

Five different electrodes were tested as cathodes for the bioelectromethanogenesis process. With all five electrodes, methane production could be observed (Figure 13). The highest methane production rate was reached with RVC foam, followed by graphite rod, carbon laying and carbon granulate, carbon fabric showed the lowest methane production rate. To improve comparability, the specific methane production rate based on the geometric electrode surface area was calculated (Figure 13). Here, graphite rod electrodes showed the best performance, followed by carbon laying and RVC foam, since the geometrical surface of the RVC foam was with 0.0124 m<sup>2</sup> higher than for the graphite rod (0.0069 m<sup>2</sup>) and for the carbon laying (0.0041 m<sup>2</sup>) (surface area of the cylinder formed by the rolled

carbon fabric sheet)). The RVC foam offered a high porosity, which is supposed to be advantageous (Logan, 2010b). The specific methane production rate for carbon granulate was very low, since the total geometric surface area of the granulate was 0.25 m<sup>2</sup>. It might be that the granulate particles did not contribute to the methane production rate at all, but only the graphite rod used for the electrical contact transfers electrons to the methanogens, as it was already suspected during the abiotic electrode characterization (section 4.2.1). If the specific methane production rate for the carbon granulate electrode would not be calculated based on the granulate surface but only on the geometrical surface of the graphite rod which was used to contact the granulate, the specific methane production rate would be 84.01 mmol\*d<sup>-1</sup>\*m<sup>-2</sup>, instead of 1.6 mmol\*d<sup>-1</sup>\*m<sup>-2</sup>. So, if only the graphite rod used for contacting the granulate would take part in the reaction, the specific methane production rate was 84.01 mmol\*d<sup>-1</sup>\*m<sup>-2</sup>, but if the granulate surface is the electroactive surface in this case, the specific methane production rate is significantly lower. A specific methane production rate of 84.01 mmol\*d<sup>-1</sup>\*m<sup>-2</sup> was, however, close to the specific methane production rate obtained during the graphite rod experiments (82.26 mmol\*d<sup>-1</sup>\*m<sup>-2</sup>), suggesting that the addition of carbon granulate did not have a positive effect on the methane production. The low performance of the carbon fabric electrode might result from surface changes, which were already observed in the abiotic characterization. These alterations could hinder effective interaction of the methanogens with the electrode and prevent efficient abiotic hydrogen production.

It would also be possible to calculate the specific methane production rate based on the total surface area of the electrodes (see also section 4.2.1). This seemed not to be useful here, since due to the unknown electron transfer mechanism it was not possible to estimate the surface area which was really accessible to the methanogens. It might be that small pores, as in graphite rods, cannot be accessed. Therefore, the geometrical surface area was used for better comparability.

The Coulombic efficiencies reached with the different electrodes varied between 27.40 % (carbon fabric) and 63.41 % (carbon granulate) (Figure 13). The addition of carbon granulate seemed to positively affect the Coulombic efficiency, which was only 47.28 % for the graphite rod without the addition of carbon granulate. The RVC foam showed the second best Coulombic efficiency of 55.60 %. A high Coulombic efficiency indicated that more electrons can actually be found in the product. For electrodes showing lower Coulombic efficiencies, the electrons could be used for an alteration of the electrodes surface charge, since no large amounts of hydrogen or other products could be detected. A correlation of the Coulombic efficiency to abiotic hydrogen and to biotic methane was not observed, suggesting that the abiotic hydrogen production and biotic electron uptake show different requirements on the electrode surface.

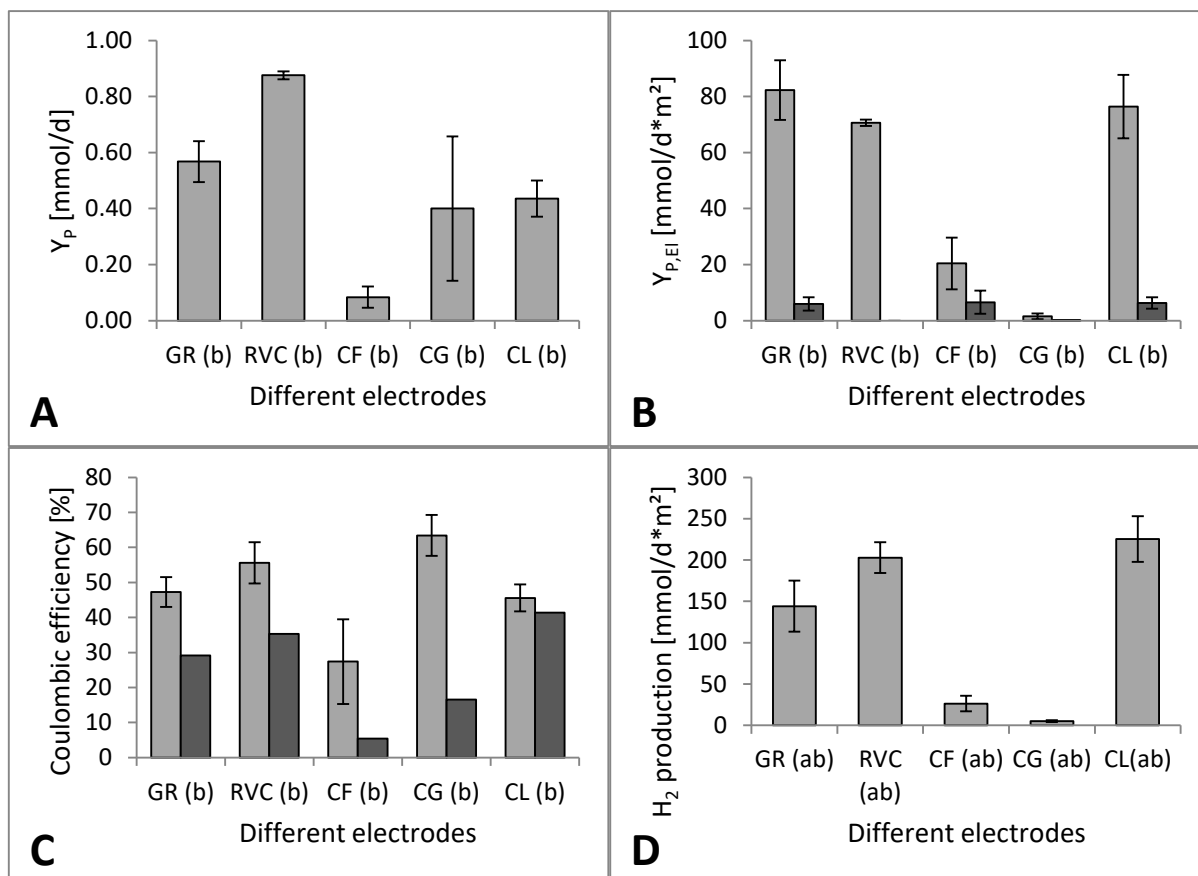


**Figure 13: Performance of the bioelectromethanogenesis process using different electrodes**

A) Methane production rate using different electrodes (GR: Graphite rod; RVC: Rectangular verticulated carbon; CF: Carbon fabric; CG: Carbon granulate; CL carbon laying); B) Light grey: Specific methane production rate using different electrodes; Dark grey: Specific biotic hydrogen production rate using different electrodes; C) Light grey: Coulombic efficiencies using different electrodes; Dark grey: Coulombic efficiencies to abiotic hydrogen under the same conditions in abiotic experiments; D) Abiotic specific hydrogen production rate using different electrodes.

The RVC foam showed a hydrogen conversion of the abiotic hydrogen of 100 %, whereas graphite rod, graphite granulate and carbon laying resulted in lower conversion rates between 95 and 98 % and a conversion rate of only 75 % was reached with carbon fabric. Abiotically produced hydrogen could be captured in the large pores of the RVC foam, thus increasing the retention time and allowing a full conversion to methane. The residual hydrogen detected in the biotic experiments was thus highest for carbon fabric ( $6.57 \text{ mmol}\cdot\text{d}^{-1}\cdot\text{m}^2$ ) although the amount of hydrogen produced abiotically was low ( $26.29 \text{ mmol}\cdot\text{d}^{-1}\cdot\text{m}^2$  and inefficient (5.40 % Coulombic efficiency for abiotic hydrogen production) compared to the other electrodes. This also led to different proportions of direct and indirect electron transfer using different electrodes, as shown in Figure 14 A. Again, the total amount of methane produced was not dependent on the ratio between direct and indirect electron transfer rate.

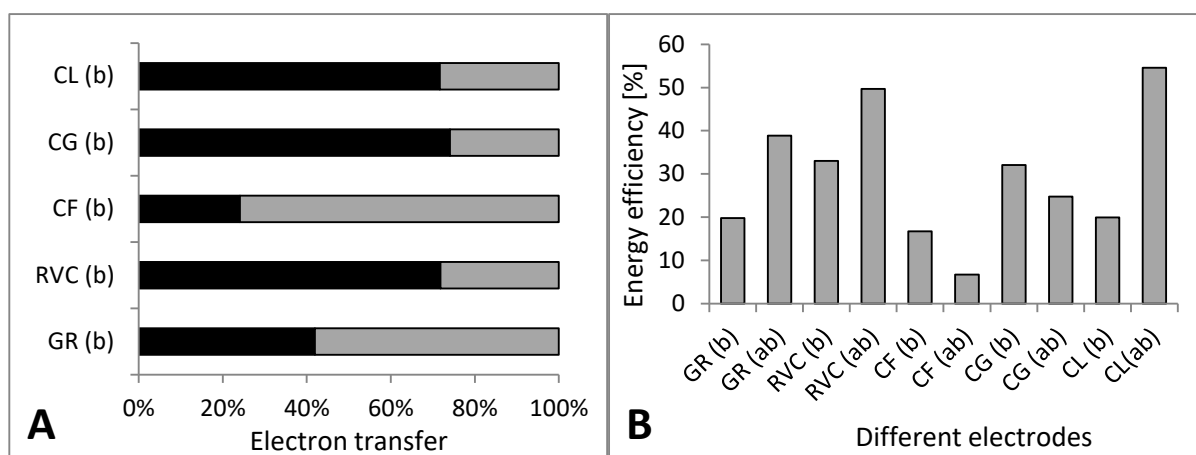


**Figure 14: Electron transfer and energy efficiency using different electrodes**

A) Black: Percentage of methane explainable by indirect electron transfer; Grey: Percentage of methane explainable by direct electron transfer; B) Energy efficiency excluding heating energy in biotic (b) and abiotic (ab) experiments using different electrodes; (GR: Graphite rod; RVC: Rectangular verticulated carbon; CF: Carbon fabric; CG: Carbon granulate; CL carbon laying).

The energy efficiency excluding heating was best for the RVC foam and the carbon granulate. Again, the energy efficiency excluding heating was mainly dependent on the current density and the terminal voltage. Except for the carbon granulate and the carbon fabric, the energy efficiency for an abiotic hydrogen production was better than for biotic methane production excluding heating. Including heating energy the energy efficiency was always better for the biotic experiment (Table 13).

**Table 13: Performance using different working electrodes**

	<b>Graphite Rod</b>	<b>RVC foam</b>	<b>Carbon fabric</b>	<b>Carbon granulate</b>	<b>Carbon laying</b>
<b>Current density</b> [A*m <sup>2</sup> ]	1.56 ± 0.06	1.12 ± 0.11	0.74 ± 0.09	0.02 ± 0.01	1.50 ± 0.2
<b>Energy efficiency</b> [%]	5.98 *10 <sup>-4</sup>	9.02 *10 <sup>-4</sup>	0.95 *10 <sup>-4</sup>	4.28 *10 <sup>-4</sup>	4.61 *10 <sup>-4</sup>
<b>Product purity</b> [%]	0.032	0.049	0.005	0.022	0.024
<b>Yield per substrate</b> [mol*mol <sup>-1</sup> ]	0.0016	0.0024	0.0002	0.0011	0.0012

The use of carbon fabric, which results in a low methane production rate, and carbon granulate, which did not positively affect the methane production rate were not suitable for the bioelectromethanogenesis process. For the other three electrode materials, different sizes were tested to find out whether the electrode size was a limiting factor for the process.

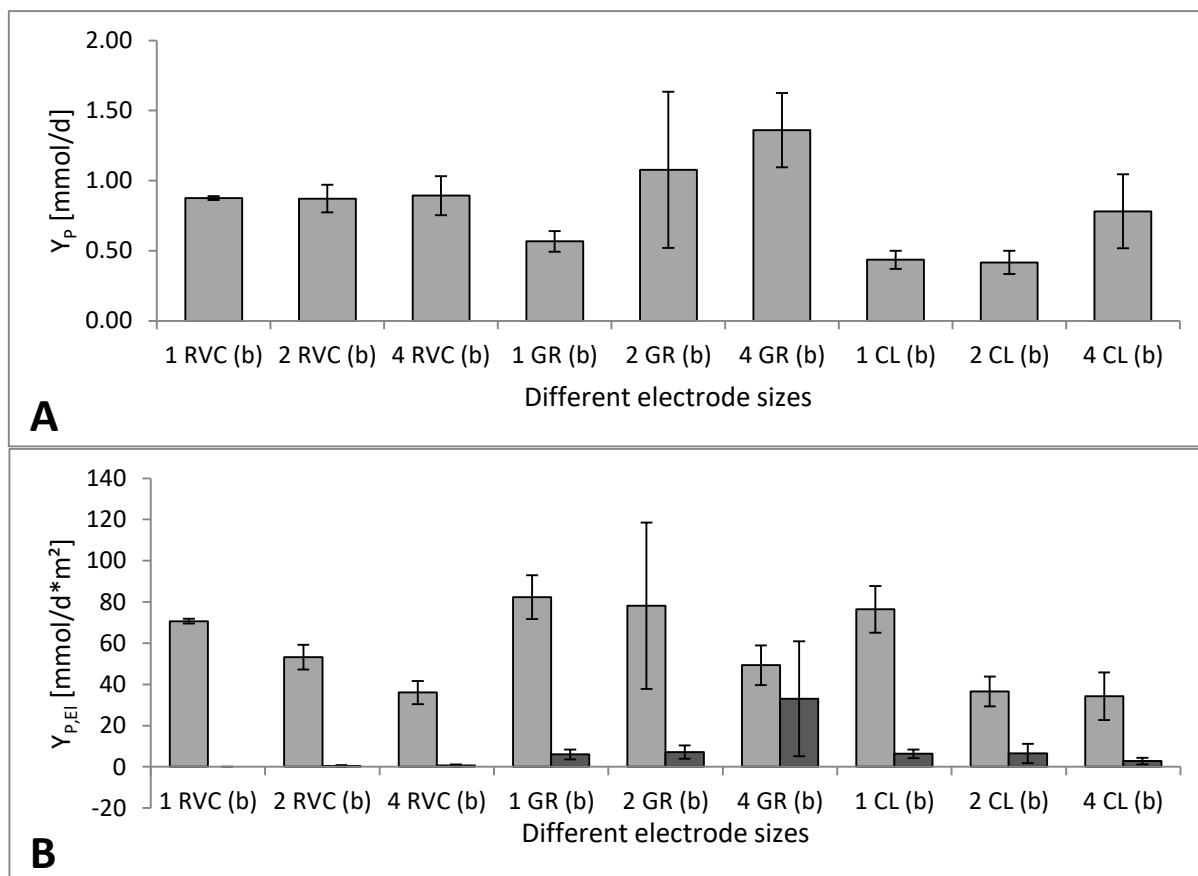


**Figure 15: Methane production rates for different electrode sizes**

A) Methane production rate for different working electrode sizes (GR: Graphite rod; RVC: Rectangular verticulated carbon; CL carbon laying); B) Light grey: Specific methane production rate for different working electrode sizes; Dark grey: Specific biotic hydrogen production at different working electrode sizes.

The results showed that the size was not limiting in case of the RVC foam. The total methane production rate did not change if the size of the foam electrode was increased, so that for every increase in electrode size the specific methane production rate decreased (Figure 15). In case of the graphite rod, the doubling of the size led to a doubling in methane production. So the specific production rate remained constant, but a further doubling of the size did not have a significant effect on the absolute methane production rate, leading to a decreased specific methane production rate (Figure 15). For these two electrode types, the Coulombic efficiency was not significantly affected by the electrode size (Figure 16 A). This was different for the carbon laying electrode, where the doubling of the electrode size did not change the methane production rate, cutting in half the specific methane production rate with the same Coulombic efficiency compared to the single electrode, but if using four pieces of carbon laying, the methane production rate increased (Figure 15), along with an increased Coulombic efficiency of 76.81 % instead of around 45 to 46 % for one and two pieces. Surprisingly, the electrode size could not be correlated to the abiotic hydrogen production rate for any electrode type (Figure 16 B). Therefore, no correlation between electrode size and Coulombic efficiency to abiotic hydrogen nor to the ratio between direct and indirect electron transfer could be observed (Figure 16).

The hydrogen conversion rates were high in all cases, between 84.93 % (4 graphite rods) and 100.00 % (1 RVC foam), but could not be correlated to electrode size or type.

For MFC studies, it was already shown that the obtained current density is often not proportional to the electrode size (Dewan et al., 2008), suggesting that other limitations do also influence the performance of a bioelectrochemical system. It was reported for MFCs that the internal system resistance decreased with increasing electrode size, which could be the cause for the higher efficiencies with four carbon laying sheets (Dewan et al., 2008). For further optimization steps of bioelectromethanogenesis (e.g. gassing optimization, membrane optimization, sections 4.3.4 and 4.3.5), 2 graphite rods were used as electrodes, combining a high total and a high specific methane production rate.

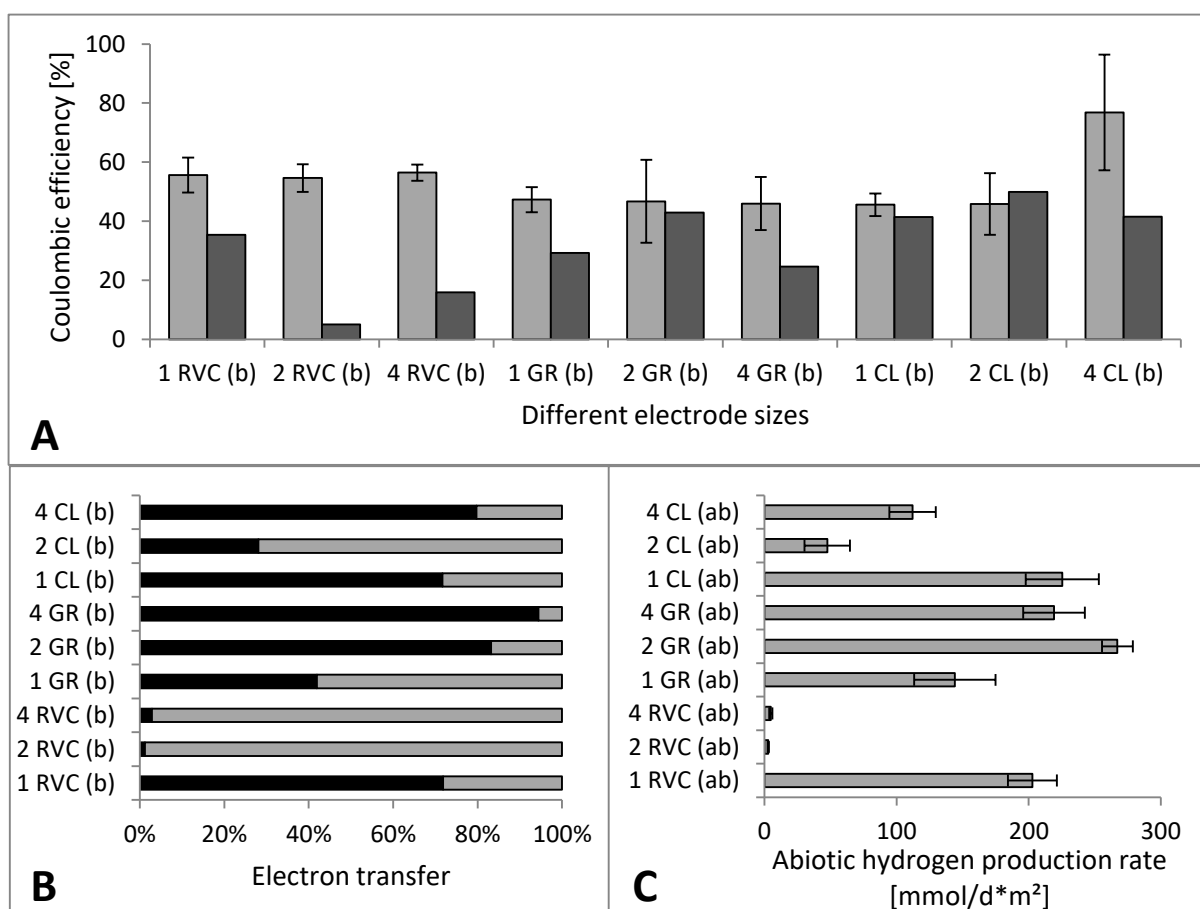


**Figure 16: Performance using different electrode sizes**

A) Light grey: Coulombic efficiency of biotic methane production for different electrode sizes (GR: Graphite rod; RVC: Rectangular verticulated carbon; CL carbon laying); Dark grey: Coulombic efficiency for abiotic hydrogen production under the same conditions; B) Light grey: Percentage of direct electron transfer to methane; Black: Percentage of indirect electron transfer to methane; C) Abiotic hydrogen production rates using different electrode sizes.

To test the influence of the counter electrode, two different electrode types were tested, carbon fabric as in the starting conditions and carbon laying as material which also had a textile-like structure. The experiments were conducted with the already shown optimizations (-1.1 V vs. Ag/AgCl, 2 graphite rod cathodes, see section 6.6.2.3) and pure CO<sub>2</sub> as in-gas after other optimization steps (section 4.3.5).

The results showed that carbon fabric was more suitable as anode material than carbon laying, since methane production rate as well as Coulombic efficiency were higher (Table 14). Also, the abiotic hydrogen evolution worked worse with carbon laying as anode material, but actually the hydrogen could effectively be converted to methane; the hydrogen conversion rate was 91.8 % using the carbon laying anode and only 76.3 % using the carbon fabric anode. In case of the carbon laying anode, the biotically produced methane could fully be explained via indirect electron transfer, and additionally hydrogen must have been transferred to another product or stored within the microorganisms to explain the value above 100 %. Since carbon laying worked a lot better as cathode material than carbon fabric, the decreased performance as anode has to result from an anodic electrochemical reaction. Apart from the lesser electrochemical properties when used as anode (lower current, lower hydrogen production), it might be that carbon laying produces toxic side products when used as anode, which diffuse through the membrane and negatively affect the biological reaction.

Table 14: Performance of bioelectromethanogenesis with different anode materials

	$Y_P$ [mmol*d <sup>-1</sup> *l <sup>-1</sup> ]	$Y_{P,EI}$ [mmol* d <sup>-1</sup> *m <sup>-2</sup> ]	$Y_{PS}$ [%]	$\gamma$ [%]	$\eta_{C,MES}$ [%]	$\eta_E$ [%]
<b>CF</b>	1.98 ± 0.47	143.7 ± 33.81	0.11 ± 0.03	0.11 ± 0.03	60.09 ± 5.65	2.66*10 <sup>-3</sup>
<b>CL</b>	1.09 ± 0.12	79.03 ± 8.63	0.06 ± 0.00	0.06 ± 0.01	45.64 ± 2.75	1.29*10 <sup>-3</sup>
	<b>H<sub>2</sub> biotic</b> [mmol* d <sup>-1</sup> *m <sup>-2</sup> ]	<b>H<sub>2</sub> abiotic</b> [mmol* d <sup>-1</sup> *m <sup>-2</sup> ]	<b>Indirect electron transfer [%]</b>	<b>Current density</b> [A*m <sup>-2</sup> ]	<b><math>\eta_{C \text{ to } H_2 \text{ abiotic}}</math></b> [%]	<b><math>\eta_E</math> excl. heating</b> [%]
<b>CF</b>	135.11 ± 36.67	569.34 ± 53.9	75.5	1.98 ± 0.21	29.91	1.29*10 <sup>-3</sup>
<b>CL</b>	37.28 ± 11.57	453.62 ± 82.08	131.7	1.56 ± 0.12	48.23	2.66*10 <sup>-3</sup>

CF: carbon fabric anode; CL: carbon laying anode

Different anode sizes were tested using carbon fabric as anode material. A doubling of the anode size by placing two sheets of carbon fabric behind each other in front of each membrane window did not increase the methane production rate (Figure 17). In contrast, using only two instead of four anode sheets approximately halved the methane production rate. This suggests that using less than four anode sheets limit the process, but larger anodes do not increase the methane production since another factor limited the bioelectromethanogenesis. It could also be possible that the arrangement of two anode sheets behind each other prevents the rear anode from taking part in the reaction efficiently. The

Coulombic efficiency to methane was highest using 4 sheets of carbon fabric, but rather low for the production of abiotic hydrogen. The production of abiotic hydrogen was similar for the halved anode size and the initial anode size, so that the lower methane productivity had to result from a biological effect; the current density using only half the anode size was with  $1.68 \text{ A}\cdot\text{m}^{-2}$  lower than with the full anode size ( $1.98 \text{ A}\cdot\text{m}^{-2}$ ) and with the double anode size ( $2.85 \text{ A}\cdot\text{m}^{-2}$ ). The increased current when using 2 layers of anode behind each other show, that the material indeed takes part in the reaction, but did not lead to an increased hydrogen or methane production; the higher current could therefore result from polarization or the large anode surface, preventing an efficient production. For further experiments, carbon fabric in the starting configurations was used as anode.

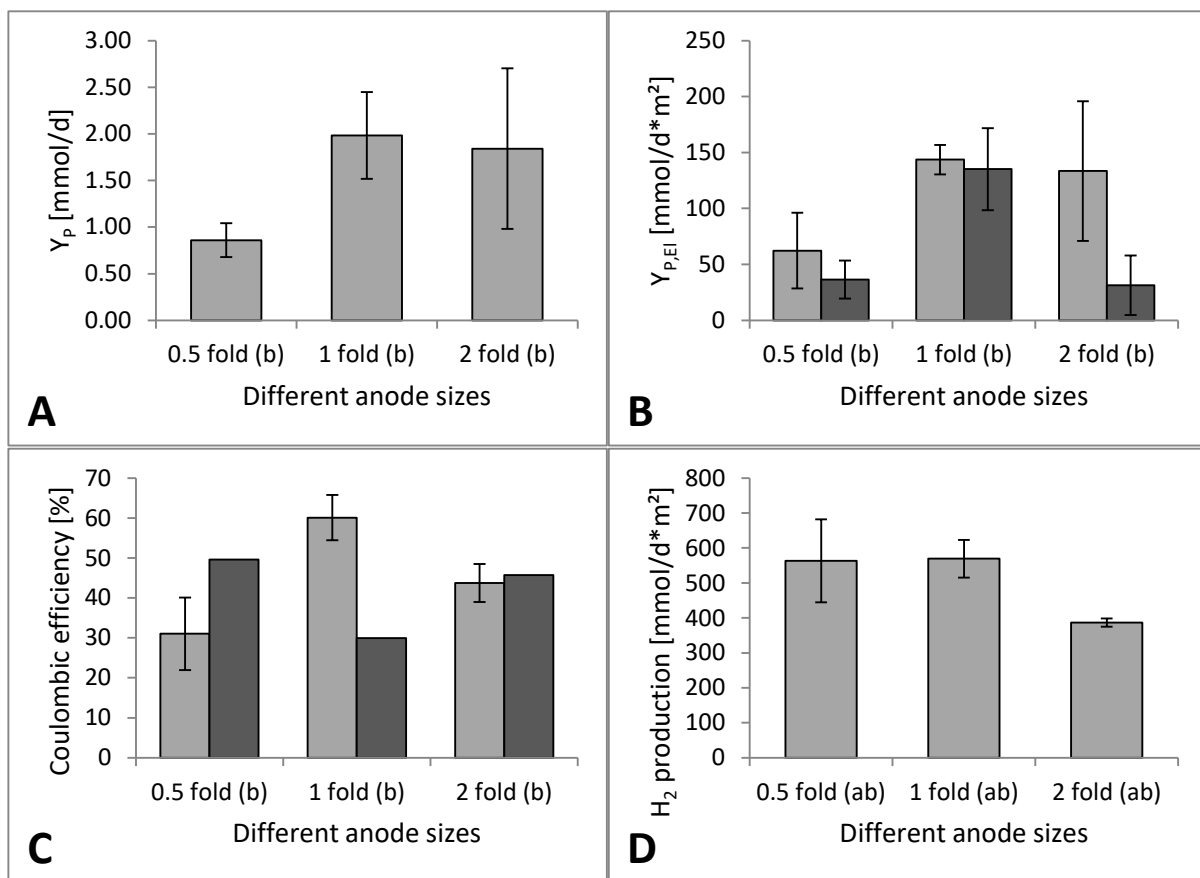


Figure 17: Performance using different anode sizes

A) Methane production rate using different anode sizes; B) Light grey: Specific methane production rate using different anode sizes; Dark grey: Specific biotic hydrogen production rate using different anode sizes; C) Light grey: Coulombic efficiencies using different anode sizes; Dark grey: Coulombic efficiencies for abiotic hydrogen production using different anode sizes; D) Abiotic specific hydrogen production rate using different anode sizes.

#### 4.3.4 Membrane Optimization

Prior to biotic experiments, the electrical resistance of the different membranes within an H-cell was tested. The results shown in Figure 18 indicated that the cation and anion exchange membrane cause a lower electrical resistance within the system than the proton exchange membrane, since the ion transport resistances of these membranes were lower. The resistance given here was the absolute resistance of a 0.00049 m<sup>2</sup> piece of each membrane in the H-cell system with MES medium on both sides of the membrane. It may change under different conditions, but the values give a reference point for the membrane behavior in a bioelectrochemical system. Although slightly higher values were reported in literature (88  $\Omega$  for AEMs and 84  $\Omega$  for CEMs and PEX membranes (Logan, 2010b)), this was well within the same range. A small deviation might result from the different used media or buffers and smaller membrane sizes.

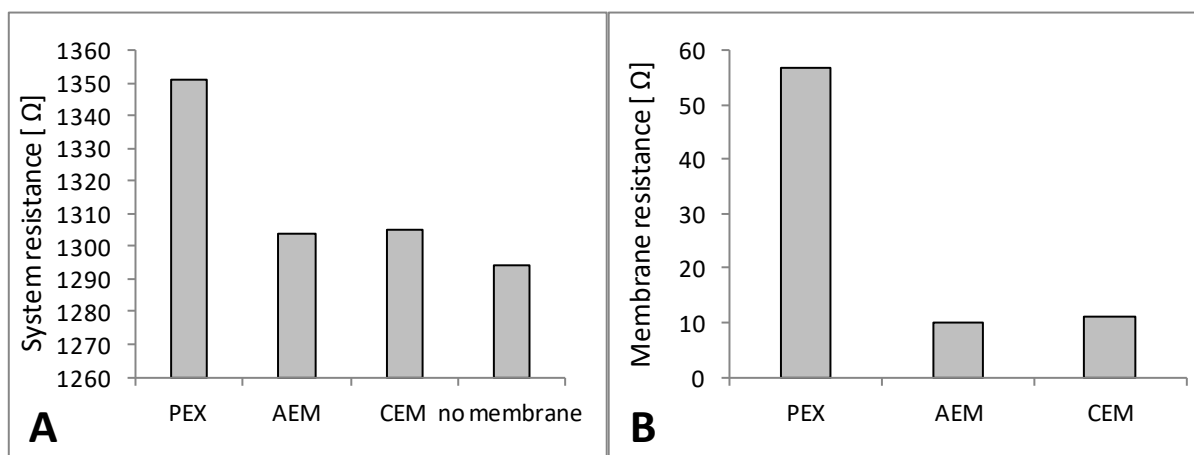


Figure 18: Resistances of different ion exchange membranes

A) System resistance of H-cell with different membranes and without membrane; B) Membrane resistance of different membranes, calculated from the difference of the system resistance with and without membrane.

According to literature, all membranes have a low mass transfer coefficient for oxygen and can therefore be used to protect the microorganisms from anodically produced oxygen (Logan, 2010b). In abiotic tests in the bubble column reactor, the pH in the working and counter chamber were surveyed. During the experiment with the cation exchange membrane, the pH of the working chamber increased slightly from 7.35 to 7.47, while the pH of the counter chamber did decrease from 7.14 to 6.97. Using the anion exchange membrane, the results were different, the pH of the working chamber decreased from 7.52 to 7.04 over 90 hours, while the pH of the counter chamber did not change significantly (from 7.04 to 7.00). The proton exchange membrane, which was already used for the starting conditions and also in other studies found in literature led to an increase of the pH in the working chamber from 7.21 to 7.39, similar to the cation exchange membrane, but the pH of the counter chamber remained nearly constant, from 6.99 to 6.96.

For cation and proton exchange membrane, the production of hydrogen from protons worked well, resulting in a slight increase of the cathodic pH, because the proton flux from anode to cathode was

slower than the reaction at the cathode. An additional factor might be the charge transfer done by cations other than  $H^+$ , in particular  $K^+$  or  $Na^+$  from the phosphate buffer, which allow the charge transfer but not the pH equilibration, as it had already been suggested before (Logan, 2010b). The concentration of  $Na^+$  and  $K^+$  in total was 0.1 M in the phosphate buffer, in contrast to  $10^{-7}$  M proton concentration at a neutral pH; therefore, the migration of cations was likely. This was also shown by the slight acidification of the anode chamber, which was a bit higher with the cation exchange membrane than with the proton exchange membrane. The anion exchange membrane, on the contrary, led to an acidification of the working chamber since anions like  $Cl^-$  and  $CO_3^{2-}$ , which are usually basic, migrated from the working chamber to the counter chamber to maintain the electric current (also suggested in (Logan, 2010b)). However, the pH shifts in all cases were relatively low, since the time frame for the shift was 90 hours. This suggested that no fast proton accumulation occurred at the anode due to the water splitting reaction, but the membranes allowed a sufficient flux of ions to maintain stable conditions.

The three different membrane types might be suitable for bioelectromethanogenesis and were therefore tested in the bubble column reactor. The experiments revealed that cation and proton exchange membranes were both suitable and showed similar methane production rates in the bubble column reactor (Figure 19). These data confirmed findings from literature, where cation exchange membranes led to similar or slightly higher methane production rates as proton exchange membranes (Babanova et al., 2017). In contrast, the anion exchange membrane resulted in much lower methane production rates (Figure 19) and due to migration of chloride ions from the working chamber to the counter chamber (Sleutels et al., 2009), chlorine gas was formed at the anode. Therefore, anion exchange membranes cannot be used for the bioelectromethanogenesis process in this case, although they turned out to be the better choice in MFC experiments according to literature (Logan, 2010b). It was already reported that the methane production rate was higher with cation exchange membranes than with anion exchange membranes (Zeppilli et al., 2016), so the results obtained here confirmed other studies.

The abiotic hydrogen production was best with the proton exchange membrane at a Coulombic efficiency of 42.90 %; as suggested, the cation exchange membrane seemed to maintain the electrical current by other ions migrating from counter to working chamber, resulting in a lower abiotic hydrogen production at a lower Coulombic efficiency. Using the anion exchange membrane, the resulting abiotic hydrogen production was low compared to the other membranes at a Coulombic efficiency of 27.19 %. The hydrogen conversion rate was best using the proton exchange membrane (97.32 %), but still high with the other membrane types (90.92 % and 89.11 % for cation and anion exchange membrane, respectively). The highest percentage of indirect electron transfer (83.21 %) resulted from the use of the proton exchange membrane, whereas the cation exchange membrane led to direct electron transfer (63.81 %) at a slightly higher electrical current of  $1.44 A \cdot m^2$  instead of

1.24 A\*m<sup>-2</sup> for the proton exchange membrane and only 0.32 A\*m<sup>-2</sup> for the anion exchange membrane. The ratio using the anion exchange membrane was in between with 35.72 % direct electron transfer. The results suggested that establishing an electrical current by anion flux from working chamber to counter chamber was less effective than by cation movement from counter to working chamber.

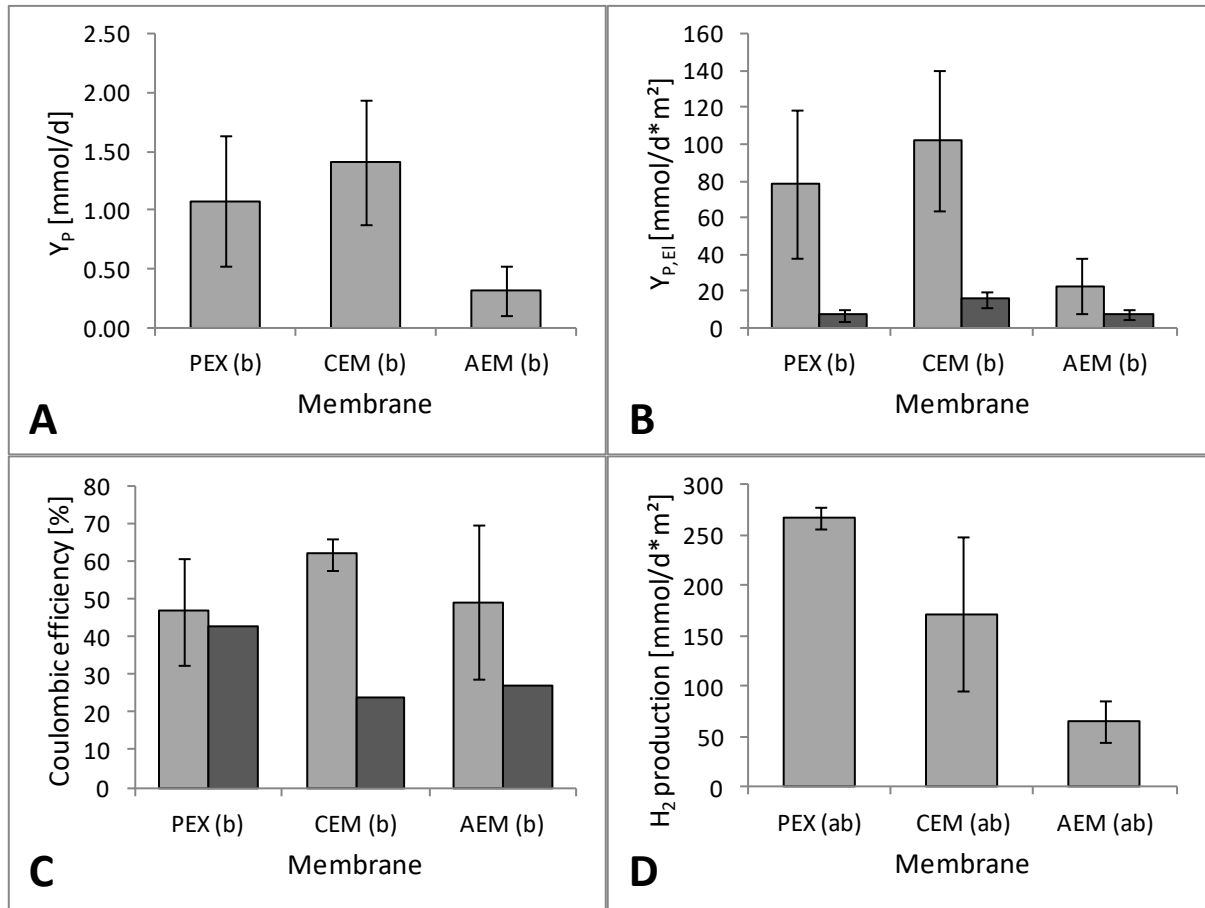


**Figure 19: Performance with different membrane types**

A) Methane production rate using different membranes (PEX: proton exchange membranes; CEM: cation exchange membrane; AEM: anion exchange membrane); B) Light grey: Specific methane production rate using different membranes; Dark grey: Specific biotic hydrogen production rate using different membranes; C) Light grey: Coulombic efficiencies using different membranes; Dark grey: Coulombic efficiencies of abiotic hydrogen production using different membranes; D) Abiotic specific hydrogen production rate using different membranes.

The better performance of the cation exchange membrane also led to an improved energy efficiency excluding the heating energy (0.00153 %, in contrast to 0.00114 % for PEX and 0.000 36 % for AEM), but was less efficient when excluding heating energy from the calculation (19.00 % instead of 19.39 % for PEX and 23.64 % for AEM). The yield per substrate (between 0.0009 and 0.0039 mol\*mol<sup>-1</sup>) and product purity (between 0.02 and 0.08 %) was low with all membranes.

Not only the type of membrane, but also the membrane size was varied using the bubble column reactor (see also section 6.2.6.4). The size was halved by closing two windows with a silicon rubber plate instead of a membrane. By closing all windows with silicone rubber, it was not possible to apply

the potential of -1.1 V to the working electrode, because the terminal voltage needed was higher than 15 V, which was the potential limit of the used potentiostat. Closing two windows with silicone rubber plates and two with PEX membrane, thus halving the membrane area, the application of the desired potential was possible. But the lower membrane size led to lower methane production rates and along with that, a lower energy efficiency, product purity and yield per substrate (Table 15). The Coulombic efficiency, however, remained nearly constant, indicating that lower current densities were reached, although the terminal voltage was -3.4 V in both experiments. A smaller membrane area probably led to an increased electrical resistance within the system, lowering the overall efficiency.

Table 15: Performance using different membrane sizes

	$Y_P$ [mmol*d <sup>-1</sup> ]	$Y_{P,EI}$ [mmol* d <sup>-1</sup> *m <sup>-2</sup> ]	$Y_{ST}$ [mmol* d <sup>-1</sup> *l <sup>-1</sup> ]	$Y_{PS}$ [%]	$\gamma$ [%]	$\eta_{C,MES}$ [%]	$\eta_E$ [%]
<b>4 membrane windows</b>	1.08 ± 0.56	78.10 ± 40.35	1.08 ± 0.56	0.30 ± 0.06	0.06 ± 0.01	46.72 ± 14.08	1.14*10 <sup>-3</sup>
<b>2 membrane windows</b>	0.71 ± 0.25	51.20 ± 18.26	0.71 ± 0.25	0.20 ± 0.07	0.04 ± 0.01	48.78 ± 11.19	7.49*10 <sup>-4</sup>

The use of a halved membrane area caused no drop in abiotically produced hydrogen, again suggesting that the biotically catalysed methane production was influenced by process parameters very differently from the electrochemical hydrogen evolution.

#### 4.3.5 Optimization of Mixing and Gassing

To improve mixing conditions in the bubble column reactor, the introduction of an external loop was tested. Medium was pumped through this loop with around 50 ml\*min<sup>-1</sup>. This did, however, not increase the methane production rate of the process, but on the contrary significantly lowered the performance (Table 16). Since the external loop did not alter the  $k_{L,a}$  as well, it seemed that the CO<sub>2</sub> availability was not improved by medium circulation, although this was unexpected, since the improved mixing should result in a better gas distribution within the reactor. It might be that due to the shear forces caused by mixing the microorganisms were inhibited, or cell attachment to the electrode, which might be necessary for direct electron transfer, was not possible anymore. It was also observed that the current density using the external loop was reduced from 1.12 A\*m<sup>-2</sup> to 0.53 A\*m<sup>-2</sup>, and the abiotic hydrogen production was significantly decreased from 202.80 mmol\*d<sup>-1</sup>\*m<sup>-2</sup> to 14.49 mmol\*d<sup>-1</sup>\*m<sup>-2</sup> at a similar Coulombic efficiency of 35.34 % and 32.38 % without and with external loop, respectively. These results indicate that the medium circulation somehow seemed to hinder the abiotic electrochemical performance of the reactor, maybe by increasing the internal resistance of the system.

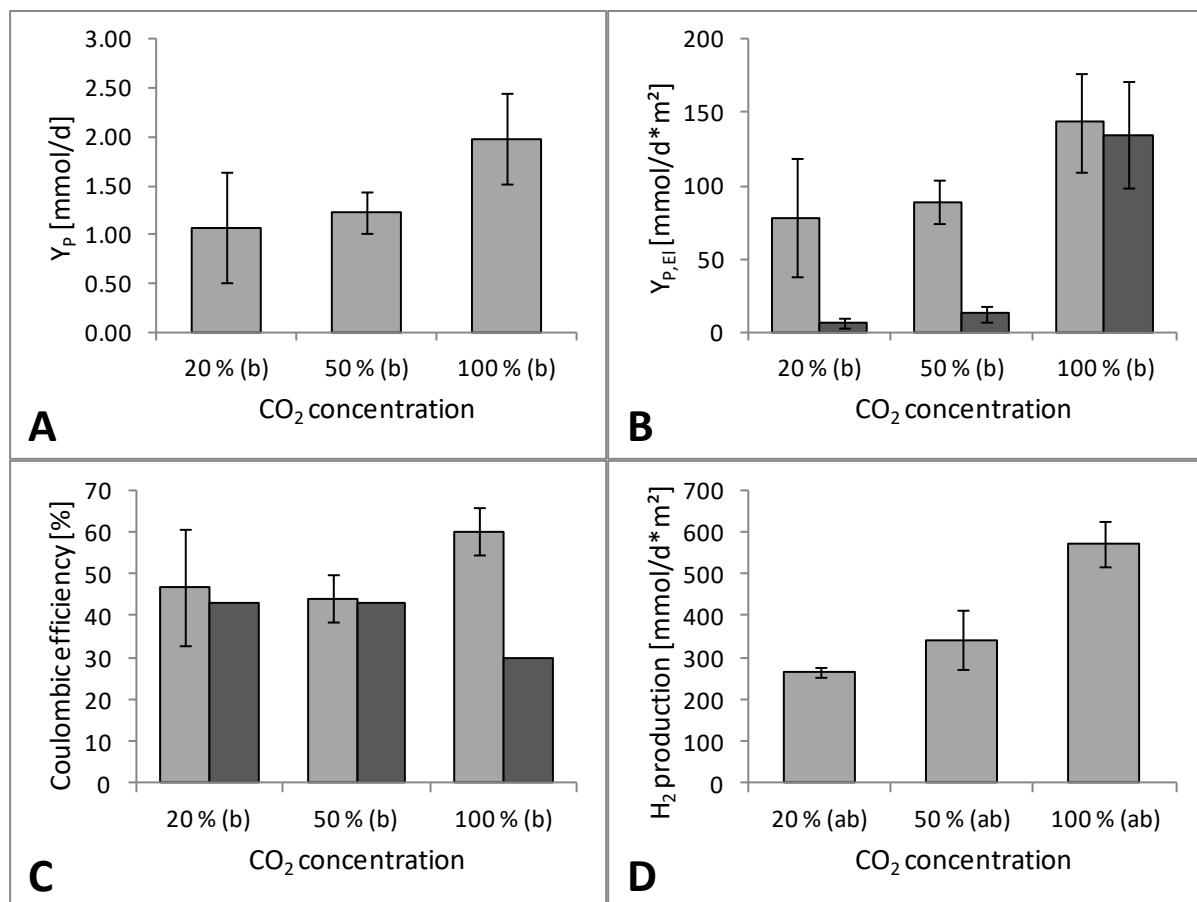
The ports for the external loop tubes were thus closed for further process optimization of bioelectromethanogenesis. If the reactor was used for processes with growing microorganisms or with a substrate dissolved in the medium, the ports might be used for continuous process operation.

Table 16: Performance alteration by application of an external loop

	$Y_P$ [mmol*d <sup>-1</sup> ]	$Y_{P,EI}$ [mmol* d <sup>-1</sup> *m <sup>-2</sup> ]	$Y_{ST}$ [mmol* d <sup>-1</sup> *l <sup>-1</sup> ]	$Y_{PS}$ [%]	$\gamma$ [%]	$\eta_{C,MES}$ [%]	$\eta_E$ [%]
<b>w/o external loop</b>	0.88 ± 0.01	70.62 ± 1.16	0.88 ± 0.01	0.24 ± 0.00	0.05 ± 0.00	55.60 ± 5.91	9.02*10 <sup>-4</sup>
<b>w external loop</b>	0.34 ± 0.04	27.28 ± 3.62	0.34 ± 0.04	0.09 ± 0.00	0.02 ± 0.09	43.78 ± 5.69	4.05*10 <sup>-4</sup>

To examine the influence of different in-gas compositions, the starting conditions of 80 % to 20 % N<sub>2</sub>/CO<sub>2</sub> mixture were altered. As a negative control in H-cells, pure nitrogen was used as in-gas, whereby no methane formation was detected, although sodium bicarbonate was present in the medium. As described in section 6.6.2.5, the CO<sub>2</sub> content in the in-gas was first increased to 50 % and then to pure CO<sub>2</sub> in the bubble column reactor. The higher the CO<sub>2</sub> content was, the higher was also the amount of methane produced (Figure 20). Since the pH decreased with increasing CO<sub>2</sub> concentrations in the in-gas, the higher proton availability had a positive impact on the methane production rate as well as on the abiotic hydrogen production rate, which was increased by a factor of 2.1. However, the Coulombic efficiency for abiotic hydrogen production could not be correlated to the CO<sub>2</sub> content in the in-gas. This revealed that indeed the substrate availability was a limiting factor of the process and that the hydrogen production is dependent on the CO<sub>2</sub> concentration in the in-gas. The gassing with pure CO<sub>2</sub> instead of N<sub>2</sub>/CO<sub>2</sub> containing gases caused a shift in the pH of the medium from 7.87 to 7.08 on average. This shift was also noticeable in different depths of the reactors, according to the slightly increasing hydraulic pressure towards the bottom of the reactor. The lower pH caused by the high CO<sub>2</sub> content still suits the growth optimum of the microorganisms used (see also 6.6.1), but it might be that pH shifts during the process due to variations in the in-gas composition lower the performance due to adaption times of the microorganisms. The hydrogen conversion rate decreased from 97.3 % to 76.3 % when altering the CO<sub>2</sub> content in the in-gas from 20 % to 100 %. In contrast, the total amount of converted hydrogen was doubled since the abiotic hydrogen production increased; thus, it is possible that the metabolism of the methanogens was too slow to convert the additionally produced hydrogen effectively. The ratio between direct and indirect electron transfer was not affected in correspondence to the CO<sub>2</sub> content (indirect electron transfer between 75 % and 92 %), leading to the conclusion that both, direct and indirect electron transfer benefit from the increased CO<sub>2</sub>

availability. The yield per substrate decreased from  $0.003 \text{ mol} \cdot \text{mol}^{-1}$  to  $0.001 \text{ mol} \cdot \text{mol}^{-1}$  due to the higher amount of  $\text{CO}_2$  fed to the reactor, although the purity increased from 0.06 % to 0.11 %.



**Figure 20: Performance of bioelectromethanogenesis using different  $\text{CO}_2$  concentrations**

A) Methane production rate using different  $\text{CO}_2$  concentrations in the in-gas; B) Light grey: Specific methane production rate using different  $\text{CO}_2$  concentrations in the in-gas; Dark grey: Specific biotic hydrogen production rate using different  $\text{CO}_2$  concentrations in the in-gas; C) Light grey: Coulombic efficiencies to methane using different  $\text{CO}_2$  concentrations in the in-gas; Dark grey: Coulombic efficiencies for abiotic hydrogen production using different  $\text{CO}_2$  concentrations in the in-gas; D) Abiotic specific hydrogen production rate using different  $\text{CO}_2$  concentrations in the in-gas.

To stabilize the pH, an additional buffer was used. The addition of  $20.9 \text{ g} \cdot \text{l}^{-1}$  3-(*N*-morpholino)-propanesulfonic acid (MOPS) buffer to the medium did not significantly alter the performance of the system in terms of methane production and was therefore not further examined for the optimization. The pH in the experiment with MOPS was 7.59 using  $\text{N}_2/\text{CO}_2$  80/20 as in-gas mixture. Interestingly, the Coulombic efficiency decreased when using MOPS, but the overall energy efficiency increased a little because besides methane, more hydrogen was detected than in the experiments without MOPS. This was also observed in the abiotic experiments, leading to the conclusion that MOPS addition improves the abiotic hydrogen production by a factor of 12.7; possibly because of the slight pH shift caused, but not the performance of the microorganisms. It was already shown before that MOPS can act as electron donor or electron shuttle in a photobiocatalytic process (Gonçalves et al., 2019), thus it might be possible that it also catalysed the abiotic hydrogen production. The addition of MOPS buffer

enhanced the indirect electron transfer, but not the direct electron transfer or the Coulombic efficiency of methane production. This suggested that the increased abiotic hydrogen production alone was responsible for the improved total methane production and not an effect of the MOPS buffer on the enzyme stability or the microorganisms. This also showed that MOPS did not act as an electron shuttle between electrode and microorganism, which would not be distinguishable from a direct electron transfer in the experimental setup and therefore increase the methane portion by direct electron transfer. The ratio between direct and indirect electron transfer was thus shifted towards indirect electron transfer (Figure 21).

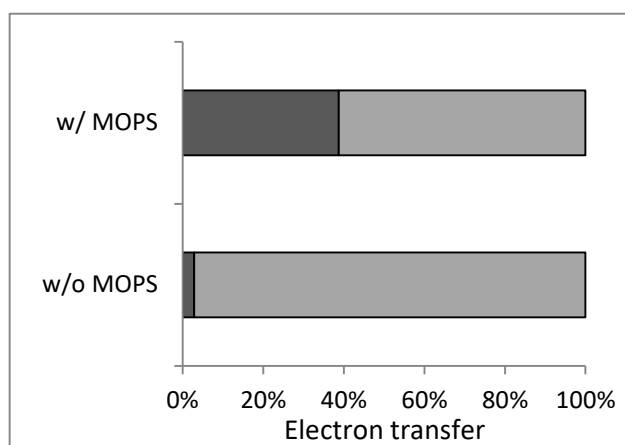


**Figure 21: Ratio between direct and indirect electron transfer by the addition of MOPS buffer**

Ratio between direct and indirect electron transfer shifts due to the addition of MOPS buffer; dark grey: proportion of indirect electron transfer; light grey: proportion of direct electron transfer, calculated from mean values of specific methane and hydrogen production rates in biotic and abiotic experiments.

MOPS could be used for industrial processes with strong fluctuations in the gas composition to stabilize the pH, but should be avoided if possible, since the addition of expensive buffers to the medium would negatively impact the economic feasibility of the process.

**Table 17: Performance alteration by addition of MOPS buffer**

	$Y_P$ [mmol* d <sup>-1</sup> ]	$Y_{P,EI}$ [mmol* d <sup>-1</sup> *m <sup>-2</sup> ]	$Y_{ST}$ [mmol* d <sup>-1</sup> *l <sup>-1</sup> ]	$Y_{PS}$ [%]	$\gamma$ [%]	$\eta_{C,MES}$ [%]	$\eta_E$ [%]
<b>w/o</b>	0.89	36.03	0.89	0.25	0.05	56.42	9.25*10 <sup>-4</sup>
<b>MOPS</b>	± 0.14	± 5.63	± 0.14	± 0.04	± 0.01	± 2.7	
<b>w/</b>	0.93	37.57	0.93	0.26	0.05	41.35	9.74*10 <sup>-4</sup>
<b>MOPS</b>	± 0.36	± 14.69	± 0.36	± 0.10	± 0.02	± 5.12	

To further minimize the limitations caused by the gas supply, the gassing rate was increased from 30 ml\*min<sup>-1</sup> to 60 ml\*min<sup>-1</sup> and then to 90 ml\*min<sup>-1</sup>. As a comparison, the gassing rate for an anaerobic bubble column reactor was set in the range of 0.03-0.07 vvm according to data found for

anaerobic bubble column reactors (Deckwer et al., 1991). This test revealed that an increase to  $60 \text{ ml} \cdot \text{min}^{-1}$  gassing rate improved the methane production times 1.3, but a further increase of the gassing rate did not significantly alter the methane production rate (Figure 22). It can be concluded that at  $30 \text{ ml} \cdot \text{min}^{-1}$  the  $\text{CO}_2$  supply is limiting the process, but when using higher gas rates, other process limitations like electron transfer or even the microbial activity overlaid the substrate limitation. It is important to note that the Coulombic efficiency for biotic methane production was not dependent on the gassing rate and increased slightly for abiotic hydrogen production. In contrast, the abiotic hydrogen production showed a dependence on the gassing rate; the percentage of methane which could be explained by indirect electron transfer was therefore similar for all gassing rates (between 72 % and 76 % indirect electron transfer at hydrogen conversion rates between 76 and 88 %). Apart from the substrate availability, the increased gassing also affected the abiotic electrochemical performance of the system by slightly increasing the hydrogen production rate, although the increase was not significant. It was already reported that gassing with  $\text{CO}_2$  could reduce overpotentials at the electrodes (Ki et al., 2016), which might explain the better performance.

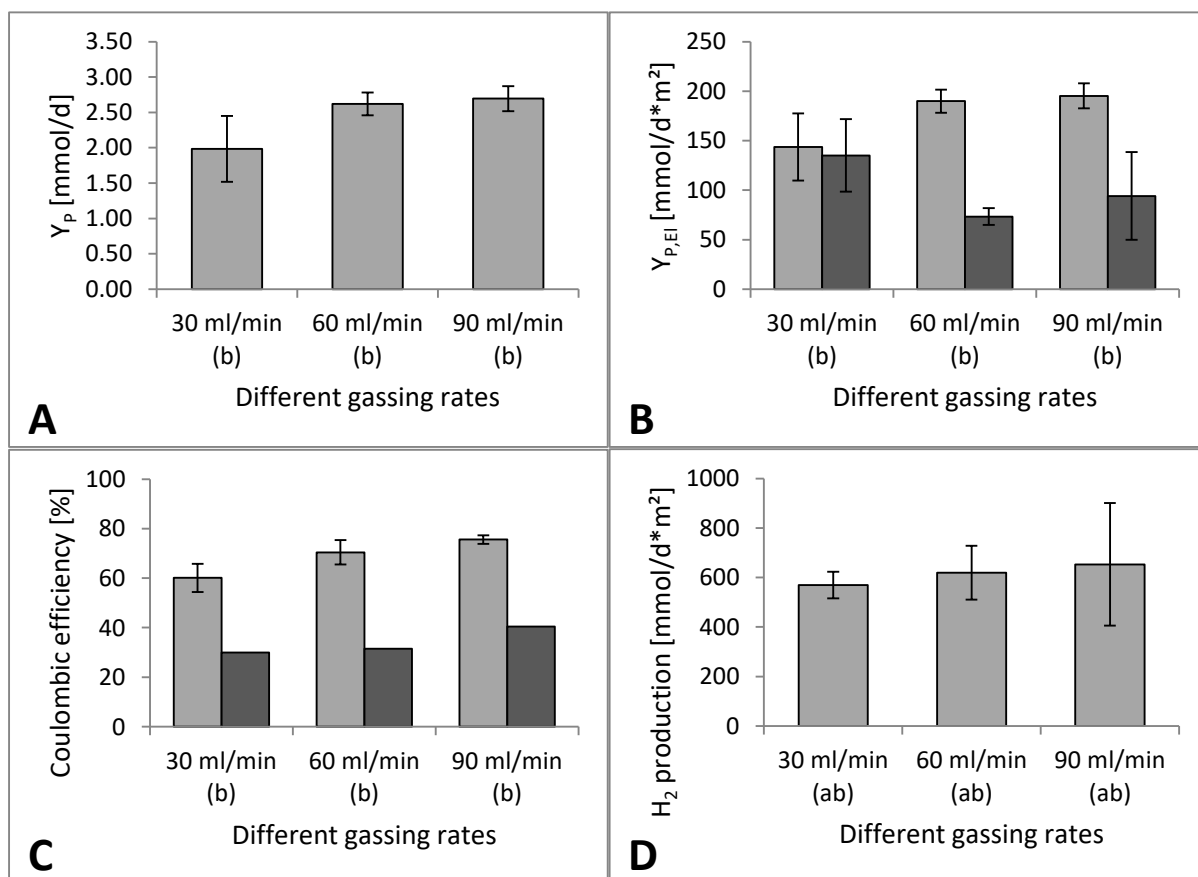
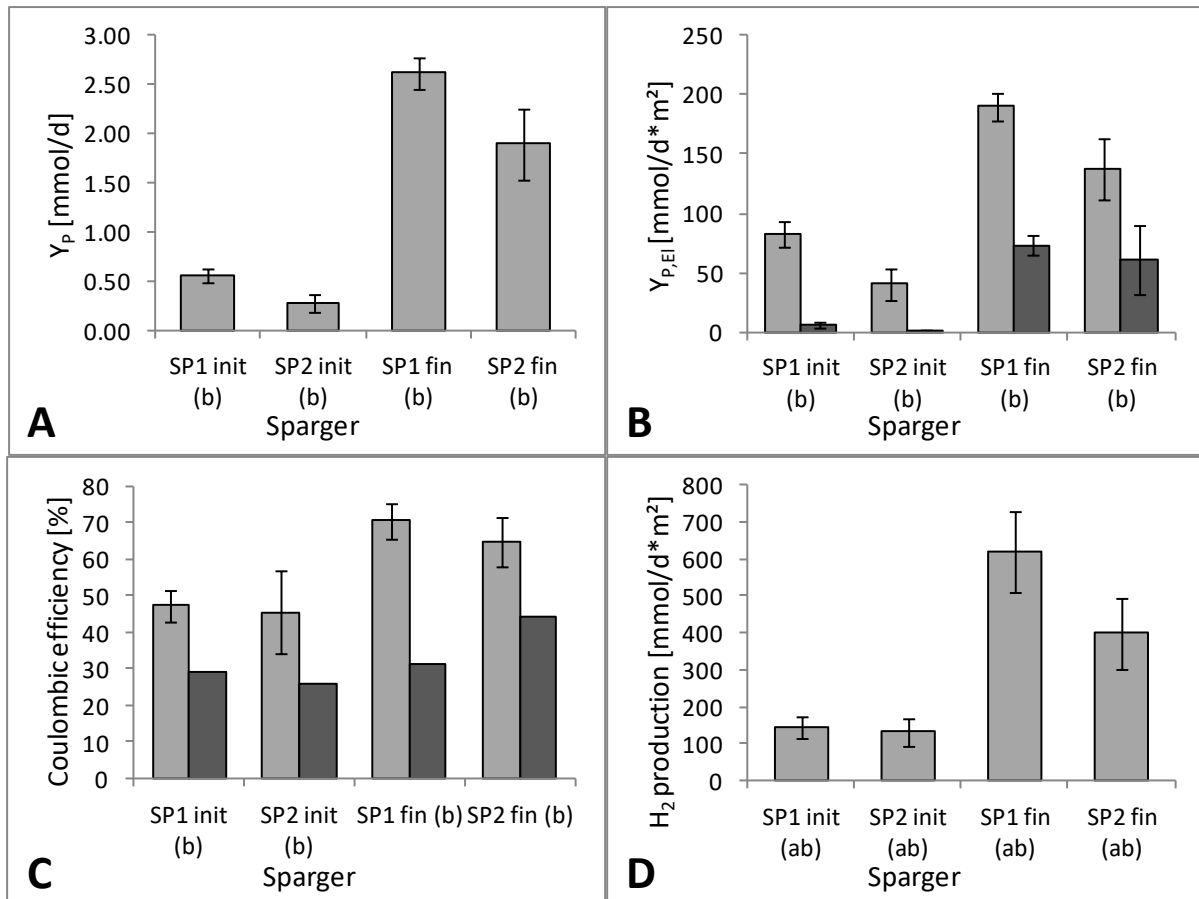


Figure 22: Performance of bioelectromethanogenesis at different gassing rates

A) Methane production rate using different gassing rates; B) Light grey: Specific methane production rate using different gassing rates; Dark grey: Specific biotic hydrogen production rate using different gassing rates; C) Light grey: Coulombic efficiencies to methane using different gassing rates; Dark grey: Coulombic efficiencies to abiotic hydrogen using different gassing rates; D) Abiotic specific hydrogen production rate using different gassing rates; (b): biotic experiments; (ab): abiotic experiments.

The energy efficiency using different gassing rates increased with increasing gassing rate if the heating energy was considered (0.0027 % to 0.0032 % from 30 ml\*min<sup>-1</sup> to 90 ml\*min<sup>-1</sup>). Negating the heating energy, the energy efficiency was 22.98 % (30 ml\*min<sup>-1</sup>), 21.73 % (60 ml\*min<sup>-1</sup>) and 26.79 % (90 ml\*min<sup>-1</sup>). The drop in efficiency at 60 ml\*min<sup>-1</sup> resulted from an increased current density, although the terminal voltage decreased with increasing gassing rate. It might be that this was a corrosion effect. The product purity and yield per substrate decreased with increasing gas velocity since the increase of the methane production was less than the increase factor of the gas velocity.

The  $k_L a$  could be increased using an alternative sparger plate with smaller perforations and 257 instead of 30 bores. It was tested whether this could also improve the methane production rate. The first test was carried out using the starting conditions with an altered applied potential to -1.1 V vs. Ag/AgCl. Interestingly, the methane production rate did not increase, but, on the contrary, halved. The test was carried out again after several optimization steps, using 2 graphite rods as working electrode and 4 sheets of carbon fabric as counter electrode, pure CO<sub>2</sub> as in-gas at 60 ml\*min<sup>-1</sup>, 4 PEX membrane windows and an applied potential of -1.1 V vs. Ag/AgCl. Again, the smaller bores did not increase the methane production rate, but on the contrary led to a lower performance (Figure 23). It was assumed that the smaller gas bubbles had a higher ability to attach to the electrode surface, which led to a decrease in electron transfer to the microorganisms. This theory was supported by the observation that under both conditions, the current density was lower using the altered sparger plate at a similar Coulombic efficiency, while the terminal voltage did not differ or was even higher than with the initial sparger plate; the resistance of the reactor using the altered sparger plate was thus higher. Also, the abiotic hydrogen production was lower with the new sparger plate. The following experiments were therefore further conducted using the initial sparger plate.



**Figure 23: Performance of bioelectromethanogenesis using different sparger plates (SP)**

A) Methane production rate using different sparger plates SP1 and SP2 under conditions similar to the starting conditions (init) and after optimization (fin); B) Specific methane production rate (light grey) and hydrogen production rate (dark grey) using different sparger plates SP1 and SP2; C) Coulombic efficiencies to methane (light grey) and abiotic hydrogen (dark grey) using different sparger plates SP1 and SP2; D) Abiotic specific hydrogen production rate using different sparger plates SP1 and SP2.

#### 4.3.6 System Stability

For the development of an industrial process, the stress response of the system needs to be evaluated. Two main possible cases of stress were identified: interruption of applied potential and interruption or composition change of in-gas. To evaluate the stability of the process under stress conditions, four different cases of system failure were simulated. These are, in particular, a breakdown of the applied potential, a breakdown of the gassing, a breakdown of the temperature control and a sudden change in gas composition. The experiments were carried out in the lab-scale bubble column reactor, except for the temperature breakdown experiment; this had to be conducted in H-cells to allow a sudden decrease in temperature.

To simulate the failure of the potentiostat, the applied potential was shut off after a runtime of 24 h and switched back on 20 h later. During the phase of electron starvation, the methane production rate decreased (Figure 24 A).

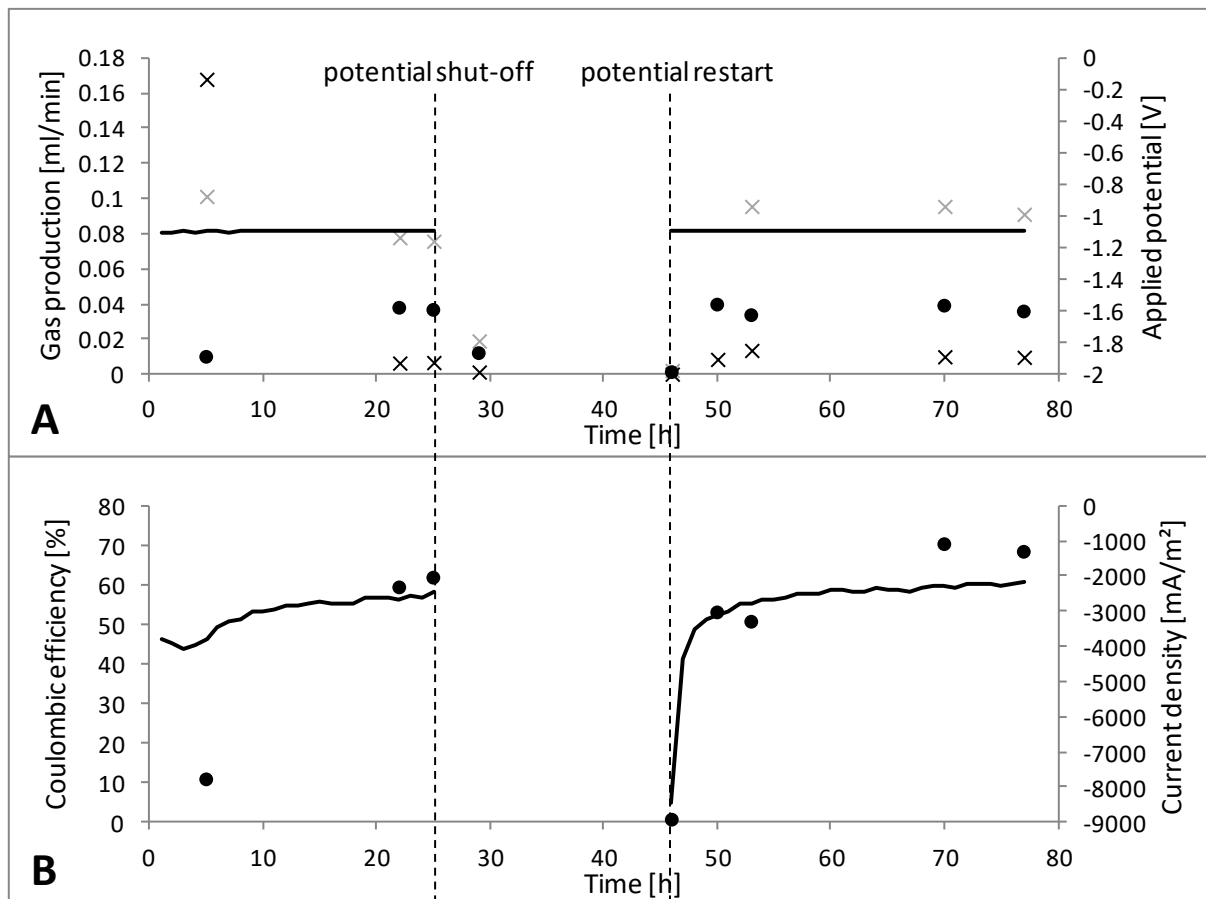


Figure 24: System performance after power gap

A) Gas production during the failure simulation experiment; grey cross: abiotic hydrogen production; black cross: biotic hydrogen production; dots: methane production; line: applied potential; B) Dots: Coulombic efficiency; line: current density.

Immediately after restart of the potentiostat, the methane production rate recovered fully. This experiment was carried out as a single run with an abiotic control. In the abiotic control a decrease in hydrogen production was observed during the potentiostat shut off, followed by a slightly increased

production after the restart. pH, OD and medium conductivity were not influenced by the breakdown of applied potential

A breakdown in the gas supply was simulated similarly by stopping the gas stream of pure CO<sub>2</sub> after 24 h of operation and restarting it 20 h later. During the stop of the gas flux, no gas sample could be taken, but a sample was taken immediately after the restart of the gas flux. This sample contained a large amount of hydrogen (1.3 % and 3.4 % in the biotic reactors, respectively) and methane (2.6 % in one, 0.9% in the other reactor), which accumulated during the phase of starvation. In the following graph (Figure 25), this point is excluded to allow for better comparability of the other values. The experiments were conducted in duplicates with one abiotic control.

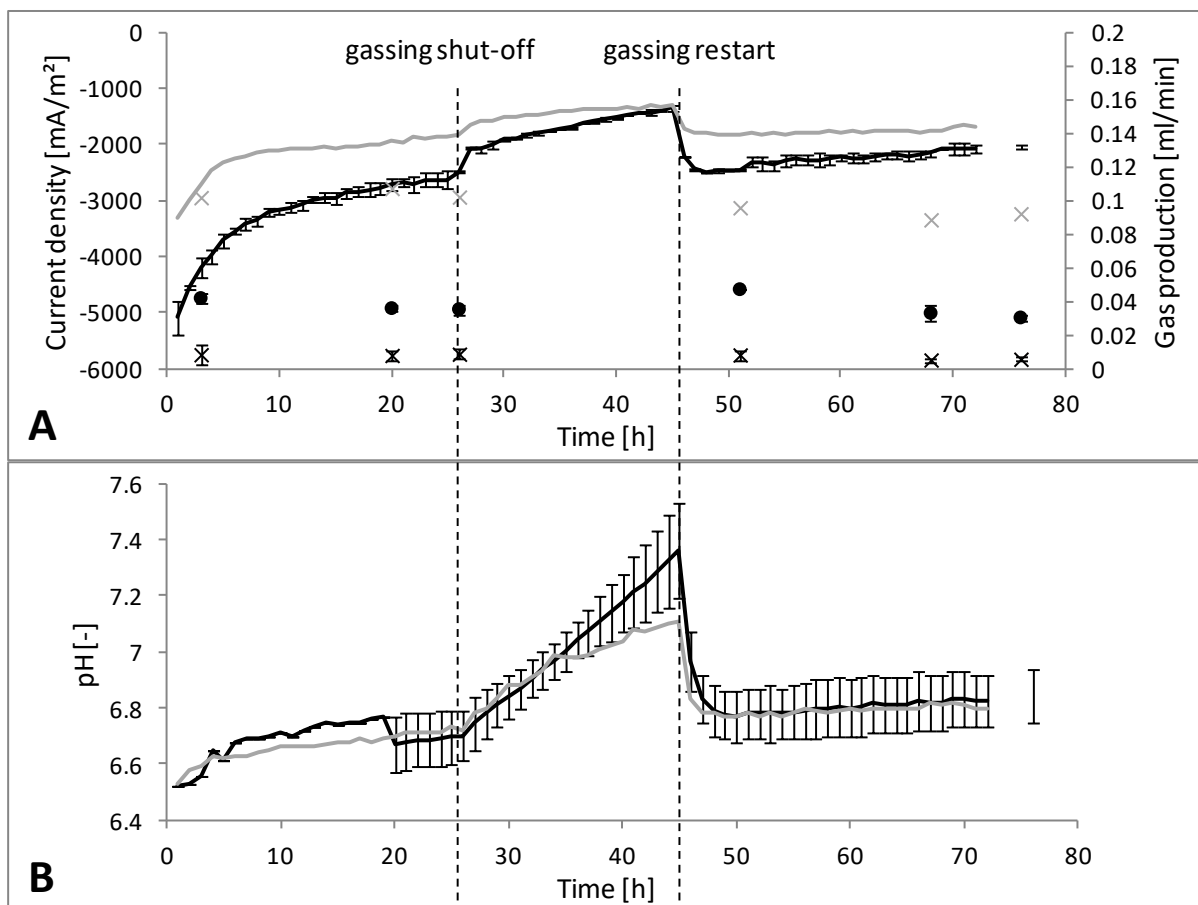


**Figure 25: System response on gassing shut-off**

A) Gas production during the failure simulation experiment; grey cross: abiotic hydrogen production; black cross: biotic hydrogen production; dots: methane production; black line: biotic current density; grey line abiotic current production; B) Black line: biotic pH in working chamber; grey line; abiotic pH in working chamber.

Interestingly, the current consumption rapidly decreased when the gassing was switched off (Figure 25). The effect was also, but less strong, observed in the abiotic control. So, as soon as there is no carbon source, the methanogens stop the uptake of current and due to bad mixing, the electron transfer is less efficient also in the abiotic electrochemical system. The gassing shut off influenced the pH of the cathode chamber, but not the conductivity and the OD. After the gassing stopped, the pH slowly

increased in the biotic as well as in the abiotic reactors due to the lowering of the  $\text{CO}_2$  concentration (Figure 25). In the biotic experiments, the pH increased faster and to a higher value; the  $\text{CO}_2$  might have been consumed by the microorganisms in the biotic control, along with the diffusion out of the reactor. Immediately after the restart of the gassing, the pH decreased rapidly and stabilized at the same level as before the failure simulation.

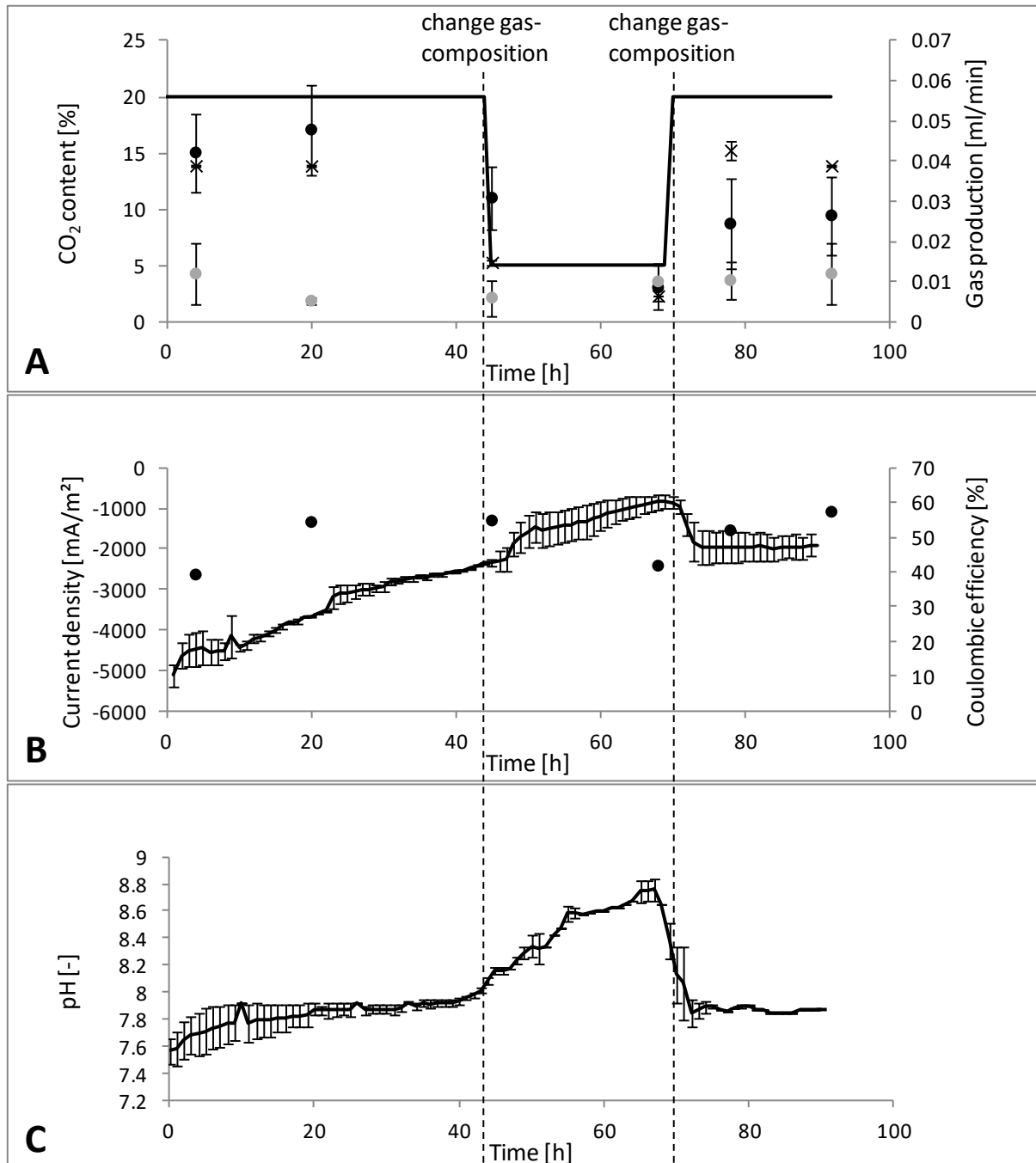


Figure 26: System response on gas composition change

A) Gas production during the failure simulation experiment; cross: hydrogen production; grey dots: methane production; black dots:  $\text{CO}_2$  content measured in off-gas; line:  $\text{CO}_2$  content set in in-gas; B) Dots: Coulombic efficiency; line: current density; C) pH working chamber.

Influences of a sudden change in gas composition were examined by gassing the reactor with an in-gas containing 20%  $\text{CO}_2$  at first, altering the mixture to 5%  $\text{CO}_2$  content after 45 h and back to 20% after

70 h. As soon as the CO<sub>2</sub> content in the in-gas was reduced, also the methane production rate decreased, while no effect on the hydrogen production was detected (Figure 26 A). The current consumption decreased, but restored as soon as the CO<sub>2</sub> content was increased again (Figure 26 B). The methane production rate recovered quickly. The pH, which is strongly dependent on the CO<sub>2</sub> content in the in-gas, increased relatively slow after the decrease of the CO<sub>2</sub> content and decreased rapidly after increase of the CO<sub>2</sub> content.

The breakdown of the temperature control was simulated in H-cells. After 20 h of operation, the incubator hood which was initially set to 35 °C was switched off and left open to cool down the cells to 20 °C (room temperature) for 28 h. Afterwards, the incubator hood was again set to 35 °C. The current uptake dropped in both, biotic and abiotic experiments when the temperature decreased and recovered again when the temperature control was switched on (Figure 27 B). Although the abiotic hydrogen production recovered fully after the failure simulation, the methane production rate stayed lower, while the biotic hydrogen production rate increased (Figure 27 A). It seems as if the methanogens have at least temporarily lowered their activity and do not convert the present hydrogen to methane as efficient as before.

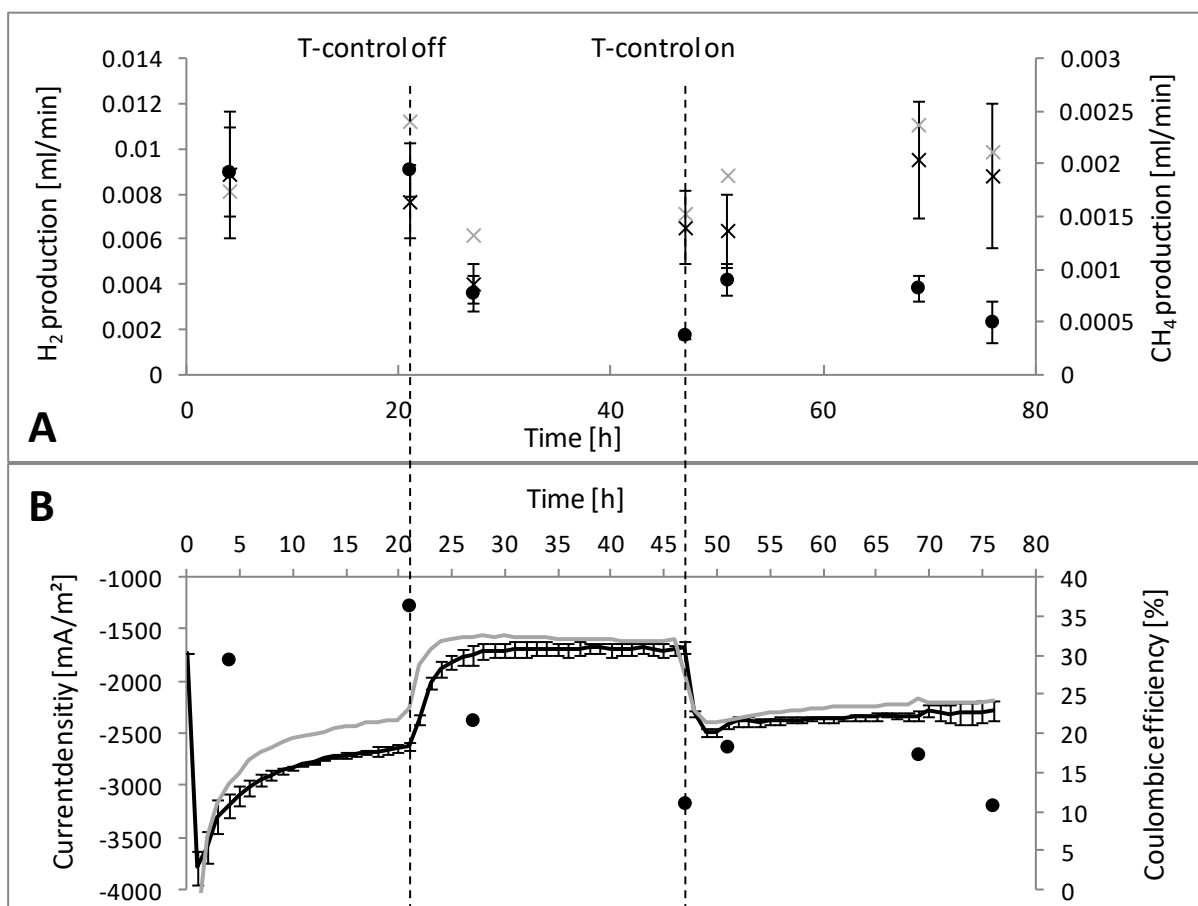
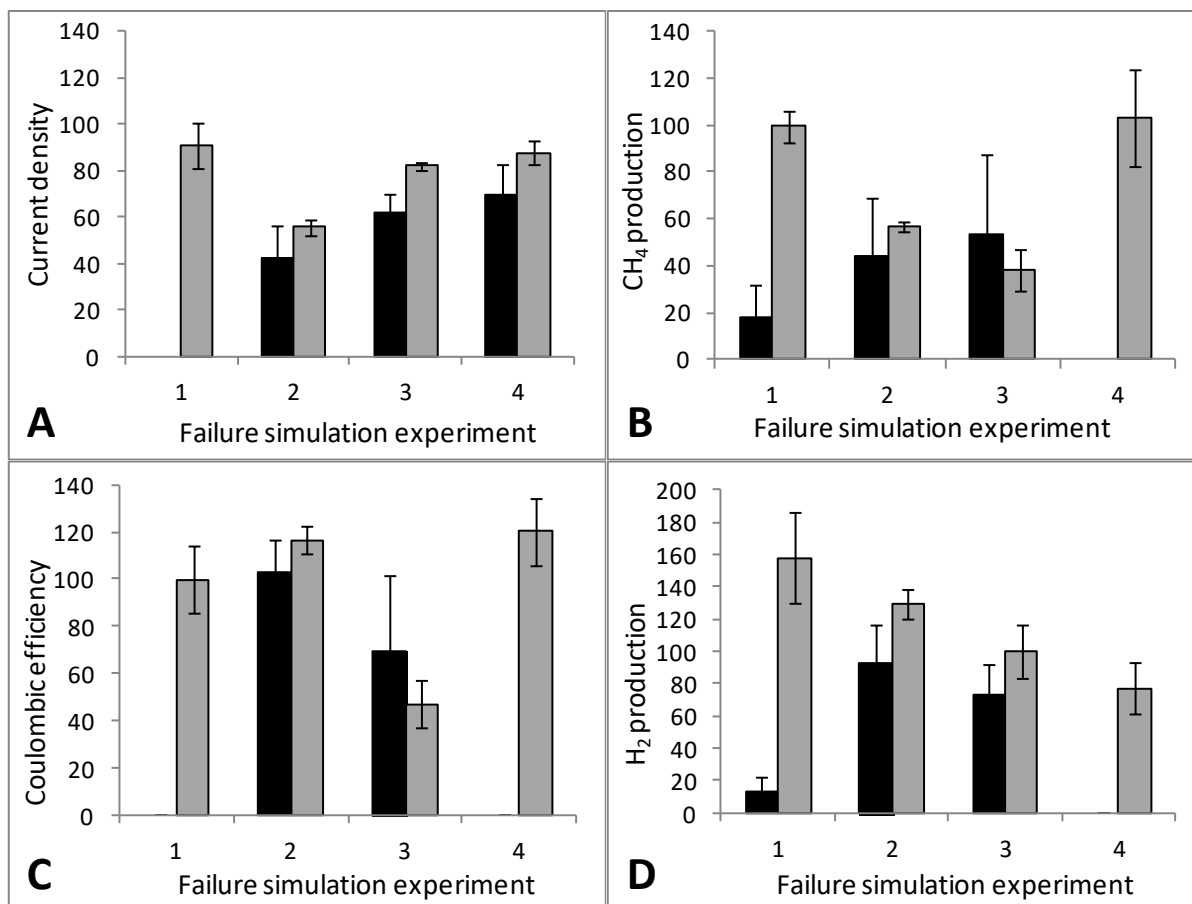


Figure 27: System response on temperature change

A) Gas production during the failure simulation experiment; grey cross: abiotic hydrogen production; dots: methane production; black cross: biotic hydrogen production; B) Dots: Coulombic efficiency; grey line: abiotic current density black line: biotic current density.

For better comparison the results of the different failure simulation experiments are shown in Figure 28.



**Figure 28: Comparison of system performances during and after failure simulation**

All values given in % of the performance before failure simulation. Failure simulations: 1) power gap; 2) change of gas composition; 3) temperature control breakdown; 4) gassing breakdown; black bars: Response during failure simulation; grey bars: response after failure simulation; A) Current density based on the working electrode geometrical surface area; B) Specific methane production rate based on the working electrode geometrical surface area; C) Coulombic efficiency; D) Specific hydrogen production rate based on the working electrode geometrical surface area. All values calculated from the mean over two experiments (except for gas composition change simulation) averaged over time with deviation over time.

A direct comparison shows that the current density was restored fully after a shut-off of the potential and the gassing, but declined after a breakdown in temperature control and significantly decreased after a sudden change in gas composition. The same result was obtained when examining the methane production rate, whereas the hydrogen production rate was not significantly affected by any kind of system failure. The Coulombic efficiency, however, dropped after the temperature control breakdown, but restored in all other experiments.

For an industrial process, the application of working potential might be unfeasible because of expensive reference electrodes and fluctuations in the electrical current due to changing reactor resistances by medium evaporation or corrosion effects. Therefore, it was tested whether cell voltage

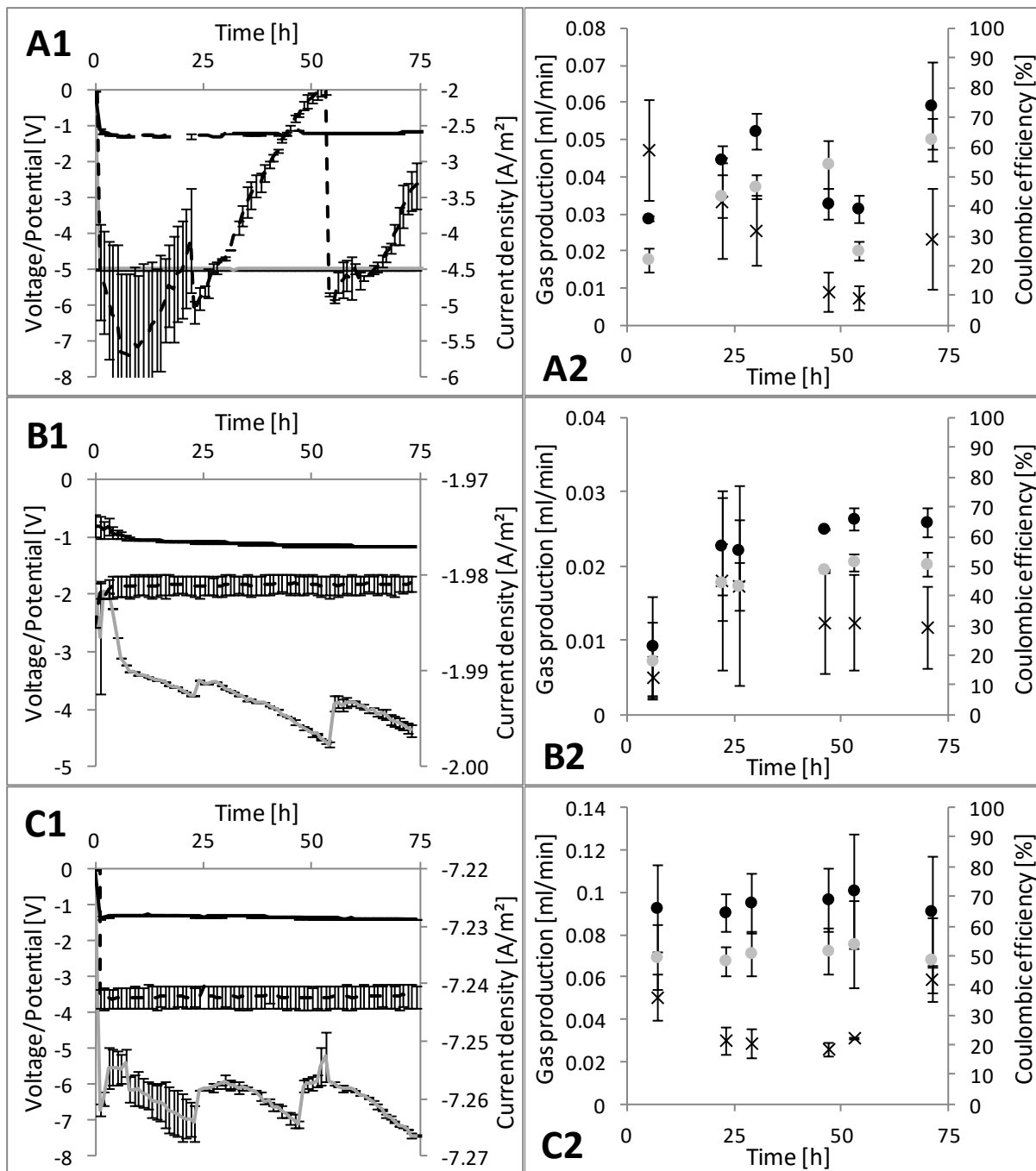
or current could be applied to the reactor to gain a more stable process (description of the operational conditions in section 6.6.2.7, results in Table 18).

Table 18: Performance of bioelectromethanogenesis using applied cell voltage or applied current

	$Y_P$ [mmol* $d^{-1}$ ]	$Y_{P,EI}$ [mmol* $d^{-1}*m^{-2}$ ]	$Y_{ST}$ [mmol* $d^{-1}*l^{-1}$ ]	$Y_{PS}$ [%]	$\gamma$ [%]	$\eta_{C,MES}$ [%]	$\eta_E$ [%]
<b>Applied</b>							
<b>potential</b>	1.98	143.7	1.98	0.0011	0.11	60.09	2.65*10
<b>-1.1 V vs. Ag/AgCl</b>	± 0.47	± 33.81	± 0.47	± 0.000	± 0.03	± 5.65	<sup>-3</sup>
<b>Applied cell voltage</b>							
<b>- 5 V</b>	2.56	185.61	2.56	0.0014	0.14	48.49	2.94*10
	± 1.22	± 48.00	± 1.22	± 0.000	± 0.04	± 12.7	<sup>-3</sup>
<b>Low</b>							
<b>applied current</b>	1.49	108.61	1.49	0.0008	0.08	48.72	1.80*10
<b>-27.4 mA</b>	± 0.12	± 8.46	± 0.12	± 0.000	± 0.01	± 3.80	<sup>-3</sup>
<b>High</b>							
<b>applied current</b>	5.74	416.04	5.74	0.0032	0.32	51.32	6.69*10
<b>-100 mA</b>	± 1.22	± 88.67	± 1.22	± 0.000	± 0.01	± 10.95	<sup>-3</sup>

The application of -5 V cell voltage (Table 18, line 2) led to strong fluctuations of the current, although the working potential remained relatively stable at -1.2 V vs. Ag/AgCl, which was close to the desired -1.1 V vs. Ag/AgCl (Figure 29 A1). Fluctuation might be caused by changing reactor resistance due to counter electrolyte evaporation or corrosion of the electrical connectors. The current fluctuations also led to fluctuating methane production rates, which made it impossible to create a stable working process (Figure 29 A2). The application of cell voltage was therefore not feasible, although the Coulombic efficiency in total was not reduced and the energy efficiency was larger than for an applied potential. In contrast to a potential application, only 59.78 % instead of 75.54 % of the methane produced could be explained via abiotically produced hydrogen, whereby the hydrogen conversion rate was higher with 87.03 % than with an applied potential (76.27 %). The energy efficiency was similar compared to the operation with an applied potential if including the heating energy (0.0029 % instead of 0.0027 %), but significantly lower excluding the heating energy (13.24 % compared to 22.98 %).

Lower deviations were obtained when applying current instead of cell voltage (Figure 29 B1). At an applied current of -27.4 mA (Table 18, line 3), the resulting working potential was stable at -1.1 V vs. Ag/AgCl. The terminal voltage showed fluctuations as observed when applying a working potential, but no effects on the methane production rate occurred. The methane production was stable, but the overall production rate was lower at a comparable Coulombic efficiency, since the applied current was a little lower than the average current resulting from applied working potential or applied cell voltage (Figure 29 B2). 69.76 % of the methane production were explainable by indirect electron transfer with a hydrogen conversion rate of 83.69 %. The energy efficiency was low when including the heating energy in the calculation (0.0018 %), and also not sufficient for an energy conversion process when excluding the heating energy (16.37 %). To further improve the methane production, a current of -100 mA was applied (Table 18, line 4). The resulting working potential was -1.4 V vs. Ag/AgCl, which was enough for efficient hydrogen production (Figure 29 C1); the energy efficiency of the abiotic process calculated from the produced hydrogen (0.0067 % including heating energy, 11.97 % excluding heating energy) was equal to that of the biotic process (0.0066 % including heating energy, 10.36 % excluding heating energy) and the biotic methane production could result from indirect electron transfer to 78.72 % (89.23 % hydrogen conversion rate). Since the methane production rate was nearly 4 times higher than at -27.4 mA applied current, the process was feasible. The abiotic hydrogen production was, however, more energy efficient, because the Coulombic efficiency for abiotic hydrogen production was with 28.29 % much lower than the Coulombic efficiency for biotic methane production, showing a better conversion of the electrical current. In terms of energy efficiency, the results confirmed that the advantage of bioelectromethanogenesis only emerges at low absolute working potentials. Apart from that, the operation with a larger applied current confirmed as the optimization of the optical density that the biocatalyst was still not the main limitation in the process; the Coulombic efficiency remains similar to that observed at lower currents, so the electron uptake was not limited by the metabolism of the methanogens so far (Figure 29 C2) Still, the maintenance demand on hydrogen was not compensated, leading to the conclusion that the microorganisms could produce much more methane, if the current supply was sufficient. Further optimizations to increase the current without increasing the applied working potential (i.e., reducing the reactor resistance or the Coulombic efficiency) would be beneficial to the process.



**Figure 29: Performance of bioelectromethanogenesis using applied cell voltage or applied current**

A) System performance at applied cell voltage of -5 V; B) System performance at applied current of -27.4 mA; C) System performance at applied current of -100 mA; 1) Current density (dashed line), working potential (solid black line) and terminal voltage (solid grey line); 2) Biotic gas production rates of methane (black dots) and hydrogen (crosses) and Coulombic efficiency (grey dots).

#### 4.3.7 Comparison to Other Reactors and Long Term Operation

After the optimization, the following conditions turned out to be the best configuration:

- 4 graphite rods as working electrode at an applied potential of -1.1 V vs. Ag/AgCl
- 1 fold carbon fabric as counter electrode in front of four CEM windows
- Gassing with 60 ml\*min<sup>-1</sup> pure CO<sub>2</sub>
- Starting OD 0.1 with *M. maripaludis*

In the bubble column reactor (BC), the optimization (potential, electrode, membrane and gassing optimization, see sections 4.3.2 to 4.3.5) led to a 9.8 fold increase of the total methane production rate (Table 19 line 1 and 2). Interestingly, the performance was not improved using 4 GRs instead of 2 GRs when gassing rate and in-gas composition maintained; other limitations might occur which have not been tested, e.g. limitation by depleting medium components. The energy efficiency including the heating energy increased nearly by a factor of 10, whereas the energy efficiency excluding heating lowered from 24.86 % to 17.74 %. With the conditions used for Scale-Up, the energy efficiency excluding heating was 9.96 % only.

Table 19: Bubble column reactor performance under starting and optimized condition

	$Y_P$ [mmol*d <sup>-1</sup> ]	$Y_{P,EI}$ [mmol* d <sup>-1</sup> *m <sup>-2</sup> ]	$Y_{ST}$ [mmol* d <sup>-1</sup> *l <sup>-1</sup> ]	$Y_{PS}$ [%]	$\gamma$ [%]	$\eta_{C,MES}$ [%]	$\eta_E$ [%]
<b>Initial conditions</b>	0.23 ± 0.01	33.84 ± 1.65	0.23 ± 0.01	0.065 ± 0.00	0.0130 ± 0.0006	50.96 ± 9.64	2.42*10 <sup>-4</sup>
<b>Optimized conditions</b>	2.25 ± 0.45	81.35 ± 16.26	2.25 ± 0.45	0.063 ± 0.011	0.063 ± 0.011	56.42 ± 2.7	2.38*10 <sup>-3</sup>
<b>Conditions used for Scale-Up</b>	1.38 ± 0.17	60.35 ± 7.56	1.38 ± 0.17	0.055 ± 0.005	0.055 ± 0.005	58.76 ± 11.83	1.46*10 <sup>-3</sup>

The abiotic hydrogen production from the starting configuration to the best configuration increased from 6.69 mmol\*d<sup>-1</sup>\*m<sup>2</sup> at 10.51 % Coulombic efficiency to 271.28 mmol\*d<sup>-1</sup>\*m<sup>2</sup> at 21.42 % Coulombic efficiency, and also the hydrogen conversion rate increased from 88.34 % to 99.87 %. Thus, the ratio between direct and indirect electron transfer was shifted from 4.37 % to 83.18 % indirect electron transfer. This led to the conclusion that the optimization of the direct electron transfer is limited, and the largest part of process optimization can be done by optimizing the indirect electron transfer.

For the comparison with other reactors, other operation conditions were used in Scale-Up and a long time experiment, since the graphite rod electrodes were not applicable to all reactor types and too

heavy for a scaled up reactor. Therefore, these experiments were conducted using 4 carbon laying electrodes, 2 CEM windows, a gassing rate of 30 ml with pure CO<sub>2</sub> and an applied potential of -1.1 V vs. Ag/AgCl (compare also section 6.6.2.8). Using these configurations, the bubble column reactor was compared to a bioelectrochemical stirred tank reactor and the H-cells equipped with the same electrode materials for anode and cathode, the same working potential and a similar specific gassing rate per working volume. The bubble column reactor released a little more methane than the stirred tank reactor (Figure 30 A), whereas the H-cell produced only small amounts of methane. Even using the specific methane production based on the electrode surface area or the space time yield, the H-cell performed worse than the stirred tank reactor and the bubble column reactor (Figure 30 B and C). The specific methane production was similar in STR and BC, but the space time yield of the STR was only half compared to that of the BC, since the electrode area per working volume was smaller. The Coulombic efficiency of the STR was slightly better than that of H-cell and BC for the biotic methane production and also for the abiotic hydrogen production (44.59 % in STR, 31.23 % in BC, 12.42 % in H-cells), probably because of the better mixing conditions within the reactor (Figure 30 D); the microorganisms and protons, respectively, contact with the electrode more often. The improved substrate availability might also increase the Coulombic efficiency in the biotic runs. The energy efficiency of the STR is with 0.00052 % even worse than in the BC reactor (0.00146 %) since the stirrer causes an additional energy input. Excluding the heating energy, the STR performs significantly better in terms of energy efficiency (37.96 % in contrast to the BC with 9.96 % and the H-cell with 25.2 %), because it released very much hydrogen with a high heating value; only 49.17 % of the abiotically produced hydrogen were converted in the STR, in contrast to the bubble column reactor with a hydrogen conversion rate of 98.08 %. In the H-cell, the conversion rate was even lower, at 17.99 %. The low energy efficiency of the H-cell mainly results from large terminal voltages due to the higher internal resistance of the system. The low hydrogen conversion rate also resulted in larger proportions of indirect electron transfer, 95.63 % for the H-cell and 76.03 % in the STR, whereas the methane formation in the bubble column could be explained fully via indirect electron transfer.

Interestingly, if applying the optimized parameters to the H-cell, the overall performance decreases a lot, perhaps since carbon fabric instead of graphite rod anodes are used, limiting the process.

Table 20: Comparison of H-cell performance under starting and optimized conditions

	$Y_P$ [mmol*d <sup>-1</sup> ]	$Y_{P,EI}$ [mmol* d <sup>-1</sup> *m <sup>-2</sup> ]	$Y_{ST}$ [mmol* d <sup>-1</sup> *l <sup>-1</sup> ]	$Y_{PS}$ [%]	$\gamma$ [%]	$\eta_{C,MES}$ [%]	$\eta_E$ [%]
<b>H-cell</b>	0.024	19.98	0.24	0.039	0.0079	47.27	n.a.
<b>initial</b>	± 0.004	± 3.49	± 0.04	± 0.000	± 0.0014	± 4.17	
<b>H-cell</b>	0.012	8.55	0.12	0.005	0.0046	42.37	n.a.
<b>optimized</b>	± 0.007	± 4.85	± 0.07	± 0.000	± 0.0036	± 20.27	

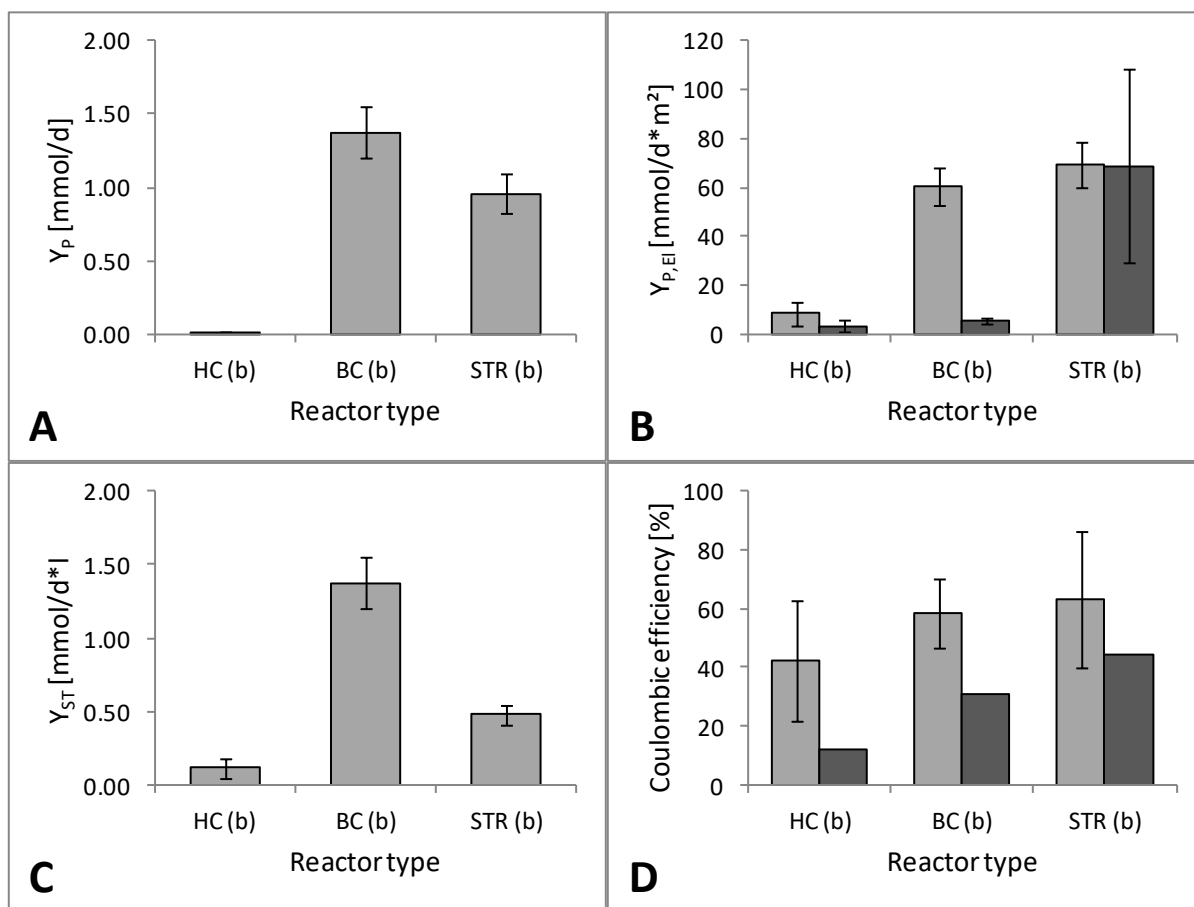


**Figure 30: Comparison of different reactors for bioelectromethanogenesis**

A) Methane production rate in different reactors (HC: H-cell; BC: Bubble column reactor; STR: Stirred tank reactor); B) Light grey: Specific methane production rate in different reactors; Dark grey: Specific biotic hydrogen production rate in different reactors; C) Space time yield of different reactors; D) Light grey: Coulombic efficiencies for biotic methane production in different reactors; Dark grey: Coulombic efficiency for abiotic hydrogen production in the different reactors.

Using the conditions used for the reactor comparison, bubble column reactors were operated for nearly three weeks (19 days) to observe the long term stability of the process. The abiotic hydrogen production rate and the biotic methane production rate were relatively constant during the experiment (Figure 31 A and B). No significant hydrogen production was detected in the biotic experiments (Figure 31 B). This also led to a stable Coulombic efficiency of 58.8 % on average (Figure 31 C). The optical density increased after one week and remained stable during the second and third week (Figure 31 D). Microscopy revealed no contamination.

The pH of the cathode chamber increased during the experiments by 0.8 pH units, whereas it decreased at the anode (0.5 pH units), the steepest slope was observed at the beginning of the experiment, while the pH altered less during the second and third week (Figure 32 A). The medium conductivity remained constant in both, anode and cathode chambers (Figure 32 B).

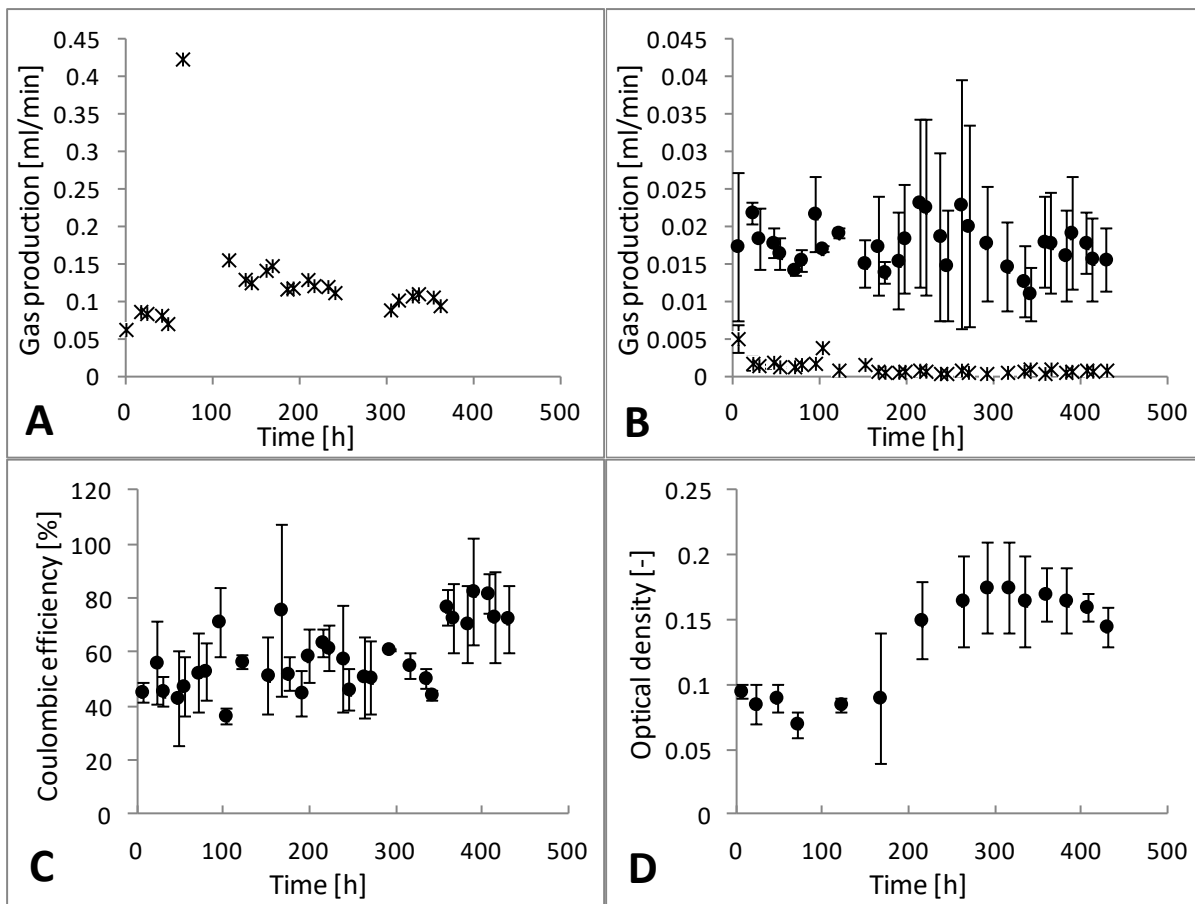


**Figure 31: Long term stability of the bioelectromethanogenesis process: production and efficiency**  
 A) \* abiotic hydrogen production; B) ● Biotic methane production and \* biotic hydrogen production; C) ● Coulombic efficiency; D) ● OD of the biotic experiments.

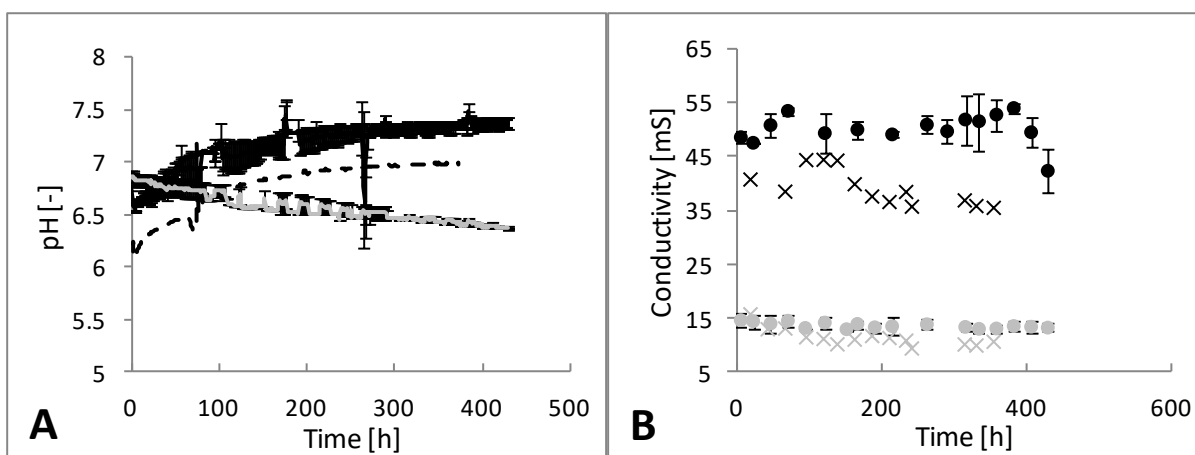


**Figure 32: Long term stability of the bioelectromethanogenesis process: pH and conductivity**  
 A) Solid black line: pH in cathode chamber (biotic), dashed black line: pH in cathode chamber (abiotic), solid grey line: pH in anode chamber (biotic); B) ● conductivity in cathode chamber (biotic), × conductivity in cathode chamber (abiotic), ● conductivity in anode chamber (biotic), × conductivity in anode chamber (abiotic).;

However, in both biotic and abiotic experiments, fluctuations in the current density occurred. After 100 h, the potentiostat was re-started after a shut-down in both, biotic and abiotic tests, leading to a second polarization time. Two other jumps in the biotic current density curve can be explained by changing the alligator clip at one of the reactors, while the second reactor (upper limit of the mean deviation bar) remained stable (Figure 33 A and B). In the abiotic control, the current density was on average higher ( $1.3 \text{ A}\cdot\text{m}^2$ ) than in the biotic experiment ( $1.1 \text{ A}\cdot\text{m}^2$ ) at a lower terminal voltage, indicating that in the biotic experiments, the microorganisms caused an additional resistance under the applied conditions. It might be that attached microorganisms for example hinder the diffusion of protons to the electrode or the diffusion of hydrogen from the electrodes, although the attachment of cells could not be proved by microscopy.

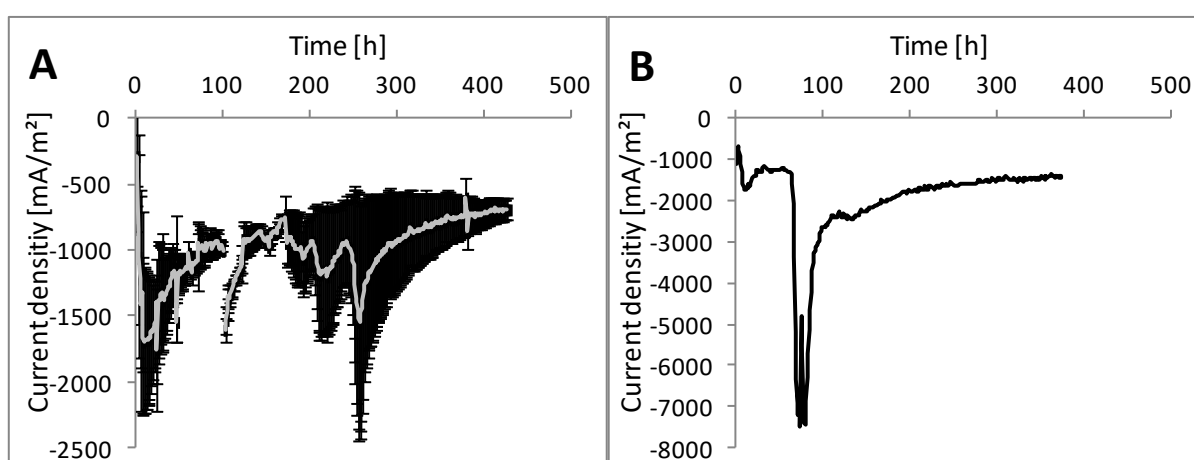


**Figure 33: Long term stability of the bioelectromethanogenesis process: current density**

A) Mean current density in biotic process with mean deviation; shutdown and re-start after 100 h, two exchanges of connectors on one reactor after 230 and 260 h; B) Current density in abiotic process; shutdown and re-start after 90 h.

It can be concluded that although the methane production remains stable in longer processes, the pH should be controlled and the electrical connections need to be improved to avoid current jumps, or the reactor needs to be operated with applied constant current instead of applied constant working potential.

#### 4.3.8 Numbering-Up

There are two main methods of designing large-scale processes. One is a Scale-Up of the reactor itself, resulting in one large reactor, the other one is a Numbering-Up by connecting several smaller vessels to form a larger plant. In case of bioelectrochemical processes, the combination of reactors can be done via an electrical connection of the reactors, either serially or in parallel, and/or by using the efflux of one reactor (medium or gaseous) as influx for the next reactor, creating a reactor-cascade. In this work, a reactor-cascade with three electrochemical bubble column reactors was created by using the off-gas of one reactor as in-gas for the next reactor, which was either not additionally electrically connected, connected in serial or connected in parallel (see also section 6.6.3, Figure 55).

The reactor cascade was operated with an in-gas stream of  $90 \text{ ml} \cdot \text{min}^{-1}$  for reactor 1, which was three times the gas stream for the compared single reactor. Already after leaving the first reactor of the cascade, the methane production was much higher than in the single reactor, which corresponded with the findings from the gassing optimization (section 4.3.5). After the second and third reactor, the total methane production increased further (Figure 34 B), whereas the specific methane production rate remained relatively stable, showing that in each reactor comparable amounts of methane were produced. Interestingly, very high Coulombic efficiencies were obtained in all reactors (around 100 %), and the deviation of the Coulombic efficiency was rather high (Figure 34 D). Also, the hydrogen production rate of the three reactors did not differ significantly due to high standard deviations; it might be that hydrogen produced in one reactor was consumed in the following reactor, but the results were not reliable (Figure 34 C). A major issue was the hydraulic pressure the in-gas had to overcome, which was tripled by connecting the three reactors. Gas accumulated until the pressure within the reactor was higher than the hydraulic pressure of the following reactor; only then the gas proceeded and flew through the next reactor. This temporary accumulation probably caused a higher solubility of  $\text{CO}_2$  and hydrogen in the medium and an increased retention time, resulting in a higher methane production than observed in a single reactor and fluctuating percentages of hydrogen and methane in the off-gas samples, depending on the accumulation time within the reactors. This caused the higher standard deviations compared to other experiments and the very high Coulombic efficiency.

Similar results were obtained when connecting the reactors in parallel (Figure 34 A), using an applied terminal voltage of -5 V instead of an applied working potential. This was chosen, since the terminal voltage in all reactors connected in parallel should be the same. Indeed, the mean working potential at the working electrodes resulted in -1.1 V vs. Ag/AgCl as desired (-1.22 V vs. Ag/AgCl, -1.04 V vs. Ag/AgCl and -1.05 V vs. Ag/AgCl in the three reactors, respectively). The results regarding methane production and Coulombic efficiency did not significantly alter from those obtained in the cascade mode without electrical connection, although the hydrogen production seemed to be a bit lower (not significant due to high deviations as explained before) (Figure 34 C). In contrast, a serial connection with an applied current of -30 mA resulted in a lower methane production rate (Figure 34 A), although the overall Coulombic efficiency was much higher (229.63 %) (Figure 34 D). The efficiency of each single reactor was lower, i.e. close to 100 %. Since the current in a serial connection is constant at each part of the system, but the methane production rate increased through all reactors, the Coulombic efficiencies of the reactors add up to an overall efficiency. Due to this calculation, an overall efficiency higher than 100 % was obtained. However, methane production rate and hydrogen production rate were significantly lower than for the other two Numbering-Up concepts (Figure 34 A, C), although the methane production rate was still higher than in three single reactors due to the improved gas transfer. One reason could be the enlarged system resistance caused by serial connection; in serial connection, the resistance of the single reactors add up to a total resistance according to Kirchhoff's Laws, in parallel connection, the reciprocals of the single reactor resistances

add up to the reciprocal resistance of the whole system, which is than lower than in serial connection. In accordance to results obtained in Numbering-Up of MFCs, the overall terminal voltage in serial connection increased to -12.9 V, whereas in parallel connection the total current increased to -131.8 mA. It was shown that the serial connection worked for MFCs using two-chamber systems, because the overall voltage and thereby the power output was increased (Dewan et al., 2008). In contrast, connecting the MFCs in parallel should increase the current, not the potential (Dewan et al., 2008). Numbering-Up experiments in microbial electrosynthesis have not been reported before.

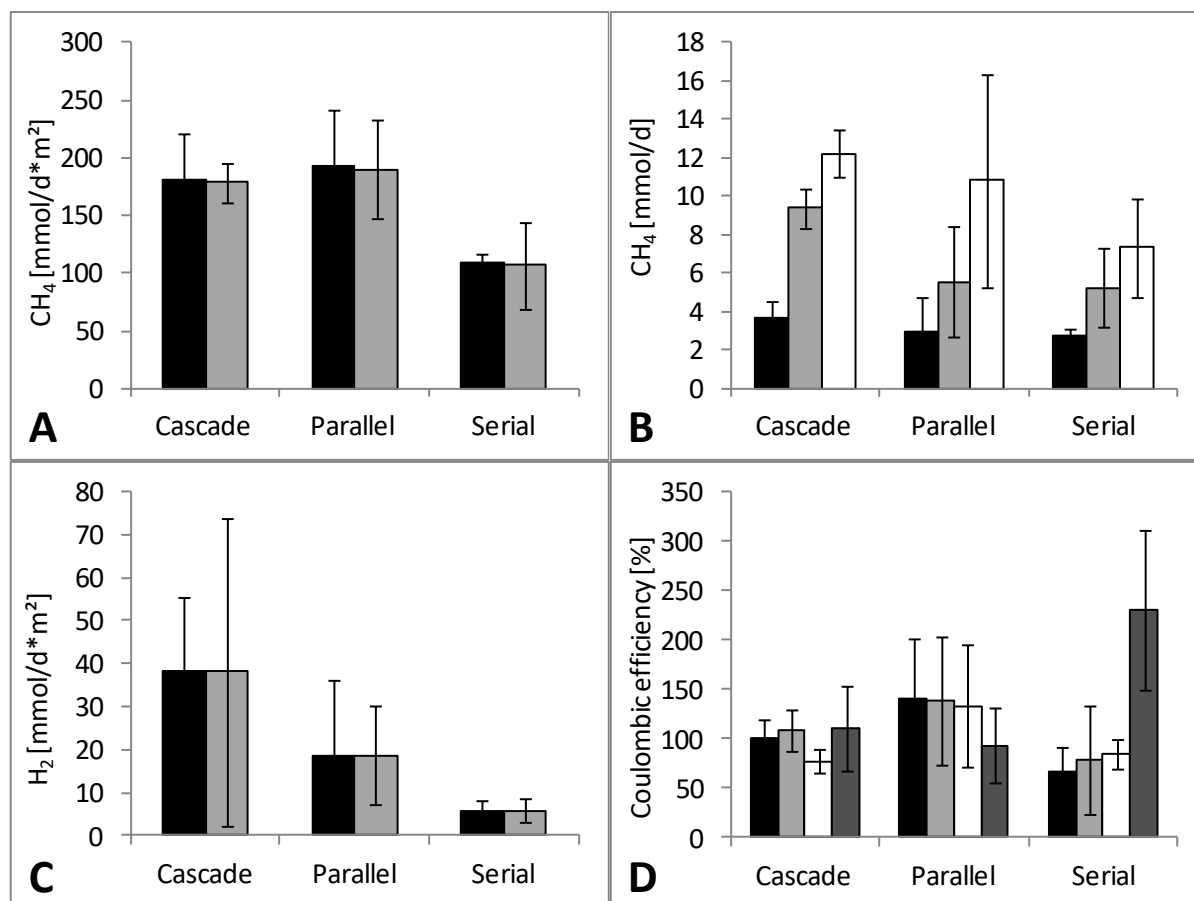


**Figure 34: Numbering-Up of bioelectromethanogenesis**

A) Mean specific methane production rate in all three reactors used for Numbering-Up (black) and total specific methane production rate (grey) resulting from the different Numbering-Up strategies; B) Absolute methane production rate measured after reactor 1 (black), reactor 2 (grey) and reactor 3 (white); gassing from reactor 1 to reactor 2 to reactor 3; C) Mean specific hydrogen production in the three reactors (black) and total specific hydrogen production (grey) of the different Numbering-Up strategies; D) Coulombic efficiencies obtained for reactor 1 (black), reactor 2 (light grey), reactor 3 (white) and the overall Coulombic efficiencies (dark grey) of the different Numbering-Up strategies.

In terms of energy efficiency, Numbering-Up resulted in an improved efficiency due to the increased methane production; for the cascade mode (0.0045 %) and the parallel connection (0.0039 %), energy efficiency including heating a little higher than for the serial connection (0.0026 %). If excluding the heat energy assuming the use of waste heat, the energy efficiencies were a lot higher (26.06 % cascade mode, 17.54 % parallel connection, 19.69 % serial connection). For a single reactor, the energy efficiency excluding heating was calculated to 9.96 % under comparable conditions used in the long

term experiment (see section 4.3.7). A further advantage of the Numbering-Up was the increased purity of the product of 0.23 % (cascade mode), 0.24 % (parallel connection) and 0.14 % (serial connection) in contrast to 0.06 % using one single reactor. This also increased the yield per substrate based on CO<sub>2</sub> from 0.0006 mol\*mol<sup>-1</sup> in one reactor to 0.0023 mol\*mol<sup>-1</sup>, 0.0024 mol\*mol<sup>-1</sup> and 0.0014 mol\*mol<sup>-1</sup> for cascade, parallel and serial mode, respectively.

#### 4.3.9 Characterization and Operation of the Pilot Scale Reactor

The larger BES reactor with 50 liter working volume was characterized similar to the smaller reactors as described in section 6.3.

The calculated superficial gas velocity in the pilot scale reactor was 0.00033 m\*s<sup>-1</sup>, giving a hydraulic residence time of 33.56 min, which is higher than the value for the smaller reactors. The gas holdup was 0.003, a little higher compared to that in the smaller reactors (0.002). These factors could increase the CO<sub>2</sub> availability for the microorganisms. During the physical characterization a bubble diameter of 0.005 m was measured, with a bubble ascend velocity of 0.093 m\*s<sup>-1</sup>. The bubbles are smaller than estimated, although the bores of the sparger had the same size as in the 1-liter reactors. This might be due to the altered pressure conditions because of the higher liquid level. The estimated interfacial area is therefore with 0.09 m<sup>2</sup> 144 times higher than in the 1-liter bubble columns, although the working volume is only 50 times larger. The smaller bubbles led to a smaller Weber number (0.306) and Bond number (0.860) compared to the smaller reactors. These two dimensionless numbers now indicate that the bubble size is stable within the reactor, according to section 6.3.2, and indeed no change of the bubble size nor coalescence of the bubbles was visible. At the water surface, relatively evenly distributed single bubbles could be observed (Figure 35).



**Figure 35: Bubbles observed in the pilot scale reactor**  
Bubbly flow with uniform bubbles in the reactor filled with 45 liter of MES medium.

Using the  $k_{La}$  correlation, the  $k_{La}$  of the large reactor was predicted to  $3.5 \text{ h}^{-1}$  and the Reynolds number to 3.6. This should guarantee a sufficient  $\text{CO}_2$  supply for the microorganisms. The calculated Reynolds number was 2.29, which is lower than the number estimated by the Scale-Up calculations (3.65), which is also due to the altered bubble size. This Reynolds number is still larger than in the small reactors. A  $k_{La}$  value of  $2.94 \text{ h}^{-1}$  was measured without working electrode; the  $k_{La}$  value estimated during Scale-Up was  $3.5 \text{ h}^{-1}$ , so the measured value is lower than the calculated one, although the gas bubbles are smaller. The reason could be that not all bores in the sparger plate are gassed through equally, so the mixing conditions are worse than estimated. But still, the  $k_{La}$  is higher than in the smaller reactor with the same vvm, which was  $1.26 \text{ h}^{-1}$ . Therefore, the  $\text{CO}_2$  supply should be sufficient for the methane production, if the working electrodes do not hinder the gas flux too much. The power input by gassing can be calculated using Equation 26 (section 6.3.2) and is 0.162 W.

The heat loss, equal to the heating power input, can be calculated as described in 6.3.2 with the values of Table 21, but counter chamber and heating jacket are just one basin for the pilot scale reactor. The heat loss through the bottom was neglected, giving a total power input by heating of 2268.4 W. The largest part was the heat loss through the counter chamber wall (2181.3 W). As for the lab-scale reactor, the pilot scale reactor should be equipped with an isolating jacket to minimize the heat loss.

Table 21: Heat loss calculation for pilot scale reactor

	Inner phase with T1	Wall material with $\lambda$ and thickness $\delta$ and surface A	Outer phase with T2
Counter chamber through wall	Water, 308.15 K	Polypropylene, $0.22 \text{ W} \cdot \text{m}^{-1} \cdot \text{K}^{-1}$ , 0.003 m, 1.322 $\text{m}^2$	Air, 293.15 K
Through bottom		Neglected	
Working chamber through wall	$\text{CO}_2$ , 308.15 K	Polypropylene, $0.22 \text{ W} \cdot \text{m}^{-1} \cdot \text{K}^{-1}$ , 0.012 m, 0.18 $\text{m}^2$	Air, 293.15 K
Working chamber through lid	$\text{CO}_2$ , 308.15 K	PVC, $0.17 \text{ W} \cdot \text{m}^{-1} \cdot \text{K}^{-1}$ , 0.02 m, 0.080 $\text{m}^2$	Air, 293.15 K

During the electrochemical characterisation it turned out that the system resistance of the pilot scale reactor was extremely low, 71.8 Ohm only, which is less than a half of the small reactors. This might be caused by a better electrical connection of the electrodes with a larger piece of platinum wire at the anode, the decreased electrode distance and in contrast to the resistances given in 4.2.1, the working electrode was made of carbon laying instead of carbon fabric.

The resistances of the different system parts were measured. Similar to the lab-scale experiments, the largest resistance arose from the counter electrode, while the electrolyte and the membrane do not significantly contribute to the system resistance (Figure 36 A).

The CV measurement (Figure 36 B) did not reveal any peaks, because the slope of the voltammogram itself overlaid all oxidation and reduction reactions. It can therefore not be said from this voltammogram at which potential the abiotic hydrogen evolution starts, but since the material has already been used in lab-scale experiments, it can be assumed that the hydrogen evolution potential is at -0.9 V vs. Ag/AgCl, as in the lab-scale reactors.

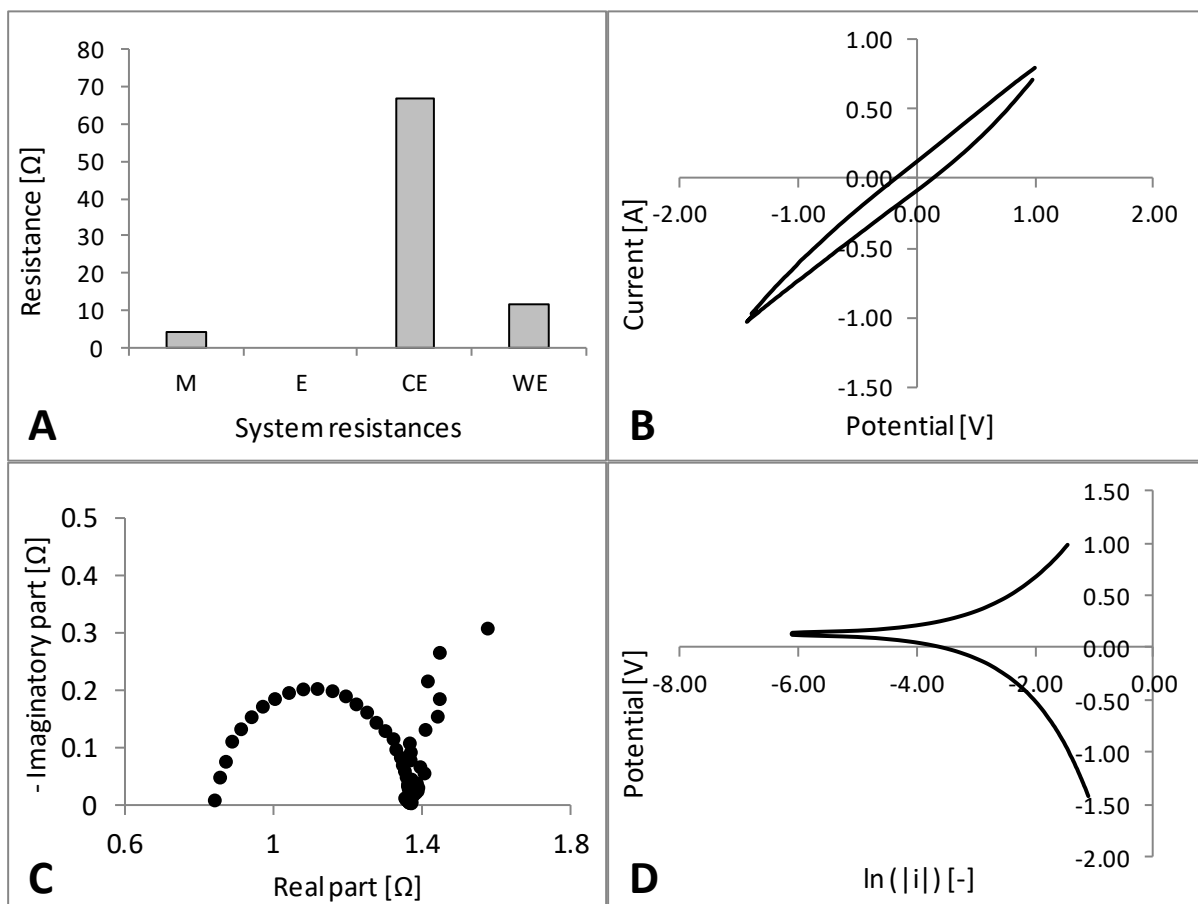


**Figure 36: Electrochemical characterization of pilot scale reactor**

A) Internal resistances of the different system parts with CEM as membrane (M), MES medium as electrolyte (E), carbon fabric as counter electrode (CE) and carbon laying as working electrode (WE); B) Cyclic voltammogram using a carbon laying electrode; C) Impedance measurement using carbon laying as working electrode; D) Tafel plot obtained from CV in B) for the calculation of the Wagner number.

From the impedance measurement, the electrolyte resistance can be estimated as 0.8  $\Omega$  and the charge transfer resistance of the working electrode as 0.6  $\Omega$  (Figure 36 C). This is extremely low compared to the results obtained in the lab-scale reactors, confirming the low overall system resistance. Either, the large electrode surface area allows an improved charge transfer, or mainly the transfer of the connecting titanium wire is measured.

The polarization time until a stable current in the abiotic system was reached was approximately 20 h, which is similar to the polarization time observed in the lab-scale reactor using carbon laying as electrode material. Using the Tafel plot (Figure 36 D), the Wagner number at -1.1 V vs. Ag/AgCl was 29.4. In the lab-scale reactor using one carbon laying electrode at -0.9 V vs. Ag/AgCl the Wagner number was 3.27, but only 1.57 if calculated for a reactor with 4 carbon laying electrodes at -1.1 V vs. Ag/AgCl. In both cases, the Wagner number did not remain constant but increased significantly, indicating a very evenly distributed electrical field.

The pilot plant reactor was operated biotically and abiotically for more than 200 h, respectively. In the biotic experiment, the methane production remained relatively stable throughout the operation, with a correspondingly low hydrogen production rate (Figure 37 A). In the abiotic control, no methane was detected. The average biotic methane production rate was  $11.67 \pm 0.77 \text{ mmol} \cdot \text{d}^{-1}$ , which was the highest methane production rate reported in pure culture bioelectromethanogenesis so far. The specific methane production rate based on the geometrical surface area of the working electrode was  $10.24 \text{ mmol} \cdot \text{d}^{-1} \cdot \text{m}^2$ .

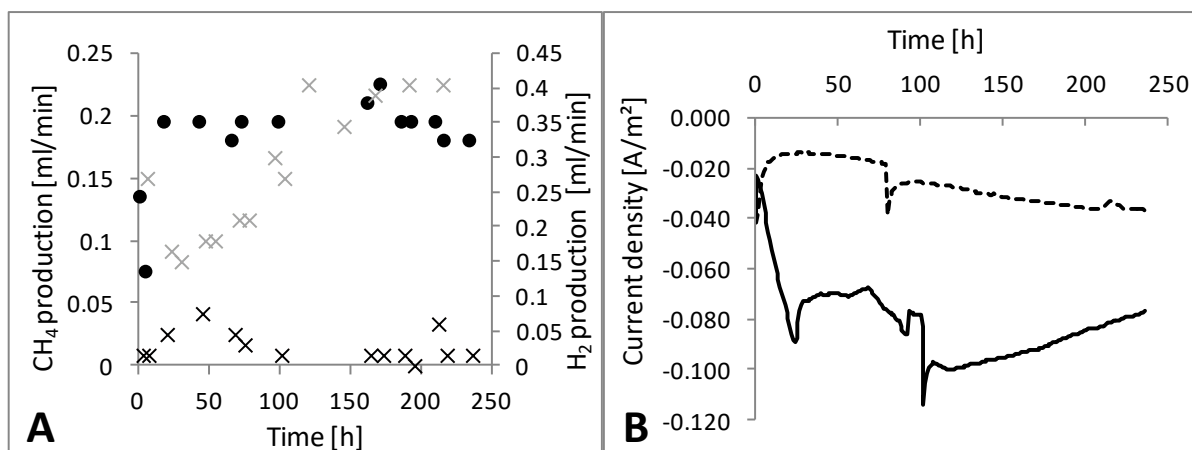


**Figure 37: Gas production rates and current densities obtained in pilot plant reactor**

A) Gas production rates; dots: methane production rate; grey crosses: abiotic hydrogen production rate; black crosses: biotic hydrogen production rate; B) Current density in the abiotic (dashed line) and biotic (solid line) experiments.

In the abiotic control, only very little hydrogen was produced ( $15.10 \text{ mmol} \cdot \text{d}^{-1} \cdot \text{m}^2 \pm 5.02 \text{ mmol} \cdot \text{d}^{-1} \cdot \text{m}^2$  at a Coulombic efficiency of 77.9 %) (Figure 37 A). If indirect electron transfer would be the only mechanism of electron transport from electrode to microorganisms, only 33.4 % of the methane formed could be explained. This suggests that direct electron transfer or indirect transfer via biotically produced hydrogen were predominant.

The current consumption in the biotic control was larger than in the abiotic operation (Figure 37 B), but still, the current density reached was low ( $85.0 \text{ mA} \cdot \text{m}^2$ ). Surprisingly, this led to a very high calculated medium Coulombic efficiency of  $113.6 \% \pm 9.0 \%$  over time. The contacting titanium wire in the working chamber showed partial corrosion, which might allow Coulombic efficiencies above

100 %. All electrons transported by the electrical current were found in the desired product, additionally, methane formation must have included other electron sources. It might be that charges present on the electrode were altered to gain additional electrons, or that the polypropylene pipe leached low molecular plasticizers, which were consumed by the microorganisms. It can however be concluded that the pilot scale reactor can be used to produce methane efficiently, in contrast to a low abiotic hydrogen production. Although the Coulombic efficiency for hydrogen production was already high, the use of an electroactive biocatalyst increased the efficiency of electron usage.

Compared to the lab scale reactor used for the reactor comparison and the long term experiment (section 6.6.2.8 for operational conditions and 4.3.7 for results), the pilot plant reactor produced in total more methane per day, but if calculating the methane production rate based on the geometrical working electrode surface area or the working volume, the performance was only 16 % of the lab scale reactor (Table 22). In contrast, the energy efficiency was much higher than in the lab scale reactor. It was differentiated between the energy efficiency including the heating energy, which is very low, and the energy efficiency excluding the heating energy, which gave a reasonable value. The high losses caused by heating were explainable, since neither the lab scale reactor nor the pilot scale reactor were thermally isolated. In an industrial application, isolation and integrated heating concepts could be applied to use waste heat and thereby increasing the total energy efficiency. If calculating the energy efficiency excluding heating, the pilot scale reactor was nearly 5 times more efficient than the lab scale reactor, including heating the efficiency was 6 times higher due to the improved volume to surface ratio of larger scales (Table 22). As for the lab-scale reactor, the pilot scale reactor should be equipped with an isolating jacket to minimize the heat loss.

Table 22: Performance comparison of pilot plant and lab scale reactor

	Lab scale	Pilot scale
<b>Absolute production rate <math>Y_p</math></b>	1.38 mmol*d <sup>-1</sup>	11.67 mmol*d <sup>-1</sup>
<b>Specific Production rate <math>Y_{PEI}</math></b>	60.4 mmol*m <sup>-2</sup> *d <sup>-1</sup>	10.2 mmol*m <sup>-2</sup> *d <sup>-1</sup>
<b>Space time yield <math>Y_{ST}</math></b>	1.38 mmol*l <sup>-1</sup> *d <sup>-1</sup>	0.23 mmol*l <sup>-1</sup> *d <sup>-1</sup>
<b>Coulomb efficiency <math>\eta_c</math></b>	58.8 %	113.6 % <sup>1)</sup>
<b>Energy efficiency <math>\eta_E</math></b>	0.0014 %	0.0055 %
<b>Energy efficiency excluding heating</b>	10.0 %	27.0 %
<b>Yield per substrate</b>	0.00055 mol*mol <sup>-1</sup>	0.00013 mol*mol <sup>-1</sup>
<b>Purity</b>	0.055 %	0.013 %

<sup>1)</sup> High Coulombic efficiency most probably caused by corrosion of contacting wire.

However, the low space time yield of the pilot scale reactor needs to be improved. It might be that not all parts of the working electrode participate in the reaction, since the inner resistance of the large electrode caused potential drop over the electrode area; the working potential might be insufficient in the peripheric electrode parts. This would also explain the extremely low current density compared to the lab scale reactor ( $85.0 \text{ mA}\cdot\text{m}^{-2}$  instead of  $1142.5 \text{ mA}\cdot\text{m}^{-2}$ ).

In contrast to the pilot scale reactor, the methane formed in the lab scale reactor under the applied conditions (see also section 6.6.2.8 for the operational conditions used and 4.3.7 for more detailed results) could fully be explained via abiotically produced hydrogen, indicating that just indirect electron transfer took place. In the pilot scale reactor, 66.63 % of the methane produced could be explained via direct electron transfer at a slightly lower hydrogen conversion rate of 90.53 %, in contrast to 98.09 % in the lab scale reactor. This was another indicator that at large parts of the electrode, the working potential was too low for abiotic hydrogen production, but may be sufficient for direct electron transfer to the methanogens. Therefore, less methane was produced, since major parts of the indirect electron transfer did not take place.

A method to overcome the unequal working potential in different working electrode zones could be the application of current instead of working potential. The working potential might then locally be larger than the desired  $-1.1 \text{ V vs. Ag/AgCl}$ , but the overall performance could improve.

A crucial factor limiting the process in the pilot plant reactor might be the design of the counter electrode. It was designed based on the membrane window area, but the ratio between counter electrode and working electrode lowered from 1.1 to 0.53 based on the working electrode sheet geometrical surface area. Additionally, the counter electrode in the pilot scale reactor was wrapped around the working chamber 2.5 times, resulting in 2 layers of counter electrode placed behind each other. It might be that the rear laying was not taking part in the reaction, limiting the process by lowering the current and the proton availability at the cathode.

Inhibition experiments with the pilot plant reactor material revealed, that the polypropylene as well as the plastic screws (fixation of the sparger plate in the pilot plant reactor) led to a decrease in methane production. Especially the polypropylene, which was used for the outer wall of the working chamber (in contrast to the lab scale reactor, where polyether ethylketone (PEEK) was used), seemed to inhibit the methanogens and decrease the specific methane production rate from  $135.7 \text{ mmol}\cdot\text{d}^{-1}\cdot\text{m}^{-2}$  to  $69.8 \text{ mmol}\cdot\text{d}^{-1}\cdot\text{m}^{-2}$  in H-cells (Figure 38 A). It is therefore likely that the performance of the pilot scale reactor could be improved by using another material. Also, the plastic screws used for the fixation of the sparger plate at the bottom of the pilot scale reactor led to a decrease in methane production, but not as large as the polyethylene. The higher overall methane production rates in H-cells compared to the 1-liter and 50-l reactor were caused by the use of graphite rod electrodes instead of carbon laying and carbon fabric. The hydrogen production was not significantly altered by the

addition of reactor materials (Figure 38 A), but the Coulombic efficiency was decreased with decreasing methane production rate (Figure 38 B). The Coulombic efficiency in H-cells was in all experiments lower than in the bubble column reactors due to the worse mixing conditions (Enzmann et al., 2019).

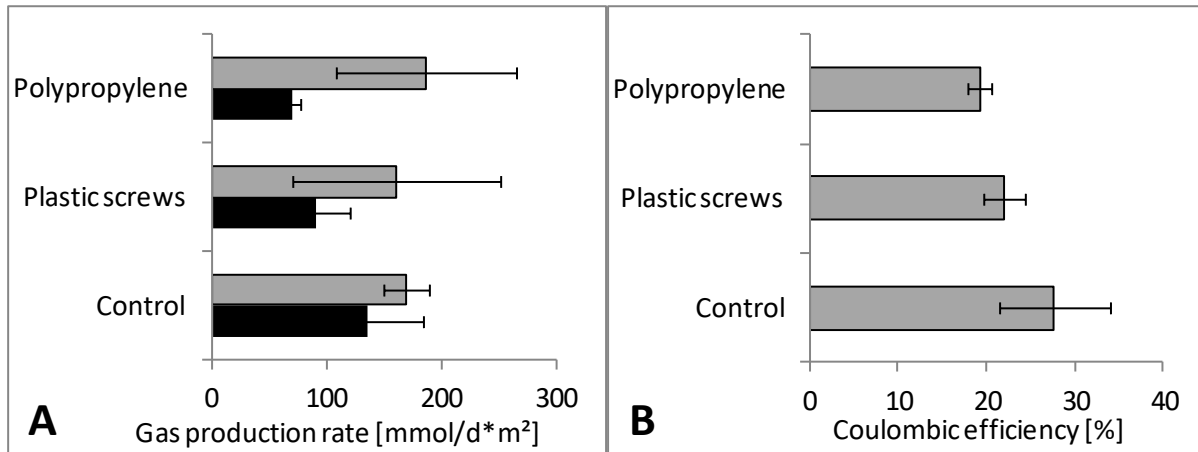


**Figure 38: Inhibition of methanogenesis by reactor materials**

A) Gas production rates of methane (black) and hydrogen (grey) in H-cells with polyethylene, plastic screws and without material (control); B) Coulombic efficiency in H-cells with polyethylene, plastic screws and without material (control).

The leaching of plasticizers from plastic screws and polypropylene might inhibit the methanogenesis. Possibly, small molecules reacted or formed a layer at the electrode surface, preventing the methanogens from getting in touch with the electrode surface efficiently. It was observed before that artificial plastics show inhibitory effects on microorganisms (Meier et al., 2013). For future constructions, reactor material should be tested prior to building of the plant.

#### 4.3.10 Comparison to Literature Data

Compared to literature data obtained with *M. maripaludis*, the results obtained in the first H-cell experiments were slightly lower. In a literature study, a comparable applied potential of -0.7 V vs. SHE (-0.9 V vs. Ag/AgCl) 30 mmol\*d<sup>-1</sup>\*m<sup>-2</sup> were obtained, while a higher potential of -0.6 V vs. SHE (-0.8 V vs. Ag/AgCl) lead to 11.4 mmol\*d<sup>-1</sup>\*m<sup>-2</sup> (Deutzmann et al., 2015; Lohner et al., 2014). These experiments were carried out in a similar H-cell with a graphite rod electrode and the same membrane as in this work. Apart from that, there are three major differences between the experiments conducted in literature and the experiments of this work, which are 1) the MES medium does not contain MOPS buffer as the medium in the literature studies; 2) the literature studies operate the H-cells with an applied gas phase and stirring, while in this work the H-cells are continuously gassed through and 3) the optical density of the methanogens in the literature studies was 0.04 while in this work the working chamber was inoculated to 0.1. It might be that the slightly higher methane production rate results from the better gas distribution and CO<sub>2</sub> availability due to the stirring, although the OD is lower. Taking this into account, the results are comparable, which is very positive because they show that the strain, the medium and the analytics lead to reliable results.

The results obtained in the bubble column reactor were also compared to methane production rates stated in literature. Only few studies reported experiments with pure cultures. Apart from Deutzmann et al. and Lohner et al. (11.4 to 30  $\text{mmol}\cdot\text{d}^{-1}\cdot\text{m}^{-2}$  with a pure culture of *M. maripaludis*, see above) (Deutzmann et al., 2015; Lohner et al., 2014), Hirano et al. 89.1  $\text{mmol}\cdot\text{d}^{-1}\cdot\text{m}^{-2}$  with a pure culture of *M. thermautotrophicus* (Hirano et al., 2013) and Beese-Vasbender 3.5  $\text{mmol}\cdot\text{d}^{-1}\cdot\text{m}^{-2}$  with a *Methanobacterium*-like strain IM1 (Beese-Vasbender et al., 2015).

The range of methane production rates using mixed cultures in bioelectrochemical systems reviewed by Blasco-Gomez ranged from 0.22  $\text{mmol}\cdot\text{d}^{-1}\cdot\text{m}^{-2}$  to 2911.99  $\text{mmol}\cdot\text{d}^{-1}\cdot\text{m}^{-2}$ , with more than half of these values below 100  $\text{mmol}\cdot\text{d}^{-1}\cdot\text{m}^{-2}$  (Blasco-Gómez et al., 2017) (Figure 39). The specific production rate of the bubble column reactor and even the pilot scale reactor was therefore comparable to other systems.

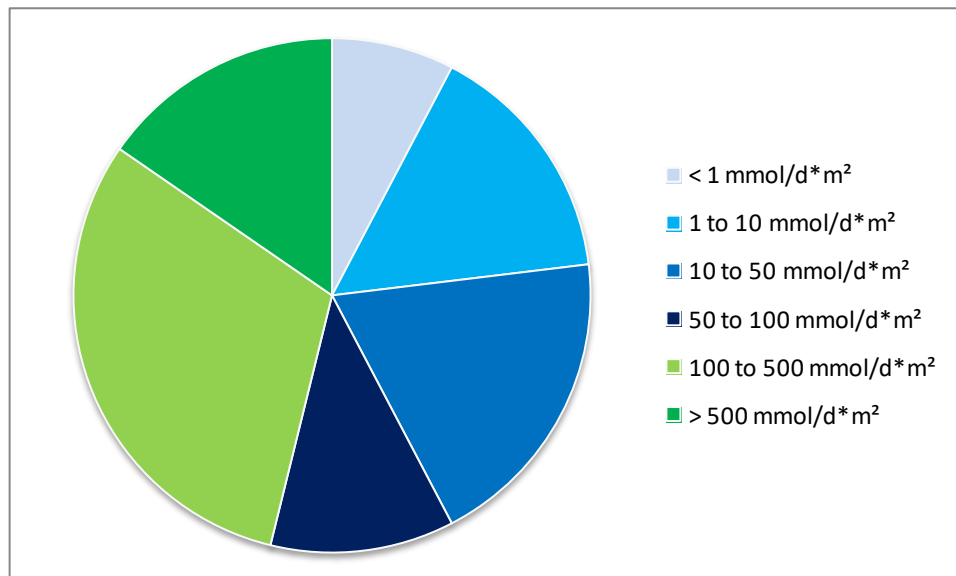


Figure 39: Specific methane production rates reviewed by Blasco-Gomez et al., 2017

Blue: specific methane production rates below 100  $\text{mmol}\cdot\text{d}^{-1}\cdot\text{m}^{-2}$ ; green: specific methane production rates above 100  $\text{mmol}\cdot\text{d}^{-1}\cdot\text{m}^{-2}$ .

Complete calculations of the energy efficiency of bioelectromethanogenesis were not published so far, but in terms of Coulombic efficiency, the mean Coulombic efficiency of the values reported by Blasco-Gomez et al. was 68.8 %, ranging between 19 % and 194 %, whereas the value of 194 % can only be explained by metabolization of organic compounds in the mixed culture setup. The mean Coulombic efficiency using the bubble column reactor was 53.4 %, so lower than the average literature value, ranging from 27.4 % with the carbon fabric electrode to 76.8 % using four carbon laying electrodes. The deviation of the results was thus lower and the results obtained are well within the values given in literature.

Comparing the methane production rates obtained in bioelectromethanogenesis to the values measured in septum flasks (see section 6.6.1), the space time yield was significantly lower in

bioelectromethanogenesis, especially when compared to values obtained in the M141 growth medium. When comparing the space time yield with that obtained in a septum flask on MES medium, the difference was lower, suggesting that in general, the methanogens are limited by any medium component present in the M141 growth medium, but not in the MES medium. The complex M141 medium was not used in bioelectromethanogenesis to avoid electrochemical interference of unknown molecules with the electrode. A further optimization strategy could thus be the separate addition of medium components to find the specific limitation. It is, however, questionable if these results are really comparable due to different optical densities, different pressure conditions and different growth phase, but they confirm the finding of the optimization, namely that the biocatalyst can perform even better and is thus not the main limitation of bioelectromethanogenesis.

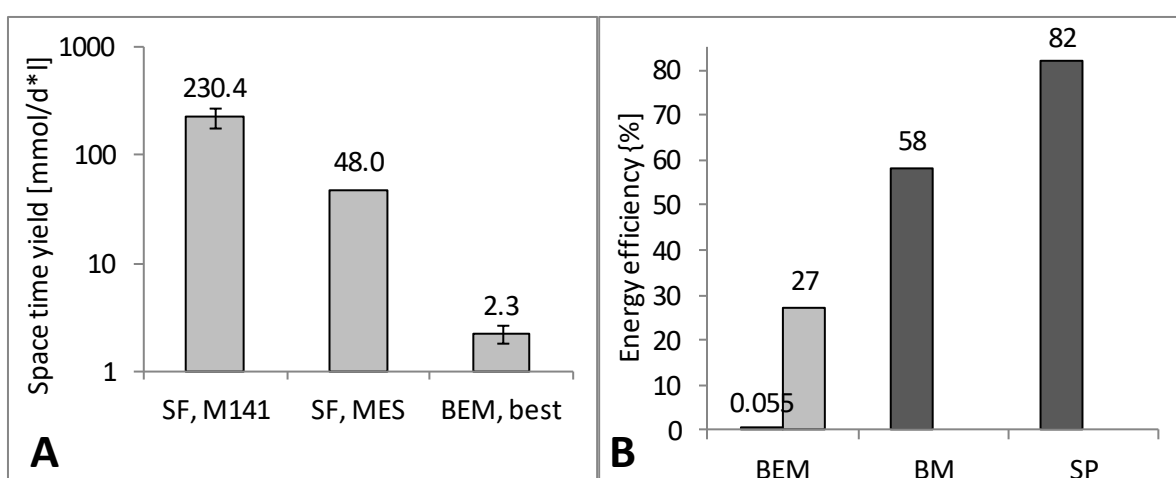


**Figure 40: Comparison of bioelectromethanogenesis to other methane producing technologies**

A) Comparison of the space time yield of bioelectromethanogenesis (BEM) to production obtained in septum flasks (SF) with M141 and MES medium, respectively; B) Comparison of the energy efficiency of bioelectromethanogenesis (BEM) to literature date for biological methanation (BM) from CO<sub>2</sub> and hydrogen and the Sabatier process (SP); Dark grey: energy efficiency including heating energy losses; light grey: energy efficiency of BEM excluding heating energy input).

Comparing the energy efficiencies of the bioelectromethanogenic process in this thesis to energy efficiencies as summarized in section 2.1.2.2 for other methane production technologies, the microbial electrotechnology can only compete with biological methanation and the Sabatier process if not considering the energy needed for maintaining the system temperature. The amount of energy needed for 1 m<sup>3</sup> of methane would still be 35.4 kWh without considering heating energy. However, the results given for the other two processes already consider retrieval of heat, so that in summary, the bioelectromethanogenesis in the 50 liter pilot plant already reached half the energy efficiency of the biomethanation, although it is yet far from industrial application. Therefore it seems that bioelectromethanogenesis could turn out to be a feasible process for fuel production and might be applied industrially in future.

#### 4.4 Microbial Fuel Cell

In order to ascertain if the designed bubble column reactor is also suitable to host other bioelectrochemical processes, it was operated as microbial fuel cell. Here, the working electrode is the anode; the anode chamber is hosting the microorganisms. In the cathode chamber (for instance, the surrounding chamber of the newly designed reactor), the counter reactions (e.g. oxygen reduction) occur.

Experiments in MFC mode were carried out using the facultatively anaerobic bacterium *Shewanella oneidensis*, which has already been described as electroactive (Bretschger et al., 2007; Watson and Logan, 2010; Zhao et al., 2013). As reported in literature, current production from the substrate lactate was observed in all three reactors. In all cases, lactate consumption could be detected, but no planctonic growth was measured. The current density measured in the experiments showed a characteristic progress obtained in the bubble column reactors, but it is similar for all reactors (Figure 41). After inoculation, the current first starts to increase up to a maximum, which is reached after approximately two days. Afterwards, the current decreases again, but does still remain above the current measured in an abiotic control experiment. Each experiment lasts 90 h.

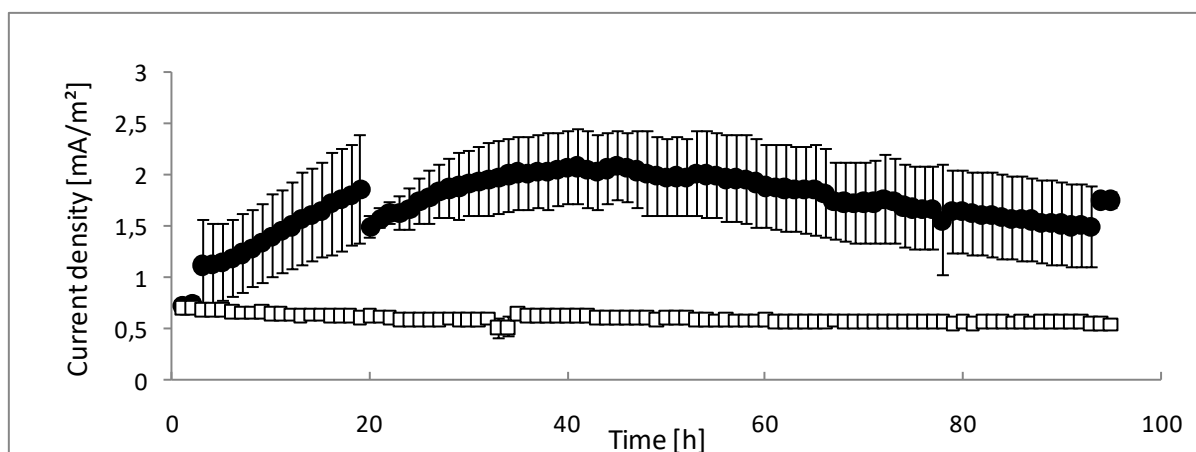
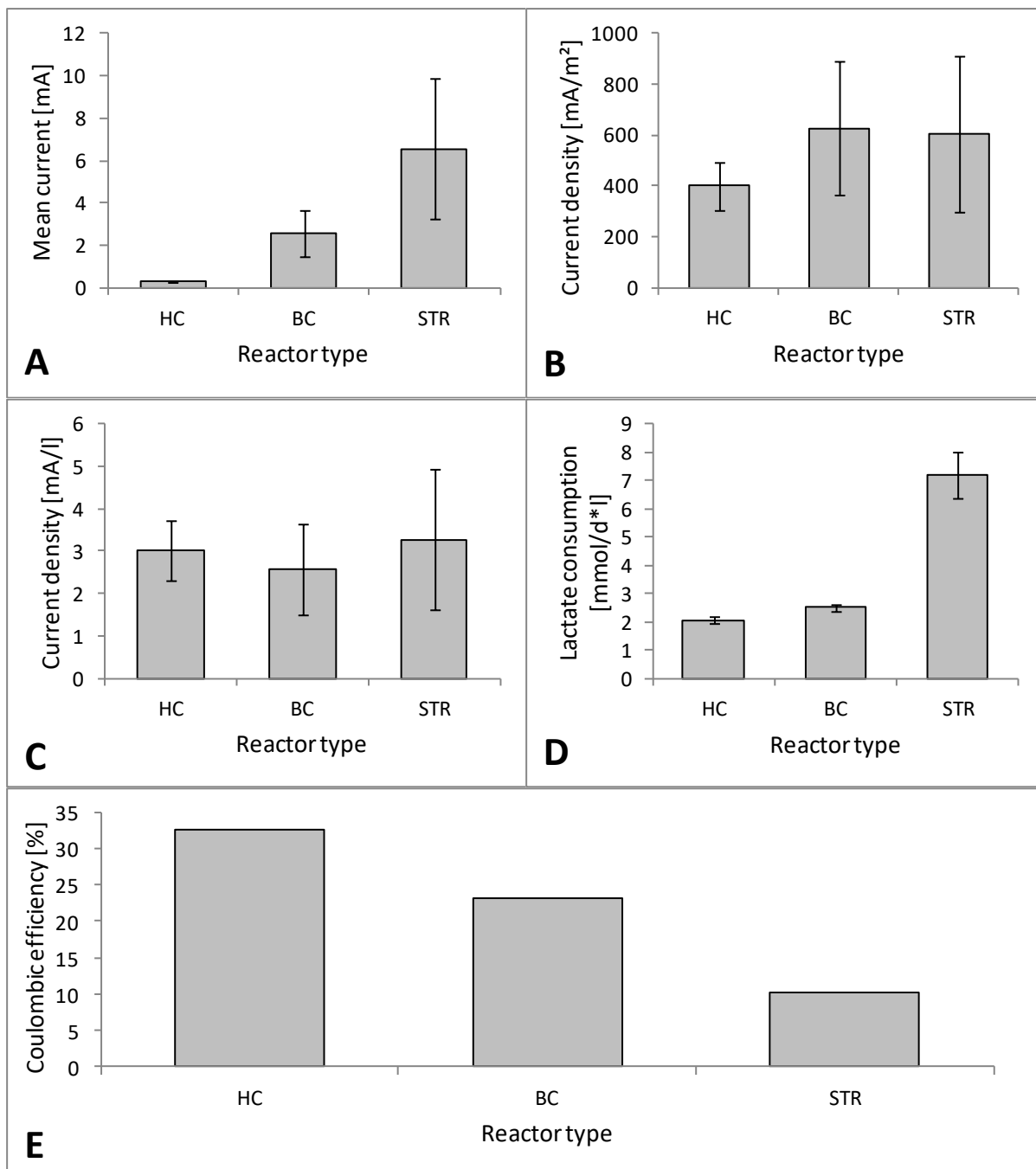


Figure 41: Current progress of MFC in bubble column reactor

Current in MFC with *Shewanella oneidensis* at 400 mV vs. Ag/AgCl in Bubble column reactor; □: Abiotic control, ●: Biotic experiments

Figure 42 shows the total current, the current density, the lactate consumption rate and the calculated Coulombic efficiency of the MFC experiments in H-cells, flat plat reactors, bubble column reactors and stirred tank reactors. The total current produced is highest when using the stirred tank reactor, which does also have the largest working volume. The current density based on the electrode surface area reveals that the bubble column and the stirred tank reactor perform similarly here, whereas the H-cell reached lower current densities. This image differs when calculating a “current density” based on the reactor working volume, where all reactors perform similar. When looking at the lactate consumption rate per liter working volume, the use of the stirred tank reactor leads to a very high lactate uptake, probably because of the improved mass transport by stirring. However, when looking at

the Coulombic efficiency, it seems that the lactate taken up by the microorganisms cannot be transferred to electrical current, since although the mixing is good, the electrode does not seem to be available for the microorganisms to donate the electrons to the acceptor. Either the electrode is too small for the large working volume or the stirring prevents the microorganisms from attaching to the electrode. In contrast, the H-cell shows a high Coulombic efficiency, probably because the microorganisms cannot take up lactate very efficiently due to the bad mixing conditions, but the lactate which is consumed can very efficiently be converted into electrical current.



**Figure 42: MFC performance in different bioelectrochemical systems**

A) Total current of MFCs using different reactors; HC: H-cell, BC: bubble column, STR: stirred tank reactor; B) Current density of MFCs using different reactors based on the geometric electrode surface area; C) Current density of MFCs using different reactors based on the reactor volume; D) Lactate consumption rate in MFCs using different reactors; E) Coulombic efficiency of MFCs using different reactors (calculated from mean current and mean lactate consumption rate).

In a comparable study with a modified stirred tank reactor using *Shewanella oneidensis* and a poised working electrode (+400 mV vs. SHE, +200mV vs. Ag/AgCl), current densities between 25 mA\*m<sup>-2</sup> (not stirred) and 500 mA\*m<sup>-2</sup> (stirred and aerated) were reached (Rosa et al., 2016). The later value is close to the current density obtained here, although the optical density is lower than in the comparable study, but using a higher applied potential. This shows, however, that the performance of the used reactors in this work is comparable to results obtained in other working groups. The designed lab-scale bubble column reactor showed a similar performance to other bioelectrochemical systems and shows even a higher current density than other systems. So, it is in any case suitable for the use as MFC and the results from for example screening experiments in H-cells can be transferred to the larger reactor for further Scale-Up studies.

It would have been possible to allow a continuous medium flux during the operation by using the two side ports. Since no growth was observed and the lactate consumption rate was relatively low (less than 10% of the lactate were consumed during one week of operation), a continuous process did not seem to be beneficial. The disadvantages of the continuous operation, such as contamination risk, cell wash out or the necessity of a cell retention, and higher demand of process equipment outweigh the potential benefit of creating a long-term stable process. So, the continuous operation was not tested in this project, but could be in focus operating the reactor with growing (mixed) cultures or high substrate consumption rates.

## 5 Conclusion and Outlook

A flexible and scalable bioelectrochemical bubble column reactor was designed to use for an optimization of bioelectromethanogenesis. Although the reactor already showed methane production rates similar to results found in literature before optimization, the total methane production was increased during the project by a factor of 9.8.

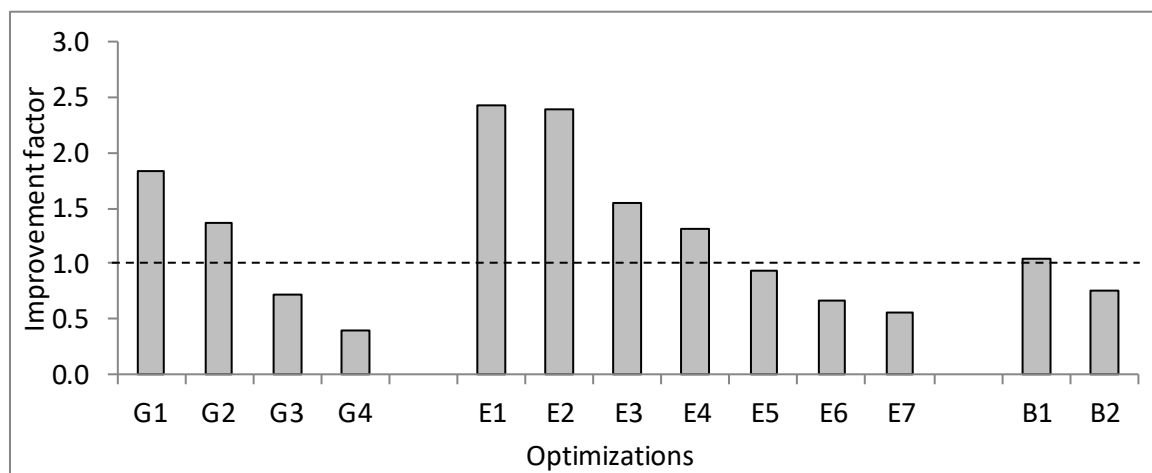


**Figure 43: Improvement of methane production rates by process optimization**

Improvement factors of the absolute methane production rates by optimization of gassing (G1: gas composition, G2: gas velocity, G3: sparger plate, G4: external loop), optimization of electrochemical parameters (E1: Working electrode size, E2: applied working potential, E3: working electrode material, E4: membrane type, E5: counter electrode size, E6: membrane size, E7 counter electrode type) and biological factors (B1: addition of MOPS, B2: optical density). Factors below 1 (dashed line) indicate that none of the tested alterations from the basic conditions did lead to an improvement.

The highest impacts on the process, and therefore the strongest process limitations, were observed while altering the electrochemical parameters, especially the working electrode size and material as well as the applied potential. This clearly indicated that the electron availability was the most critical point of the process, followed by the CO<sub>2</sub> supply. The biocatalyst did not seem to limit the methane production rate. This was confirmed by applying a high current of -100 mA to the system, instead of an applied working potential, which could again increase the methane production rate by a factor of 2.9 without losses in the Coulombic efficiency. Thus demonstrating that the biocatalyst still converted the same percentage of electrons supplied to methane and was therefore not limiting. It has to be mentioned, that at high currents and correspondingly low working potentials, the abiotic hydrogen production was more energy efficient than a bioelectrochemical fuel production.

It was presented in this thesis that process recovery was fast after failures in electricity and gas supply, but not during changes of the in-gas composition or the working temperature. Mixed cultures, the use of buffers or additional hydrogen supply during power gaps could increase the stability of the process, i.e. by providing alternative carbon or electron sources during failures or by stabilizing the pH.

A rational Scale-Up based on Similarity Theory was carried out for the first time in this thesis. Although the total methane production rate was the highest reported for pure cultures so far, the space time yield was significantly lower than in the lab scale reactor. Especially the low current densities due to high internal resistances of the larger electrode restricted the methane production. Although the volumetric methane production was low, the energy efficiency of the pilot plant was higher than that reached in the lab scale reactors. It would be interesting for future research to also operate the pilot scale reactor as microbial fuel cell or use it in other bioelectrochemical processes, to identify the main process limitations by comparisons to lab scale results.

When Numbering-Up was conducted, the specific methane production compared to a single lab scale reactor improved significantly. Instead of one large reactor, Numbering-Up of several smaller reactors seems to avoid large internal resistances of the electrodes and thereby increasing the volumetric methane production rate. Due to the economy of scales and the better energy efficiency, an industrial process should work with a combination of Numbering-Up and Scale-Up to allow high production rates at high energy efficiencies. Numbering-Up proved to be efficient in cascade mode or at parallel connection, whereas serial connection of reactors should be avoided. Parts of the improvement in methane yield could be explained by slight overpressure in the reactors and an increased hydraulic retention time, which gives opportunities for further optimizations in follow-up projects. To further increase the production of methane in an industrial relevant scale, it could be beneficial to operate the reactors with an applied current instead of an applied working potential, since the potential might drop over large electrode surfaces. To further increase the methane content in the off-gas stream, circulation of the gas could be performed to allow a higher residence time within the working chamber and increase the Coulombic efficiency. Also, the enforcement of the membranes to allow pressure application to the system should be considered. Another option would be the use of mixed microbial cultures, which could result in higher yields and a more stable process.

A major drawback might be the low energy efficiency of the process, if heating energy is taken into account. Only if the process can be operated using waste heat and integrated heat concepts, an energy efficient storage of electricity in methane can be possible. The highest efficiencies reached within this project were around 30 %, so further improvements are necessary to compete with other energy conversion processes.

The process of bioelectromethanogenesis could after further optimization, especially regarding the energy efficiency, be used to treat CO<sub>2</sub> rich industrial off-gas streams. Another feasible option is the use as a method to upgrade the methane content of biogas, which is produced in more than 8000 biogas plants in Germany. The reactor also could be integrated into the usual purification line of biogas to reduce the amount of CO<sub>2</sub> released to the environment.

From an economical point of view, bioelectromethanogenesis seems not to be feasible by now, since common techniques are still more energy efficient and productive. However, the design of a scalable reactor offers possibilities for the bioelectrochemical production of high-value products. It was shown that electroactive methanogens can be cultivated within this reactor; An interesting opportunity could be the production of compounds with genetically modified methanogens, as for example the production of geraniol. It has already been demonstrated that geraniol can be produced from CO<sub>2</sub> and hydrogen using a modified *Methanococcus maripaludis* strain (Lyu et al., 2016), which is also electroactive as it has been verified in this work. This provides a possible future use for the scalable bioelectrochemical reactor developed, which might meet the requirements for an economical and ecological production.

The developed bubble column reactor was successfully used for two different bioelectrochemical processes. It was also comparable to other lab-scale reactors, which allows for universal usage in screening and optimization experiments; it will also be possible to transfer results obtained from smaller reactors, e.g. H-cells, to the bubble column reactor, increasing the possibilities of applications and allowing combined screening, optimization and Scale-Up processes.

## 6 Materials and Methods

### 6.1 Chemicals and Gases

A list of all chemicals used can be found in the appendix; all chemicals used were of analytical grade. The composition of all media used for the experiments is also listed in the appendix.

Used gases were

- N<sub>2</sub> (5.0) for MFC, MES with 50/50 N<sub>2</sub>/CO<sub>2</sub> composition and k<sub>L</sub>a measurements
- CO<sub>2</sub> (5.0) for MES and k<sub>L</sub>a measurements
- N<sub>2</sub>/CO<sub>2</sub> (80/20, ALIGAL 12, Air Liquide, Düsseldorf, Germany) for MES and medium preparation
- N<sub>2</sub>/CO<sub>2</sub>/H<sub>2</sub> (80/13/7, Air Liquide, Düsseldorf, Germany) for MES experiments
- H<sub>2</sub>/CO<sub>2</sub> (80/20, Air Liquide, Düsseldorf, Germany) for methanogen cultivation
- Ar (6.0) and He (6.0) for gas chromatography

### 6.2 Lab-Scale Reactors

The aim of this work was to develop a new reactor for BES processes. Two different existing lab-scale reactors and the developed bubble column reactor were tested abiotically and in two different bioelectrochemical processes for comparison.

#### 6.2.1 Main Process Equipment

The used measurement equipment for all reactors can be seen in Table 23.

Table 23: Process and measuring equipment

Sensor	Type	Used for system/system part
pH meter	Mettler Toledo (Mettler, GieBen, Deutschland) + Bioengineering pH module (Bioengineering, Wald, Switzerland)	Bubble column and stirred tank (Working chamber), k <sub>L</sub> a measurement
	Voltcraft PH100ATC (Voltcraft, Hirschau, Germany)	Bubble column (counter chamber), H-cell (start and endpoint measurements)
Temperature sensor	DASGIP® TC4 module (Eppendorf, Hamburg, Germany)	Bubble column (working chamber)
Potentiostat	Multi Master 2.1 (Material Mates,	Bubble column

	Milano, Italy) + Software (Multibatt)	(chronoamperometry); H-cells (chronoamperometry)
	Gamry Interface 1000 (Gamry instruments, Warminster, USA)	All impedance measurements and CVs; stirred tank reactor (chronoamperometry)
Rotameter	Rotameter (Wagner Mess- und Regeltechnik, Offenbach a.M., Germany)	Gasflux control of all BES
Multimeter	OWON B35 (Fujian Lilliput Optoelectronics Technology Co, Zhangzhou, China)	Terminal voltage of all BES, system resistances and potentials, internal resistance electrodes
Conductivity sensor	HI99301 conductivity meter (Hanna instruments, Vöhringen, Germany)	Media conductivity
	Incubator hood (Bibby Scientific Stuart SI60D Forced Air Incubator, Stone, UK)	H-cells
Temperature control	Titanium heater tube (Schego heater tube controlled by universal thermostat tx.3, sygonix (Conrad electronics, Hirschau, Germany))	Bubble column (Heating jacket)
	Heating stick with bioengineering temperature module (Bioengineering, Wald, Switzerland) and refrigerated circulating bath (VWR, Darmstadt, Germany)	Stirred tank reactor
Gas analysis via gas chromatography (GC)	Agilent technologies 490 Micro GC (with external 2-point-calibration) (Agilent, Santa Clara, USA)	Off gas analysis; detects H <sub>2</sub> , CO <sub>2</sub> , CH <sub>4</sub> , O <sub>2</sub> , N <sub>2</sub> and H <sub>2</sub> S
Ag/AgCl Reference	Ag/AgCl Reference electrode (+200mV vs. SHE, SE 21, (SensortechnikMeinsberg/ Xylem Analytics, Weilheim Germany)) placed in Haber Luggin capillary (Glass, closed with magnesia diaphragm, Fischer Labortechnik, Frankfurt a.M., Germany) filled with 0.5 M Na <sub>2</sub> SO <sub>4</sub> .	Bubble column, stirred tank reactor: Capillary D 0.5 cm, L 22 cm, total length 35 cm H-cell: Capillary D 0.5 cm, L 8.5 cm, total length 21.5 cm

High performance liquid chromatography (HPLC)	Prominence 20 series (Shimadzu Deutschland GmbH, Duisburg, Germany)	Samples during MFC processes
	WPA Biowave CO8000 Cell	
Photometer	Density Meter, 600 nm, (Biochrom Ltd, Cambridge, Great Britain)	Optical density of all samples

Current and applied voltage were constantly monitored in all experiments. Gas samples were taken twice a day from all reactors. For analysis of the off gas samples, approximately 50 ml of off-gas were sampled directly from the reactor outlet in a gas tight plastic bag (Restek GmbH, Bad Homburg, Germany). The GC pumped the sample out of the bag onto three different GC columns, where the gas composition is measured. The three columns are:

- Channel 1 PoraPLOT U pre-column and Molsieve 5A main column with argon as carrier gas
- Channel 2 PoraPLOT U pre-column and Molsieve 5A main column with helium as carrier gas
- Channel 3 PoraPLOT U as pre column and main column with helium as carrier gas.

The GC operated with an injector temperature of 100 °C and a column temperature of 60 °C. A thermal conductivity detector was used. Hydrogen was detected on channel 1, oxygen and nitrogen on channel 2 and methane and carbon dioxide on channel 3. An external 2 point calibration was done for N<sub>2</sub>, O<sub>2</sub>, H<sub>2</sub>, CO<sub>2</sub>, CH<sub>4</sub> and CO. The sampling time was set to 30 s, the total runtime to 3 min. For MFC, lactate consumption and acetate production were analyzed via HPLC using a Rezex ROA organic acid H<sup>+</sup> (8%) column (Phenomenex, Aschaffenburg, Germany). Acidic water (5 mM H<sub>2</sub>SO<sub>4</sub>) was used as mobile phase with a flux of 0.6 ml\*min<sup>-1</sup> at a temperature of 30 °C. The runtime added up to 7 min; detection was done via a PDA detector at 205 nm.

### 6.2.2 H-Cell

The used H-cells (Fischer Labortechnik, Frankfurt am Main, Germany) consisted of two 100 ml glass bottles with three side ports each, connected via a glass bridge to form the shape of an H. A proton exchange membrane (4.91\*10<sup>-4</sup> m<sup>2</sup> Nafion117, DuPont, Wilmington, USA) was inserted in the bridge if not stated otherwise. Graphite rods (Metallpulver 24, St. Augustin, Germany) with a geometrical surface area of 0.00118 m<sup>2</sup> were used as anode and cathode, respectively, if not stated otherwise. The electrical contact to the electrodes was done via a titanium wire (0.5 mm, Goodfellow, Bad Nauheim, Germany) which was pierced through a butyl septum (Glasgerätebau Ochs, Bovenden, Germany) closing the main opening of each chamber. The working chamber was equipped with an Ag/AgCl reference via one of the side ports. Gassing of the working chamber was done using a cannula pierced through a septum in one of the side ports of the working chamber (0.6\*80 mm needle, gassing rate

0.5 ml\*min<sup>-1</sup> if not stated otherwise), another cannula (0.6\*30 mm needle) served as gas outlet. The counter chamber was equipped with one cannula (0.6\*30 mm needle) to avoid pressurizing by gas evolution at the counter electrode. The three electrodes were connected to a potentiostat using metal alligator clips, setting the potential of -1.1 V between the working electrode and the reference electrode. The H-cells were placed in an incubator hood for temperature control. The liquid volume in both chambers was 100 ml with 47 ml headspace remaining. pH and medium conductivity of both chambers and optical density of the working chamber were measured prior to the and after the experiment. The terminal voltage was controlled daily.

### 6.2.3 Bubble Column Reactor

The working chamber of the newly designed bubble column reactor is made of a PEEK-pipe with an inner diameter of 85 mm and an outer diameter of 126 mm (Figure 44 A). PEEK is autoclavable, non-conductive and mechanically and chemically stable. The lid of the reactor was a stainless steel plate (DASGIP® headplate no. 78107157) with several ports, i.e. seven Pg 13.5 ports, one D6 port and one M30 port in the center of the plate. The head plate was installed on the reactor by an aluminum ring. The M30 port in the center of the lid was closed with a butylseptum (Glasgerätebau Ochs, Bovenden, Germany, septum for GL45). A titanium wire (0.5 mm diameter, Goodfellow, Bad Nauheim, Germany) was pierced through this septum to contact the working electrode, ensuring electrical isolation from the reactor lid. The Pg 13.5 ports were used for pH probe, reference, sample pipe and gas outlet (Figure 44 B). The temperature sensor was placed in the D6 port. The outer wall of the cathode chamber included four windows of the same size (43\*70mm) (Figure 44 C), into which the membranes were placed. It was possible to vary the membrane area by closing windows with silicon plates instead of ion exchange membrane. In front of each window, a counter electrode out of carbon fabric (Kynol, Hamburg, Germany, ACC5092-15, size 15\*10 cm) was placed if not stated otherwise. The counter electrodes could be contacted via a titanium wire, a stainless steel wire or a platinum wire (0.5 mm diameter each, Goodfellow, Bad Nauheim, Germany), the single electrodes were contacted via a carbon fabric bridge between the units (Figure 44 D). Two pipe connectors on the outer wall allowed for the connection of a pipe for an external loop operation mode.

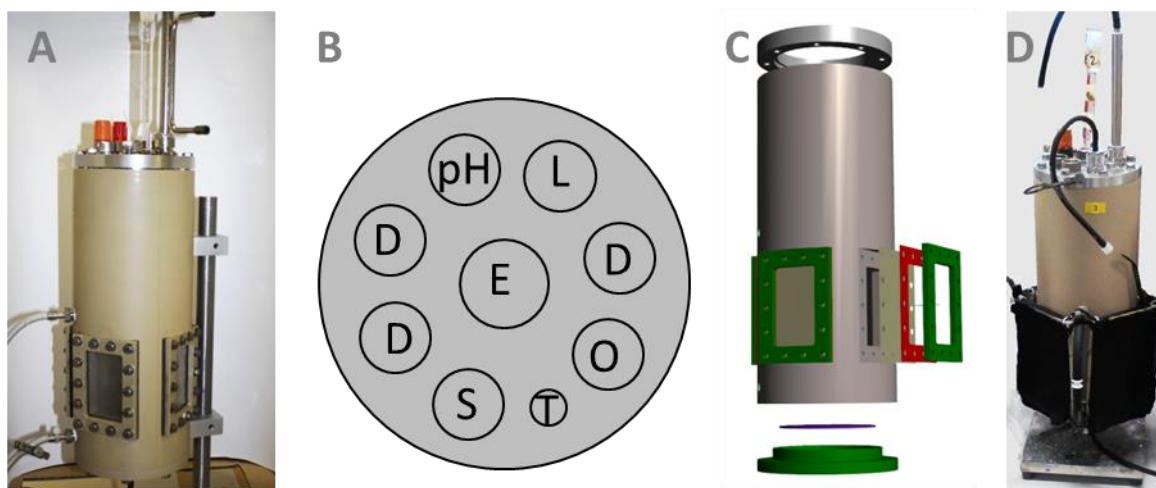


**Figure 44: Bubble column reactor side views and head plate**

A) Side view of the bubble column reactor; B) Scheme of head plate of the reactor with inserted pH electrodes (pH), Luggin capillary (L), dummy plugs (D), off gas (O), temperature sensor (T) and sample port (S); C) Explosion sketch of the reactor with scheme of the membrane window; D) Reactor with counter electrodes wrapped around the working chamber.

Close to the bottom, a PTFE sparger plate with perforations was inserted to ensure small bubbles in bubble column mode (Figure 45). The bottom itself was also made of PEEK, holding a port for the gas pipe (Figure 45). The reactor was 300 mm high, whereas the liquid level was at 160 mm (145 mm from the PTFE plate) when filled up to 1 l; 0.79 liter headspace volume remained. The counter chamber was filled with 10 liter 0.1 M phosphate buffer pH 6.8 and surrounded by a heating jacket holding 5.5 liter of water. To ensure even heat distribution, the water circulated driven by a peristaltic pump (Bioengineering, fixed Speed 50 rpm) with  $88.89 \pm 4.00 \text{ ml} \cdot \text{min}^{-1}$ ; the temperature sensor was placed in the counter chamber.

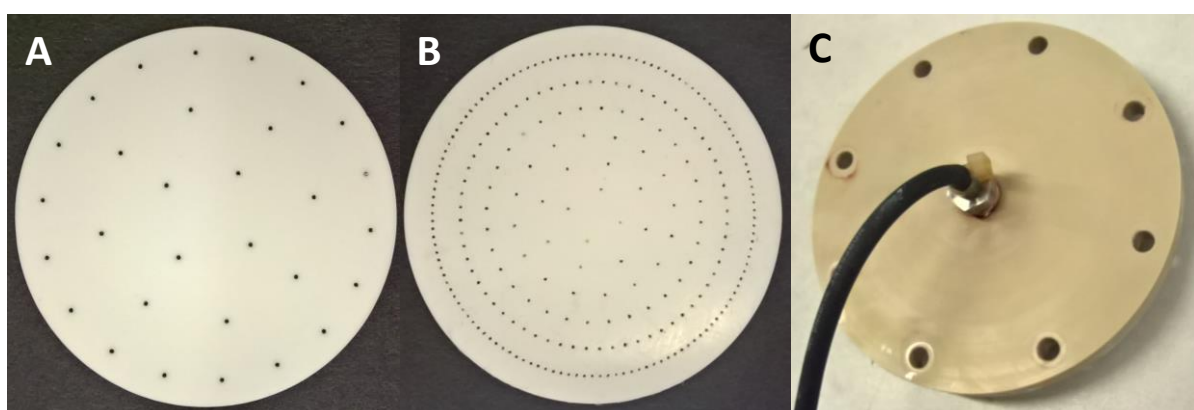


**Figure 45: PTFE spargers and bottom of bubble column reactor**

A) Sparger plate with 1 mm pores (Sparger 1); B) Sparger plate with 0.7 mm pores (Sparger 2); C) Bottom lid with gassing tube.

The possible modes of operation were the bubble column mode and the external loop mode. For the bubble column mode, the two connectors at the side of the reactor were connected with a short tube. For the external loop mode, the two connectors at the side were connected to a longer tube clamped into a peristaltic pump (Ismatech Ecoline, Cole-Parmer GmbH; Wertheim, Germany). The pump rate was set to the setpoint of 30, which was equal to  $47.22 \pm 1.40 \text{ ml} \cdot \text{min}^{-1}$ . The reactor was gassed through from the bottom with  $30 \text{ ml} \cdot \text{min}^{-1}$ .

An exhaust gas pipe at the top of the reactor allowed for sampling of gas and safe dissipation of off-gas into a fume hood. The exhaust gas pipe could also be cooled to avoid evaporation of medium. To test the effect of gassing through, the reactor could also be operated without gassing and dummy plug instead of an exhaust gas outlet (closed mode). For characterization of the electrical field, it was possible to replace the stainless steel lid by a stainless steel mesh (open setup).

The reactors were operated in a three-electrode mode. Terminal voltage, temperature and pH of both chambers were monitored continuously; samples for optical density measurement and medium conductivity were taken daily.

#### 6.2.4 Modified Stirred Tank Reactor

A bioelectrochemical stirred tank reactor was developed by Krieg et al. (Krieg et al., 2018a), inserting an installation holding electrodes into a bioreactor. The used bioreactor was a 3 liter bioengineering K4 glass fermenter, equipped with a stirrer with two 6-blade Rushton turbines, a sparger for gassing, gas outlet, temperature control via sensor, heating and cooling stick, sample line, overpressure valve, stainless steel lid with several ports and pH sensor. The PEEK inlay for bioelectrochemical processes consisted of a counter chamber and a frame for the working electrode. The counter chamber was filled with 200 ml of electrolyte and held two ports for gas and medium inlet and outlet, a membrane window of 5 cm\*5 cm (0.0025 m<sup>2</sup>) and a port for the electrode contact. The counter electrode was a piece of carbon fabric, 12 cm \* 12 cm (0.0144 m<sup>2</sup>) rolled up to form a cylinder.

The frame for the working electrode held a cloth-type electrode of 12 cm \* 12 cm, of which 9 cm \* 12 cm were accessible after clamping it between the frames. Additionally, the stainless steel lid of the bioreactor was equipped with two nonconductive ports for the electrode contact and a port for the reference electrode. After the assembly, the remaining working volume is 2 liter for liquid medium and 0.42 liter of headspace (Figure 46).

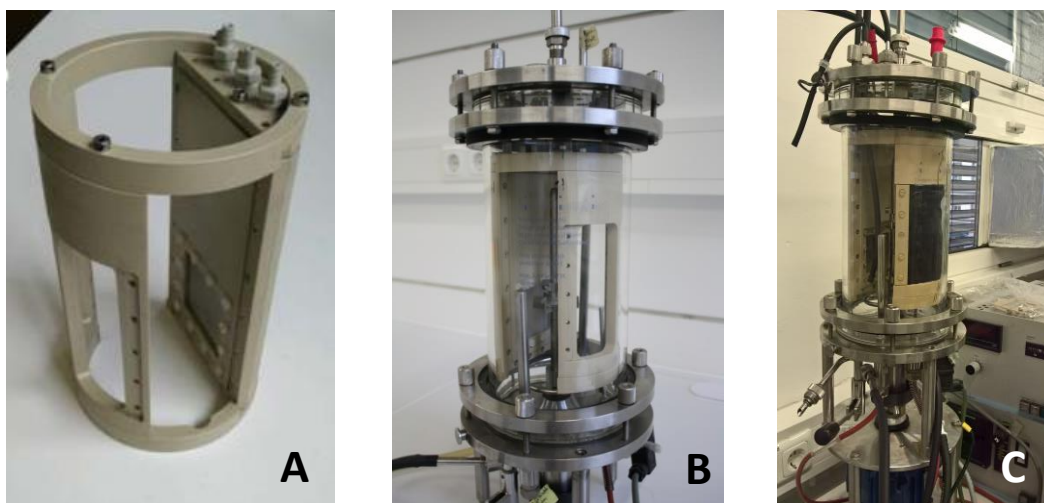


**Figure 46: Bioelectrochemical stirred tank reactor**

A) Installation holding electrodes and membrane; B) Installation inserted into 3-liter-stirred tank reactor; C) Reactor equipped with installation holding electrodes.

The temperature was regulated via a bioengineering module, which started the heating stick if the temperature measured by the temperature sensor was below the set temperature. If the measured temperature was above the setpoint, a valve from the refrigerated circulating bath to the cooling stick opened, resulting in the circulation of 19° C cool water through the cooling stick. The stirrer was set to 100 rpm throughout the experiments. pH was measured continuously in the working chamber. The terminal voltage and medium conductivity and optical density of the working chamber were measured daily.

## 6.3 Reactor Characterization

### 6.3.1 Electrochemical Characterization

#### 6.3.1.1 Preexplorative Chronoamperometric Measurement

Abiotic, chronoamperometric measurements in bubble column reactors were used to examine start up and polarization time, temperature control and abiotic pH effects. Each chronoamperometric measurement lasted 90 hours. Since the main goal was the production of methane, the starting point conditions for the optimization of the methane production were used, namely -900 mV vs. Ag/AgCl at 35 °C with a gassing rate of 30 ml\*min<sup>-1</sup> N<sub>2</sub>/CO<sub>2</sub> 80/20 (v/v) and MES medium. In the bubble column reactor, several electrodes were tested with and without external loop. Table 24 gives an overview of the chronoamperometric measurements.

Table 24: Abiotic chronoamperometric experiments

Reactor	Cathode	Membrane	Potential	Medium
Bubble column	Graphite rod, 0.0069 m <sup>2</sup>	Nafion, 0.012 m <sup>2</sup>	-900mV vs. Ag/AgCl	MES
Bubble column	RVC foam, 0.124 m <sup>2</sup>	Nafion, 0.012 m <sup>2</sup>	-900mV vs. Ag/AgCl	MES
Bubble column	Carbon fabric, 0.0041 m <sup>2</sup>	Nafion, 0.012 m <sup>2</sup>	-900mV vs. Ag/AgCl	MES
Bubble column	Carbon laying, 0.0057 m <sup>2</sup>	Nafion, 0.012 m <sup>2</sup>	-900mV vs. Ag/AgCl	MES
Bubble column	Carbon granulate, 150 g, contact with graphite rod	Nafion, 0.012 m <sup>2</sup>	-900mV vs. Ag/AgCl	MES
External loop	Graphite rod, 0.0069 m <sup>2</sup>	Nafion, 0.012 m <sup>2</sup>	-900mV vs. Ag/AgCl	MES
External loop	RVC foam, 0.124 m <sup>2</sup>	Nafion, 0.012 m <sup>2</sup>	-900mV vs. Ag/AgCl	MES
External loop	Carbon fabric, 0.0041 m <sup>2</sup>	Nafion, 0.012 m <sup>2</sup>	-900mV vs. Ag/AgCl	MES

Similar chronoamperometric measurements were carried out at -1.1 V vs. Ag/AgCl, CO<sub>2</sub> as in-gas and a carbon laying cathode in all three tested reactors; apart from that, an abiotic control experiment was done for all tested parameters if not stated otherwise.

#### 6.3.1.2 Electrochemical Calculations

The electrical current was measured during the electrochemical experiments. To gain comparable information, the current density  $i$  was calculated based on the geometrical working electrode surface area. For a more precise comparison, the total surface area of the electrode measured via physisorption could be used (Sharma et al., 2014).

From the electrical current, the electron transfer rate in mol\*s<sup>-1</sup> was calculated using elementary charge  $e$  (1.602\*10<sup>-19</sup>As) and Avogadro constant  $N_A$  (6.022\*10<sup>23</sup>mol<sup>-1</sup>) (Equation 13).

$$r_{e,I} = \frac{I}{e * N_A} \quad \text{Equation 13}$$

The Wagner number is a dimensionless number also important for Scale-Up. It was calculated for an electrochemical system using Equation 14 (Tafel's approach (Andricacos et al., 1999)).

$$Wa_T = \frac{\kappa * b}{L * |i|} \quad \text{Equation 14}$$

The parameter b is defined as the Tafel slope, which was gained from the Tafel plot of the system (Bhandari et al., 2012), an example for the bubble column system with a graphite rod electrode is given in Figure 47.

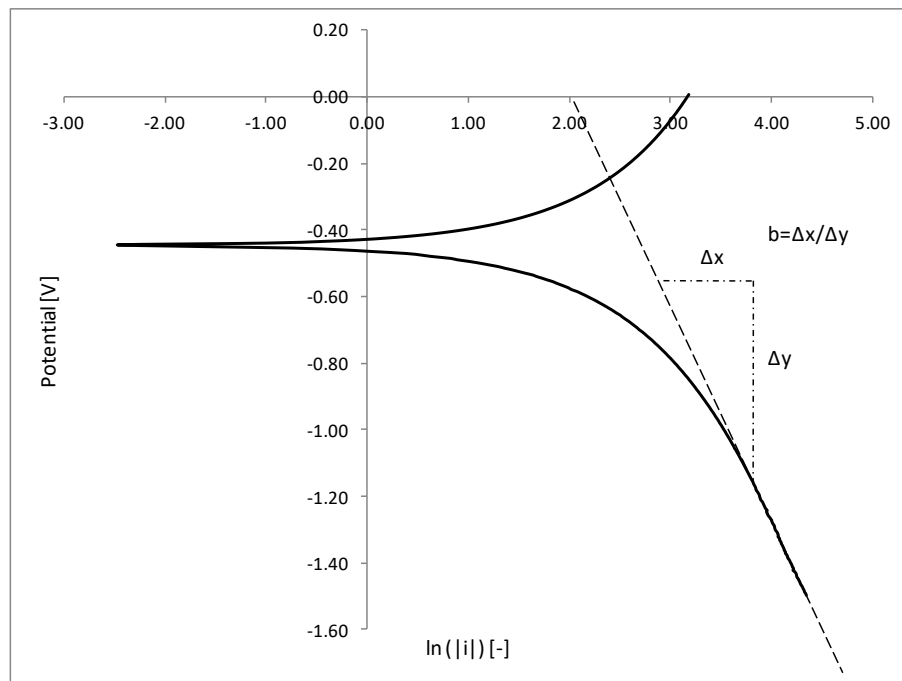


**Figure 47: Tafel plot obtained from CV in bubble column reactor with graphite rod electrode**  
The dashed line fits the slope of the lower arm of the curve and is used to calculate the Tafel slope b.

The characteristic length L of the system was the electrode distance, the absolute value of the current density was estimated based on the average current after polarization divided by the geometric electrode surface. In general, systems with an evenly distributed electrical field around the electrode show high Wagner numbers (>1 to 10). Smaller numbers (<1) are related to a non-uniform current distribution of the electrical field. Scaling up an electrochemical system, the Wagner number should be kept constant (Sulaymon and Abbar, 2012).

The electrical power  $P_{EL}$  was calculated as the product of system voltage and resulting current (Equation 15).

$$P_{EL} = U_T * I$$

Equation 15

### 6.3.1.3 Cell Resistance and Electrical Field

Each BES system shows a specific cell resistance, which comprises ohmic resistance (membrane resistance, electrolyte resistance, electrode resistance) and charge transfer resistance of the electrodes (He and Mansfeld, 2009). To measure the system resistance of the four different reactors tested, a current of 5 mA was applied to the systems and the terminal voltage was measured. To examine the quantities of the individual resistances of the different system parts the potential between different positions (Figure 48) in the bubble column reactor were measured using one or two reference electrodes and a multimeter at an applied current of 5 mA. This method was used because it was assumed that the ohmic resistances are dominant in the abiotic reactors (He and Mansfeld, 2009).

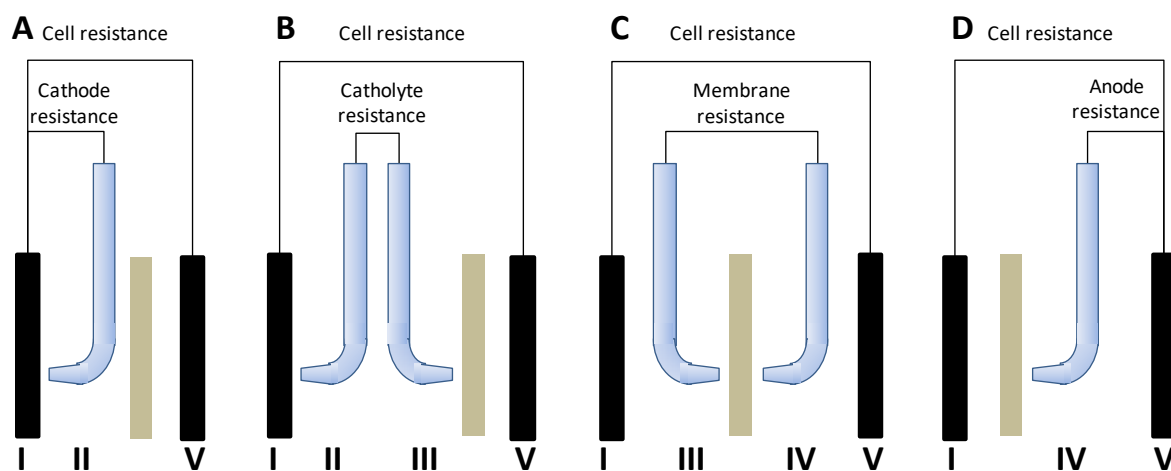


**Figure 48: Measuring points for resistances**

A) Measurement of cell resistance between I (cathode) and V (anode) and cathode resistance between I and II (reference electrode); B) Measurement of catholyte resistance between two reference electrodes II and III; C) Measurement of membrane resistance between two reference electrodes III and IV (membrane in beige); D) Measurement of anode resistance between IV and V.

The resistance between those two points was calculated from Equation 16.

$$R_x = \frac{U_{1,2}}{I_{app}} \quad \text{Equation 16}$$

The electrical field of the bubble column reactor was examined during the late phase of chronoamperometric measurements in an open reactor (without lid). A second reference was placed at various positions within the reactor, the potential between the second reference and the working electrode was measured. This gave lines of equal potentials within the reactor; the electrical flux lines are rectangular to those equipotential lines.

### 6.3.2 Physical Characterization

#### 6.3.2.1 Gassing

A correlation between CO<sub>2</sub> and pH was determined by gassing the reactor with different partial pressures of CO<sub>2</sub> in the in-gas while monitoring the pH. Via a calibration curve (Figure 49A), the amount of dissolved CO<sub>2</sub> can be calculated from the medium pH, as long as no electrical potential is applied which can potentially disturb the pH measurement and no biological processes change the pH, overlying the pH change caused by the CO<sub>2</sub> concentration.

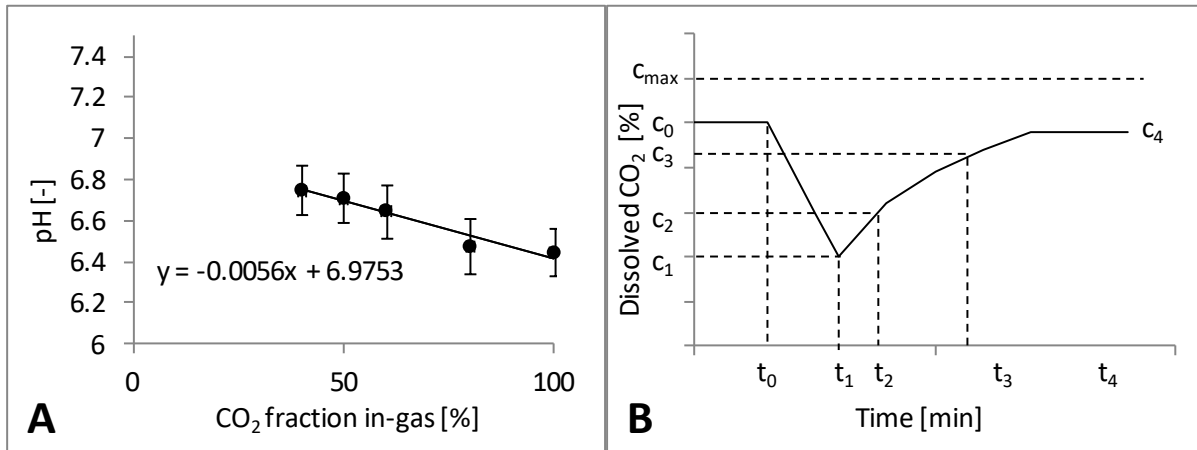


Figure 49: Dynamic method for  $k_La$  measurement

A) Calibration curve pH vs. CO<sub>2</sub> fraction of the in-gas; B) Dynamic measurement process; Measurement starts with the initial dissolved CO<sub>2</sub> concentration  $c_0$ . At timepoint  $t_0$ , the gassing is switched to N<sub>2</sub> up to timepoint  $t_1$ , where the dissolved CO<sub>2</sub> concentration dropped to  $c_1$ . At timepoint  $t_1$ , the gassing is switched back to CO<sub>2</sub>, so the dissolved CO<sub>2</sub> concentration recovers ( $c_2$  at timepoint  $t_2$ ,  $c_3$  at timepoint  $t_3$ ) and reaches a stable level again ( $c_4$ ) at timepoint  $t_4$ .

The  $k_La$  value was estimated using the dynamic method. The medium was gassed with CO<sub>2</sub> prior to the measurement. To start the experiment, gassing was switched to N<sub>2</sub>, monitoring the decrease of dissolved CO<sub>2</sub> in the medium over time according to the pH. After 10 minutes, the inlet gas is switched to CO<sub>2</sub> again, and the increase of dissolved CO<sub>2</sub> is monitored over 20 minutes. The procedure is done using different gassing rates of 30, 60 and 90 ml\*min<sup>-1</sup> for both, N<sub>2</sub> and CO<sub>2</sub> inlet. The  $k_La$  can be calculated from Equation 17 according to Figure 49B, whereas the CO<sub>2</sub> partial pressure can be used instead of the CO<sub>2</sub> concentration according to Henry's Law (Hass and Pörtner, 2011) (Sander, 2015).

$$k_La = \frac{\ln\left(\frac{c_{CO_2}(t_4) - c_{CO_2}(t_2)}{c_{CO_2}(t_4) - c_{CO_2}(t_3)}\right)}{t_3 - t_2}$$

Equation 17

The  $k_L a$  measurement has to be done prior to inoculation and potential application.

Additionally, the gas hold up of the reactor was measured at three different gassing rates (30, 60, 90 ml\*min<sup>-1</sup>) by measurement of the liquid level. The gas hold up is defined as the percentage of gas volume in the total working volume and can be used to estimate the interfacial area between gas and liquid in the system (Shah et al., 1982). The amount of gas in the medium can be calculated using Equation 18, the gas hold up using Equation 19, and a rough estimation of the interfacial area based on the mean bubble diameter using Equation 20.

$$V_{GH} = (A_R * h_{LL}) - (A_R * h_{LL,g}) \quad \text{Equation 18}$$

$$\epsilon_{GH} = \frac{V_{GH}}{A_R * h_{LL,g}} \quad \text{Equation 19}$$

$$A_{GL} = \frac{3 * V_{GH}}{D_B} \quad \text{Equation 20}$$

The superficial gas velocity in the reactor was calculated using the gas stream and the cross sectional area of the reactor (Equation 21, (Takors, 2014)); this value is needed to calculate the hydraulic residence time of the gas (Equation 22).

$$u_G = \frac{\dot{V}_G}{A_R} \quad \text{Equation 21}$$

$$t_{r,G} = \frac{h_{LL,g}}{u_G} \quad \text{Equation 22}$$

The flow regime was estimated using the superficial gas velocity and the reactor diameter (Figure 50A and B), modified from (Shah et al., 1982)).

Three more dimensionless numbers were calculated to further characterize the gassing (Table 25) (Shah et al., 1982); (Montes et al., 1999).

Table 25: Dimensionless numbers for bubble columns

Bond number 
$$Bd = \frac{\rho_L * g * D_B^2}{4\sigma}$$
 Equation 23

Reynolds number (Bubble column) 
$$Re_B = \frac{\rho_L * u_G * D_B}{\mu_{vis}}$$
 Equation 24

Weber number 
$$We = \frac{\rho_L * u_B^2 * D_B}{2\sigma}$$
 Equation 25

With Bond number and Weber number, a diagram (Figure 50C) shows whether the bubble size within the reactor is stable. For the calculation, the bubble diameter and the bubble rise velocity is required. These parameters were determined by filming the bubble ascend through a membrane window and evaluated using the software “imageJ” for determining the bubble size (average of 10 bubbles, 9 frames evaluated for each bubble) and the ascend velocity.

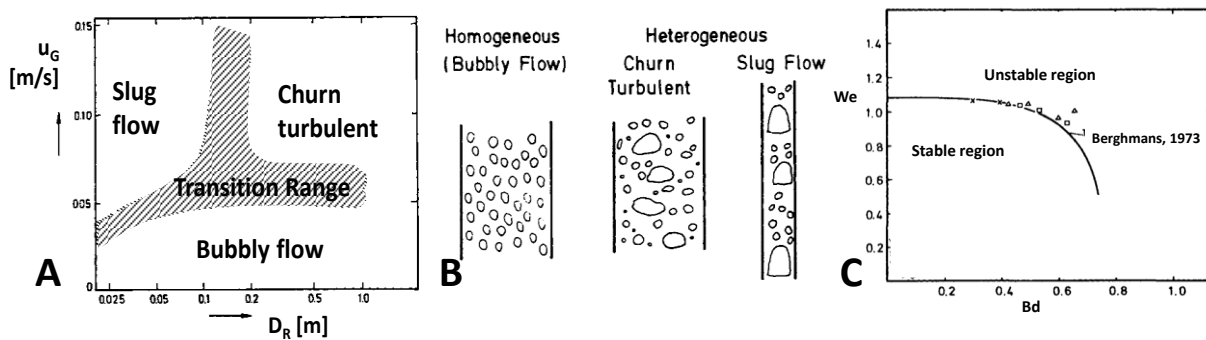


Figure 50: Flow regimes in bubble column reactors

A) Flow regimes can be estimated using the superficial gas velocity  $u_G$  and the reactor diameter  $D_R$  (Shah et al., 1982); B) Different flow regimes show different bubble distribution within the reactor (Shah et al., 1982). C) Stability of bubble size determined based on Weber and Bond number (modified from (Shah et al., 1982))

In bubble columns, the power input caused by gassing is given by Equation 26 (Chisti and Moo-Young, 1989).

$$P_G = V_R * \rho_L * g * u_G$$
 Equation 26

### 6.3.2.2 Stirring

In the stirred tank reactor, a stirrer ensures better mixing conditions. Several parameters are necessary to compare or Scale-Up stirred tank reactors (Table 26 (Takors, 2014); (Hass and Pörtner, 2011)).

Table 26: Parameters of stirred tank reactors

Stirrer tip velocity	$v_{ST} = \pi * n_S * D_S$	Equation 27
----------------------	----------------------------	-------------

Reynolds number (Stirrer)	$Re_S = \frac{\rho * n_S * D_S^2}{\mu_{vis}}$	Equation 28
---------------------------	---	-------------

Newton number	$Ne = \frac{P_S}{\rho * n_S^3 * D_S^5}$	Equation 29
---------------	---	-------------

Power input (Stirrer)	$P_S = Ne * \rho * n_S^3 * D_S^5$	Equation 30
-----------------------	-----------------------------------	-------------

Power input (Gassing in STRs)	$P_{G,S} = 0,1P_S * \left(\frac{n_S^2 D_S^4}{g * h_{RT} * V_R^{0,667}}\right)^{-0,2} * \left(\frac{V_G}{n_S * V_R}\right)^{-0,25}$	Equation 31
-------------------------------	--	-------------

The Newton number was determined according to a Newton-Reynolds diagram (Figure 51) after calculation of the Reynolds number. Afterwards, the Newton number was used to calculate the power input caused by the stirrer (Equation 30). The power input of gassing was given by Equation 31, different from the power input of the gassing in a bubble column reactor.

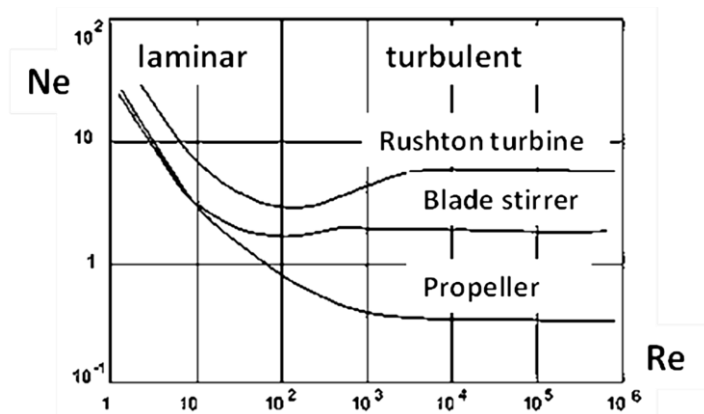


Figure 51: Newton-Reynolds diagram for different stirrer types

Different stirrer types show different Newton number dependencies on the Reynolds number under laminar and turbulent flow conditions (adapted from (Chmiel, 2011)).

### 6.3.2.3 Heat Loss

For the calculation of an overall energy consumption of the process, it was necessary to gain information about the power demand for system heating. For the bubble column and the stirred tank reactor, heating was done by a heating stick, either installed in a heating jacket (bubble column) or directly in the reactor (STR). Reliable information on the on/off times and the power demand of the heating stick could not be gained. Therefore, the waste heat of the systems was determined; it was assumed that the waste heat and the heat added to the system by the heating stick are the same, if a stable temperature is retained within the system. Figure 52 shows where system heat of the bubble column reactor was lost. Each of these heat streams was calculated separately. For the stirred tank, only four streams occurred, the heat loss through the bottom, the lid and the wall and the heat loss due to the heating of the off-gas stream. The calculations were simplified by leaving out the effects of measuring equipment inserted in the lids.

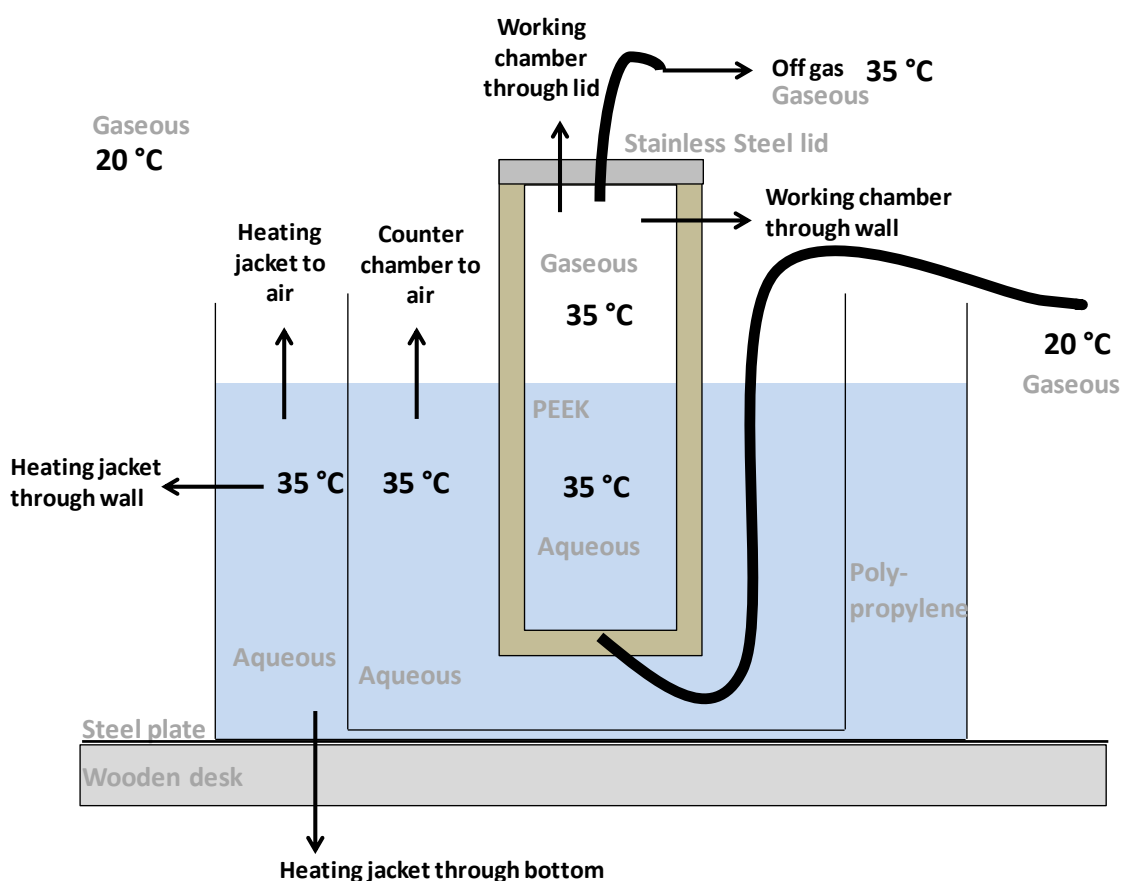


Figure 52: Heat loss of the bubble column system

7 heat loss streams identified (marked as black arrows) through the reactor walls and from liquid media to surrounding air. The temperature within the reactor and of all liquid media is 35 °C and of the environment and the in-gas 20 °C. Materials are given in grey.

With Equation 32 - Equation 34, the heat loss through a wall or plate was calculated, assuming a constant temperature of the aqueous and gaseous phase. This was possible because of the heat control of the reactor and the laboratory (VDI, 2003).

$$\dot{Q}_{Wall} = \frac{A * \lambda * (T_1 - T_2)}{\delta} \quad \text{Equation 32}$$

$$\dot{Q}_{Lid} = \frac{A * \lambda * (T_1 - T_2)}{\delta} \quad \text{Equation 33}$$

$$\dot{Q}_{Bottom} = \frac{A * (T_1 - T_2)}{\sum \frac{\delta}{\lambda}} \quad \text{Equation 34}$$

Table 27 shows the parameters for the different heat loss streams through a wall in bubble column and stirred tank reactor (VDI, 2003).

Table 27: Variables for the calculation of heat losses through reactor walls

	Inner phase with T1	Wall material with $\lambda$ and thickness $\delta$ and surface A	Outer phase with T2
BC: Heating Jacket through wall	Water, 308.15 K	Polypropylene, 0.22 W*m <sup>-1</sup> *K <sup>-1</sup> , 0.002 m, 0.265 m <sup>2</sup>	Air, 293.15 K
BC: Heating jacket trough bottom	Water, 308.15 K	Polypropylene, 0.22 W*m <sup>-1</sup> *K <sup>-1</sup> , 0.002 m Stainless steel, 57 W*m <sup>-1</sup> *K <sup>-1</sup> , 0.003 m Wood, 0.12 W*m <sup>-1</sup> *K <sup>-1</sup> , 0.022 m, 0.084 m <sup>2</sup>	Air, 293.15 K
BC: Working chamber through wall	N <sub>2</sub> and/or CO <sub>2</sub> 308.15 K	PEEK, 0.25 W*m <sup>-1</sup> *K <sup>-1</sup> , 0.0205 m, 0.044 m <sup>2</sup>	Air, 293.15 K
BC: Working chamber through lid	N <sub>2</sub> and/or CO <sub>2</sub> 308.15 K	Stainless steel, 57 W*m <sup>-1</sup> *K <sup>-1</sup> , 0.009 m, 0.0057 m <sup>2</sup>	Air, 293.15 K
STR: Through wall	Aqueous medium, 308.15 K	Glass, 1.05 W*m <sup>-1</sup> *K <sup>-1</sup> , 0,004 m, 0.122 m <sup>2</sup>	Air, 293.15 K
STR: Through lid	Aqueous medium, 308.15 K	Stainless steel, 57 W*m <sup>-1</sup> *K <sup>-1</sup> , 0.011 m, 0.0133 m <sup>2</sup>	Air, 293.15 K
STR: Through bottom	Aqueous medium, 308.15 K	Stainless steel, 57 W*m <sup>-1</sup> *K <sup>-1</sup> , 0.011 m, 0.0133 m <sup>2</sup>	Air, 293.15 K

Equation 35 determined the waste heat released from a surface of a liquid to the surrounding air in the bubble column reactor; the overall heat transfer coefficient  $\alpha_{1,2}$  was assumed as  $5 \text{ W}\cdot\text{m}^{-1}\cdot\text{K}^{-1}$  (for resting or slow moving fluids, a range from  $2\text{-}10 \text{ W}\cdot\text{m}^{-1}\cdot\text{K}^{-1}$  was suggested in literature (VDI, 2003)). The exchange surface area was  $0.073\text{m}^2$  and the temperature difference  $15 \text{ K}$ .

$$\dot{Q}_{Air} = \alpha_{1,2} * A * (T_1 - T_2) \quad \text{Equation 35}$$

Equation 36 led to the heat loss by heating up the gas stream from  $20 \text{ }^\circ\text{C}$  (surrounding environment) to  $35 \text{ }^\circ\text{C}$  (system temperature), whereas the isobaric heat capacity of  $\text{CO}_2$  is  $0,85 \text{ kJ}\cdot\text{kg}^{-1}\cdot\text{K}^{-1}$  (VDI, 2003).

$$\dot{Q}_{Gas} = \frac{\dot{V}_G * \rho_G * c_{p,CO_2} * (T_1 - T_2)}{0.001 \frac{\text{kJ}}{\text{J}}} \quad \text{Equation 36}$$

The total power which is necessary to maintain a constant temperature level was estimated by summing up the heat losses (Equation 37). The heat production by the microbial metabolism is neglected here due to the low optical density and the low productivity of methanogens.

$$P_H = \dot{Q}_{Wall} + \dot{Q}_{Lid} + \dot{Q}_{Bottom} + \dot{Q}_{Air} + \dot{Q}_{Gas} \quad \text{Equation 37}$$

## 6.4 Electrode Materials

Five different electrode materials were tested as cathodes for MES (Figure 53). These were, in particular, graphite rod, RVC foam, carbon fabric, carbon laying and glassy carbon granulate. The materials were chosen because of their low costs compared to precious metal electrodes and, in case of the graphite rod and the carbon fabric, due to their wide spread use in bioelectrochemistry. The surface structures of the carbon based materials was significantly different, as shown by the scanning electron microscopy images for graphite rod, RVC foam, carbon fabric and carbon laying (Figure 54). It was shown that the polarization resistances of carbon electrodes are relatively low, making them an interesting alternative to metal electrodes (He and Mansfeld, 2009; Logan, 2010b). After each experiment, the electrodes were placed in a citric acid solution to dissolve salt residues on the surface and afterwards rinsed with desalinated water prior to the next use. All electrodes were contacted with titanium wire (0.5 mm, Goodfellow, Bad Nauheim, Germany) which was wrapped around the upper part (app. 1 cm) of the electrodes.



**Figure 53: Different electrode materials**

From left to right: graphite rod, RVC foam, carbon fabric, carbon granulate and carbon laying

The graphite rods used (Metallpulver 24, St. Augustin, Germany) in the bubble column reactors were 1 cm in diameter and 15 cm in length; for the H-cells, graphite rods with 0.5 cm diameter and 7.5 cm length were used. The relatively brittle RVC foam (45 ppi (pores per inch), ERG Aerospace Corp., Oakland, USA) was utilized in form of 1 cm \* 2 cm \* 20 cm rectangular sticks. The activated carbon fabric (ACC5092-15, Kynol, Hamburg, Germany) was cut into 12 cm\*11.5 cm rectangular pieces and each piece was rolled into a rod, giving a cylindrical shape with 12 cm length and 1.1 cm diameter. The roll was fixed with cable ties on both ends. As pretreatment, carbon fabric was either autoclaved or heated up to 80 °C for one hour prior to use. The carbon laying (HP-T450C, HP textiles, Schapen, Germany) was also cut into 12 cm\* 11.5 cm rectangular pieces, rolled to rods of 12 cm length and 1.5 cm diameter and fixed at both ends with cable ties, similar to the carbon fabric. The glassy carbon granulate (Sigradur G granulate, 2-3.15 mm particle size, HTW Germany, Thierhaupten, Germany) was placed directly on the PTFE plate at the bottom of the reactor and turned into a fluidized bed as soon as the gassing started. It was contacted via a graphite rod 5 mm in diameter and 28 cm long. The graphite rod was placed in the middle of the granulate bed. The glassy carbon was autoclaved and washed with desalinated water three times as cleaning procedure.

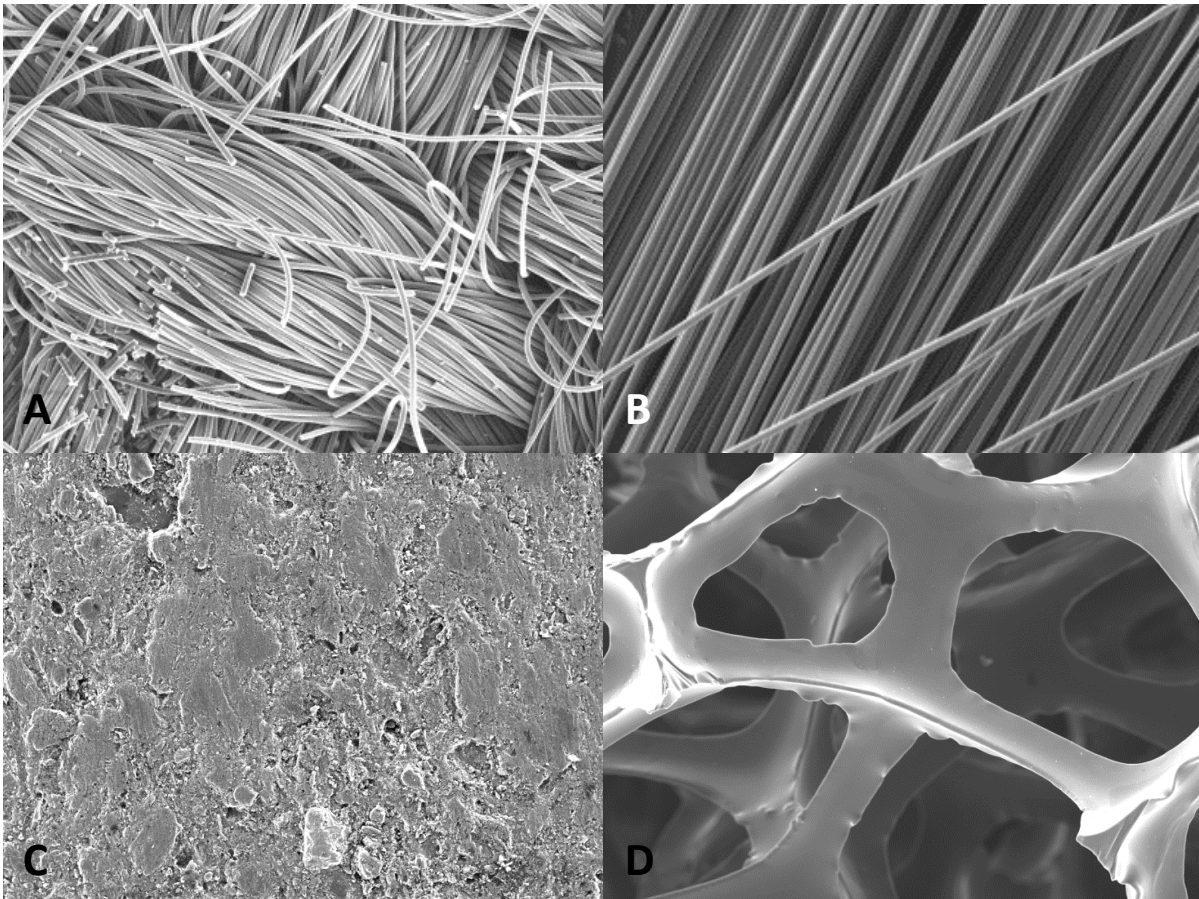


Figure 54: Scanning electron microscopy images of different electrodes, 250x magnification  
 A) Carbon fabric; B) Carbon laying; C) Graphite rod; D) RVC foam.

The internal resistance of the electrodes was measured with a multimeter (OWON B35, Fujian Lilliput Optoelectronics Technology Co, Zhangzhou, China), leading to the total resistance of the measured electrode. The specific resistance was then calculated (Equation 38).

$$R_{spec} = \frac{R * A_{CS,E}}{l_E} \quad \text{Equation 38}$$

The contact resistance was measured the same way; the electrode with the contacting wire was measured, the measured resistance minus the electrode and the wire resistance gave the contact resistance Table 28 gives an overview of the properties of the five electrode materials..

Table 28: Electrode material properties

	<b>Graphite rod</b>	<b>RVC foam</b>	<b>Carbon fabric</b>	<b>Carbon Granulate</b>	<b>Carbon laying</b>
Material	Graphite	Carbon	Activated carbon	Glassy carbon	Carbon
Density [kg*m <sup>-3</sup> ]	1595.71	46.84	283.33	856.80	382.98
Density of bulk material [kg*m <sup>-3</sup> ]	2279.58	1561.42		1420.00	
Porosity [-]	0.30	0.97		0 (particle) 0.397 (bed porosity)	
Specific surface area [m <sup>2</sup> *g <sup>-1</sup> ] (measured by BET)	25.231	4.196	1635.293	0.0017 *	0.888

\*Calculated based on assumption: Spheres with 2 mm diameter; below measurement limit.

The charge transfer resistance was estimated by electrical impedance spectroscopy (EIS) in a three electrode mode. Alternating frequencies from 100000 to 0.01 Hz were applied to the electrode material with small signal amplitude of 25 mV to not alter the system performance. Similar ranges were found in literature (Dewan et al., 2008; He and Mansfeld, 2009). The resulting resistance was measured. Using a Software (Echem Analyst), two plots could be obtained from the EIS. The Nyquist plot usually showed a semi-circle or parts of a semi-circle, which was used to estimate the charge transfer resistance, which equals the diameter of this circle (He and Mansfeld, 2009). The Bode plot could be used to estimate the electrolyte resistance, which was detected at high frequencies (He and Mansfeld, 2009).

The polarization time of each electrode until a stable current after potential application established was obtained from the chronoamperometric measurements. During the chronoamperometric measurement, the abiotic H<sub>2</sub> production was obtained from gas samples analyzed by gas chromatography. Related to this, cyclic voltammetry (CV) was applied to detect the necessary potential for H<sub>2</sub> generation at the cathode. During this measurement, potentials from -1.5 to 1 V were linearly applied to the system with a scan rate of 0.05 V\*s<sup>-1</sup>, describing a cyclic form (from -1.5 to 1 to -1.5 to 1 V and so on). Measurement of the current resulted in a cyclic voltammogram. In this voltammogram, the start of

reactions like H<sub>2</sub> production was indicated by a rapid slope of the current answer. CV was performed prior to and after chronoamperometric measurements. If the voltammogram changed in shape, the electrode surface did changed over time, e.g. by oxidation or reduction of modified surface groups.

## 6.5 Membranes

Three different membranes were tested for bioelectromethanogenesis. These are a Fumasep®FAS-PET-130 anion exchange membrane (Fumatech, Bietigheim-Bissingen; Germany), a Fumasep®FKS-PET-130 cation exchange membrane (Fumatech, Bietigheim-Bissingen; Germany) and a Nafion 117 proton exchange membrane (DuPont, Wilmington, USA). The proton exchange membrane was activated before usage and regularly after experiments to maintain the performance. The membrane was boiled in 3% H<sub>2</sub>O<sub>2</sub> in ddH<sub>2</sub>O for 1 h, then washed, boiled in 0.5 M H<sub>2</sub>SO<sub>4</sub> in ddH<sub>2</sub>O for 1.5 h, washed again and boiled in ddH<sub>2</sub>O for 1 h. The Fumasep membranes were rinsed with MES medium before the first use. All membranes were stored in ddH<sub>2</sub>O at 4 °C if not in use. All membranes were autoclaved prior to each biotic experiments.

Prior to bioelectromethanogenesis experiments, the different electrical resistances of the membranes were measured. For this purpose, each membrane was inserted into an H-cell, both chambers were filled with 100 ml of MES medium and N<sub>2</sub>/CO<sub>2</sub> 80/20 gas atmosphere to 1 bar. An electrical current of 1 mA was applied to the H-cells and the voltage was measured, giving the resistance of the whole system (Equation 16). The membrane resistances were calculated when repeating the measurement in an H-cell without membrane as the difference between the two system resistances.

## 6.6 Bioelectromethanogenesis

### 6.6.1 *Methanococcus maripaludis*

*M. maripaludis* S2 (DSZM, strain 14266) was used as the standard organism for the experiments, since it was already described as electroactive and is capable of producing methane in a bioelectrochemical system. Its biological properties according to literature data are given in Table 29.

Table 29: Properties of *Methanococcus maripaludis*

<i>M. maripaludis</i> (Jones et al., 1983)	
Maximum growth rate	0.345 1*h <sup>-1</sup> (on H <sub>2</sub> /CO <sub>2</sub> )
Temperature optimum	38 °C
pH optimum	6.8-7.2
Location of isolation	Salt marsh sediment, South Carolina

A growth curve was monitored by measuring the optical density. The cultures grew in 200 ml Septum flasks filled with 50 ml M141 medium and pressurized to 2 bar with H<sub>2</sub>/CO<sub>2</sub>. The gas phase was exchanged daily and the cultures were stored at 37 °C and 180 rpm in the incubator. The growth rate of planctonic cells was calculated using Monod's model via OD measured at several timepoints (WPA Biowave CO8000 Cell Density Meter, 600 nm, Biochrom Ltd, Cambridge, England, Equation 39) (Takors, 2014), showing a growth rate of 0.24 ± 0.03 1\*h<sup>-1</sup> in septum flasks with a methane production rate of 0.48 ± 0.1 mmol\*h<sup>-1</sup>. On MES medium in septum flasks, growth was observed after a lag phase of 58 h with a medium growth rate of 0.051 ± 0.0038 1\*h<sup>-1</sup> at a methane production rate of 0.11 ± 0.05 mmol\*h<sup>-1</sup>.

$$\mu = \frac{\ln\left(\frac{OD(t_1)}{OD(t_0)}\right)}{(t_1 - t_0)} \quad \text{Equation 39}$$

The maintenance demand on hydrogen and CO<sub>2</sub> for a culture in a 50 ml septum flask was determined (Heijnen, 2002). For hydrogen, the maintenance demand was 0.0035 mol\*d<sup>-1</sup>\*OD(50ml), for CO<sub>2</sub> 0.0013 mol\*d<sup>-1</sup>\*OD(50ml)

The precultures for the inoculation of all bioelectrochemical systems were cultivated in 1 liter septum flasks with 300 ml of M141 medium and 2 bar H<sub>2</sub>/CO<sub>2</sub> 80/20 gas atmosphere to an optical density of approximately 1 at 180 rpm and 37 °C. A first electroactivity test was conducted under standard conditions in an H-cell. Therefore, 100 ml of MES medium were filled into the working chamber, 100 ml of phosphate buffer (100 mM, pH 6.9) into the counter chamber; It has already been reported that phosphate buffer can be used as counter electrolyte (Dewan et al., 2008). The working chamber

was gassed with 5 ml\*min<sup>-1</sup> N<sub>2</sub>/CO<sub>2</sub> 80/20 and a potential of -900 mV vs. Ag/AgCl was applied to the working electrode. Both, working and counter electrodes were graphite rods. The working chamber was inoculated to an OD of 0.1. Over 90 h, current consumption was measured continuously; gas samples and terminal voltage values were taken daily. The experiments were conducted in duplicates with an abiotic control. Two biotic negative controls were also conducted in H-cells; in the first, the working chamber was gassed with 5 ml\*min<sup>-1</sup> CO<sub>2</sub>, but no potential was applied to the working electrode. In the second, a potential of -1.1 V vs. Ag/AgCl was applied, but the working chamber was gassed with N<sub>2</sub> only.

## 6.6.2 Process Development and Optimization in Lab-Scale

### 6.6.2.1 Starting Conditions

The starting conditions for process optimization in the designed bubble column reactor are given in Table 30.

Table 30: Starting conditions for process optimization

System part	Starting condition
Biocatalyst	<i>M. maripaludis</i> , OD 0.1
Working electrode	Graphite rod, geometrical surface area 0.0069 m <sup>2</sup>
Working electrolyte	MES medium, 1 l
Counter electrode	Carbon fabric, 0.06 m <sup>2</sup>
Counter electrolyte	0.1 M phosphate buffer pH 6.8, 10 liter
Membrane	Proton exchange membrane, 0.012 m <sup>2</sup>
In-gas	N <sub>2</sub> /CO <sub>2</sub> (80/20 v/v), 30 ml*min <sup>-1</sup>
Applied potential	-900 mV vs. Ag/AgCl

The graphite rod was used because it is the standard-electrode for experiments in H-cells and therefore allows comparison with lab-scale experiments. The temperature was set to 35 °C, no external loop was used and no medium components were added during the 90 h chronoamperometric measurements; the potential was applied shortly before the inoculation. The current consumption and terminal voltage were measured continuously over 90 h; gas samples were taken twice a day and measured with gas chromatography. The OD of the precultures was usually around 1, so around 100 ml of MES medium in the reactor were replaced by the same volume of preculture. If not stated otherwise, each experiment was carried out in two independent biotic replicates and one abiotic control; the mean values given in the results part are calculated as average over time of the mean values of the duplicates.

From this starting point, several parameters of the process were changed to optimize the production according to Table 31. The main parameters applied to compare the experiments were methane production and Coulombic efficiency, along with other performance parameters given in Table 7. The basic parameters, which have been used for the abiotic characterization as well, namely anolyte, catholyte and temperature have not been varied for these experiments.

Table 31: Process optimization parameters

Process condition	Alteration 1	Alteration 2
Potential	Different potentials applied vs. Ag/AgCl: -0.7 V, -0.9 V, -1.1 V	Terminal voltage of -5.0 V applied; current of -27.4 mA or -100 mA applied
Electrode	Different working electrodes tested: GR, CG, CF, CL, RVC; three of those (GR, CL and RVC) with different sizes	CL and CF tested as counter electrodes; Size alteration of counter electrode
Membrane	Three different membranes tested: CEM, AEM, PEX	Alteration of membrane size
Aeration	Test of different gas mixtures: N <sub>2</sub> /CO <sub>2</sub> in 80/20, 50/50 and 0/100; N <sub>2</sub> /CO <sub>2</sub> /H <sub>2</sub> in 80/13/7 (v/v/v)	Alteration of in-gas velocity (30 ml*min <sup>-1</sup> , 60 ml*min <sup>-1</sup> , 90 ml*min <sup>-1</sup> ), test of two different spargers and EL
Optical density	OD of 0.1 and 0.2 were tested	OD 0.05, 0.1 and 0.2 were tested after optimization

AEM: anion exchange membrane; CEM: cation exchange membrane; BC: bubble column; EL: external loop; GR: graphite Rod; CF: carbon fabric; CG: carbon granulate

### 6.6.2.2 Potential Optimization

To optimize the potential for the production of methane, three different potentials were tested, -700 mV vs. Ag/AgCl, -900 mV vs. Ag/AgCl and -1.1 V vs. Ag/AgCl. Apart from the potential, these experiments were done with the starting conditions. The potential was applied using a reference electrode.

### 6.6.2.3 Electrode Influence

To choose the most suitable working electrode material for the process of bioelectromethanogenesis, five different electrode materials (described in 6.4) were tested in the bubble column reactor. To investigate the effect of the working electrode surface area, 1, 2 and 4 pieces (all contacted with one titanium wire) of carbon laying and graphite rod were used as cathode, respectively. For the RVC foam, also 1 and 2 sticks and one larger stick (20 cm \* 4 cm \* 2 cm) were tested as electrode,

respectively. The experiments for electrode optimization were, apart from the electrode, conducted with the starting conditions, whereby the potential was lowered from 900 mV vs. Ag/AgCl to -1.1 mV vs. Ag/AgCl as a result of the potential optimization.

Two different counter electrodes were tested, which are carbon laying and carbon fabric. These two textile-like materials were cut to rectangular sheets and placed in front of each membrane window. The influence of the anode size was investigated by conducting an experiment with only two carbon fabric sheets as anode instead of four, so the anode size is halved, and doubling the anode size to eight sheets by placing two sheets behind each other in front of each window. The conditions in these experiments were the same as shown in Table 34 with a potential of -1.1 V and altering the counter electrode.

#### 6.6.2.4 Membrane Influence

A suitable membrane was chosen by conducting experiments in the bubble column reactor with three different membrane types (see also section 6.5). For this test, all four membrane windows were closed with the same type of membrane under the conditions shown in Table 32 .

Table 32: Operating conditions for membrane optimization

System part	Operating condition
Biocatalyst	<i>M. maripaludis</i> , OD 0.1
Working electrode	2 graphite rods, geometrical surface area 0.0138 m <sup>2</sup>
Working electrolyte	MES medium, 1 liter
Counter electrode	Carbon fabric, 0.06 m <sup>2</sup>
Counter electrolyte	0.1 M phosphate buffer pH 6.8, 10 liter
Potential	-1.1 V vs. Ag/AgCl
In-gas	N <sub>2</sub> /CO <sub>2</sub> , (80/20 v/v) 30 ml*min <sup>-1</sup>

For an additional test, all four windows were closed with silicone rubber as an abiotic chronoamperometric experiment to ensure that the silicon rubber is not conductive itself. Afterwards, the process was operated under the same conditions biotically and abiotically, closing 2 membrane windows with silicone rubber and 2 with proton exchange membrane (halved membrane area).

### 6.6.2.5 Gassing

To further improve mixing conditions, an external loop was used as described in 6.2.3. The medium was pumped through the loop with  $47.22 \pm 1.40 \text{ ml} \cdot \text{min}^{-1}$ . The operation conditions are given in Table 33.

Table 33: Operating conditions for gassing optimization

System part	Conditions external loop	Conditions gas composition
Biocatalyst	<i>M. maripaludis</i> , OD 0.1	<i>M. maripaludis</i> , OD 0.1
Working electrode	Large RVC, 0.0248 m <sup>2</sup>	2 graphite rods 0.0138 m <sup>2</sup>
Working electrolyte	MES medium, 1 l	MES medium, 1 l
Counter electrode	Carbon fabric, 0.06 m <sup>2</sup>	Carbon fabric, 0.06 m <sup>2</sup>
Counter electrolyte	0.1 M phosphate buffer pH 6.8, 10 liter	0.1 M phosphate buffer pH 6.8, 10 liter
Membrane	PEX, 0.012 m <sup>2</sup>	PEX, 0.012 m <sup>2</sup>
Potential	-1.1 V vs. Ag/AgCl	-1.1 V vs. Ag/AgCl
In-gas	N <sub>2</sub> /CO <sub>2</sub> , (80/20 v/v) 30 ml*min <sup>-1</sup>	divers

Different in-gas compositions were investigated. Those were the starting gas mixture (80/20 N<sub>2</sub>/CO<sub>2</sub>), a gas composition with increased CO<sub>2</sub> content (50/50 N<sub>2</sub>/CO<sub>2</sub>) and pure CO<sub>2</sub>. To improve the gas transfer into the medium, three gassing velocities were tested; 30 ml\*min<sup>-1</sup> (starting condition), 60 ml\*min<sup>-1</sup> and 90 ml\*min<sup>-1</sup> with CO<sub>2</sub> as in-gas (conditions as for gas composition optimization). Another method to improve the gas transfer seems to be the alteration of the sparger geometry, so a second sparger was constructed (Figure 45) with a perforation size of 0.7 mm instead of 1 mm. The  $k_{La}$  of the new plate was measured as described in 6.3.2. To get a deeper insight into the process limitations, the new plate was tested with the starting conditions and with optimized conditions as for the gassing optimization (Table 33) with 60 ml\*min<sup>-1</sup> CO<sub>2</sub> in-gas.

To stabilize the pH, 20.9 g\*l<sup>-1</sup> MOPS buffer was added to the medium. This was tested in the bubble column using the large RVC foam as electrode, an applied potential of -1.1 V and the initial N<sub>2</sub>/CO<sub>2</sub> 80/20 (v/v) in-gas with 30 ml\*min<sup>-1</sup> gas flux.

### 6.6.2.6 Initial Optical Density

The optical density in the starting conditions was 0.1. To observe whether the amount of microorganisms was limiting, the OD was increased to 0.2 using the starting conditions and optimized conditions (altered starting conditions with 2 graphite rods as electrode, -1.1 V vs. Ag/AgCl and CO<sub>2</sub> with 60 ml\*min<sup>-1</sup> as in-gas). Under optimized conditions, also a halved initial OD of 0.05 was tested.

### 6.6.2.7 Failure Simulation Experiments

The bubble column reactors for the failure simulation tests were equipped with 2 graphite rods as working electrode and 4 pieces of proton exchange membrane. The gassing was set to 30 ml\*min<sup>-1</sup> (pure CO<sub>2</sub> for potentiostat and gassing breakdown simulation, N<sub>2</sub>/CO<sub>2</sub> 80/20 (v/v) for gas composition shift).

To simulate the failure of the potentiostat, the applied potential was shut off after a runtime of 24 h and switched back on 20 h later. During that time, the OCP was monitored. A breakdown in the gas supply was simulated similarly by stopping the gas stream of pure CO<sub>2</sub> after 24 h of operation and restarting it 20 h later. The second experiment was conducted likewise, but during the time of potential shutdown, the system was fed with a gas mixture containing hydrogen (N<sub>2</sub>/CO<sub>2</sub>/H<sub>2</sub> 80/13/7 v/v/v)

Influences of a sudden change in gas composition were examined by gassing the reactor with an in-gas containing 20% CO<sub>2</sub> at first, altering the mixture to 5 % CO<sub>2</sub> content after 45 h and back to 20 % after 70 h total runtime. To observe the behavior of the methanogens exposed to changing temperature conditions, H-cells were operated at an applied potential of -1.1 V vs. Ag/AgCl and with a gassing of 5 ml\*min<sup>-1</sup> pure CO<sub>2</sub> for 20 hours, than the incubator hood was switched of so that the temperature was 20 °C instead of 35 °C. The incubator hood was switched on again after another 28 hours to observe alterations in the performance. The experiments for gassing failure, gas composition change and temperature change were carried out in duplicate, the simulation of a potentiostat breakdown as single experiment. Abiotic controls were done for the gassing failure, the potentiostat failure and the temperature change.

For industrial application, this might not be the most suitable approach because of the use of a costly reference electrode and potentiostat. So, after optimization of other parameters, the application of a terminal voltage of -5 V (similar to the terminal voltage measured for a potential application of -1.1 V vs. Ag/AgCl) and the application of current of -27.4 mA (mean current when applying -1.1 V vs. Ag/AgCl) and -100 mA were tested using optimized process conditions as given in Table 34.

Table 34: Optimized conditions for experiments with applied voltage and applied current

System part	Operating condition
Biocatalyst	<i>M. maripaludis</i> , OD 0.1
Working electrode	2 graphite rods, total geometrical surface area 0.0138 m <sup>2</sup>
Working electrolyte	MES medium, 1 liter
Counter electrode	Carbon fabric, 0.06 m <sup>2</sup>
Counter electrolyte	0.1 M phosphate buffer pH 6.8, 10 liter
Membrane	Proton exchange membrane, 0.012 m <sup>2</sup>
In-gas	CO <sub>2</sub> , 30 ml*min <sup>-1</sup>

### 6.6.2.8 Long Term Operation and Comparison to Other Reactors

After the optimization of different parameters, the reactor was operated using a combination of the best parameters for a chronoamperometric measurement at -1.1 V vs. Ag/AgCl in the regular MES medium (parameters shown in Table 35).

Table 35: Optimal conditions found for the bubble column reactor

	<b>Biology</b>	<b>Membrane</b>	<b>Anode</b>	<b>Cathode</b>	<b>Gassing</b>
Optimum conditions	<i>M. maripaludis</i> , OD 0.1	CEM, 0.012 m <sup>2</sup>	Carbon fabric, 0.06 m <sup>2</sup>	4 graphite rods, 0.0276 m <sup>2</sup>	Sparger 1, 100 % CO <sub>2</sub> , 60 ml*min <sup>-1</sup>

For Scale-Up and comparison to other reactors, other parameters were used, since the working electrode needed to be applicable in all three reactor types chosen for comparison and in a larger reactor. Therefore, according to the results of the optimization tests, carbon laying was used. Apart from that, the membrane size was halved for Scale-Up. To gain reliable and reproducible percentages of methane in the off-gas, the gas flux was set to 30 ml\*min<sup>-1</sup>. The reactor was operated using the chosen parameters for three weeks (parameter overview see Table 36). Comparable conditions for the long term experiment were also applied to an H-cell and the stirred tank reactor in an 80 h chronoamperometric experiment (Table 36). For the bubble column, sparger plate 1 was used.

Table 36: Comparison of bioelectromethanogenesis in different reactors

	<b>Bubble column</b>	<b>Stirred tank</b>	<b>H-cell</b>
Cathode	Carbon laying 0.023 m <sup>2</sup>	Carbon laying, 0.0144 m <sup>2</sup>	Carbon laying, 0.0056 m <sup>2</sup>
Anode	Carbon fabric, 0.06 m <sup>2</sup>	Carbon fabric, 0.0144 m <sup>2</sup>	Carbon fabric, 0.00056 m <sup>2</sup>
Membrane	CEM 0.006 m <sup>2</sup>	CEM 0.0025 m <sup>2</sup>	CEM 0.00049 m <sup>2</sup>
In-gas	CO <sub>2</sub> , 30 ml*min <sup>-1</sup> (0.3 vvm)	CO <sub>2</sub> , 60 ml*min <sup>-1</sup> (0.3 vvm)	CO <sub>2</sub> , 5 ml*min <sup>-1</sup> (0.5 vvm)
Applied potential	-1.1 V vs. Ag/AgCl	-1.1 V vs. Ag/AgCl	-1.1 V vs. Ag/AgCl
Working volume and optical density	1 l, OD 0.1	2 l, OD 0.1	0.1 l, OD 0.1
Medium	MES	MES	MES

### 6.6.3 Numbering-Up of the Process

A Numbering-Up with three 1 liter bubble column reactors was carried out. The initial operating conditions were as in the long term operation for comparability (see section 6.6.2.8, Table 36).

First, each reactor was electrically connected separately, but the experiment can be considered as reactor cascade (Figure 55 C) since one gas stream ran through all three reactors. Therefore, the gassing of the first reactor was set to  $90 \text{ ml} \cdot \text{min}^{-1}$  pure  $\text{CO}_2$ , the gas outlet of the first reactor was connected to the inlet of the second reactor and the gas outlet of the second reactor was connected to the gas inlet of the third reactor, respectively. A potential of  $-1.1 \text{ V}$  vs.  $\text{Ag}/\text{AgCl}$  was applied to each reactor separately. The reactors were all inoculated to an OD of 0.1 and operated for four days. After this time, the gassing conditions remained, but the reactors were connected electrically in parallel (Figure 55 B) with an applied terminal voltage of  $-5 \text{ V}$  (close to the terminal voltage in one single reactor). In parallel connection, the potential is the same for all parallel connected reactors. After another four days, the electrical connection was switched and the three reactors were connected serially. A current of  $-20 \text{ mA}$  was applied, which is similar to the current observed in one reactor, since in a serial connection the current in all three reactors is the same. The gassing conditions remained.

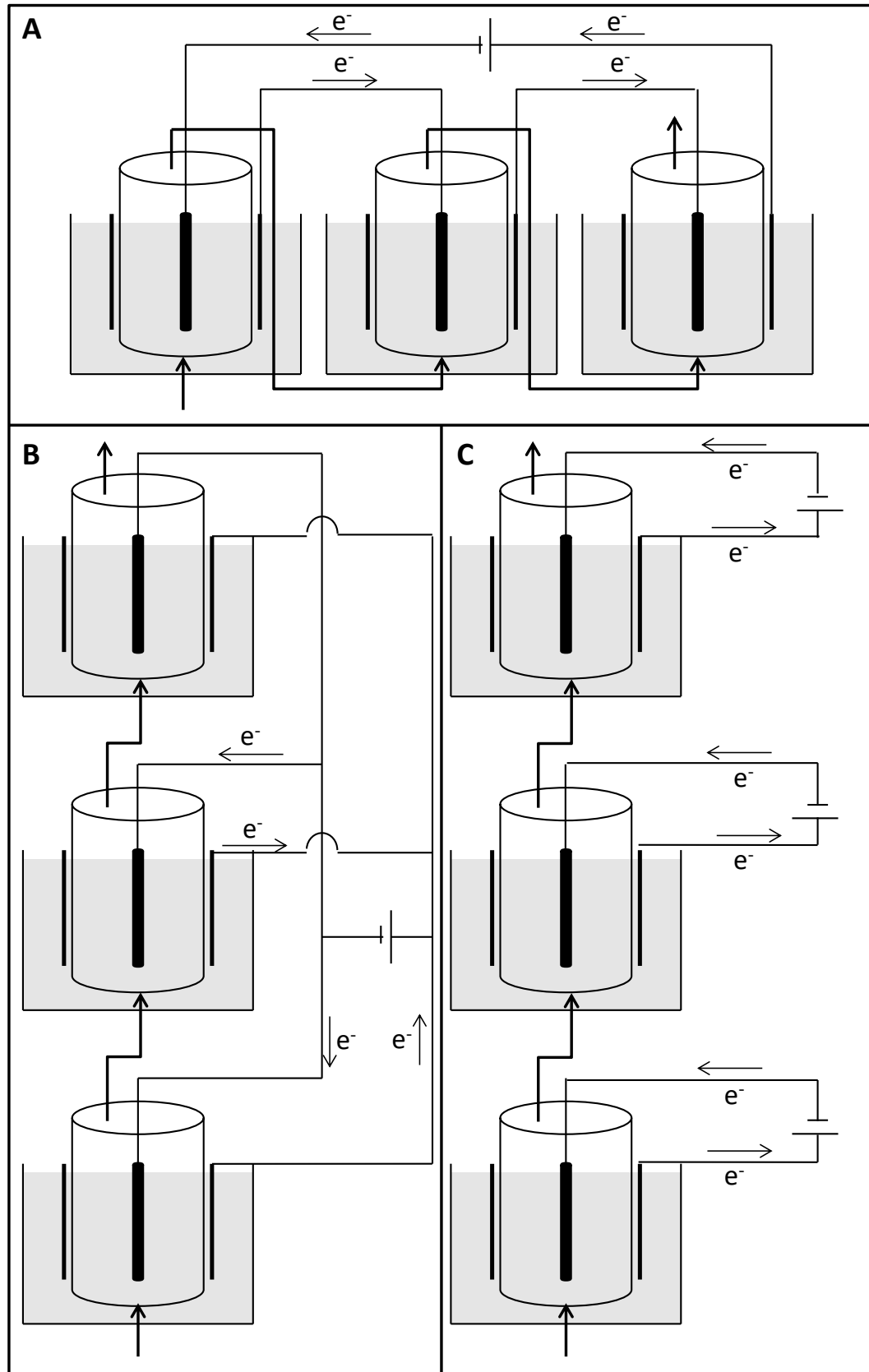


**Figure 55: Different operational conditions for numbering up**

A) Serial connection of three one-liter-reactors with separated gassing; B) Parallel connection of three one-liter-reactors with separated gassing; C) Parallel connection of three one-liter-reactors with connected gassing

#### 6.6.4 Scale-Up of the Process

The bubble column reactor was scaled up to a pilot-scale of 50 liter working volume. Six parts of the reactor and one operational parameter were identified for Scale-Up via Similarity Theory. These are working chamber, counter chamber, working electrode, counter electrode, membrane and sparger plate as reactor parts and gassing as operational parameter. For some of these parts, more than one possibility for Scale-Up exist, leading to in total 108 different possible configurations of how to Scale-Up the reactor.

The diameter of the working chamber was scaled up using geometrical similarity (0.31 m).

$$D_{LR} = \left(\frac{V_{LR}}{V_R}\right)^{\frac{1}{3}} * D_R^* \quad \text{Equation 40}$$

The liquid level (0.65 m) was determined using the diameter of the reactor and the desired working volume. Two possibilities remained for the calculation of the working chamber total height. Either, the ratio of headspace volume to working volume remains constant, resulting in a total height of 1.17 m, or the height of the gas phase (0.12 m) remains constant, giving a total height of 0.77 m. It was chosen to keep the total headspace height constant, since the headspace in a gassed bubble column is needed to prevent medium efflux by foaming and not for mass transfer of gas to liquid. For the Scale-Up of the counter chamber, the height was set to 0.85 m, which equals the liquid level of the working chamber plus 20 cm for the gas tube coming from the bottom part of the reactor. For the diameter, two alternatives exist; either the ratio of working volume to counter volume remains constant or the diameter is calculated using the working chamber diameter increased by 20 cm to allow space for the counter electrode. The first possibility would result in 500 liter counter electrolyte, which will lead to a huge amount of energy needed for heating; therefore, the diameter was set to 0.51 m using possibility two, resulting in a counter volume of 125.6 liter. The dimensions of the larger working electrode were calculated keeping the ratio of electrode surface area to working volume constant. The geometrical surface area of the carbon laying sheet and the cylindrical electrode roll was used for the calculation to avoid limitations if the microorganisms can use the inner parts of the rolled up electrode, too. The length of the working electrode may not be larger than the liquid level and four electrode sheets shall be introduced into the reactor. This led to four carbon laying sheets of 0.65 m \* 1.15 m with a total geometrical surface area of 3 m<sup>2</sup> and a mass of 0.57 kg, rolled to cylindrical rods with 14 cm diameter. The membrane could be scaled up using either the ratio of membrane area to working electrode surface area, the ratio of membrane area to working volume or the membrane area to the reactor wall area. Since the first two possibilities led to membranes larger than the available wall area, the third possibility was chosen. The size of each membrane window may not exceed 0.022 m<sup>2</sup> to keep the pressure per membrane area as large as in the lab scale reactor, otherwise the membrane might crack.

This led to the use of 20 windows (3 cm\* 23 cm each) with a total area of 0.16 m<sup>2</sup>. Three methods to Scale-Up the counter electrode were considered. These methods are keeping the ratio of counter electrode surface area to working electrode surface area constant, keeping the ratio between counter electrode surface area and working volume constant or keeping the ratio of counter electrode surface area to membrane area constant. The first two methods led to similar results because the ratio of working electrode surface area to working volume was held constant before. However, the four calculated counter electrodes were each longer than the circumference of the working chamber; this would result in more than four overlapping layers of counter electrode wrapped around the working chamber, which would cause a large electrical resistance and the inner layers would probably not take part in the counter reaction efficiently. Therefore, the ratio of counter electrode surface area to membrane area was kept constant. This led to four sheets of carbon fabric with 0.61 m length each, so 2.5 layers of carbon fabric are wrapped around the working chamber. The height of the counter electrode was limited by the liquid level of the working chamber to 0.65 m. The total counter electrode surface area added up to 1.59 m<sup>2</sup>. The bubble diameter should remain constant during the Scale-Up, resulting in a constant Weber and Bond number (see Equation 23 and Equation 25). The bubble diameter is only related to the orifice diameter (Akita and Yoshida, 1974) as long as the same medium at the same temperature and pressure is used. The perforation size was therefore kept constant at 1.0 mm. The number of perforations per sparger area was kept constant, leading to 407 holes. To design the gassing for the large reactor, either the vvm, the  $k_La$  or the Reynolds number can be kept constant according to Similarity Theory. To estimate the new  $k_La$ , a correlation of Schumpe and Grund was used which fitted the values for the one liter reactor (Equation 43) (Kantarci et al., 2005). The viscosity was assumed as 0.000719 Pa\*s.

$$k_La = 0.42 * u_G^{0.82} * \mu_{vis}^{-0.39} \quad \text{Equation 41}$$

Using the vvm as Scale-Up criterion, a gas flux of 1.5 l\*min<sup>-1</sup> needs to be applied, using the  $k_La$  0.431 l\*min<sup>-1</sup> and using the Reynolds number 0.407 l\*min<sup>-1</sup>. Since the gas flux is not only used for substrate supply but also for mixing, it was chosen to use the vvm and the largest calculated gas stream to avoid limitations.

### 6.6.5 Design and Operation of the Pilot Plant

The pilot plant with 50 liter working volume was constructed using a polypropylen pipe (REHAU Unlimited polymer solutions, Rehau, Germany) of 0.31 m inner diameter, 0.77 m height and 0.012 m wall thickness. The total inner volume of the working chamber was 59.55 liter. 20 membrane windows were cut into the pipe, each 3 cm \* 23 cm, arranged staggered in two rows (Figure 56 A). The membranes were sandwiched between two silicon rubber frames and screwed to the reactor using a PVC frame (Figure 56 B), threaded rods and nuts. The threaded rods were glued to the reactor and sealed with silicone. After assembling, the nuts were covered with isolating tape to avoid an electrical connection to the counter electrode (Figure 56 C).

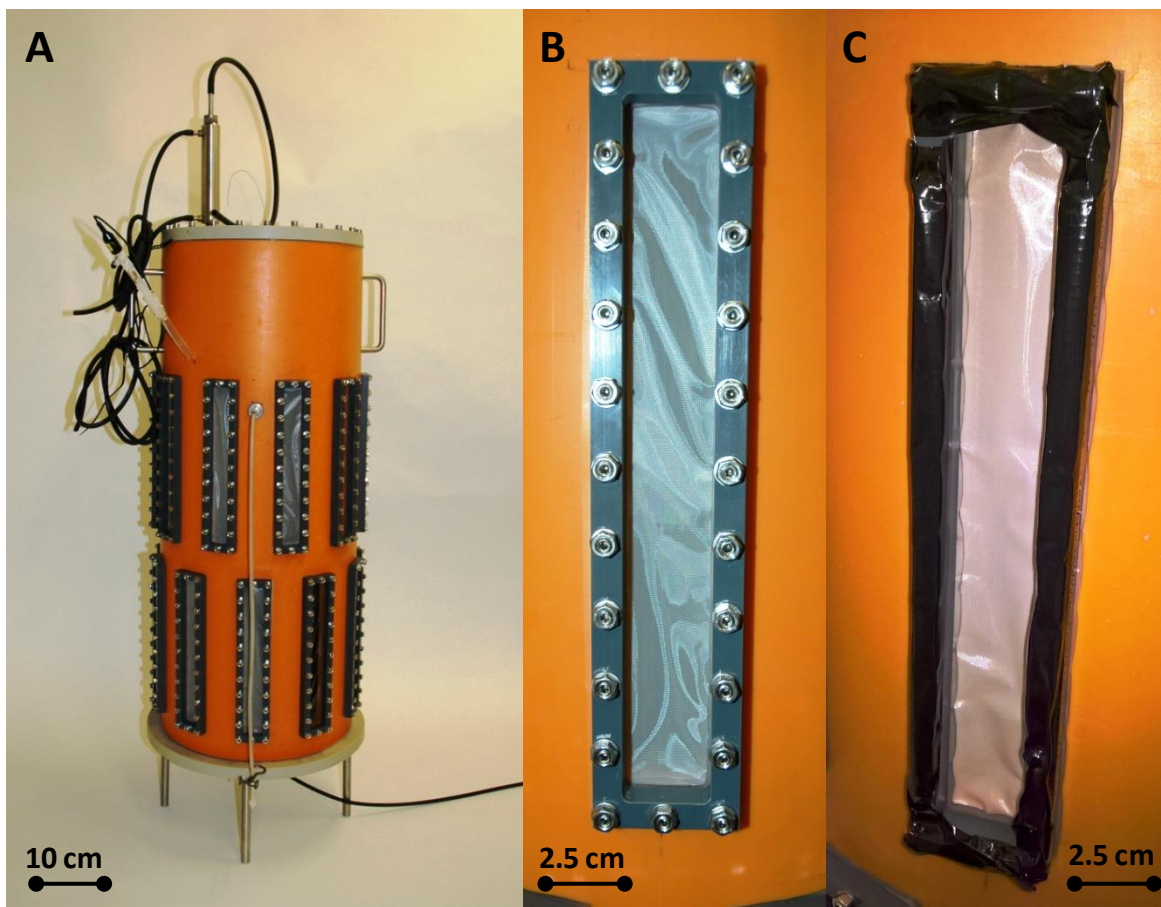


**Figure 56: Working chamber and membrane windows pilot scale reactor**

A) Working chamber with 20 membrane windows in two staggered rows; B) CEM attached to the reactor using threaded rods, nuts and a PVC frame; C) Metal parts of membrane window were isolated before operation.

A PVC plate was used for the bottom plate and the lid, respectively, and screwed to the reactor with a silicon rubber sealing sandwiched between pipe and PVC plate. The bottom plate held a pipe connector for the gassing in the middle of the plate. Apart from that, several spacers (Figure 57 A) were located at the inner side of the bottom plate. On these spacers, the perforated PTFE plate (sparger) was fixed with plastic screws (Figure 57 B and C). The sparger plate was sealed with silicone to avoid gas slip.



**Figure 57: Bottom plate and gas sparger of pilot scale reactor**

A) Bottom plate with gas inlet in the center and spacers to hold PTFE sparger plate; B) PTFE sparger plate; C) PTFE sparger plate placed in the reactor and fixed to bottom plate with plastic screws.

The lid held a butyl septum (Glasgerätebau Ochs, Bovenden, Germany; GL 45 septum) for the electrode connection and a gas outlet (Figure 58 A). The off gas was cooled to 10 °C by a refrigerated circulating bath.

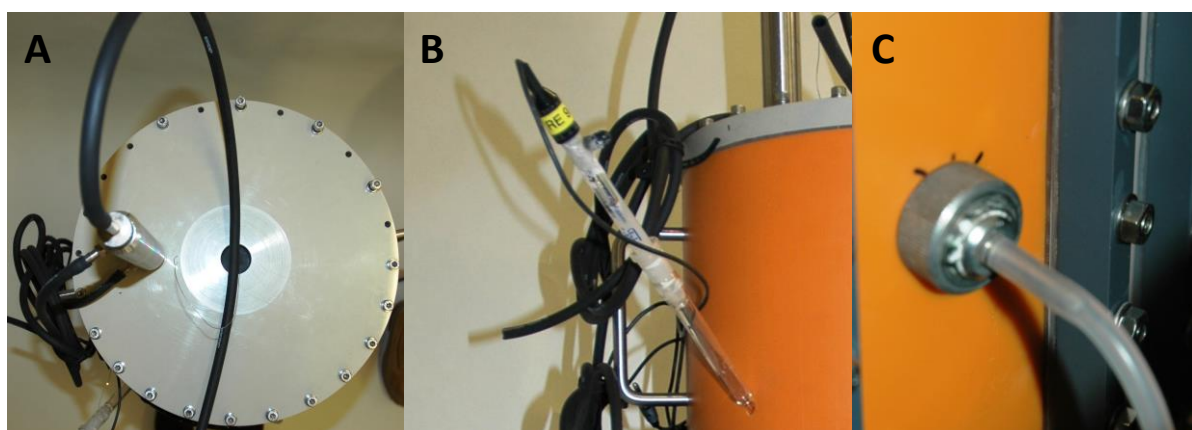


**Figure 58: Lid and side ports of pilot scale reactor**

A) Lid with electrode inlet in the center and gas outlet with gas cooler; B) Sloping side bore with Luggin capillary and reference electrode; C) Side bore with sample port.

A sloping bore for the Luggin capillary (Figure 58 B) and a straight one for a sample port were drilled in the working chamber wall (Figure 58 C). Luggin capillary and sample port were glued into the bored with silicone.

The working electrode was made of four pieces of carbon laying (0.65 m \* 1.15 m), rolled into cylinders with a diameter of 14 cm (Figure 59 A). Each electrode cylinder was contacted using a titanium wire, the four wires were connected and one of them was pierced through the butyl septum in the lid and connected to the potentiostat (Gamry Interface 1000, Gamry Instruments, Westminster, USA). The electrodes were placed in the reactor working chamber, the electrode distance between working and counter electrode was 3.7 cm (Figure 59 B).

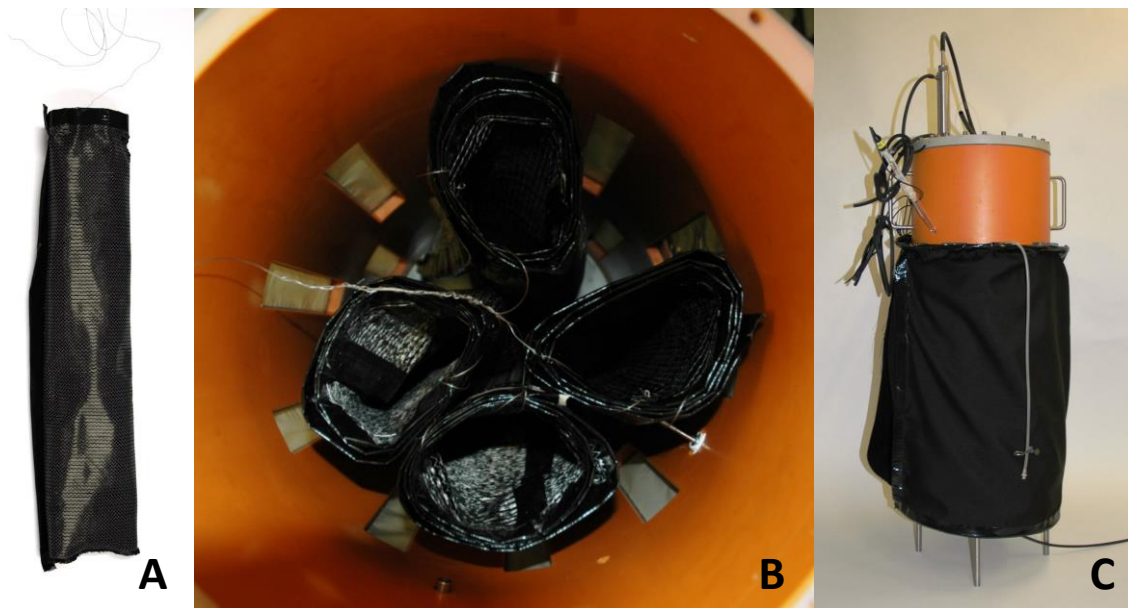


**Figure 59: Electrodes of pilot scale reactor**

A) One of four working electrodes; B) Four working electrodes placed in the working chamber ; C) Working chamber surrounded by counter electrode.

The carbon fabric counter electrodes (4 pieces 0.61m \* 0.65 m) were attached to two PTFE tubes to create a hose-like form which was placed around the working chamber (Figure 59 C). The electrode was contacted using a platinum wire (0.5 mm Goodfellow, Bad Nauheim, Germany). The working chamber with the surrounding counter electrode was sterilized using UV-light and afterwards placed in a water basin of 203 liter volume and filled with 50 liter sterile filtrated MES medium. The water basin was filled with 145 liter phosphate buffer. The basin was 77 cm high, 42 cm in diameter at the bottom and 66 cm \* 66 cm at the top (Figure 60 A) and equipped with a heating coil out of PTFE tubes, set to 35 °C using a refrigerated circulating bath (Figure 60 B). The temperature in the water basin was indicated by a bioengineering temperature module.

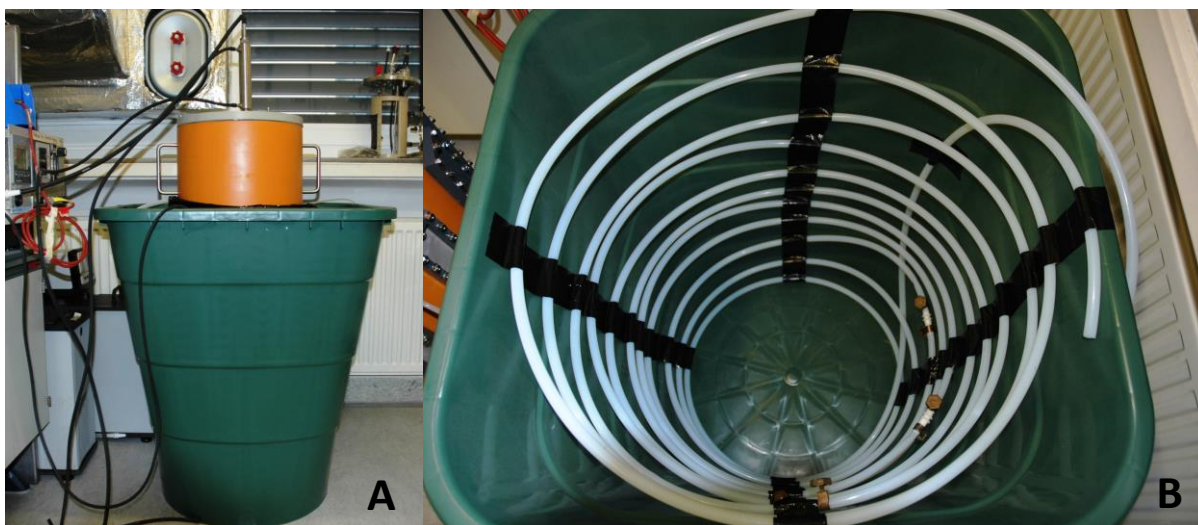


**Figure 60: Pilot scale reactor with counter chamber**

A) Pilot scale reactor in counter chamber; B) Heating coil in counter chamber.

The gas flux of pure CO<sub>2</sub> was set to 1.5 l\*min<sup>-1</sup> using the bioengineering temperature module, which also contained a rotameter. The refrigerated circulating bath for heating the water basin and the gas flux was switched on 5 h before starting an experiment. The Ag/AgCl reference electrode was placed in the Luggin capillary filled with 0.5 M Na<sub>2</sub>SO<sub>4</sub>. All electrodes were connected to a Gamry interface 1000 potentiostat, setting a potential of -1.1 V vs. Ag/AgCl. After gassing, 250 g NaHCO<sub>3</sub> were added before switching on the potential. For the biotic experiments, 5 liter of MES medium were replaced by *M. maripaludis* preculture grown in 10 liter septum flasks for one week to an OD of approximately 1.

Prior to the first experiment, the gas hold up, k<sub>L</sub>a, and bubble size were measured as described in 6.3.2, followed by the calculation of the relevant dimensionless numbers (section 6.3.2). Also, the reactor resistance was measured at 5 mA and a CV and Impedance spectroscopy was measured as described in 5.3.1 and 5.4.

During one experiment, which lasted for 230 h, gas samples, terminal voltage, conductivity and pH in both chambers were measured daily, as well as the OD in the working chamber. The current was monitored continuously. One biotic experiment with *M. maripaludis* and 1 abiotic control experiment were carried out.

Inhibition experiments were carried out in H-cells at -1.1 V vs. Ag/AgCl with a graphite rod anode and cathode at 35 °C. At the anode, 100 ml of 0.1 M phosphate buffer pH 6.8 was used as electrolyte, at the cathode 100 ml of MES medium. Pieces of reactor material used in the larger reactor but not in the smaller reactors were added to the cathode chamber: two plastic screws or two 1.5\*1.5\*0.6 cm pieces of polypropylene per cathode chamber, respectively. The experiments were carried out for 50 h in duplicates with biotic control (without addition of material). Mean values were calculated from data between 5 and 50 h to avoid influences of the electrode polarization phase and the inoculation.

## 6.7 Microbial Fuel Cell

*Shewanella oneidensis* MR-1 was used for microbial fuel cell experiments. The organism was cultivated aerobic on LB medium (pre-culture 1) for one day and transferred to aerobic LSBM medium in a ratio of 1:100 (pre-culture 2) one day before the start of the MFC experiment (see appendix for media composition). Both cultivations were carried out at 30 °C shaking at 180 rpm. The initial optical density in the reactor was set to 0.3 at the beginning of each experiment, calculated by Equation 42.

$$V_{PC2} = \frac{OD_{PC2}}{V_R * OD_{R,i}} \quad \text{Equation 42}$$

The necessary volume of preculture 2 was centrifuged for 15 minutes at 4700 rpm, the supernatant was disposed and the cell pellet resuspended in 20 ml of LSBM per liter reactor working volume. MFC experiments were carried out in batch mode in the bubble column reactor, in the stirred tank reactor and in the H-cell for comparison (see Table 37 for conditions and section 6.2 for process monitoring).

The reactors were prepared prior to inoculation by gassing the working chamber with N<sub>2</sub> (0.03 vvm) to create anaerobic conditions, heating to 35 °C and polarization to +400 mV vs. Ag/AgCl. The medium of the anode (working) chamber was LSBM; the cathode (counter) chamber was filled with 100 mM phosphate buffer pH 6.9. The inoculation was done after anaerobization and polarization of the electrodes. The MFCs were operated at +400 mV and 30 °C for 90 h under continuous N<sub>2</sub> flux for maintaining anaerobic conditions.

Table 37: Operation conditions for MFC experiments

	Bubble column	H-cell	Stirred tank
Anode	Carbon fabric, 0.0047 m <sup>2</sup>	Carbon fabric, 0.00075 m <sup>2</sup>	Carbon fabric, 0.0108 m <sup>2</sup>
Anolyte	LSBM, 1 l	LSBM, 0.1 l	LSBM, 2 l
Catholyte	Phosphate buffer, 10 l	Phosphate buffer, 0.1 l	Phosphate buffer 0.3 l
Cathode	Carbon fabric, 0.06 m <sup>2</sup>	Carbon fabric 0.00138 m <sup>2</sup>	Carbon fabric, 0.0144 m <sup>2</sup>
Membrane	Nafion, 0.012 m <sup>2</sup>	Nafion, 0.00049 m <sup>2</sup>	Nafion, 0.014 m <sup>2</sup>
Gas anode chamber	Headspace 800 ml, gassing 30 ml*min <sup>-1</sup> N <sub>2</sub>	Headspace 47 ml, gassing 5 ml*min <sup>-1</sup> N <sub>2</sub>	Headspace 0.42 l, gassing 60 ml*min <sup>-1</sup> N <sub>2</sub>
Gas cathode chamber	open to air	open to air	open to air

Samples for OD measurement and HPLC analyses of lactate and acetate were taken daily. For the HPLC samples, 1 ml of culture broth was centrifuged; the supernatant was stored at -20 °C until the analysis. A calibration curve was done using LSBM medium with different concentrations of lactate, formate and acetate between 5 and 100 mM each.

Using this calibration curve as external standard, the acetate and lactate concentrations of the samples were calculated, giving the lactate consumption rate (Equation 43)

$$r_{lac,con} = \frac{(c_{lac}(t_1) - c_{lac}(t_2)) * V_R}{t_2 - t_1} \quad \text{Equation 43}$$

For each mol of lactate converted to acetate, 4 mol of electrons are transferred to the anode, according to Equation 1. Therefore, the number of electrons which were produced by metabolism per second have to be calculated using Equation 44.

$$r_{e,m} = 4 * r_{lac,con} \quad \text{Equation 44}$$

The Coulombic efficiency was calculated as described in Equation 9 in section 2.2.2.

## Symbols

$A_{cs,E}$	Electrode cross sectional area	$m^2$
$A_{El}$	Geometrical electrode surface area	$m^2$
$A_{GL}$	Gas-Liquid interfacial area	$m^2$
$A_R$	Reactor cross sectional area	$m^2$
$b$	Tafel slope	V
$Bd$	Bond number	-
$c_{p,CO_2}$	Isobaric heat capacity	$kJ*kg^{-1}*K^{-1}$
$c_{y(tx)}$	Concentration of y (dissolved) at timepoint x	$mol*m^{-3}$
$D$	Dilution rate	$l*s^{-1}$
$D_B$	Bubble diameter	m
$D_S$	Stirrer Diameter	m
$e$	Elementary charge	$1.602*10^{-19}As$
$g$	gravitational acceleration	$9.81 m*s^{-1}$
$H^{cp}_{(T)}$	Henry constant at Temperature T	$mol*m^{-3}*Pa^{-1}$
$h_{LL}$	Liquid level	m
$h_{LL,g}$	Liquid level during gassing	m
$h_{RT}$	Height Rushton turbine	m
$I$	Electrical current	A
$I_{app}$	Applied electrical current	A
$i$	Current density	$A*m^{-2}$
$ i $	Absolute value of current density	$A*m^{-1}$
$k_{La}$	Gas transport coefficient	$l*s^{-1}$
$L$	Characteristic length	m
$l_{1,2}$	Distance between point 1 and 2	m
$l_E$	electrode length	m
$N_A$	Avogadro constant	$6.022*10^{23} l*mol^{-1}$
$Ne$	Newton number	-
$n_s$	Agitator speed	$l*s^{-1}$
$OCP$	Open circuit potential	V
$OD$	Optical density	-
$OD_{PC2}$	Optical density of second preculture	-
$OD_{R,i}$	Initial optical density in reactor	-
$P_{in/out}$	Total power input/total power output	W
$P_{EL}$	Electrical power	W

$P_G$	Power input gassing	W
$P_{G,S}$	Power input gassing while stirring	W
$P_H$	Power input heating	W
$P_S$	Power input stirring	-
$p_{y(tx)}$	Partial pressure of y in gas phase at timepoint x	Pa
$Q_{Loss}$	Heat loss	W
$Q_{Prod}$	Heat production	W
$R$	Resistance	$\Omega$
$R_{EL}$	Electrolyte resistance	$\Omega$
$R_{spec}$	Specific resistance	$\Omega$
$R_x$	Cell resistance	$\Omega$
$r_{e,I}$	Electron transfer rate from or to current	$1*s^{-1}$
$r_{e,m}$	Electron transfer rate from or to metabolite	$1*s^{-1}$
$r_{y,pro}$	Production rate of y	$mol*s^{-1}$
$r_{y,con}$	Consumption rate of y	$mol*s^{-1}$
$Re_{aer}$	Reynolds number aeration	-
$Re_{str}$	Reynolds number stirring	-
$T$	Temperature	K
$T_{1/2}$	Temperature of inner (1) and outer (2) medium	K
$t_{r,G}$	Hydraulic residence time of G	s
$t_x$	Time at timepoint x	s
$U_{1,2}$	Potential difference between point 1 and 2	V
$u_B$	Bubble ascent velocity	$m*s^{-1}$
$u_G$	Superficial gas velocity	$m*s^{-1}$
$U_T$	Terminal voltage	V
$V_{GH}$	Gas holdup	$m^3$
$V_{PC2}$	Volume second pre-culture	$m^3$
$V_R$	Reactor working volume	$m^3$
$\dot{V}_G$	Gas flux	$m^3*s^{-1}$
$\dot{V}$	Medium flux	$m^3*s^{-1}$
vvm	Vessel volumes per minute	-
$v_{ST}$	Stirrer tip velocity	$m*s^{-1}$
$Wa_T$	Wagner number	-
$w_y$	Fraction of y in off-gas (if not stated in-gas)	%
We	Weber number	-
$Y_P$	Production rate	$mol*d^{-1}$

$Y_{PEI}$	Specific production rate	$\text{mol} \cdot \text{m}^2 \cdot \text{d}^{-1}$
$Y_{PS}$	Product yield per substrate	$\text{mol} \cdot \text{mol}^{-1}$
$Y_{ST}$	Space time yield	$\text{mol} \cdot \text{l}^{-1} \cdot \text{d}^{-1}$
$\alpha_{1/2}$	Heat transfer coefficient of inner (1) and outer (2) medium	$\text{W} \cdot \text{m}^{-2} \cdot \text{K}^{-1}$
$\gamma$	Product purity	%
$\delta$	Wall thickness	m
$\Delta H_{R}^{298\text{K}}$	Reaction enthalpy at 298 K	$\text{kJ} \cdot \text{mol}^{-1}$
$\epsilon_{GH}$	Gas hold up	%
$\eta_{C,MES}$	Coulombic efficiency in MES	%
$\eta_{C,MFC}$	Coulombic efficiency in MFC	%
$\eta_E$	Energy efficiency	%
$\kappa$	Electrolyte conductivity	$\text{A} \cdot \text{V}^{-1}$
$\gamma$	Thermal conductivity coefficient	$\text{W} \cdot \text{m}^{-1} \cdot \text{K}^{-1}$
$\mu$	Growth rate	$\text{l} \cdot \text{s}^{-1}$
$\mu_{Vis}$	Viscosity	$\text{kg} \cdot \text{m}^{-1} \cdot \text{s}^{-1}$
$\rho_G$	Gas density	$\text{kg} \cdot \text{m}^{-3}$
$\rho_L$	Medium density	$\text{kg} \cdot \text{m}^{-3}$
$\sigma$	Interfacial tension	$\text{N} \cdot \text{m}^{-1}$

## Abbreviations

AEM	Anion exchange membrane
BES	Bioelectrochemical system
CEM	Cation exchange membrane
CV	Cyclic voltammetry
GC	Gas chromatography
HPLC	High performance liquid chromatography
MEC	Microbial electrolysis cell
MES	Microbial electrosynthesis
MFC	Microbial fuel cell
PEEK	Polyether ethylketone
PEX	Proton exchange membrane
ppi	Pores per inch
RVC	Reticulated Vitreous Carbon
SHE	Standard hydrogen electrode
STR	Stirred tank reactor

## References

- Akita, K., Yoshida, F., 1974. Bubble Size, Interfacial Area, and Liquid-Phase Mass Transfer Coefficient in Bubble Columns. *Ind. Eng. Chem. Process Des. Dev.* 13, 84–91. <https://doi.org/10.1021/i260049a016>
- Alpana, S., Vishwakarma, P., Adhya, T.K., Inubushi, K., Dubey, S.K., 2017. Molecular ecological perspective of methanogenic archaeal community in rice agroecosystem. *Sci. Total Environ.* 596–597, 136–146. <https://doi.org/10.1016/j.scitotenv.2017.04.011>
- Andriani, D., Wresta, A., Atmaja, T.D., Saepudin, A., 2014. A Review on Optimization Production and Upgrading Biogas Through CO<sub>2</sub> Removal Using Various Techniques. *Appl. Biochem. Biotechnol.* 172, 1909–1928. <https://doi.org/10.1007/s12010-013-0652-x>
- Andricacos, P.C., Searson, P.C., Reidsema-Simpson, C., Allongue, P., Stickney, J.L., Oleszek, G.M., 1999. *Electrochemical Processing in ULSI Fabrication and Semiconductor/Metal Deposition II*. The Electrochemical Society, Pennington, NJ.
- Babanova, S., Carpenter, K., Phadke, S., Suzuki, S., Ishii, S., Phan, T., Grossi-Soyster, E., Flynn, M., Hogan, J., Bretschger, O., 2017. The Effect of Membrane Type on the Performance of Microbial Electrosynthesis Cells for Methane Production. *J. Electrochem. Soc.* 164, H3015–H3023. <https://doi.org/10.1149/2.0051703jes>
- Bajracharya, S., Srikanth, S., Mohanakrishna, G., Zacharia, R., Strik, D.P., Pant, D., 2017. Biotransformation of carbon dioxide in bioelectrochemical systems: State of the art and future prospects. *J. Power Sources* 356, 256–273.
- Bär, K., Mörs, F., Götz, M., Graf, F., 2015. Vergleich der biologischen und katalytischen Methanisierung für den Einsatz bei PtG-Konzepten. *gwf-Gas* 7, 1–8.
- Bassani, I., Kougiaris, P.G., Treu, L., Angelidaki, I., 2015. Biogas Upgrading via Hydrogenotrophic Methanogenesis in Two-Stage Continuous Stirred Tank Reactors at Mesophilic and Thermophilic Conditions. *Environ. Sci. Technol.* 49, 12585–12593. <https://doi.org/10.1021/acs.est.5b03451>
- Battle-Vilanova, P., Puig, S., Gonzalez-Olmos, R., Balaguer, M.D., Colprim, J., 2016. Continuous acetate production through microbial electrosynthesis from CO<sub>2</sub> with microbial mixed culture. *J. Chem. Technol. Biotechnol.* 91, 921–927. <https://doi.org/10.1002/jctb.4657>
- Battle-Vilanova, P., Puig, S., Gonzalez-Olmos, R., Vilajeliu-Pons, A., Balaguer, M.D., Colprim, J., 2015. Deciphering the electron transfer mechanisms for biogas upgrading to biomethane within a mixed culture biocathode. *RSC Adv.* 5, 52243–52251. <https://doi.org/10.1039/C5RA09039C>
- Baudler, A., Schmidt, I., Langner, M., Greiner, A., Schröder, U., 2015. Does it have to be carbon? Metal anodes in microbial fuel cells and related bioelectrochemical systems. *Energy Environ. Sci.* 8, 2048–2055. <https://doi.org/10.1039/C5EE00866B>
- Beese-Vasbender, P.F., Grote, J.-P., Garrelfs, J., Stratmann, M., Mayrhofer, K.J.J., 2015. Selective microbial electrosynthesis of methane by a pure culture of a marine lithoautotrophic archaeon. *Bioelectrochemistry* 102, 50–55. <https://doi.org/10.1016/j.bioelechem.2014.11.004>
- Bhandari, H., Anoop, S., K., S., 2012. Conducting Polymer Nanocomposites for Anticorrosive and Antistatic Applications, in: *Nanocomposites - New Trends and Developments*. InTech, p. Ch. 0. <https://doi.org/10.5772/50470>
- Blasco-Gómez, R., Battle-Vilanova, P., Villano, M., Balaguer, M., Colprim, J., Puig, S., 2017. On the Edge of Research and Technological Application: A Critical Review of Electromethanogenesis. *Int. J. Mol. Sci.* 18, 874. <https://doi.org/10.3390/ijms18040874>
- Bo, T., Zhu, X., Zhang, L., Tao, Y., He, X., Li, D., Yan, Z., 2014. A new upgraded biogas production process: Coupling microbial electrolysis cell and anaerobic digestion in single-chamber, barrel-shape stainless steel reactor. *Electrochem. Commun.* 45, 67–70. <https://doi.org/10.1016/j.elecom.2014.05.026>
- Bretschger, O., Obraztsova, A., Sturm, C.A., In, S.C., Gorby, Y.A., Reed, S.B., Culley, D.E., Reardon, C.L., Barua, S., Romine, M.F., Zhou, J., Beliaev, A.S., Bouhenni, R., Saffarini, D., Mansfeld, F., Kim, B.H., Fredrickson, J.K., Nealson, K.H., 2007. Current production and metal oxide reduction by *Shewanella oneidensis* MR-1 wild type and mutants. *Appl. Environ. Microbiol.* 73, 7003–7012. <https://doi.org/10.1128/AEM.01087-07>
- Brooks, K.P., Hu, J., Zhu, H., Kee, R.J., 2007. Methanation of carbon dioxide by hydrogen reduction using the Sabatier process in microchannel reactors. *Chem. Eng. Sci.* 62, 1161–1170. <https://doi.org/10.1016/j.ces.2006.11.020>
- Brown, R.K., Harnisch, F., Wirth, S., Wahlandt, H., Dockhorn, T., Dichtl, N., Schröder, U., 2014. Evaluating the effects of scaling up on the performance of bioelectrochemical systems using a technical scale microbial electrolysis cell. *Bioresour. Technol.* 163, 206–213. <https://doi.org/10.1016/j.biortech.2014.04.044>

- Butler, C.S., Lovley, D.R., 2016. How to Sustainably Feed a Microbe : Strategies for Biological Production of Carbon-Based Commodities with Renewable Electricity. *Front. Microbiol.* 7, 1879. <https://doi.org/10.3389/fmicb.2016.01879>
- Chae, K.J., Choi, M., Ajayi, F.F., Park, W., Chang, I.S., Kim, I.S., 2008. Mass Transport through a Proton Exchange Membrane (Nafion) in Microbial Fuel Cells. *Energy & Fuels* 22, 169–176. <https://doi.org/10.1021/ef700308u>
- Cheng, K.Y., Ho, G., Cord-Ruwisch, R., 2011. Novel Methanogenic Rotatable Bioelectrochemical System Operated with Polarity Inversion. *Environ. Sci. Technol.* 45, 796–802. <https://doi.org/10.1021/es102482j>
- Cheng, S., Logan, B.E., 2011. Increasing power generation for scaling up single-chamber air cathode microbial fuel cells. *Bioresour. Technol.* 102, 4468–4473. <https://doi.org/10.1016/j.biortech.2010.12.104>
- Cheng, S., Logan, B.E., 2007. Ammonia treatment of carbon cloth anodes to enhance power generation of microbial fuel cells. *Electrochem. commun.* 9, 492–496. <https://doi.org/10.1016/j.elecom.2006.10.023>
- Cheng, S., Xing, D., Call, D.F., Logan, B.E., 2009. Direct Biological Conversion of Electrical Current into Methane by Electromethanogenesis. *Environ. Sci. Technol.* 43, 3953–3958. <https://doi.org/10.1021/es803531g>
- Chisti, Y., Moo-Young, M., 1989. On the calculation of shear rate and apparent viscosity in airlift and bubble column bioreactors. *Biotechnol. Bioeng.* 34, 1391–1392. <https://doi.org/10.1002/bit.260341107>
- Chmiel, H., 2011. *Bioprozesstechnik*, 3., neu be. ed. Spektrum Akademischer Verlag, Heidelberg. <https://doi.org/10.1007/978-3-8274-2477-8>
- Choi, O., Sang, B.-I., 2016. Extracellular electron transfer from cathode to microbes: application for biofuel production. *Biotechnol. Biofuels* 9, 11. <https://doi.org/10.1186/s13068-016-0426-0>
- Clauwaert, P., Aelterman, P., Pham, T.H., De Schamphelaire, L., Carballa, M., Rabaey, K., Verstraete, W., 2008. Minimizing losses in bio-electrochemical systems: The road to applications. *Appl. Microbiol. Biotechnol.* 79, 901–913. <https://doi.org/10.1007/s00253-008-1522-2>
- Cusick, R.D., Bryan, B., Parker, D.S., Merrill, M.D., Mehanna, M., Kiely, P.D., Liu, G., Logan, B.E., 2011. Performance of a pilot-scale continuous flow microbial electrolysis cell fed winery wastewater. *Appl. Microbiol. Biotechnol.* 89, 2053–2063. <https://doi.org/10.1007/s00253-011-3130-9>
- de Campos Rodrigues, T., Rosenbaum, M.A., 2014. Microbial Electroreduction: Screening for New Cathodic Biocatalysts. *ChemElectroChem* 1, 1916–1922. <https://doi.org/10.1002/celc.201402239>
- Deckwer, W.-D., Guenzel, B., Yonsel, S., Carduck, F.-J., Kretschmann, J., 1991. Anaerobic microbial conversion of substrate to metabolite. DE4010523 A1.
- Deutzmann, J.S., Sahin, M., Spormann, A.M., 2015. Extracellular Enzymes Facilitate Electron Uptake in Biocorrosion and Bioelectrosynthesis. *MBio* 6, e00496-15. <https://doi.org/10.1128/mBio.00496-15>
- Deutzmann, J.S., Spormann, A.M., 2017. Enhanced microbial electrosynthesis by using defined co-cultures. *ISME J.* 11, 704–714. <https://doi.org/10.1038/ismej.2016.149>
- Dewan, A., Beyenal, H., Lewandowski, Z., 2008. Scaling up microbial fuel cells. *Environ. Sci. Technol.* 42, 7643–7648. <https://doi.org/10.1021/es800775d>
- Ditzig, J., Liu, H., Logan, B.E., 2007. Production of hydrogen from domestic wastewater using a bioelectrochemically assisted microbial reactor (BEAMR). *Int. J. Hydrogen Energy* 32, 2296–2304. <https://doi.org/10.1016/j.ijhydene.2007.02.035>
- Du, Z., Li, H., Gu, T., 2007. A state of the art review on microbial fuel cells: A promising technology for wastewater treatment and bioenergy. *Biotechnol. Adv.* 25, 464–482. <https://doi.org/10.1016/j.biotechadv.2007.05.004>
- Dürre, P., Eikmanns, B.J., 2015. C1-carbon sources for chemical and fuel production by microbial gas fermentation. *Curr. Opin. Biotechnol.* 35, 63–72. <https://doi.org/10.1016/j.copbio.2015.03.008>
- Durst, F., 2008. Similarity Theory, in: Durst, F. (Ed.), *Fluid Mechanics*. Springer Berlin Heidelberg, Berlin, Heidelberg, pp. 193–219. [https://doi.org/10.1007/978-3-540-71343-2\\_7](https://doi.org/10.1007/978-3-540-71343-2_7)
- Dykstra, C.M., Pavlostathis, S.G., 2017. Evaluation of gas and carbon transport in a methanogenic bioelectrochemical system (BES). *Biotechnol. Bioeng.* 114, 961–969. <https://doi.org/10.1002/bit.26230>
- Dykstra, J.E., Biesheuvel, P.M., Bruning, H., Ter Heijne, A., 2014. Theory of ion transport with fast acid-base equilibrations in bioelectrochemical systems. *Phys. Rev. E* 90, 13302. <https://doi.org/10.1103/PhysRevE.90.013302>

- Enzmann, F., Mayer, F., Stöckl, M., Mangold, K.-M., Hommel, R., Holtmann, D., 2019. Transferring bioelectrochemical processes from H-cells to a scalable bubble column reactor. *Chem. Eng. Sci.* 193, 133–143. <https://doi.org/10.1016/j.ces.2018.08.056>
- Escapa, A., San-Martín, M.I., Mateos, R., Morán, A., 2015. Scaling-up of membraneless microbial electrolysis cells (MECs) for domestic wastewater treatment: Bottlenecks and limitations. *Bioresour. Technol.* 180, 72–78. <https://doi.org/10.1016/j.biortech.2014.12.096>
- Fachverband Biogas e.V., n.d. Zahlen und Fakten. URL <http://www.biogas.org/edcom/webfbv.nsf/id/DE-Zahlen-und-Fakten> (accessed 4.18.17).
- Fan, Y., Sharbrough, E., Liu, H., 2008. Quantification of the Internal Resistance Distribution of Microbial Fuel Cells. *Environ. Sci. Technol.* 42, 8101–8107. <https://doi.org/10.1021/es801229j>
- Fu, Q., Kuramochi, Y., Fukushima, N., Maeda, H., Sato, K., Kobayashi, H., 2015. Bioelectrochemical Analyses of the Development of a Thermophilic Biocathode Catalyzing Electromethanogenesis. *Environ. Sci. Technol.* 49, 1225–1232. <https://doi.org/10.1021/es5052233>
- Gajaraj, S., Huang, Y., Zheng, P., Hu, Z., 2017. Methane production improvement and associated methanogenic assemblages in bioelectrochemically assisted anaerobic digestion. *Biochem. Eng. J.* 117, 105–112. <https://doi.org/10.1016/j.bej.2016.11.003>
- Garcia, J.-L., Patel, B.K., Ollivier, B., 2000. Taxonomic, Phylogenetic, and Ecological Diversity of Methanogenic Archaea. *Anaerobe* 6, 205–226. <https://doi.org/10.1006/anae.2000.0345>
- Geppert, F., Liu, D., van Eerten-Jansen, M., Weidner, E., Buisman, C., ter Heijne, A., 2016. Bioelectrochemical Power-to-Gas: State of the Art and Future Perspectives. *Trends Biotechnol.* 34, 879–894. <https://doi.org/10.1016/j.tibtech.2016.08.010>
- Ghaib, K., Nitz, K., Ben-Fares, F.-Z., 2016. Katalytische Methanisierung von Kohlenstoffdioxid. *Chemie Ing. Tech.* 88, 1435–1443. <https://doi.org/10.1002/cite.201600066>
- Gil-Carrera, L., Escapa, A., Mehta, P., Santoyo, G., Guiot, S.R., Morán, A., Tartakovsky, B., 2013. Microbial electrolysis cell scale-up for combined wastewater treatment and hydrogen production. *Bioresour. Technol.* 130, 584–591. <https://doi.org/10.1016/j.biortech.2012.12.062>
- Gil-Carrera, L., Mehta, P., Escapa, A., Morán, A., García, V., Guiot, S.R., Tartakovsky, B., 2011. Optimizing the electrode size and arrangement in a microbial electrolysis cell. *Bioresour. Technol.* 102, 9593–9598. <https://doi.org/10.1016/j.biortech.2011.08.026>
- Gonçalves, L.C.P., Mansouri, H.R., Bastos, E.L., Abdellah, M., Fadiga, B.S., Sá, J., Rudroff, F., Mihovilovic, M.D., 2019. Morpholine-based buffers activate aerobic photobiocatalysis via spin correlated ion pair formation. *Catal. Sci. Technol.* <https://doi.org/10.1039/c8cy02524j>
- Gorby, Y.A., Yanina, S., McLean, J.S., Rosso, K.M., Moyles, D., Dohnalkova, A., Beveridge, T.J., Chang, I.S., Kim, B.H., Kim, K.S., Culley, D.E., Reed, S.B., Romine, M.F., Saffarini, D.A., Hill, E.A., Shi, L., Elias, D.A., Kennedy, D.W., Pinchuk, G., Watanabe, K., Ishii, S., Logan, B., Nealson, K.H., Fredrickson, J.K., 2006. Electrically conductive bacterial nanowires produced by *Shewanella oneidensis* strain MR-1 and other microorganisms. *Proc. Natl. Acad. Sci.* 103, 11358–11363. <https://doi.org/10.1073/pnas.0604517103>
- Günther, B., 1975. Dimensional analysis and theory of biological similarity. *Physiol. Rev.* 55, 659–699. <https://doi.org/10.1152/physrev.1975.55.4.659>
- Guo, Z., Thangavel, S., Wang, L., He, Z., Cai, W., Wang, A., Liu, W., 2017. Efficient Methane Production from Beer Wastewater in a Membraneless Microbial Electrolysis Cell with a Stacked Cathode: The Effect of the Cathode/Anode Ratio on Bioenergy Recovery. *Energy & Fuels* 31, 615–620. <https://doi.org/10.1021/acs.energyfuels.6b02375>
- Hafenbradl, D., Hein, M., 2015. A solution for energy storage. *Gas Energy* 26–29.
- Hara, M., Onaka, Y., Kobayashi, H., Fu, Q., Kawaguchi, H., Vilcaez, J., Sato, K., 2013. Mechanism of Electromethanogenic Reduction of CO<sub>2</sub> by a Thermophilic Methanogen. *Energy Procedia* 37, 7021–7028. <https://doi.org/10.1016/j.egypro.2013.06.637>
- Harnisch, F., Schröder, U., Scholz, F., 2008. The Suitability of Monopolar and Bipolar Ion Exchange Membranes as Separators for Biological Fuel Cells. *Environ. Sci. Technol.* 42, 1740–1746. <https://doi.org/10.1021/es702224a>
- Hass, V.C., Pörtner, R., 2011. Praxis der Bioprozesstechnik: Mit virtuellem Praktikum, 2. Aufl. ed. Spektrum Akad. Verl., Heidelberg.

- He, Z., Mansfeld, F., 2009. Exploring the use of electrochemical impedance spectroscopy (EIS) in microbial fuel cell studies. *Energy Environ. Sci.* 2, 215–219. <https://doi.org/10.1039/b814914c>
- Heidrich, E.S., Edwards, S.R., Dolfing, J., Cotterill, S.E., Curtis, T.P., 2014. Performance of a pilot scale microbial electrolysis cell fed on domestic wastewater at ambient temperatures for a 12month period. *Bioresour. Technol.* 173, 87–95. <https://doi.org/10.1016/j.biortech.2014.09.083>
- Heijnen, J.J., 2002. Bioenergetics of Microbial Growth, in: *Encyclopedia of Bioprocess Technology*. John Wiley & Sons, Inc., Hoboken, NJ, USA, pp. 267–290. <https://doi.org/10.1002/0471250589.ebt026>
- Hindatu, Y., Annuar, M.S.M., Gumel, A.M., 2017. Mini-review: Anode modification for improved performance of microbial fuel cell. *Renew. Sustain. Energy Rev.* 73, 236–248. <https://doi.org/10.1016/j.rser.2017.01.138>
- Hintermayer, S., Yu, S., Krömer, J.O., Weuster-Botz, D., 2016. Anodic respiration of *Pseudomonas putida* KT2440 in a stirred-tank bioreactor. *Biochem. Eng. J.* 115, 1–13. <https://doi.org/10.1016/j.bej.2016.07.020>
- Hirano, S., Matsumoto, N., Morita, M., Sasaki, K., Ohmura, N., 2013. Electrochemical control of redox potential affects methanogenesis of the hydrogenotrophic methanogen *Methanothermobacter thermautotrophicus*. *Lett. Appl. Microbiol.* 315–321. <https://doi.org/10.1111/lam.12059>
- Jabłoński, S.J., Rodowicz, P., Łukaszewicz, M., 2015. Methanogens. URL <http://metanogen.biotech.uni.wroc.pl/> (accessed 4.18.17).
- Janicek, A., Fan, Y., Liu, H., 2014. Design of microbial fuel cells for practical application: a review and analysis of scale-up studies. *Biofuels* 5, 79–92. <https://doi.org/10.4155/bfs.13.69>
- Jiang, Y., Su, M., Li, D., 2014. Removal of Sulfide and Production of Methane from Carbon Dioxide in Microbial Fuel Cells–Microbial Electrolysis Cell (MFCs–MEC) Coupled System. *Appl. Biochem. Biotechnol.* 172, 2720–2731. <https://doi.org/10.1007/s12010-013-0718-9>
- Jiang, Y., Su, M., Zhang, Y., Zhan, G., Tao, Y., Li, D., 2013. Bioelectrochemical systems for simultaneously production of methane and acetate from carbon dioxide at relatively high rate. *Int. J. Hydrogen Energy* 38, 3497–3502. <https://doi.org/10.1016/j.ijhydene.2012.12.107>
- Jones, W.J., Paynter, M.J.B., Gupta, R., 1983. Characterization of *Methanococcus maripaludis* sp. nov., a new methanogen isolated from salt marsh sediment. *Arch. Microbiol.* 135, 91–97. <https://doi.org/10.1007/BF00408015>
- Jourdin, L., Freguía, S., Donose, B.C., Chen, J., Wallace, G.G., Keller, J., Flexer, V., 2014. A novel carbon nanotube modified scaffold as an efficient biocathode material for improved microbial electrosynthesis. *J. Mater. Chem. A* 2, 13093. <https://doi.org/10.1039/C4TA03101F>
- Kadier, A., Simayi, Y., Abdeshahian, P., Azman, N.F., Chandrasekhar, K., Kalil, M.S., 2016. A comprehensive review of microbial electrolysis cells (MEC) reactor designs and configurations for sustainable hydrogen gas production. *Alexandria Eng. J.* 55, 427–443. <https://doi.org/10.1016/j.aej.2015.10.008>
- Kantarci, N., Borak, F., Ulgen, K.O., 2005. Bubble column reactors. *Process Biochem.* 40, 2263–2283. <https://doi.org/10.1016/j.procbio.2004.10.004>
- Ki, D., Papat, S.C., Torres, C.I., 2016. Reduced overpotentials in microbial electrolysis cells through improved design, operation, and electrochemical characterization. *Chem. Eng. J.* 287, 181–188. <https://doi.org/10.1016/j.cej.2015.11.022>
- Kiener, A., Leisinger, T., 1983. Oxygen Sensitivity of Methanogenic Bacteria. *Syst. Appl. Microbiol.* 4, 305–312. [https://doi.org/10.1016/S0723-2020\(83\)80017-4](https://doi.org/10.1016/S0723-2020(83)80017-4)
- Kim, J.R., Cheng, S., Oh, S.-E., Logan, B.E., 2007. Power Generation Using Different Cation, Anion, and Ultrafiltration Membranes in Microbial Fuel Cells. *Environ. Sci. Technol.* 41, 1004–1009. <https://doi.org/10.1021/es062202m>
- Kobayashi, H., Saito, N., Fu, Q., Kawaguchi, H., Vilcaez, J., Wakayama, T., Maeda, H., Sato, K., 2013. Bio-electrochemical property and phylogenetic diversity of microbial communities associated with bioelectrodes of an electromethanogenic reactor. *J. Biosci. Bioeng.* 116, 114–117. <https://doi.org/10.1016/j.jbiosc.2013.01.001>
- Koch, C., Harnisch, F., 2016a. What Is the Essence of Microbial Electroactivity? *Front. Microbiol.* 7, 1890. <https://doi.org/10.3389/fmicb.2016.01890>
- Koch, C., Harnisch, F., 2016b. Is there a Specific Ecological Niche for Electroactive Microorganisms? *ChemElectroChem* 3, 1282–1295. <https://doi.org/10.1002/celec.201600079>
- Krieg, T., Enzmann, F., Sell, D., Schrader, J., Holtmann, D., 2017. Simulation of the current generation of a microbial fuel cell in a laboratory wastewater treatment plant. *Appl. Energy* 195, 942–949.

- <https://doi.org/10.1016/j.apenergy.2017.03.101>
- Krieg, T., Phan, L.M.P., Wood, J.A., Sydow, A., Vassilev, I., Krömer, J.O., Mangold, K.-M., Holtmann, D., 2018a. Characterization of a membrane separated and a membrane-less electrobioreactor for bioelectrochemical syntheses. *Biotechnol. Bioeng.* <https://doi.org/10.1002/bit.26600>
- Krieg, T., Sydow, A., Faust, S., Huth, I., Holtmann, D., 2018b. CO<sub>2</sub> to Terpenes: Autotrophic and Electroautotrophic  $\alpha$ -Humulene Production with *Cupriavidus necator*. *Angew. Chemie Int. Ed.* 57, 1879–1882. <https://doi.org/10.1002/anie.201711302>
- Krieg, T., Sydow, A., Schröder, U., Schrader, J., Holtmann, D., 2014. Reactor concepts for bioelectrochemical syntheses and energy conversion. *Trends Biotechnol.* 32, 645–655. <https://doi.org/10.1016/j.tibtech.2014.10.004>
- Kumar, R., Singh, L., Zularisam, A.W., Hai, F.I., 2018. Microbial fuel cell is emerging as a versatile technology: a review on its possible applications, challenges and strategies to improve the performances. *Int. J. Energy Res.* 42, 369–394. <https://doi.org/10.1002/er.3780>
- Kuramochi, Y., Fu, Q., Kobayashi, H., Ikarashi, M., Wakayama, T., Kawaguchi, H., Vilcaez, J., Maeda, H., Sato, K., 2013. Electromethanogenic CO<sub>2</sub> Conversion by Subsurface-reservoir Microorganisms. *Energy Procedia* 37, 7014–7020. <https://doi.org/10.1016/j.egypro.2013.06.636>
- Lang, K., Schuldes, J., Klingl, A., Poehlein, A., Daniel, R., Brune, A., 2015. New mode of energy metabolism in the seventh order of methanogens as revealed by comparative genome analysis of “*Candidatus Methanoplasma termitum*.” *Appl. Environ. Microbiol.* 81, 1338–1352. <https://doi.org/10.1128/AEM.03389-14>
- Lanthier, M., Gregory, K.B., Lovley, D.R., 2008. Growth with high planktonic biomass in *Shewanella oneidensis* fuel cells. *FEMS Microbiol. Lett.* 278, 29–35. <https://doi.org/10.1111/j.1574-6968.2007.00964.x>
- Lee, J.-Y., Lee, S.-H., Park, H.-D., 2016. Enrichment of specific electro-active microorganisms and enhancement of methane production by adding granular activated carbon in anaerobic reactors. *Bioresour. Technol.* 205, 205–212. <https://doi.org/10.1016/j.biortech.2016.01.054>
- Leipertz, A., 2006. Engineering thermodynamics for mechanical engineers, production engineers, and chemical and bioengineers, 3., korrig. ed. ESYTEC Energie- und Systemtechnik GmbH, Erlangen.
- Leong, J.X., Daud, W.R.W., Ghasemi, M., Liew, K. Ben, Ismail, M., 2013. Ion exchange membranes as separators in microbial fuel cells for bioenergy conversion: A comprehensive review. *Renew. Sustain. Energy Rev.* 28, 575–587. <https://doi.org/10.1016/j.rser.2013.08.052>
- Li, J., He, Z., 2016. Development of a dynamic mathematical model for membrane bioelectrochemical reactors with different configurations. *Environ. Sci. Pollut. Res.* 23, 3897–3906. <https://doi.org/10.1007/s11356-015-5611-3>
- Liu, F., Rotaru, A.-E., Shrestha, P.M., Malvankar, N.S., Nevin, K.P., Lovley, D.R., 2012. Promoting direct interspecies electron transfer with activated carbon. *Energy Environ. Sci.* 5, 8982. <https://doi.org/10.1039/c2ee22459c>
- Liu, Y., Whitman, W.B., 2008. Metabolic, Phylogenetic, and Ecological Diversity of the Methanogenic Archaea. *Ann. N. Y. Acad. Sci.* 1125, 171–189. <https://doi.org/10.1196/annals.1419.019>
- Logan, B.E., 2010a. Scaling up microbial fuel cells and other bioelectrochemical systems. *Appl. Microbiol. Biotechnol.* 85, 1665–1671. <https://doi.org/10.1007/s00253-009-2378-9>
- Logan, B.E., 2010b. Materials for BES, in: Rabaey, K., Angenent, L.T., Schröder, U., Keller, J. (Eds.), *Bioelectrochemical Systems*. IWA Publishing, London, pp. 185–204.
- Logan, B.E., Hamelers, B., Rozendal, R., Schröder, U., Keller, J., Freguia, S., Aelterman, P., Verstraete, W., Rabaey, K., 2006. Microbial fuel cells: Methodology and technology. *Environ. Sci. Technol.* 40, 5181–5192. <https://doi.org/10.1021/es0605016>
- Logan, B.E., Rabaey, K., 2012. Conversion of Wastes into Bioelectricity and Chemicals by Using Microbial Electrochemical Technologies. *Science* (80-. ). 337, 686–690. <https://doi.org/10.1126/science.1217412>
- Lohner, S.T., Deutzmann, J.S., Logan, B.E., Leigh, J., Spormann, A.M., 2014. Hydrogenase-independent uptake and metabolism of electrons by the archaeon *Methanococcus maripaludis*. *ISME J.* 8, 1673–1681. <https://doi.org/10.1038/ismej.2014.82>
- Lovley, D.R., Nevin, K.P., 2013. Electrobiocommodities: powering microbial production of fuels and commodity chemicals from carbon dioxide with electricity. *Curr. Opin. Biotechnol.* 24, 385–390. <https://doi.org/10.1016/j.copbio.2013.02.012>

- Lunsford, J.H., 2000. Catalytic conversion of methane to more useful chemicals and fuels: a challenge for the 21st century. *Catal. Today* 63, 165–174. [https://doi.org/10.1016/S0920-5861\(00\)00456-9](https://doi.org/10.1016/S0920-5861(00)00456-9)
- Luo, G., Angelidaki, I., 2012. Integrated biogas upgrading and hydrogen utilization in an anaerobic reactor containing enriched hydrogenotrophic methanogenic culture. *Biotechnol. Bioeng.* 109, 2729–2736. <https://doi.org/10.1002/bit.24557>
- Luo, G., Johansson, S., Boe, K., Xie, L., Zhou, Q., Angelidaki, I., 2012. Simultaneous hydrogen utilization and in situ biogas upgrading in an anaerobic reactor. *Biotechnol. Bioeng.* 109, 1088–1094. <https://doi.org/10.1002/bit.24360>
- Luo, X., Zhang, F., Liu, J., Zhang, X., Huang, X., Logan, B.E., 2014. Methane Production in Microbial Reverse-Electrodialysis Methanogenesis Cells (MRMCs) Using Thermolytic Solutions. *Environ. Sci. Technol.* 48, 8911–8918. <https://doi.org/10.1021/es501979z>
- Lyu, Z., Jain, R., Smith, P., Fetchko, T., Yan, Y., Whitman, W.B., 2016. Engineering the Autotroph *Methanococcus maripaludis* for Geraniol Production. *ACS Synth. Biol.* 5, 577–581. <https://doi.org/10.1021/acssynbio.5b00267>
- Marques, M.P.C., Cabral, J.M.S., Fernandes, P., 2010. Bioprocess scale-up: quest for the parameters to be used as criterion to move from microreactors to lab-scale. *J. Chem. Technol. Biotechnol.* 85, 1184–1198. <https://doi.org/10.1002/jctb.2387>
- Martín, A.J., Larrazábal, G.O., Pérez-Ramírez, J., 2015. Towards sustainable fuels and chemicals through the electrochemical reduction of CO<sub>2</sub>: Lessons from water electrolysis. *Green Chem* 17, 5114–5130. <https://doi.org/10.1039/c5gc01893e>
- Meier, K., Herweg, E., Schmidt, B., Klement, T., Regestein, L., Büchs, J., 2013. Quantifying the release of polymer additives from single-use materials by respiration activity monitoring. *Polym. Test.* 32, 1064–1071. <https://doi.org/10.1016/j.polymertesting.2013.06.004>
- Min, F., Kopke, M., Dennis, S., 2013. Gas Fermentation for Commercial Biofuels Production, in: Fang, Z. (Ed.), *Liquid, Gaseous and Solid Biofuels - Conversion Techniques*. InTech, pp. 125–173. <https://doi.org/10.5772/52164>
- Montes, F.J., Galan, M.A., Cerro, R.L., 1999. Mass transfer from oscillating bubbles in bioreactors. *Chem. Eng. Sci.* 54, 3127–3136. [https://doi.org/10.1016/S0009-2509\(98\)00314-5](https://doi.org/10.1016/S0009-2509(98)00314-5)
- Newton, G.J., Mori, S., Nakamura, R., Hashimoto, K., Watanabe, K., 2009. Analyses of Current-Generating Mechanisms of *Shewanella loihica* PV-4 and *Shewanella oneidensis* MR-1 in Microbial Fuel Cells. *Appl. Environ. Microbiol.* 75, 7674–7681. <https://doi.org/10.1128/AEM.01142-09>
- Nicolopoulou, E.P., Kontargyri, V.T., Gonos, I.F., Tsekouras, G.J., Pyrgioti, E.C., Stathopoulos, I.A., Campus, Z., Science, C., Academy, H.N., Hatzikiakiou, T., 2013. Experimental Application of the Similarity Theory on Scaled Strip Electrode Configurations for the calculation of the grounding impedance, in: 18th International Symposium on High Voltage Engineering. Seoul, pp. 434–439.
- Nie, H., Zhang, T., Cui, M., Lu, H., Lovley, D.R., Russell, T.P., 2013. Improved cathode for high efficient microbial-catalyzed reduction in microbial electrosynthesis cells. *Phys. Chem. Chem. Phys.* 15, 14290. <https://doi.org/10.1039/c3cp52697f>
- Olah, G.A., 2005. Beyond Oil and Gas: The Methanol Economy. *Angew. Chemie Int. Ed.* 44, 2636–2639. <https://doi.org/10.1002/anie.200462121>
- Patil, S.A., Gildemyn, S., Pant, D., Zengler, K., Logan, B.E., Rabaey, K., 2015. A logical data representation framework for electricity-driven bioproduction processes. *Biotechnol. Adv.* 33, 736–744. <https://doi.org/10.1016/j.biotechadv.2015.03.002>
- Pauss, A., Andre, G., Perrier, M., Guiot, S.R., 1990. Liquid-to-Gas Mass Transfer in Anaerobic Processes: Inevitable Transfer Limitations of Methane and Hydrogen in the Biomethanation Process 56, 1636–1644.
- Pozo, G., Jourdin, L., Lu, Y., Ledezma, P., Keller, J., Freguia, S., 2015. *Methanobacterium* enables high rate electricity-driven autotrophic sulfate reduction. *RSC Adv.* 5, 89368–89374. <https://doi.org/10.1039/C5RA18444D>
- Rabaey, K., Clauwaert, P., Aelterman, P., Verstraete, W., 2005. Tubular Microbial Fuel Cells for Efficient Electricity Generation 39, 8077–8082. <https://doi.org/10.1021/es050986i>
- Rader, G.K., Logan, B.E., 2010. Multi-electrode continuous flow microbial electrolysis cell for biogas production from acetate. *Int. J. Hydrogen Energy* 35, 8848–8854. <https://doi.org/10.1016/j.ijhydene.2010.06.033>
- Ren, T., Patel, M., Blok, K., 2008. Steam cracking and methane to olefins: Energy use, CO<sub>2</sub> emissions and production costs. *Energy* 817–833. <https://doi.org/10.1016/j.energy.2008.01.002>
- Ribot-Llobet, E., Nam, J.-Y., Tokash, J.C., Guisasola, A., Logan, B.E., 2013. Assessment of four different cathode materials

- at different initial pHs using unbuffered catholytes in microbial electrolysis cells. *Int. J. Hydrogen Energy* 38, 2951–2956. <https://doi.org/10.1016/j.ijhydene.2012.12.037>
- Rodriguez, J., Premier, G.C., 2010. Towards a mathematical description of bioelectrochemical systems, in: Rabaey, K. (Ed.), *Bioelectrochemical Systems, Integrated Environmental Technology Series*. IWA Publishing, London and New York, pp. 423–448.
- Rosa, L.F.M., Hunger, S., Gimkiewicz, C., Zehnsdorf, A., Harnisch, F., 2016. Paving the way for bioelectrotechnology: Integrating electrochemistry into bioreactors. *Eng. Life Sci.* 17, 77–85. <https://doi.org/10.1002/elsc.201600105>
- Rosellen, M., Gezork, K., 2017. Auslegungssache Scale up und Engineering von Fermentern. *CITplus* 20, 16–18.
- Rossi, G., 2001. The design of bioreactors. *Hydrometallurgy* 59, 217–231. [https://doi.org/10.1016/S0304-386X\(00\)00161-4](https://doi.org/10.1016/S0304-386X(00)00161-4)
- Rotaru, A.-E., Shrestha, P.M., Liu, F., Markovaite, B., Chen, S., Nevin, K.P., Lovley, D.R., 2014a. Direct Interspecies Electron Transfer between *Geobacter metallireducens* and *Methanosarcina barkeri*. *Appl. Environ. Microbiol.* 80, 4599–4605. <https://doi.org/10.1128/AEM.00895-14>
- Rotaru, A.-E., Shrestha, P.M., Liu, F., Shrestha, M., Shrestha, D., Embree, M., Zengler, K., Wardman, C., Nevin, K.P., Lovley, D.R., 2014b. A new model for electron flow during anaerobic digestion: direct interspecies electron transfer to *Methanosaeta* for the reduction of carbon dioxide to methane. *Energy Environ. Sci.* 7, 408–415. <https://doi.org/10.1039/C3EE42189A>
- Roy, S., Schievano, A., Pant, D., 2016. Electro-stimulated microbial factory for value added product synthesis. *Bioresour. Technol.* 213, 129–139. <https://doi.org/10.1016/j.biortech.2016.03.052>
- Sander, R., 2015. Compilation of Henry's law constants (version 4.0) for water as solvent. *Atmos. Chem. Phys.* 15, 4399–4981. <https://doi.org/10.5194/acp-15-4399-2015>
- Sasaki, D., Sasaki, K., Watanabe, A., Morita, M., Igarashi, Y., Ohmura, N., 2013a. Efficient production of methane from artificial garbage waste by a cylindrical bioelectrochemical reactor containing carbon fiber textiles. *AMB Express* 3, 17. <https://doi.org/10.1186/2191-0855-3-17>
- Sasaki, D., Sasaki, K., Watanabe, A., Morita, M., Matsumoto, N., Igarashi, Y., Ohmura, N., 2013b. Operation of a cylindrical bioelectrochemical reactor containing carbon fiber fabric for efficient methane fermentation from thickened sewage sludge. *Bioresour. Technol.* 129, 366–373. <https://doi.org/10.1016/j.biortech.2012.11.048>
- Sasaki, K., Hirano, S., Morita, M., Sasaki, D., Matsumoto, N., Ohmura, N., Igarashi, Y., 2011. Bioelectrochemical system accelerates microbial growth and degradation of filter paper. *Appl. Microbiol. Biotechnol.* 89, 449–455. <https://doi.org/10.1007/s00253-010-2972-x>
- Schlager, S., Haberbauer, M., Fuchsbauer, A., Hemmelair, C., Dumitru, L.M., Hinterberger, G., Neugebauer, H., Sariciftci, N.S., 2017. Bio-Electrocatalytic Application of Microorganisms for Carbon Dioxide Reduction to Methane. *ChemSusChem* 10, 226–233. <https://doi.org/10.1002/cssc.201600963>
- Schmidt, F.R., 2005. Optimization and scale up of industrial fermentation processes. *Appl. Microbiol. Biotechnol.* 68, 425–435. <https://doi.org/10.1007/s00253-005-0003-0>
- Schröder, U., Harnisch, F., Angenent, L.T., 2015. Microbial electrochemistry and technology: terminology and classification. *Energy Environ. Sci.* 8, 513–519. <https://doi.org/10.1039/C4EE03359K>
- Scott, K., Murano, C., Rambu, G.A., 2007. A tubular microbial fuel cell. *J Appl Electrochem* 37, 1063–1068. <https://doi.org/10.1007/s10800-007-9355-8>
- Seifert, A.H., Rittmann, S., Herwig, C., 2014. Analysis of process related factors to increase volumetric productivity and quality of biomethane with *Methanothermobacter marburgensis*. *Appl. Energy* 132, 155–162. <https://doi.org/10.1016/j.apenergy.2014.07.002>
- Selumbo, P.A., Merrill, M.D., Logan, B.E., 2009. The use of stainless steel and nickel alloys as low-cost cathodes in microbial electrolysis cells. *J. Power Sources* 190, 271–278. <https://doi.org/10.1016/j.jpowsour.2008.12.144>
- Severinghaus, J.W., Freeman Bradley, A., 1958. Electrodes for Blood P<sub>O</sub>, and p<sub>CO</sub>, Determination1. *J. Appl. Physiol.* 13, 515–520.
- Shah, Y.T., Kelkar, B.G., Godbole, S.P., Deckwer, W.-D., 1982. Design parameters estimations for bubble column reactors. *AIChE J.* 28, 353–379.
- Sharma, M., Bajracharya, S., Gildemyn, S., Patil, S.A., Alvarez-Gallego, Y., Pant, D., Rabaey, K., Dominguez-Benetton, X., 2014. A critical revisit of the key parameters used to describe microbial electrochemical systems. *Electrochim. Acta*

- 140, 191–208. <https://doi.org/10.1016/j.electacta.2014.02.111>
- Shehab, N., Li, D., Amy, G.L., Logan, B.E., Saikaly, P.E., 2013. Characterization of bacterial and archaeal communities in air-cathode microbial fuel cells, open circuit and sealed-off reactors. *Appl. Microbiol. Biotechnol.* 97, 9885–9895. <https://doi.org/10.1007/s00253-013-5025-4>
- Siegert, M., Yates, M.D., Call, D.F., Zhu, X., Spormann, A., Logan, B.E., 2014. Comparison of Nonprecious Metal Cathode Materials for Methane Production by Electromethanogenesis. *ACS Sustain. Chem. Eng.* 2, 910–917. <https://doi.org/10.1021/sc400520x>
- Sleutels, T.H.J.A., Hamelers, H.V.M., Rozendal, R.A., Buisman, C.J.N., 2009. Ion transport resistance in Microbial Electrolysis Cells with anion and cation exchange membranes. *Int. J. Hydrogen Energy* 34, 3612–3620. <https://doi.org/10.1016/j.ijhydene.2009.03.004>
- Sonawane, J.M., Yadav, A., Ghosh, P.C., Adeloju, S.B., 2017. Recent advances in the development and utilization of modern anode materials for high performance microbial fuel cells. *Biosens. Bioelectron.* 90, 558–576. <https://doi.org/10.1016/j.bios.2016.10.014>
- Stadtman, T.C., Barker, H.A., 1951. Studies on the methane fermentation. X. A new formate-decomposing bacterium, *Methanococcus vannielii*. *J. Bacteriol.* 62, 269–280.
- Strong, P.J., Xie, S., Clarke, W.P., 2015. Methane as a resource: Can the methanotrophs add value? *Environ. Sci. Technol.* 49, 4001–4018. <https://doi.org/10.1021/es504242n>
- Sulaymon, A.H., Abbar, A.H., 2012. Scale-Up of Electrochemical Reactors, in: Pesek, K. (Ed.), *Electrolysis*. InTech, pp. 111–133. <https://doi.org/10.5772/48728>
- Sydow, A., Krieg, T., Mayer, F., Schrader, J., Holtmann, D., 2014. Electroactive bacteria - molecular mechanisms and genetic tools. *Appl. Microbiol. Biotechnol.* 98, 8481–8495. <https://doi.org/10.1007/s00253-014-6005-z>
- Takors, R., 2014. *Kommentierte Formelsammlung Bioverfahrenstechnik*. Springer Berlin Heidelberg, Berlin, Heidelberg. <https://doi.org/10.1007/978-3-642-41903-4>
- Thauer, R.K., Kaster, A.-K., Goenrich, M., Schick, M., Hiromoto, T., Shima, S., 2010. Hydrogenases from methanogenic archaea, nickel, a novel cofactor, and H<sub>2</sub> storage. *Annu. Rev. Biochem.* 79, 507–536. <https://doi.org/10.1146/annurev.biochem.030508.152103>
- Thauer, R.K., Kaster, A.-K., Seedorf, H., Buckel, W., Hedderich, R., 2008. Methanogenic archaea: ecologically relevant differences in energy conservation. *Nat. Rev. Microbiol.* 6, 579–591. <https://doi.org/10.1038/nrmicro1931>
- Thrash, J.C., Coates, J.D., 2008. Review: Direct and Indirect Electrical Stimulation of Microbial Metabolism. *Environ. Sci. Technol.* 42, 3921–3931. <https://doi.org/10.1021/es702668w>
- Vassilev, I., Hernandez, P.A., Batlle-Vilanova, P., Freguia, S., Krömer, J.O., Keller, J., Ledezma, P., Viridis, B., 2018. Microbial Electrosynthesis of Isobutyric, Butyric, Caproic Acids, and Corresponding Alcohols from Carbon Dioxide. *ACS Sustain. Chem. Eng.* 6, 8485–8493. <https://doi.org/10.1021/acssuschemeng.8b00739>
- VDI, 2003. *VDI Wärmeatlas*. Springer Berlin Heidelberg, Berlin Heidelberg. <https://doi.org/10.1007/978-3-642-19981-3>
- Vignais, P.M., Billoud, B., 2007. Occurrence, Classification, and Biological Function of Hydrogenases: An Overview. *Chem. Rev.* 107, 4206–4272. <https://doi.org/10.1021/cr050196r>
- Villano, M., Aulenta, F., Ciucci, C., Ferri, T., Giuliano, A., Majone, M., 2010. Bioelectrochemical reduction of CO<sub>2</sub> to CH<sub>4</sub> via direct and indirect extracellular electron transfer by a hydrogenophilic methanogenic culture. *Bioresour. Technol.* 101, 3085–3090. <https://doi.org/10.1016/j.biortech.2009.12.077>
- Villano, M., Monaco, G., Aulenta, F., Majone, M., 2011. Electrochemically assisted methane production in a biofilm reactor. *J. Power Sources* 196, 9467–9472. <https://doi.org/10.1016/j.jpowsour.2011.07.016>
- Votruba, J., Sobotka, M., 1992. Physiological similarity and bioreactor scale-up. *Folia Microbiol. Off. J. Inst. Microbiol. Acad. Sci. Czech Repub.* 37, 331–345. <https://doi.org/10.1007/BF02815659>
- Wang, A., Liu, W., Ren, N., Cheng, H., Lee, D.J., 2010. Reduced internal resistance of microbial electrolysis cell (MEC) as factors of configuration and stuffing with granular activated carbon. *Int. J. Hydrogen Energy* 35, 13488–13492. <https://doi.org/10.1016/j.ijhydene.2009.11.124>
- Watano, S., Sato, Y., Miyanami, K., 1996. Scale-Up of Agitation Fluidized Bed Granulation. IV Scale-Up Theory Based on the Kinetic Energy Similarity. *Chem. Pharm. Bull.* 43, 1227–1230.

- Watson, V.J., Logan, B.E., 2010. Power production in MFCs inoculated with *Shewanella oneidensis* MR-1 or mixed cultures. *Biotechnol. Bioeng.* 105, 489–498. <https://doi.org/10.1002/bit.22556>
- Weiland, P., 2010. Biogas production: current state and perspectives. *Appl. Microbiol. Biotechnol.* 85, 849–860. <https://doi.org/10.1007/s00253-009-2246-7>
- Wilhelm, E., Battino, R., Wilcock, R.J., 1977. Low-pressure solubility of gases in liquid water. *Chem. Rev.* 77, 219–262. <https://doi.org/10.1021/cr60306a003>
- Williams, J.A., 2002. Keys to Bioreactor Selections. *CEP* 34–41.
- Xu, H., Wang, K., Holmes, D.E., 2014. Bioelectrochemical removal of carbon dioxide (CO<sub>2</sub>): An innovative method for biogas upgrading. *Bioresour. Technol.* 173, 392–398. <https://doi.org/10.1016/j.biortech.2014.09.127>
- Yan, H., Catania, C., Bazan, G.C., 2015. Membrane-intercalating conjugated oligoelectrolytes: Impact on bioelectrochemical systems. *Adv. Mater.* 27, 2958–2973. <https://doi.org/10.1002/adma.201500487>
- Ye, Z., Ellis, M.W., Nain, A.S., Behkam, B., 2017. Effect of electrode sub-micron surface feature size on current generation of *Shewanella oneidensis* in microbial fuel cells. *J. Power Sources* 347, 270–276. <https://doi.org/10.1016/j.jpowsour.2017.02.032>
- Zeppilli, M., Lai, A., Villano, M., Majone, M., 2016. Anion vs cation exchange membrane strongly affect mechanisms and yield of CO<sub>2</sub> fixation in a microbial electrolysis cell. *Chem. Eng. J.* 304, 10–19. <https://doi.org/10.1016/j.cej.2016.06.020>
- Zhang, T., Nie, H., Bain, T.S., Lu, H., Cui, M., Snoeyenbos-West, O.L., Franks, A.E., Nevin, K.P., Russell, T.P., Lovley, D.R., 2013. Improved cathode materials for microbial electrosynthesis. *Energy Environ. Sci.* 6, 217–224. <https://doi.org/10.1039/c2ee23350a>
- Zhang, Y., Merrill, M.D., Logan, B.E., 2010. The use and optimization of stainless steel mesh cathodes in microbial electrolysis cells. *Int. J. Hydrogen Energy* 35, 12020–12028. <https://doi.org/10.1016/j.ijhydene.2010.08.064>
- Zhao, C., Wang, Y., Shi, F., Zhang, J., Zhu, J.-J., 2013. High biocurrent generation in *Shewanella*-inoculated microbial fuel cells using ionic liquid functionalized graphene nanosheets as an anode. *Chem. Commun.* 49, 6668. <https://doi.org/10.1039/c3cc42068j>
- Zhen, G., Kobayashi, T., Lu, X., Xu, K., 2015. Understanding methane bioelectrosynthesis from carbon dioxide in a two-chamber microbial electrolysis cells (MECs) containing a carbon biocathode. *Bioresour. Technol.* 186, 141–148. <https://doi.org/10.1016/j.biortech.2015.03.064>

## List of Figures

Figure 1: Different bioelectrochemical applications .....	3
Figure 2: Methanogenesis pathways .....	7
Figure 3: Possible means of electron uptake in bioelectromethanogenesis.....	8
Figure 4: Current time course in chronoamperometric, abiotic experiments with different electrodes.....	28
Figure 5: System resistances of three different systems .....	29
Figure 6: Resistances of the different system parts in bubble column reactor and H-cell .....	29
Figure 7: Nyquist plot for carbon fabric electrode.....	32
Figure 8: Cyclic voltammograms of different electrodes.....	34
Figure 9: Equipotential lines in bubble column reactor with different electrodes .....	36
Figure 10: Temperature in bubble column reactor.....	37
Figure 11: Performance of bioelectromethanogenesis using different ODs.....	45
Figure 12: Results of the potential optimization in the bubble column reactor.....	47
Figure 13: Performance of the bioelectromethanogenesis process using different electrodes .....	49
Figure 14: Electron transfer and energy efficiency using different electrodes.....	50
Figure 15: Methane production rates for different electrode sizes.....	51
Figure 16: Performance using different electrode sizes .....	52
Figure 17: Performance using different anode sizes .....	54
Figure 18: Resistances of different ion exchange membranes .....	55
Figure 19: Performance with different membrane types.....	57
Figure 20: Performance of bioelectromethanogenesis using different CO <sub>2</sub> concentrations .....	60
Figure 21: Ratio between direct and indirect electron transfer by the addition of MOPS buffer .....	61
Figure 22: Performance of bioelectromethanogenesis at different gassing rates .....	62
Figure 23: Performance of bioelectromethanogenesis using different sparger plates (SP) .....	64
Figure 24: System performance after power gap .....	65
Figure 25: System response on gassing shut-off.....	66
Figure 26: System response on gas composition change .....	67
Figure 27: System response on temperature change .....	68
Figure 28: Comparison of system performances during and after failure simulation .....	69
Figure 29: Performance of bioelectromethanogenesis using applied cell voltage or applied current .....	72
Figure 30: Comparison of different reactors for bioelectromethanogenesis .....	75
Figure 31: Long term stability of the bioelectromethanogenesis process: production and efficiency.....	76
Figure 32: Long term stability of the bioelectromethanogenesis process: pH and conductivity .....	76
Figure 33: Long term stability of the bioelectromethanogenesis process: current density.....	77
Figure 34: Numbering-Up of bioelectromethanogenesis .....	79
Figure 35: Bubbles observed in the pilot scale reactor .....	80
Figure 36: Electrochemical characterization of pilot scale reactor .....	82
Figure 37: Gas production rates and current densities obtained in pilot plant reactor .....	83
Figure 38: Inhibition of methanogenesis by reactor materials .....	86
Figure 39: Specific methane production rates reviewed by Blasco-Gomez et al., 2017 .....	87
Figure 40: Comparison of bioelectromethanogenesis to other methane producing technologies .....	88
Figure 41: Current progress of MFC in bubble column reactor.....	89
Figure 42: MFC performance in different bioelectrochemical systems.....	90
Figure 43: Improvement of methane production rates by process optimization .....	92
Figure 44: Bubble column reactor side views and head plate.....	99

---

Figure 45: PTFE spargers and bottom of bubble column reactor .....	99
Figure 46: Bioelectrochemical stirred tank reactor .....	101
Figure 47: Tafel plot obtained from CV in bubble column reactor with graphite rod electrode.....	103
Figure 48: Measuring points for resistances.....	105
Figure 49: Dynamic method for $k_L a$ measurement.....	106
Figure 50: Flow regimes in bubble column reactors .....	108
Figure 51: Newton-Reynolds diagram for different stirrer types .....	109
Figure 52: Heat loss of the bubble column system.....	110
Figure 53: Different electrode materials.....	113
Figure 54: Scanning electron microscopy images of different electrodes, 250x magnification .....	114
Figure 55: Different operational conditions for numbering up.....	125
Figure 56: Working chamber and membrane windows pilot scale reactor.....	128
Figure 57: Bottom plate and gas sparger of pilot scale reactor.....	129
Figure 58: Lid and side ports of pilot scale reactor .....	129
Figure 59: Electrodes of pilot scale reactor .....	130
Figure 60: Pilot scale reactor with counter chamber .....	130

## List of Tables

Table 1: Current generation in MFCs inoculated with <i>S. oneidensis</i> MR-1.....	5
Table 2: Enriched methanogens in electroactive microbial consortia (Jabłoński et al., 2015).....	10
Table 3: Reactor types for methanogenic MES .....	14
Table 4: Process characterization: Geometrical and physical parameters.....	16
Table 5: Process characterization: electrochemical parameters .....	17
Table 6: Process characterization: biological parameters .....	17
Table 7: Process characterization: Evaluation parameters .....	18
Table 8: Cathode materials for MES .....	21
Table 9: Parameters of abiotically tested electrodes .....	30
Table 10: Heat losses for the bubble column and the stirred tank reactor.....	38
Table 11: Gassing parameters for different reactor systems .....	39
Table 12: Results of the first bioelectromethanogenic tests at -0.9 V vs. Ag/AgCl.....	42
Table 13: Performance using different working electrodes .....	50
Table 14: Performance of bioelectromethanogenesis with different anode materials.....	53
Table 15: Performance using different membrane sizes .....	58
Table 16: Performance alteration by application of an external loop .....	59
Table 17: Performance alteration by addition of MOPS buffer .....	61
Table 18: Performance of bioelectromethanogenesis using applied cell voltage or applied current.....	70
Table 19: Bubble column reactor performance under starting and optimized condition .....	73
Table 20: Comparison of H-cell performance under starting and optimized conditions.....	74
Table 21: Heat loss calculation for pilot scale reactor .....	81
Table 22: Performance comparison of pilot plant and lab scale reactor .....	84
Table 23: Process and measuring equipment .....	95
Table 24: Abiotic chronoamperometric experiments.....	102
Table 25: Dimensionless numbers for bubble columns .....	108
Table 26: Parameters of Stirred tank reactors .....	109
Table 27: Variables for the calculation of heat losses through reactor walls .....	111
Table 28: Electrode material properties .....	115
Table 29: Properties of <i>Methanococcus maripaludis</i> .....	117
Table 30: Starting conditions for process optimization .....	118
Table 31: Process optimization parameters .....	119
Table 32: Operating conditions for membrane optimization .....	120
Table 33: Operating conditions for gassing optimization .....	121
Table 34: Optimized conditions for experiments with applied voltage and applied current .....	122
Table 35: Optimal conditions found for the bubble column reactor .....	123
Table 36: Comparison of bioelectromethanogenesis in different reactors .....	123
Table 37: Operation conditions for MFC experiments .....	132

## Appendix

### Used chemicals

Chemical	CAS number	Purity	Supplier
$(\text{NH}_4)_2\text{SO}_4$	7783-20-2	99.50%	Carl Roth GmbH & Co KG, Karlsruhe, Germany
Na-DL-lactate solution	72-17-3	50%	Sigma Aldrich Inc., now Merck KGaA, Darmstadt, Germany
Biotin	58-85-8	99%	Sigma Aldrich Inc., now Merck KGaA, Darmstadt, Germany
$\text{CaCl}_2 \cdot 2 \text{H}_2\text{O}$	10035-04-8	p.a.	Merck KGaA, Darmstadt, Germany
Citric acid	77-92-9	99.50%	Carl Roth GmbH & Co KG, Karlsruhe, Germany
$\text{CoCl}_2$	7646-79-9	p.a.	Fluka, now Merck KGaA, Darmstadt, Germany
$\text{CoSO}_4 \cdot 7 \text{H}_2\text{O}$	10026-24-1	p.a.	Merck KGaA, Darmstadt, Germany
$\text{CuSO}_4 \cdot 5 \text{H}_2\text{O}$	7758-99-8	98%	Sigma Aldrich Inc., now Merck KGaA, Darmstadt, Germany
Cystein-HCl	52-89-1	98%	Sigma Aldrich Inc., now Merck KGaA, Darmstadt, Germany
Ca-pantothenate	137-08-6		Sigma Aldrich Inc., now Merck KGaA, Darmstadt, Germany
$\text{Fe}(\text{NH}_4)_2(\text{SO}_4)_2 \cdot 6 \text{H}_2\text{O}$	7783-85-9	p.a.	Sigma Aldrich Inc., now Merck KGaA, Darmstadt, Germany
$\text{FeSO}_4 \cdot 7 \text{H}_2\text{O}$	7782-63-0	99.50%	Sigma Aldrich Inc., now Merck KGaA, Darmstadt, Germany
Folic acid	59-30-3	97%	Fluka, now Merck KGaA, Darmstadt, Germany
$\text{H}_2\text{O}_2$	7722-84-1	30%	Carl Roth GmbH & Co KG, Karlsruhe, Germany
$\text{H}_2\text{SO}_4$	7664-93-9	96%	Carl Roth GmbH & Co KG, Karlsruhe, Germany
$\text{H}_3\text{BO}_3$	10043-35-3	p.a.	Carl Roth GmbH & Co KG, Karlsruhe, Germany
HEPES buffer	7365-45-9		Carl Roth GmbH & Co KG, Karlsruhe, Germany

$K_2HPO_4$	7758-11-4	p.a.	Carl Roth GmbH & Co KG, Karlsruhe, Germany
$KAl(SO_4)_2 \cdot 12 H_2O$	7784-24-9	p.a.	Alfa Aesar, now Thermo Fisher (Kandel) GmbH, Landau, Germany
KCl	7447-40-7	puriss.	Carl Roth GmbH & Co KG, Karlsruhe, Germany
$KH_2PO_4$	7365-45-9	> 99 %	Carl Roth GmbH & Co KG, Karlsruhe, Germany
KOH	04.11.7758	85%	Carl Roth GmbH & Co KG, Karlsruhe, Germany
LB medium		for molecular biology	Carl Roth GmbH & Co KG, Karlsruhe, Germany
Lipoic acid	1077-28-7	98%	Sigma Aldrich Inc., now Merck KGaA, Darmstadt, Germany
$MgCl_2 \cdot 6 H_2O$	7791-18-6	puriss.	Sigma Aldrich Inc., now Merck KGaA, Darmstadt, Germany
$MgSO_4 \cdot 7 H_2O$	10034-99-8	p.a.	Carl Roth GmbH & Co KG, Karlsruhe, Germany
$MnSO_4 \cdot H_2O$	10034-34-96-5	p.a.	Merck KGaA, Darmstadt, Germany
MOPS buffer	1132-61-2	p.a.	Carl Roth GmbH & Co KG, Karlsruhe, Germany
$Na_2HPO_4$	7558-79-4	99%	Carl Roth GmbH & Co KG, Karlsruhe, Germany
$Na_2MoO_4 \cdot 2 H_2O$	10102-40-6	> 99 %	Carl Roth GmbH & Co KG, Karlsruhe, Germany
$Na_2S \cdot 9 H_2O$	1313-84-4	98%	Sigma Aldrich Inc., now Merck KGaA, Darmstadt, Germany
$Na_2SeO_3 \cdot 5 H_2O$	26970-82-1	p.a.	Fluka, now Merck KGaA, Darmstadt, Germany
$Na_2WO_4 \cdot 2 H_2O$	10213-10-2	> 99% BioUltra	Sigma Aldrich Inc., now Merck KGaA, Darmstadt, Germany
Na-Acetate	127-09-3	> 99 %	Merck KGaA, Darmstadt, Germany
NaCl	7647-14-5	puriss.	Carl Roth GmbH & Co KG, Karlsruhe, Germany
$NaHCO_3$	144-55-8	p.a.	Sigma Aldrich Inc., now Merck KGaA, Darmstadt, Germany
$NH_4Cl$	12125-02-9	puriss.	Sigma Aldrich Inc., now Merck

			KGaA, Darmstadt, Germany
NiCl <sub>2</sub>	7718-54-9	98%	Fluka, now Merck KGaA, Darmstadt, Germany
NiCl <sub>2</sub> * 6 H <sub>2</sub> O	7719-20-0	puriss.	Fluka, now Merck KGaA, Darmstadt, Germany
Nicotinic acid	59-67-6	p.a.	Fluka, now Merck KGaA, Darmstadt, Germany
Nitriloacetic acid	139-13-9	99%	Sigma Aldrich Inc., now Merck KGaA, Darmstadt, Germany
p-aminobenzoic acid	150-13-0	p.a.	Sigma Aldrich Inc., now Merck KGaA, Darmstadt, Germany
Peptone	91079-40-2	from Caseine	Carl Roth GmbH & Co KG, Karlsruhe, Germany
Pyridoxine-HCl	58-56-0	> 99 %	Carl Roth GmbH & Co KG, Karlsruhe, Germany
Riboflavin	83-88-5	p.a.	Sigma Aldrich Inc., now Merck KGaA, Darmstadt, Germany
Thiamine-HCl * 2 H <sub>2</sub> O	67-03-8	p.a.	Merck KGaA, Darmstadt, Germany
Vitamine B12	68-19-9	analytical standard	Sigma Aldrich Inc., now Merck KGaA, Darmstadt, Germany
Yeast extract	02.01.8013	f. bactereology	Carl Roth GmbH & Co KG, Karlsruhe, Germany
NiCl <sub>2</sub>	7646-85-7	98%	Sigma Aldrich Inc., now Merck KGaA, Darmstadt, Germany
ZnSO <sub>4</sub> * 7 H <sub>2</sub> O	7446-20-0	p.a.	Sigma Aldrich Inc., now Merck KGaA, Darmstadt, Germany

## Culture and BES media

### M141 Complex growth medium for cultivation of *M. maripaludis*

0.35 g<sup>\*l</sup><sup>-1</sup> KCl; 4 g<sup>\*l</sup><sup>-1</sup> MgCl<sub>2</sub> \* 6 H<sub>2</sub>O, 3.45 g<sup>\*l</sup><sup>-1</sup> MgSO<sub>4</sub> \* 7 H<sub>2</sub>O; 0.25 g<sup>\*l</sup><sup>-1</sup> NH<sub>4</sub>Cl; 0.14 g<sup>\*l</sup><sup>-1</sup> CaCl<sub>2</sub> \* 2 H<sub>2</sub>O; 0.14 g<sup>\*l</sup><sup>-1</sup> K<sub>2</sub>HPO<sub>4</sub>; 18 g<sup>\*l</sup><sup>-1</sup> NaCl; 0.002 g<sup>\*l</sup><sup>-1</sup> Fe(NH<sub>4</sub>)<sub>2</sub>(SO<sub>4</sub>)<sub>2</sub> \* 6 H<sub>2</sub>O; 1 g<sup>\*l</sup><sup>-1</sup> Na-Acetate; 2 g<sup>\*l</sup><sup>-1</sup> petone; 2 g<sup>\*l</sup><sup>-1</sup> yeast extract; 5 g<sup>\*l</sup><sup>-1</sup> NaHCO<sub>3</sub>; 10 ml<sup>\*l</sup><sup>-1</sup> trace element solution 141; 10 ml<sup>\*l</sup><sup>-1</sup> vitamin solution 141; 0.5 g<sup>\*l</sup><sup>-1</sup> Cystein-HCl; 0.5 g<sup>\*l</sup><sup>-1</sup> Na<sub>2</sub>S \* 9 H<sub>2</sub>O

All components besides vitamin solution, NaHCO<sub>3</sub>, Na<sub>2</sub>S \* 9 H<sub>2</sub>O and Cystein-HCl were dissolved in deionized water and purged with N<sub>2</sub>/CO<sub>2</sub> (80/20) gas mixture for 45 min under permanent stirring for anaerobization. Than NaHCO<sub>3</sub> was added and the medium was filled into septum flasks (either 50 ml in 250 ml septum flask or 300 ml in 1 liter septum flask) anaerobically and sealed. Vitamin solution, Na<sub>2</sub>S x 9 H<sub>2</sub>O and Cystein-HCl were filtrated and added sterile after autoclaving.

### Vitamin solution 141

2 mg<sup>\*l</sup><sup>-1</sup> biotin; 2 mg<sup>\*l</sup><sup>-1</sup> folic acid; 10 mg<sup>\*l</sup><sup>-1</sup> pyridoxine-HCl; 5 mg<sup>\*l</sup><sup>-1</sup> thiamine-HCl 2 H<sub>2</sub>O; 5 mg<sup>\*l</sup><sup>-1</sup> riboflavin; 5 mg<sup>\*l</sup><sup>-1</sup> nicotinic acid; 5 mg<sup>\*l</sup><sup>-1</sup> Ca-pantothenate; 0.1 mg<sup>\*l</sup><sup>-1</sup> vitamine B12; 5 mg<sup>\*l</sup><sup>-1</sup> p-aminobenzoic acid; 5 mg<sup>\*l</sup><sup>-1</sup> lipoic acid

### Trace element solution 141

1.5 g<sup>\*l</sup><sup>-1</sup> nitriloacetic acid; 3 g<sup>\*l</sup><sup>-1</sup> MgSO<sub>4</sub> \* 7 H<sub>2</sub>O; 0.5 g<sup>\*l</sup><sup>-1</sup> MnSO<sub>4</sub> \* H<sub>2</sub>O; 1 g<sup>\*l</sup><sup>-1</sup> NaCl; 0.1 g<sup>\*l</sup><sup>-1</sup> FeSO<sub>4</sub> \* 7 H<sub>2</sub>O; 0.18 g<sup>\*l</sup><sup>-1</sup> CoSO<sub>4</sub> \* 7 H<sub>2</sub>O; 0.1 g<sup>\*l</sup><sup>-1</sup> CaCl<sub>2</sub> \* 2 H<sub>2</sub>O; 0.18 g<sup>\*l</sup><sup>-1</sup> ZnSO<sub>4</sub> \* 7 H<sub>2</sub>O; 0.01 g<sup>\*l</sup><sup>-1</sup> CuSO<sub>4</sub> \* 5 H<sub>2</sub>O; 0.02 g<sup>\*l</sup><sup>-1</sup> KAl(SO<sub>4</sub>)<sub>2</sub> \* 12 H<sub>2</sub>O; 0.01 g<sup>\*l</sup><sup>-1</sup> H<sub>3</sub>BO<sub>3</sub>; 0.01 g<sup>\*l</sup><sup>-1</sup> Na<sub>2</sub>MoO<sub>4</sub> \* 2 H<sub>2</sub>O; 0.03 g<sup>\*l</sup><sup>-1</sup> NiCl<sub>2</sub> \* 6 H<sub>2</sub>O; 0.3 mg<sup>\*l</sup><sup>-1</sup> Na<sub>2</sub>SeO<sub>3</sub> \* 5 H<sub>2</sub>O; 0.4 mg<sup>\*l</sup><sup>-1</sup> Na<sub>2</sub>WO<sub>4</sub> \* 2 H<sub>2</sub>O

### MES for Bioelectromethanogenesis experiments

0.35 g<sup>\*l</sup><sup>-1</sup> KCl; 4 g<sup>\*l</sup><sup>-1</sup> MgCl<sub>2</sub> \* 6 H<sub>2</sub>O, 3.45 g<sup>\*l</sup><sup>-1</sup> MgSO<sub>4</sub> \* 7 H<sub>2</sub>O; 0.25 g<sup>\*l</sup><sup>-1</sup> NH<sub>4</sub>Cl; 0.14 g<sup>\*l</sup><sup>-1</sup> CaCl<sub>2</sub> \* 2 H<sub>2</sub>O; 0.14 g<sup>\*l</sup><sup>-1</sup> K<sub>2</sub>HPO<sub>4</sub>; 18 g<sup>\*l</sup><sup>-1</sup> NaCl; 0.002 g<sup>\*l</sup><sup>-1</sup> Fe(NH<sub>4</sub>)<sub>2</sub>(SO<sub>4</sub>)<sub>2</sub> \* 6 H<sub>2</sub>O; 1 g<sup>\*l</sup><sup>-1</sup> 5 g<sup>\*l</sup><sup>-1</sup> NaHCO<sub>3</sub>; 10 ml<sup>\*l</sup><sup>-1</sup> trace element solution 141; 10 ml<sup>\*l</sup><sup>-1</sup> vitamin solution 141

All components besides vitamin solution and NaHCO<sub>3</sub>, were dissolved in deionized water and autoclaved within the used reactor. After sparging with the desired gas mixture for the process NaHCO<sub>3</sub> and vitamin solution were added sterile.

### Phosphate buffer for bioelectrochemical experiments

5.6 g<sup>\*l</sup><sup>-1</sup> KH<sub>2</sub>PO<sub>4</sub>; 9.2 g<sup>\*l</sup><sup>-1</sup> Na<sub>2</sub>HPO<sub>4</sub>

**LB**

Purchased from Carl Roth GmbH & Co KG, Karlsruhe, Germany.

**LSBM**

19.62 g<sup>\*l</sup><sup>-1</sup> 50 % NaC<sub>3</sub>H<sub>5</sub>O<sub>3</sub> solution; 23.83 g<sup>\*l</sup><sup>-1</sup> HEPES buffer; 0.225 g<sup>\*l</sup><sup>-1</sup> KH<sub>2</sub>PO<sub>4</sub>; 0.225 g<sup>\*l</sup><sup>-1</sup> K<sub>2</sub>HPO<sub>4</sub>; 0.46 g<sup>\*l</sup><sup>-1</sup> NaCl; 0.225 g<sup>\*l</sup><sup>-1</sup> (NH<sub>4</sub>)SO<sub>4</sub>; 5 ml<sup>\*l</sup><sup>-1</sup> trace element solution; 5 ml<sup>\*l</sup><sup>-1</sup> vitamin solution.

All components were dissolved in deionized water and the pH set to pH = 6.5 with KOH.

**Trace element solution LSBM**

23.4 g<sup>\*l</sup><sup>-1</sup> MgSO<sub>4</sub> \* 7 H<sub>2</sub>O; 26 g<sup>\*l</sup><sup>-1</sup> ZnCl<sub>2</sub>; 5 g<sup>\*l</sup><sup>-1</sup> Na<sub>2</sub>MoO<sub>4</sub> \* 2 H<sub>2</sub>O; 4.8 g<sup>\*l</sup><sup>-1</sup> NiCl<sub>2</sub>; 5 g<sup>\*l</sup><sup>-1</sup> Na<sub>2</sub>WO<sub>4</sub> \* 2 H<sub>2</sub>O; 1.5 g<sup>\*l</sup><sup>-1</sup> C<sub>6</sub>H<sub>9</sub>NO<sub>6</sub>; 0.452 g<sup>\*l</sup><sup>-1</sup> MnSO<sub>4</sub> \* 1 H<sub>2</sub>O; 1 g<sup>\*l</sup><sup>-1</sup> NaCl; 0.1 g<sup>\*l</sup><sup>-1</sup> FeSO<sub>4</sub> \* 7 H<sub>2</sub>O; 0.1 g<sup>\*l</sup><sup>-1</sup> CoCl<sub>2</sub>; 0.1 g<sup>\*l</sup><sup>-1</sup> CaCl<sub>2</sub> \* 2 H<sub>2</sub>O; 0.01 g<sup>\*l</sup><sup>-1</sup> CuSO<sub>4</sub> \* 5 H<sub>2</sub>O; 0.01 g<sup>\*l</sup><sup>-1</sup> AlK(SO<sub>4</sub>)<sub>2</sub> \* 12 H<sub>2</sub>O; 0.018 g<sup>\*l</sup><sup>-1</sup> H<sub>3</sub>BO<sub>3</sub>

**Vitamin solution LSBM**

0.002 g<sup>\*l</sup><sup>-1</sup> biotin; 0.002 g<sup>\*l</sup><sup>-1</sup> folic acid; 0.01 g<sup>\*l</sup><sup>-1</sup> pyridoxine-HCl; 0.005 g<sup>\*l</sup><sup>-1</sup> thiamine-HCl; 0.005 g<sup>\*l</sup><sup>-1</sup> riboflavin; 0.005 g<sup>\*l</sup><sup>-1</sup> nicotinic acid; 0.005 g<sup>\*l</sup><sup>-1</sup> Ca-pantothenate; 0.0001 g<sup>\*l</sup><sup>-1</sup> cyanocobalamin; 0.005 g<sup>\*l</sup><sup>-1</sup> p-aminobenzoic acid; 0.005 g<sup>\*l</sup><sup>-1</sup> lipoic acid